Entwicklung des Fast Timing $\overline{\text{P}}$ANDA Barrel Time-of-Flight Detektors

Development of the Fast Timing $\overline{\text{P}}$ANDA Barrel Time-of-Flight Detector

Dissertation zur Erlangung des Doktorgrades der Naturwissenschaften
an der Justus-Liebig-Universität Gießen

vorgelegt von

Sebastian Zimmermann

Oktober 2020

1. Gutachter: Prof. Dr. K.-Th. Brinkmann

2. Gutachter: Priv.-Doz. Dr. J. Marton

Contents

Zusammenfassung

Der Barrel Time-of-Flight Detektor (B-ToF) ist ein Timing-Detektor für das $\overline{\text{P}}$ANDA Experiment, das derzeit an der Facility for Anitproton and Ion Research (FAIR) in Darmstadt, Deutschland, gebaut wird. Offene Fragen der Hadronenphysik werden in fixed-target $\bar{p}p$ Kollisionen untersucht. Für diese werden Antiprotonen bis zu einem Impuls von 15 GeV/c beschleunigt und dabei eine Schwerpunktsenergie von bis zu 5.5 GeV erzeugt. Die untersuchten Themen umfassen die Charmonium-Spektroskopie und die Suche nach exotischen Teilchen und Hybriden, sowie die Untersuchung von Hyperkernen und von Hadronen in der Materie. In diesem Zusammenhang ergänzt der B-ToF die Teilchenidentifikationsinformation der DIRC-Detektoren und liefert durch relative Flugzeitmessungen wertvolle Informationen über Teilchen im unteren Impulsbereich bis etwa 1 GeV/c.

Eine >1800 mm lange Leiterplatte verbindet die SiPMs auf den Szintillatoren zur Front-End-Elektronik, bietet mechanische Unterstützung für die Szintillatorkacheln und fungiert als Rückgrat des Detektors. Um das optimale Layout zu bestimmen werden drei Prototyp-Iterationen getestet und auf die Crosstalk-Stärke sowie das Ausmaß der Signaldämpfungseffekte untersucht. Während das Übersprechen in allen Design-Iterationen vernachlässigbar ist, kann eine Amplitudenreduktion von (11.7 ± 0.5) % für den neuesten Leiterplatten-Prototypen unter Verwendung verlustarmer Materialien beobachtet werden. Dies liegt weit über der Dämpfung eines koaxialen Standard Kabel. Große Signalanstiegszeiterhöhungen aufgrund der verwendeten Steckverbinder führen zu einer Verdoppelung der Anstiegszeit. Das Ausmaß dieser Effekte auf die Zeitauflösung ist jedoch noch zu bestimmen.

Um die angestrebte Funktionalität zu erreichen, ist ein hochgranulares und effizientes Detektordesign mit einer Zeitauflösung von unter 100 ps erforderlich. Der Detektor besteht aus 16 identischen Abschnitten mit jeweils 120 szintillierenden Kacheln, die von einem Array aus vier in Reihe geschalteten Silicon Photomultiplier (SiPMs) ausgelesen werden.

Diese Arbeit präsentiert Zeitauflösungsscans mit einer ^{90}Sr-Quelle über die gesamte Szintillatorfläche, um die Detektorleistung zu bewerten und die optimale Dicke der Szintillatorkacheln zu bestimmen. Im Vergleich von vier 3 mm bis 6 mm dicken Szintillatorkacheln, zeigen die Messungen, dass ein 5 mm dicker Szintillator, der eine mittlere Zeitauflösung von 52,3 ps mit einer Streuung von ±5,9 ps über die gesamte Oberfläche, die optimale Wahl für den Detektor darstellt. Zusätzlich wurde die Leistung in Tests an der T9-beamline am CERN unter Bedingungen näher an den zu erwarteten Bedingungen in $\overline{\text{P}}$ANDA verifiziert. Unter Verwendung eines Mischteilchenstrahls, der hauptsächlich Pionen und Kaonen enthält, wurden drei Szintillator Module mit SiPMs verschiedener Hersteller untersucht. Zeitauflösungen von (55.8 ± 4.3) ps bis (80.1 ± 1.5) ps wurden für Detektormodule gemessen.

Abstract

The Barrel Time-of-Flight Detector (B-ToF) is a timing detector for the $\overline{\text{P}}$ANDA experiment which is currently under construction at the Facility for Antiproton and Ion Research (FAIR) in Darmstadt, Germany. In fixed target $\bar{p}p$ collisions, with antiprotons accelerated up to a momentum of 15 GeV/c producing a center of mass energy of up to 5.5 GeV, open questions of hadron physics will be studied. This effort includes charmonium spectroscopy and the search for exotics and hybrids as well as the study of hypernuclei and of hadrons in matter. In this context the B-ToF complements the particle identification information of the DIRC detectors and provides valuable information for particles in the lower momentum range up to about 1 GeV/c via relative time-of-flight measurements.

A >1800 mm long transmission line PCB connects the SiPMs on the scintillators to the front-end electronics and provides mechanical support to the scintillator tiles acts as the backbone of the detector. In order to determine the best performing layout three prototype iterations are examined and tested for the crosstalk level and signal attenuation effects. While the crosstalk is negligible in all design iterations an amplitude reduction of (11.7 ± 0.5) % is observed for the newest board prototype using low loss materials. This is well above the attenuation of a standard coaxial cable. The employed connections lead to a doubling of the signal rise time. The effect of this on the time resolution is yet to be determined.

To achieve intended functionality a highly granular and efficient detector design is necessary providing a time resolution of below 100 ps. The detector is made up of 16 identical sections each carrying 120 scintillating tiles, which are read out by an array of four SiPMs connected in series.

This work presents time resolution scans using a ^{90}Sr source over the entire scintillator surface in order to evaluate the detector performance and determine the optimal scintillator tile thickness. Comparing four 3 mm to 6 mm thick scintillator tiles, the measurements show that a 5 mm thick scintillator providing a mean time resolution of 52.3 ps with a spread of $\pm$5.9 ps over the entire surface, is the optimal choice for the detector. In addition the performance was verified in test beam measurements at the T9 beamline at CERN under conditions closer to the expected conditions in $\overline{\text{P}}$ANDA using mixed particle beam mainly containing pions and kaons. Time resolutions of (55.8 ± 4.3) ps to (80.1 ± 1.5) ps were measured for detector modules utilizing SiPMs by different manufacturers.

Chapter 1

Introduction

While there is a push towards higher and higher energy experiments in hadron physics, reaching regimes that never have been probed before pushing the frontier into new territories, many more accessible energy regimes are left understudied. The $\overline{\text{P}}$ANDA experiment is making efforts to address this by providing collisions of up to 15 GeV/c antiprotons on protons in a fixed target experiment reaching center of mass energies of up to 5.5 GeV.

One question $\overline{\text{P}}$ANDA aims to answer is what makes up the mass of a hadron. Today it is unclear what exactly constitutes more than 98 % of the nucleon mass since less than 2 % can be attributed to the rest mass of the valence quarks making up the particle. Large parts of this energy are bound in the kinetic energy and interactions between the quarks, but this is not well understood. Other areas of interest include hadron spectroscopy and the search for exotic particles, hypernuclei as well as studies of the nucleon structure.

Like other modern experiments, $\overline{\text{P}}$ANDA consists of many subdetectors each providing information on a particular aspect of the interaction, in order to reconstruct the $\bar{p}p$ annihilation processes. For a full picture of the interactions the particles need to be identified. Since measurements of the particle mass or energy directly, lack the necessary resolution other dedicated particle identification systems are required. $\overline{\text{P}}$ANDA will utilize a DIRC system which however is blind for slow particles below momenta of 0.5 GeV/c to 1 GeV/c. For reactions like $\bar{p} + p \rightarrow \Xi^- \bar{\Xi}^+$, in which $\bar{\Xi}^+$ decays into at least two positive kaons with a momentum distribution around 500 MeV/c, additional identification information is necessary. The Barrel Time-of-Flight Detector aims to provide this information by measuring the time-of-flight of a particle from the interaction point to the detector with an excellent time resolution. Combining this information with particle momentum information the mass and hence, the identity of a particle can be determined.

In order to produce the rare states which are the subject of studies at $\overline{\text{P}}$ANDA in significant numbers to be able to draw reliable conclusions, high interactions rates are necessary. To separate the collision events occurring in rapid succession a detector system with a sufficient time resolution such as the Barrel Time-of-Flight Detector is necessary.

This work provides an introduction to the Barrel Time-of-Flight Detector highlighting key aspects of its highly efficient design such as the serial connection of the SiPMs and the large PCB for data transmission. The working principle of the B-ToF which to be precise does not measure the time-of-flight but determines its

most likely value via relative ToF calculations, is explained.

The B-ToF will be equipped with large PCBs for the signal transmission, providing a compact and efficient way of connecting the photosensors to the readout electronics. The influence of different design parameters on the signal amplitude, rise time and crosstalk are studied.

Additionally time resolution measurements using events produced by a ^{90}Sr source are employed to determine the optimal scintillator thickness and surface treatment. To evaluate the detector performance closer to the conditions in $\overline{\text{P}}$ANDA, data from a beamtime at CERN is evaluated showing performance differences for different SiPM manufacturers and SiPM configurations.

Chapter 2

$\overline{\text{P}}$anda at FAIR

The $\overline{\text{P}}$ANDA experiment will be part of the FAIR facility which is being built in Darmstadt.

2.1 The FAIR Facility

FAIR is an international accelerator facility hosting multiple different experiments, covering Atomic, Plasma Physics and Application (**APPA**), Nuclear Structure, Astrophysics and Reactions (**NUSTAR**), Nuclear Matter Physics (**CBM**) and Physics with High Energy Antiprotons (**$\overline{\text{P}}$anda**).

Atomic, Plasma physics and Applications (APPA): A collaboration with diverse research interest spreading from low energy antiprotons and antiproton beams to high energy density experiments and studies on the effects of prolonged exposure of biological tissue and materials to cosmic radiation [1].

Compressed Baryonic Matter Experiment (CBM): Using high energy nucleus-nucleus collisions this collaboration plans on exploring the QCD phase diagram in the region of high baryon densities, including studies of the equation-of-state of nuclear matter at neutron star densities [2].

Nuclear Structure, Astrophysics and Reactions (NUSTAR): A diverse collaboration centering on the use of the high resolution magnetic spectrometer, the Fragment Separator, studying the nuclear limits of stability, a more detailed understanding of the strong force and possible applications of nuclear physics to other fields [3].

Antiproton Annihilation at Darmstadt Experiment (PANDA): In order to study Hadrons, antiprotons produced by a primary proton beam, stored in the High Energy Storage Ring with an excellent momentum resolution collide with stationary protons. The annihilation of anti protons and protons offers many areas of study, such as a precise spectroscopy of all states in the charmonium system as well as the search for glue balls. The reactions are measured in a versatile 4π detector [4].

FAIR shown in Fig. 2.1 will be built as an extension of the preexisting *GSI Helmholtzzentrum für Schwerionenforschung* (GSI). In addition to the universal

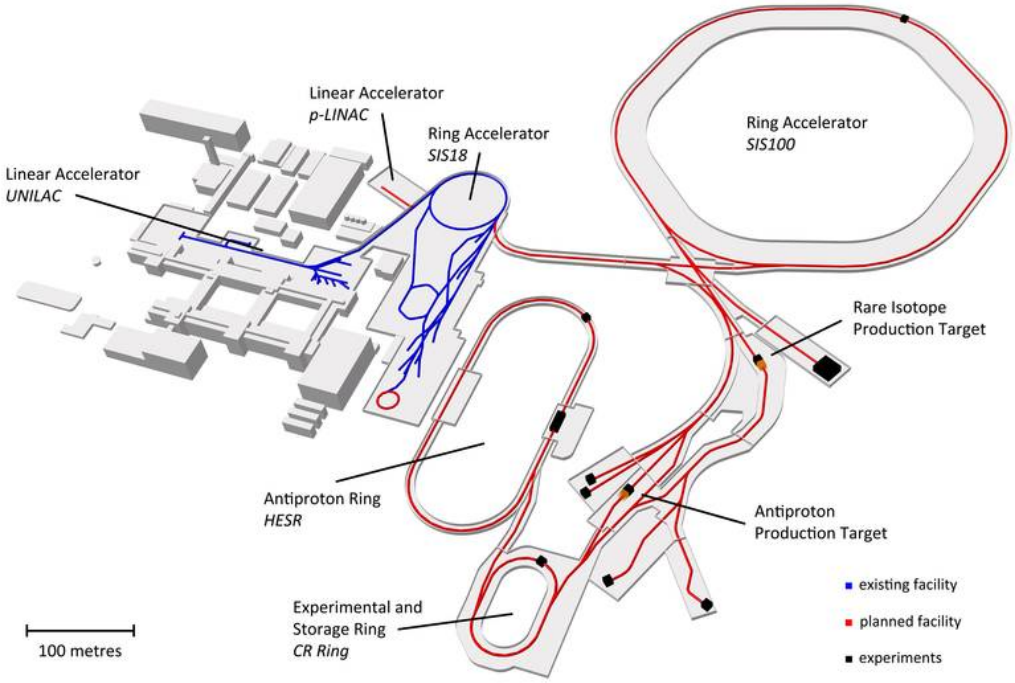

Figure 2.1: *Planned layout of the FAIR facility at Darmstadt, shown together with the already existing GSI facility in blue and the location of planned experiments as black boxes.*

linear accelerator (UNILAC), the heavy ion Synchrotron (SIS18) and the experimental storage ring (ESR) the facility will be expanded by adding two separate synchrotron rings, the SIS100 and the SIS300 which will be built on top of each other with the same circumference of 1100 m. These rings are named after their magnetic rigidity of 100 Tm and 300 Tm respectively. Both accelerators are able to work in parallel and provide multiple experiments with a beam of protons or ions of up to 35 GeV/u to 45 GeV/u for ions or 29 GeV for protons at the same time [5].

Antiprotons are produced by shooting the proton beam on a copper target and collecting the resulting antiprotons in the Collector Ring (CR) which applies first stochastic cooling. The cooled antiprotons are then fed into the High Energy Storage Ring (HESR) where the $\overline{\text{P}}$ANDA experiment is located.

2.1.1 High Energy Storage Ring (HESR)

One of the key facilities for $\overline{\text{P}}$ANDA is the High Energy Storage Ring (HESR). It provides a stable beam of antiprotons harvested from the antiproton production target. The HESR delivers antiprotons with a momentum from 1.5 GeV/c to 15 GeV/c. To ensure the best conditions for the respective measurement two modes of operation are available. The high precision mode delivers antiprotons

with a limited upper momentum of 9 GeV/c and a relative momentum spread of down to almost 10^{-5} by using a combination of stochastic and electron cooling [6]. This mode can be used to perform high precision scans of the width of resonances in search for new states.

The high luminosity mode is limited to stochastic cooling and sacrifices one order of magnitude on the relative beam momentum resolution but is able to produce a beam with a luminosity of up to $2 \cdot 10^{32}\,\mathrm{cm}^{-2}\,\mathrm{s}^{-1}$ for 10^{11} $\bar{p}$ one order of magnitude larger than for the high precision mode [6].

2.2 The Panda Detector

The PANDA detector as depicted in Figure 2.2 is built as a fixed target experiment with a maximum center of mass energy of about 5.5 GeV. As such it has a distinct direction into which a large part of the interaction products are emitted. For this reason one part of the detector, the *Forward Spectrometer* (FS) is built in beam direction covering a the polar angles of up to 5 % vertically and 10 % horizontally.

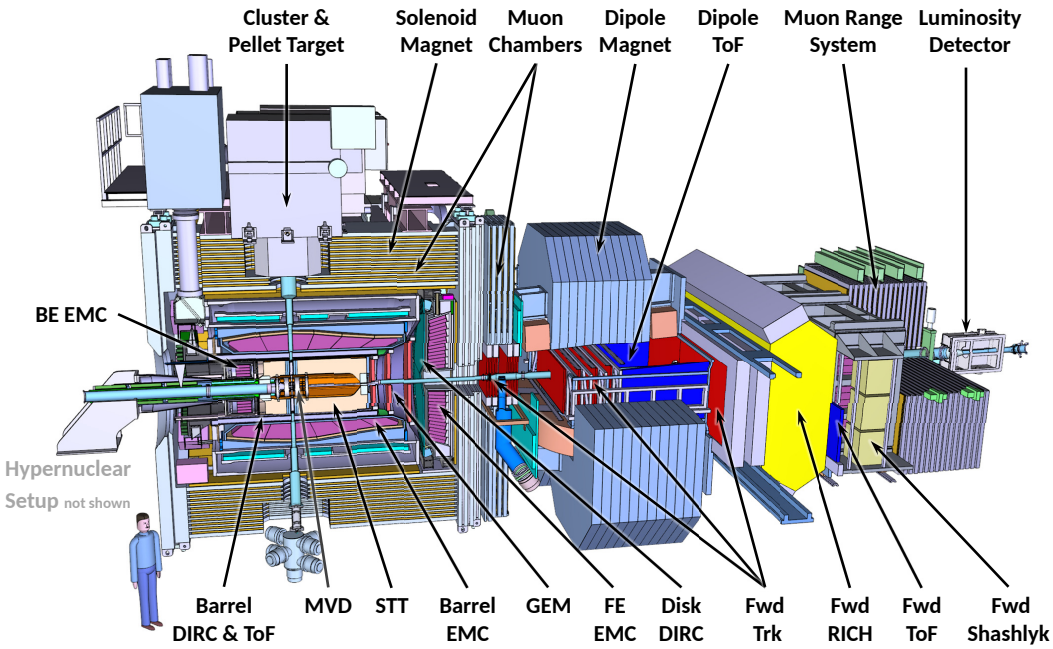

Figure 2.2: *Drawing of the full* PANDA *detector setup with labels for each subsystem [7].*

The second part, the *Target Spectrometer* (TS) of the detector is built around the interaction point. Angles above 22° are covered by the barrel while angles down to the acceptance angles of the FS are covered by the endcap.

2.2.1 The Target System

The target system for PANDA will have to be able to provide proton targets in controlled states and minimize the impact of introducing material into the beam vacuum. For this two main target systems have been developed, the Cluster Jet

Target and the Pellet Target. These systems are interchangeable so that the appropriate system can be mounted for the respective measurement goal.

The **Cluster Jet Target** releases pre-cooled gas through a nozzle with a micro sized throat. Injected into the vacuum the gas cools down due to adiabatic cooling and forms a supersonic beam. If the right conditions are met the gas will condensate creating nanoparticles, the so-called clusters. This produces a very thin target with minimal widening of the cluster beam shape. By controlling the gas pressure and temperature as well as the nozzle size it is possible to influence the cluster size and density in the target [8].

In order to achieve higher detector luminosities the **Pellet Target** will be employed. The pellets are formed in a triple-point chamber by injecting cryogenic liquid into a gas filled chamber close to triple-point conditions. By exciting the nozzle droplets form, which when passing into the vacuum chamber experience surface evaporation and freeze. These pellets can be tracked optically and provide a comparably thick target for the antiproton beam. The challenge here however is to reduce the large variances in effective target thickness from interaction to interaction [8].

2.2.2 The Tracking System

Particle trajectories play a vital role in understanding the scattering process undergone inside the $\overline{\text{P}}$ANDA detector. While the bending radius of the track curve reveals the particle momentum the track length information helps the time-of-flight systems reconstruct particle velocities. With sufficiently precise position resolution displaced vertices can be reconstructed. In order to tracking information throughout the detector multiple distinct detector systems are employed.

The Micro Vertex Detector (MVD)

The Micro Vertex Detector (MVD) comprises the inner most layer of the $\overline{\text{P}}$ANDA experiment. As such it delivers the first possible measurements of an interaction. Its main purpose is to resolve displaced vertices of secondary decays of short lived particles. It will also provide a first estimate of the interaction time and deliver complementary energy deposition information useful for particle identification.

It consist of multiple layers of different silicon detectors arranged as a barrel and a forward part as shown in Figure 2.3. The two inner layers of the barrel part are equipped with silicon hybrid pixel-detectors to deliver the highest precision achieved by the high granularity of the pixel cells.

To reduce the number of readout channels which is proportional the the material budget of the detector the outer two layers are equipped with double sided silicon micro-strip detectors able to readout a much larger surface area with less channels.

A similar construction is chosen for the disks of the forward part where the first four and the inner region of the last two of the six silicon discs will be equipped with pixel detectors while the outer regions are covered by strip-line detectors [9].

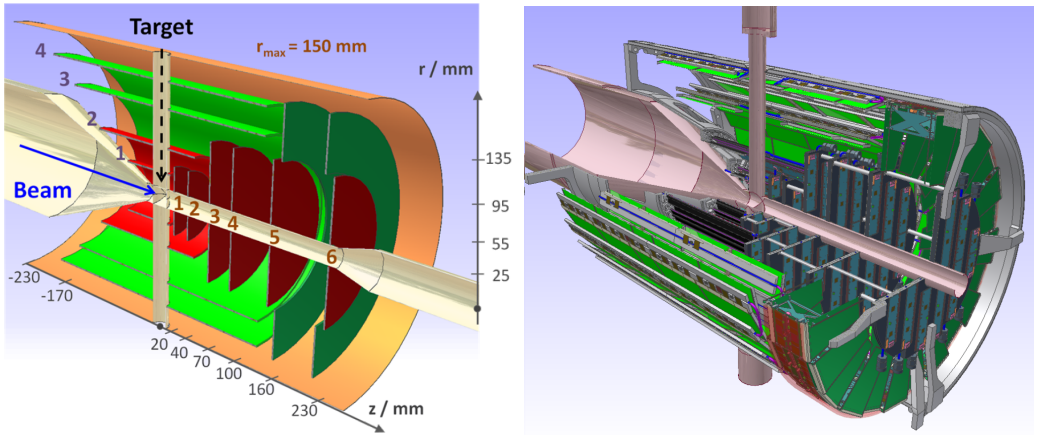

Figure 2.3: *Left: Schematic drawing of the inner parts of the MVD. Areas colored in red are equipped with silicon hybrid pixel-detectors while green areas silicon micro-strip detectors utilize [9]. Right: Realistic engineering drawing with supporting mechanics. The intersecting beam and target pipes are shown [10].*

Straw Tube Tracker

The MVD is followed by the Straw Tube Tracker (STT), the main detector providing track information of charged particles inside of PANDA. Its operational range is from a few 100 MeV/c up to 8 GeV/c in which it is supposed to deliver precise information on the particle trajectories, determine the particle momentum by measuring the curvature of the trajectory in the magnetic field and measure the specific energy loss of passing particles to aid in particle identification below about 1 GeV/c.

The STT is made up of 4636 individual straws used to measure the energy loss of passing particles. Each of these straws is a gas-filled cylindrical tube with a wire running through its center and a conductive coating on the inside of the straw which is made out of two layers of 12 µm thin aluminized Mylar. The general design of the STT can be seen in Figure 2.4.

Along the trajectory of the charged particles the filler gas becomes ionized separating electrons from the rest of the ion. By applying a potential difference of a few kV between the outer straw and the central wire the electrons and ions are separated. By choosing a thin wire with a gauge of some 10 µm the electric field close to the wire becomes so strong electrons in that region start to produce further ionizations. Due to this gain an electrical signal can be measured at the wire.

The drift time of the first electrons to reach the wire, determined by the drift time difference of the ions and electrons, can be used to measure the distance of the particle trajectory from the wire. By combining multiple straws that were hit by the same particle a track can be reconstructed. The amplitude of the single straw signal is proportional to the characteristic energy loss of the passing particle. By accumulating all measurements of the hit straws a mean energy loss can be determined [10].

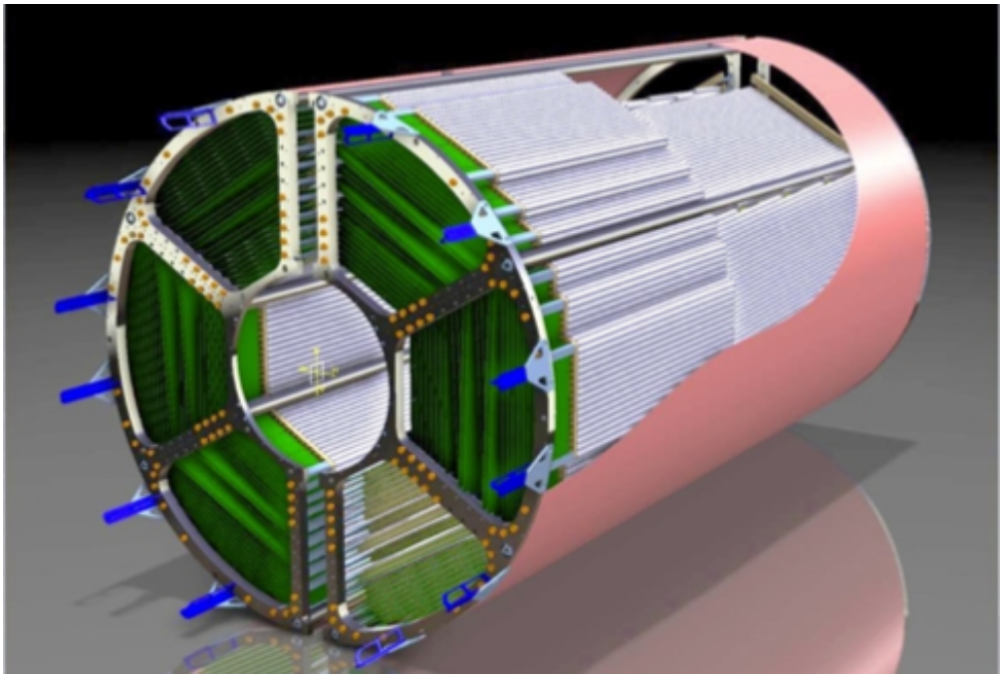

Figure 2.4: *Drawing of the STT implementation in the* $\overline{\text{P}}$ANDA *detector [10].*

GEM Foils

To complete the tracking in the outer forward region at angles between 5° and 22° three layers of Gas Electron Multiplier (GEM) foils are used. These are made of thin polymer foils coated with a thin metal layer on both sides interspersed with holes. By applying an electric field from the one side of the foil to the other electrons created by passing particles in a cathode window are accelerated inside of the holes ionizing the filler gas. By collecting the resulting charge on an striped anode the detector receives its position resolution to complement the other tracking detectors [11].

Forward Tracker

The Forward Tracker in the forward spectrometer is the counter part to the STT in the TS. It consist of the same straw tubes as the STT. This time they however are not arranged in a barrel but rather a wall of multiple layers.

2.2.3 Magnets

In order to measure particle momenta their trajectory needs to be curved. This is achieved by applying a strong magnetic field throughout the TS. A superconducting solenoid magnet providing a filed strength of up to 2 T with a homogeneity of below 2 % variation over the length of 4 m will be positioned around the EMC and the rest of the TS. To allow the beam pipe to reach the interaction point it will be split into three parts [12]. In the forward region a dipole magnet will provide a magnetic field with a bending power of 2 T m. Figure 2.5 shows the solenoid and

dipole magnet with the produced magnetic field. The color red corresponds to the full filed strength of the solenoid with 2 T.

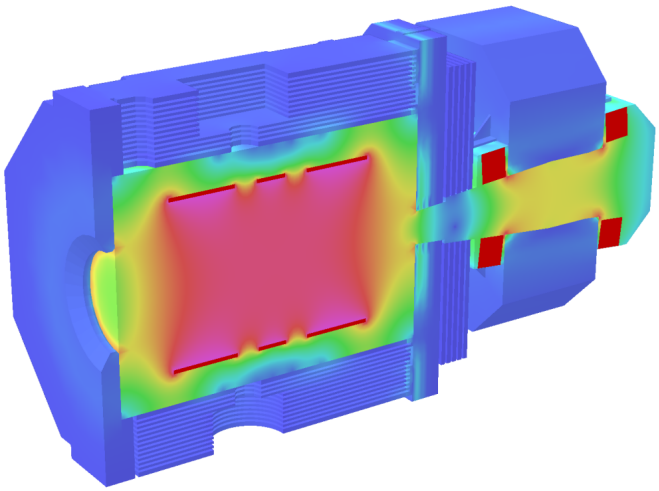

Figure 2.5: *Simulation of the magnetic field strength throughout the* PANDA *detector provided by a solenoid in the TS region and a dipole magnet in the region of the FS [12].*

2.2.4 Particle Identification

The main detectors responsible for particle identity information are the DIRC detectors as well as the time-of-flight detectors . Supplemental information however is provided in form of the characteristic energy loss ($\mathrm{d}E/\mathrm{d}x$) by multiple other systems enhancing the identification performance.

DIRC Detectors

To provide particle identification for particles with a momentum of >1 GeV/c across most of the experiments solid angle, two DIRC subdetector systems are implemented, the Barrel DIRC [13] and the Disc DIRC [14] both depicted in Figure 2.6. Both are made of fused silica and provide particle identity information by measuring the Cherenkov angle of fast particles traversing the glass bars or plates by detecting internally reflected Cherenkov light (DIRC) and focusing it on an MCP-PMT readout system.

The Disc DIRC is made of four large parts with focusing elements sitting on bars attached to the 2 cm thick radiator all around the outer edges of the detector. It covers the polar angle range from 22° down to 5° respectively 10°. The Barrel DIRC detector consists of 16 segments of three 17 mm thick, 53 mm wide and 2400 mm long quartz bars, covering the polar angle range from 22° to 140°. Each module is housed in light tight carbon reinforced polymer (CFRP) boxes and mounted in a metal frame. Focusing elements on the backside of the detector in front of the interaction point are read out by an MCP-PMT array of 11 sensors.

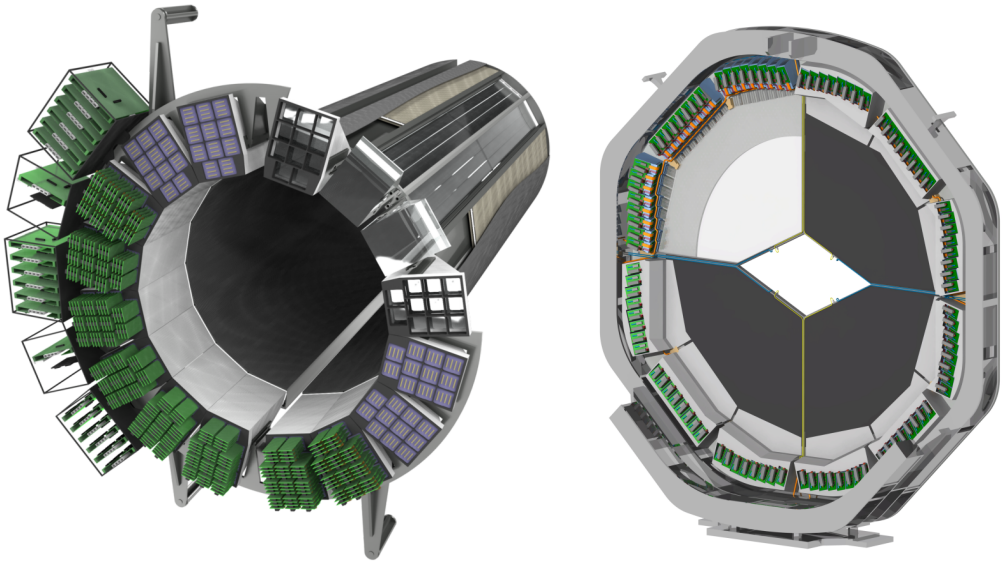

Figure 2.6: *Drawings of the Barrel DIRC [13] detector on the left and the Disc DIRC detector [14] on the right.*

Time-of-Flight Detectors

Below the Cherenkov threshold it is impossible for the DIRC detectors to operate. For particles in this region, below 1 GeV/c, it falls to the time-of-flight detectors in combination with the tracking information to provide particle identities. The Barrel Time-of-Flight Detector in the TS provides coverage for particles inside the range of 22.5° to 140°. It shares the same holding structure and general shape of the Barrel DIRC detector and is situated right behind it. It consists of 16 individual segments equipped with two rows of 60 scintillating tiles roughly $90 \times 30 \times 5\,\text{mm}^3$, read out by SiPMs connected in series.

The ToF detector in the FS is the Forward Time of Flight detector [15] and is position 7.5 m downstream of the interaction point. It covers a sensitive area of $5.6 \times 1.4\,\text{m}^2$ with 2.5 cm thick and between 5 cm and 10 cm wide organic scintillator tiles.

2.2.5 Calorimeters

As the main detectors for the detection of electromagnetic probes, such as high energetic photons and electrons in a wide energy range, the electromagnetic calorimeters play a vital role for the $\overline{\text{P}}$ANDA experiment since many channels include photons or electrons in their final state.

As part of the TS three instances of the electromagnetic calorimeter are implemented, the barrel EMC [16], the Forward Endcap [17] as well as the Backward Endcap. For these three detectors a total of 15 552 crystals, made out of lead tungstate ($PbWO_4$ or PWO), are tightly packed and oriented to look towards the interaction region as can be seen in Figure 2.7. To increase the light yield the crystals are cooled to −25 °C and are wrapped with reflective foil. PWO crystals have been used by other large experiments such as CMS at CERN and are chosen

due to the materials compactness with a radiation length of only $X_0 = 0.98\,\text{cm}$. Additionally new growing methods have been developed, further increasing the light yield, making it PWO-II. All crystals are placed in a carbon fiber frame individually. They are read out by Large Area Avalanche Photo Diodes (LAAPDs) and Vacuum Photo TeTrodes (VPTTs). This setup provides an energy resolution of $\frac{\sigma}{E} = 1\,\% \oplus \frac{2\,\%}{\sqrt{E[GeV]}}$.

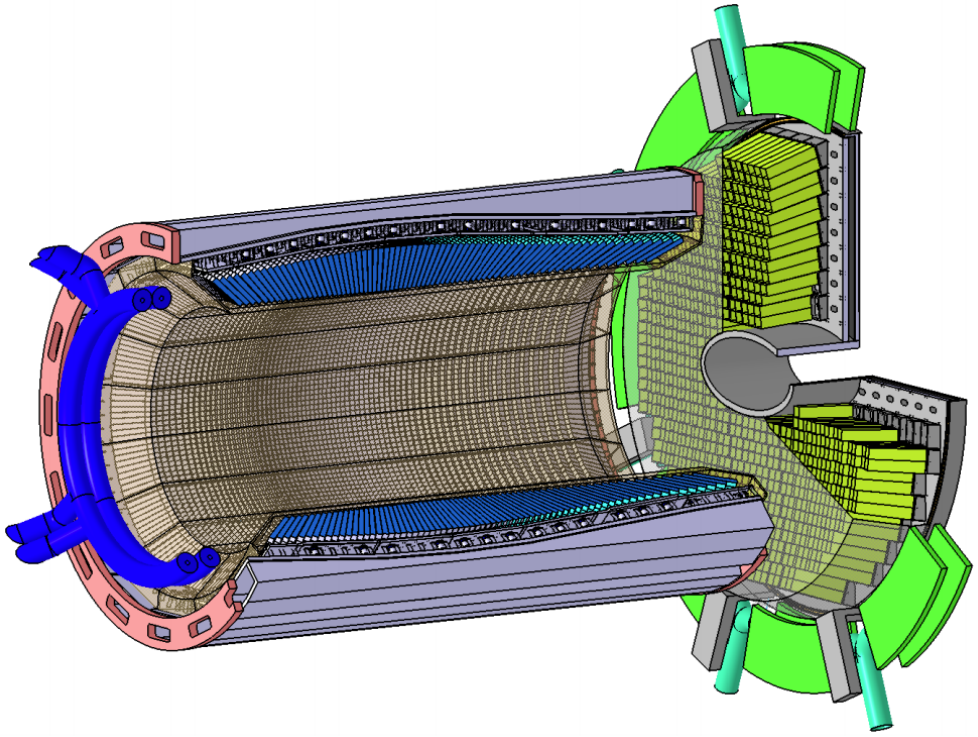

Figure 2.7: *Schematic drawing of the barrel EMC and its forward endcap [17].*

To achieve a coverage of almost 4π a sampling calorimeter is placed in the FS, about 7 m downstream of the interaction point. It forms a wall and is made out of 378 modules with 380 alternating layers perpendicular to the beam of active scintillator material, a polystyrene doped with 1.5 % paraterphenyle and 0.04 % POPOP, and passive lead absorber plates. The scintillation light of each scintillator layer is transported by wavelength shifting fibers to PMTs at the back end of the detector. The fibers penetrate all layers like a skewer giving this kind of calorimeter the descriptive name of shashlyk type calorimeter. This detector is able to achieve an energy resolution of $\frac{\sigma}{E} = 1.3\,\% \oplus \frac{2.8\,\%}{\sqrt{E[GeV]}}$.

2.2.6 Luminosity Detector

In order to measure interaction rates and cross sections one has to know how large the number of possible events is. This value is measured by the luminosity of an experiment. In order to evaluate the cross section for a measured finite amount of interactions the luminosity over a set period of time, e.g. the length of an

experimental run, has to be integrated over this time producing the integrated luminosity.

To do this in $\overline{\text{P}}$ANDA a dedicated luminosity measuring system is setup about 11 m from the interaction point down the beam line behind all major $\overline{\text{P}}$ANDA detector elements. This detector will monitor the elastic scattering process of $\bar{p}p$ interactions which is a very stable process by measuring tracks of the forward scattered antiprotons at small angles of 3 mrad to 8 mrad. To track the antiprotons the detector is equipped with four planes of silicon pixel sensors as shown in Figure 2.8 [18].

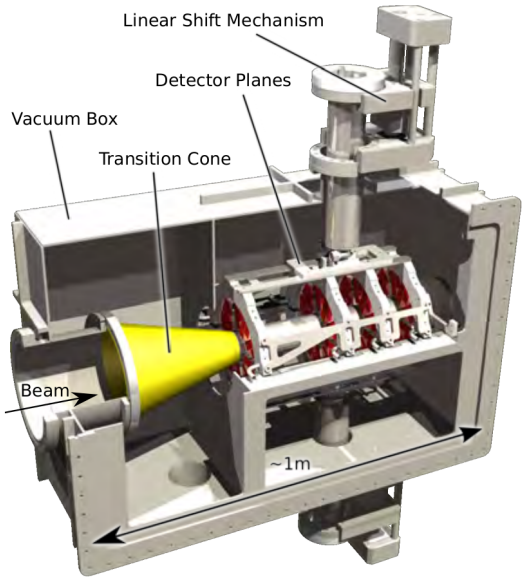

Figure 2.8: *Drawing of the* $\overline{\text{P}}$ANDA *luminosity detector with its four antiproton tracking planes [18].*

2.2.7 Data Acquisition

Without a dedicated hardware trigger the data acquisition will be running nonstop producing data rates of several 100 GB/s. Incoming data at this rate can not be stored permanently but has to be filtered as the data comes in. A system to unite the timing information of all subdetector systems is the so called SODA (Synchronization Of Data Acquisition) system which provides a common reference signal over a network of optical connections. The system will be able to provide the timing signal with a consistency of less than 20 ps RMS [19].

2.3 Physics Program

Unlike Quantum Electrodynamics (QED) which is better understood than most any other theory Quantum Chromodynamics (QCD) is far from being understood. Like QED, QCD, the theory of the strong force, can be approximated by perturbation

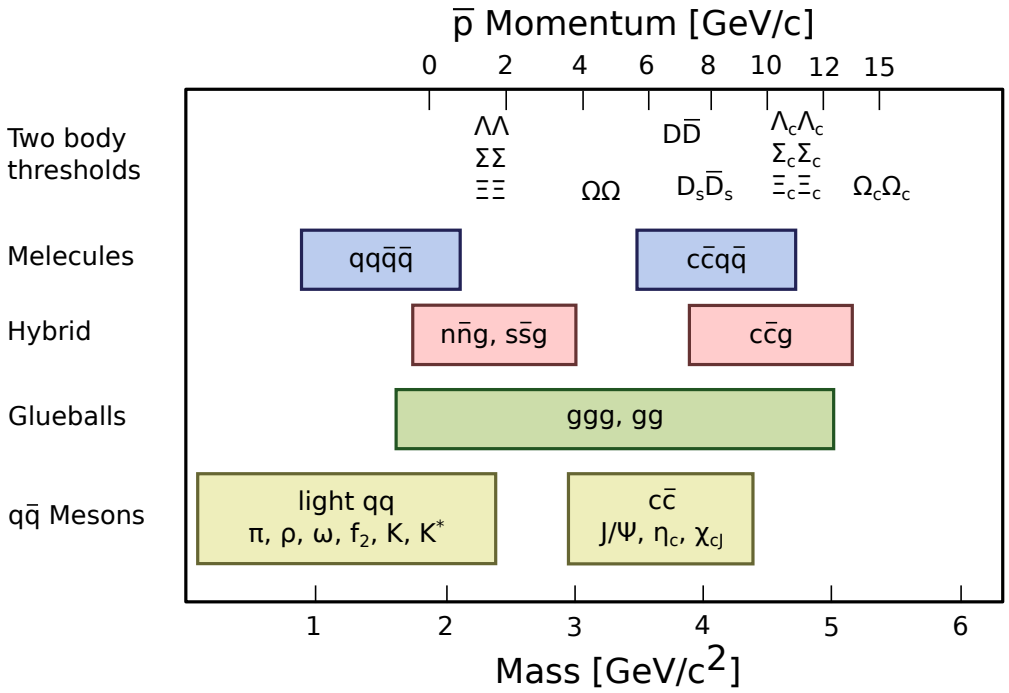

Figure 2.9: *Production thresholds and expected energy regions for hadrons that are within the mass range accessible by* $\overline{\text{P}}$ANDA *with a center of mass energy of up to 5.5 GeV depicted on the bottom scale. The top scale shows the necessary beam momentum to produce the respective hadrons in fixed target antiproton proton annihilations.*

theory at high energies where the strong coupling constant becomes small. At lower energy however perturbation theory breaks down and the theory of strongly-coupled forces shows many aspects which are not well understood making quantitative predictions starting from first principles very hard. This energy region for which little experimental data is available, mostly recorded using electromagnetic probes, will be targeted by the $\overline{\text{P}}$ANDA detector reaching a center of mass energy of up to 5.5 GeV. The mass range of hadrons that are accessible at $\overline{\text{P}}$ANDA is shown in Figure 2.9, listing molecules, hybrids, glueballs and simple mesons.

Setting $\overline{\text{P}}$ANDA apart from other experiments studying interactions in this energy region, such as BaBar [20] and Belle [21] which are e^+e^- colliders, is the fact that by producing $\bar{p}p$ interactions all quantum numbers are directly accessible. Not being limited to quantum numbers of photons $J^{PC} = 1^{--}$ also allows for far higher cross sections for the states of interest.

Studying the charmonium states we see that there is a lack of understanding for many of these states properties. Determining the width of these states in conventional measurements for example is limited by the resolution of the subdetector systems of the experiment. $\overline{\text{P}}$ANDA however will be able to perform highly accurate scans of the state width by modulating the momentum of the $\bar{p}$ beam which is is handled by the highly effective cooling system of the HESR. This together with the high center of mass energy is well suited for the study of narrow states slightly above the open charm threshold ($\bar{D}D$). One such state is the understudied X(3872) state, the mass of which can not be explained by the naive quark model [22]. By

being able to produce it directly from the $\bar{p}p$ collisions, $\overline{\text{P}}$ANDA will be able to produce multiple thousand $\bar{c}c$ states per day, providing necessary statistics for a thorough investigation into the nature of these states [4].

In contrast to photons in QED the mediators of the strong force in QCD, the gluons are self interacting. This produces a much richer spectrum of states than predicted by the quark model. The gluons cannot only couple to quarks and produce quark gluon hybrid states with a quark, anti-quark and an excited gluon but also produce pure gluon hadrons, the glue balls consisting of two or more gluons. 15 of such glueballs predicted by Lattice QCD are expected withing the momentum range of $\overline{\text{P}}$ANDA. The gluons introduce additional degrees of freedom that allow exotic quantum numbers not found for normal mesons comprising a quark anti-quark pair, such as $J^{PC} = 0^{+-}, 1^{-+}, 2^{+-}$, due to which these states will be easily separated from conventional hadrons [23]. The study of glueballs and hybrids offers a unique view into the long range features of QCD from which fundamental insights into the QCD vacuum structure can be drawn. $\overline{\text{P}}$ANDA is able to produce these in in large numbers since hadron annihilations produce a gluon-rich environment [24].

Studies of the mass change of hadrons inside a nuclear medium have been performed for mesons containing light quarks at experiments such as Crystal Ball and HADES at GSI. This effect is produced by partial restoration of the chiral symmetry in a hadronic environment and will be studied by replacing the pellet or cluster jet target with different nuclear targets [4, 25]. This allows $\overline{\text{P}}$ANDA to extend the measurements towards the charm sector for the first time [26].

Chapter 3

The Barrel Time-of-Flight Detector

3.1 Requirements and Capabilities

To understand some of the choices made in the design process it is important to understand the context of the B-ToF detector and its requirements.

The $\overline{\text{P}}$ANDA B-ToF was not included in the original design of the experiment. Over time however it became clear that a system with superior timing performance would greatly enhance the capabilities of the $\overline{\text{P}}$ANDA experiment as a whole. A time-of-flight (ToF) system would add necessary particle identification (PID) capabilities in energy regions not accessible by the dedicated PID system.

Moreover the $\overline{\text{P}}$ANDA experiment will be run without a hardware trigger. Individual events will be registered from which interactions can be reconstructed guiding the decision records of which event to keep and to analyze further. This makes the B-ToF, one of the fastest systems in the experiment, crucial to early stage event building.

To fulfill this role it has to meet a clear set of criteria. It has to

- fit inside of very limited available radial space directly behind the Barrel DIRC,
- utilize a minimal material budget in the order of a few percent of radiation length as to not spoil the performance of the EMC behind it,
- provide a system time resolution of below 100 ps,
- have sufficient radiation hardness in order to survive a 10 year dose of up to 10 kGy.

3.1.1 Mechanical Limitations

As a timing detector the performance depends on the detectors distance to the interaction point. The farther the particles travel to reach the B-ToF the longer their time of flight which reduces the relative impact of the limited time resolution. This increases the performance of the detector. The majority of particles will be absorbed in the EMC which suggests the ideal position of the B-ToF is directly in front of it.

Since the B-ToF was not part of the original layout of the experiment very limited radial space is available for this timing detector. Hence it will be integrated

in to the holding structure of the Barrel DIRC which can be seen in Figure 3.1. Depicted is one half of the $\overline{\text{P}}$ANDA barrel, which only spans 172° leaving two 8° gaps to allow the target system to reach the interaction point, as well as a close up of the Barrel DIRC and B-ToF slots.

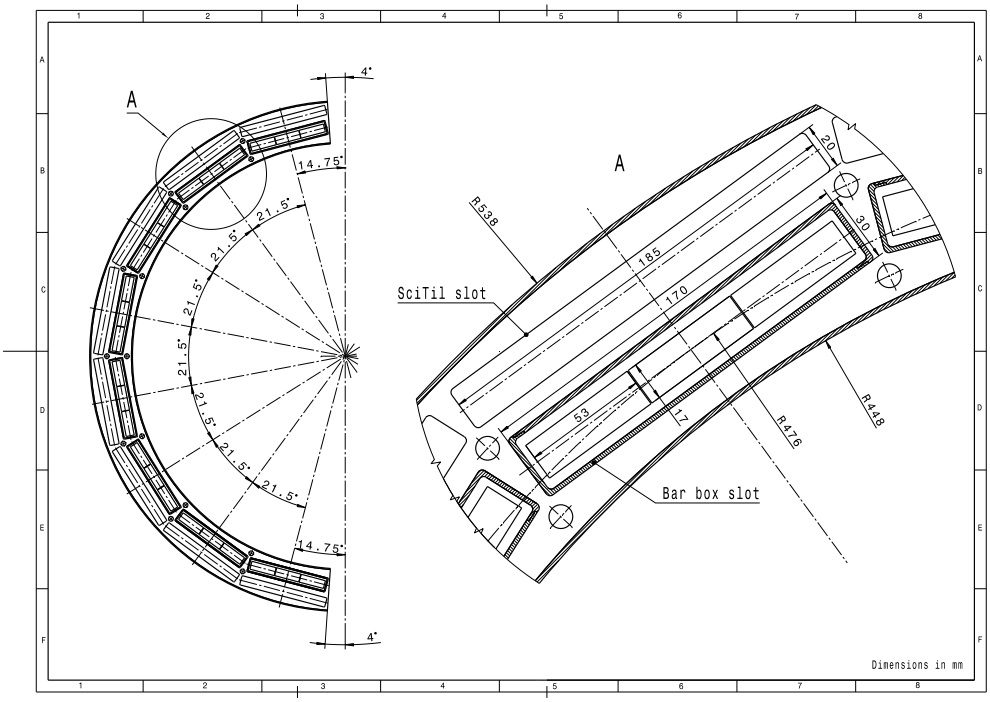

Figure 3.1: *Schematics of the* $\overline{\text{P}}$ANDA *Barrel DIRC and B-ToF here called SciTil.*

The Barrel DIRC system comprises 16 segments, 8 each per side, mounted as flat bars along the barrel. This dictates the general layout of the B-ToF which has to take on the same form. Each segment of the B-ToF will be mounted at radius of about 500 mm from the interaction point in slots 185 mm wide and 20 mm high. The height is especially limiting as these measurements must include the inner holding structure of the detector as well as the outer casing.

3.1.2 Particle Identification

The main means of particle identification in $\overline{\text{P}}$ANDA are the DIRC systems. These operate by using the velocity dependent angle of photons emitted in Cherenkov radiation. Cherenkov radiation however only occurs for particles passing through a medium at a velocity higher than the respective speed of light in that medium. If this threshold is not surpassed the DIRC detectors can not operate. For protons, kaons and pions this threshold lies at 868 MeV/c, 457 MeV/c and 129 MeV/c. This momentum region is where a particles time of flight is the longest and a ToF based system performance is at its best.

By combining track length and momentum information provided by other detectors of the tracking system and time-of-flight information provided by the B-ToF

the particles mass can be calculated. The slower the particles the better the ToF resolution.

Up until and beyond the momentum range at which particles start producing Cherenkov radiation the Barrel Time-of-Flight Detector must be able to provide particle identity information and support the DIRC detectors. To fulfill this role a sufficient time resolution is required.

3.1.3 Event Sorting

Since $\overline{\text{P}}$ANDA will be operated without a hardware trigger with the HESR providing a continuous beam without particle bunches, a stream of hits in all subdetectors can be expected. In systems without sufficient time resolution no distinct events will be recognizable. An example simulation showing the hit distribution for a 50 MHz interaction rate first as seen by a detector with a time resolution of 100 ps and second as seen by a detector with a time resolution of 2 ns, similar to what is expected of the EMC, is shown in Figure 3.2. The hits of one event, meaning an underlying $\bar{p}p$ annihilation producing secondary particles, in this figure are differentiated by various colors, a repeating cycle of black, red and blue. In the first distribution of a hypothetical detector with a time resolution of 100 ps these events are clearly separated. The second distribution however shows a large degree of overlap and hit mixing making some events indistinguishable from each other.

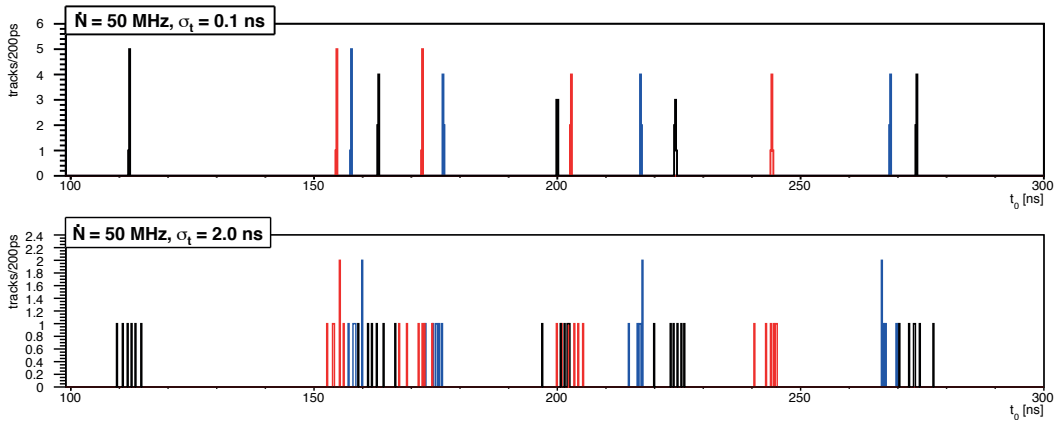

Figure 3.2: *Eventsorting comparing the hit spread in detectors with a time resolution of 100 ps to 2 ns for interactions in the* $\overline{\text{P}}$ANDA *experiment [27].*

$\overline{\text{P}}$ANDA is designed to operate in two modes of the HESR, one high precision mode providing a beam with a clearly defined momentum resolution and a high luminosity mode in order to generate enough collisions to study elusive interactions with sufficient statistical power. This latter mode provides a beam with a luminosity of $\mathcal{L} = 2 \cdot 10^{32}\text{cm}^2\text{s}^{-1}$ for $\bar{p}p$ annihilations with a cross section of $\sigma_{tot} \approx 100\,\text{mb}$. This results in an average interaction rate of about 20 MHz.

Due to the nature of the irregular distribution of antiprotons in the HESR overlapping with the casual crossing of the pellet target, short bursts of significantly higher event rates are possible. These can reach up momentary rates of 100 MHz.

If $\overline{\text{P}}$ANDA is not able to separate consecutive events the events can not be properly analyzed and are lost leading to a reduction in efficiency. This efficiency reduction is especially pronounced at the high interaction rates discussed above. Improving the time resolution from 1 ns to 0.1 ns would improve the efficiency of a simple event sorting algorithm isolating events that have a 3 σ separation, by around 30 % [27].

The aforementioned event rate of 20 MHz refers to $\bar{p}p$ collisions and offers little information on the expected hit rates at the individual detectors. To receive an accurate estimation of the actual hit rates of the detectors one has to take the geometry and the event multiplicity into account. Simulation studies done by D. Steinschaden addressed this [28]. The event rate per tile can reach up to 38 kHz for scintillators in the forward region of the detector as shown in Figure 3.3. Since $\overline{\text{P}}$ANDA is a fixed target experiment a sharp drop off towards the backward region can be seen. These interaction rates need to be handled by the B-ToF detector.

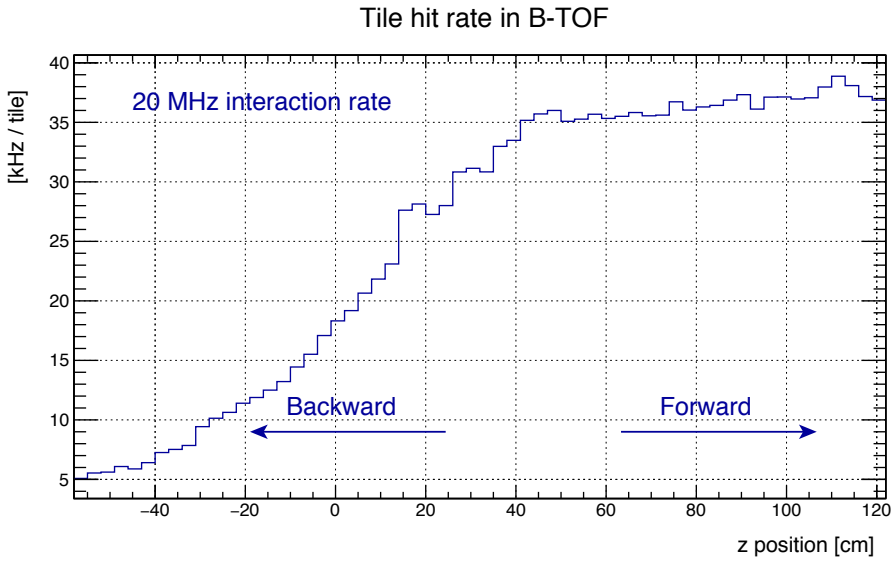

Figure 3.3: *Expected mean hit rate per B-ToF scintillator along the beam axis for an interaction rate of 20 MHz [28].*

3.1.4 Track Seeding

Tracking detectors provide a series of hits which later need to be connected to form particle tracks through the detector. These detectors are not optimized for speed but for position resolution, giving them, especially the Straw Tube Tracker (STT), large overlaps between the events.

The B-ToF should be able to provide track seeds from which hits inside the Central Tracker (CT) will be able to be connected. To disentangle these tracks and assign them to specific events a precise timing detector with sufficient spacial granularity in ϕ and z direction is necessary.

3.1.5 Preshowers and EMC Preshower Detection

One major component of $\overline{\text{P}}$ANDA is its EMC, designed to detect photons or γ-rays of a wide energy range and measure their energy with high precision. Any material between the interaction point and the EMC layer deteriorates its performance. Photons passing material have a non-zero chance to interact and produce an electromagnetic shower, called a conversion, before reaching the EMC crystals. Such events are called *Preshowers*, one of the main external limits of the calorimeters energy resolution.

Electromagnetic showers are caused by any material in a photons trajectory. They are either initiated by Compton scattering or pair production of a high energy photon. As the cross section for Compton scattering decreases for growing γ energies it rises for pair production events as can be seen in Figure 3.4, depicting the cross section of the main photon scattering processes. High energy electrons produced this way then quickly lose energy predominantly via bremsstrahlung emitting a high energy photon which then again can interact producing more electrons, cascading back and forth through the material.

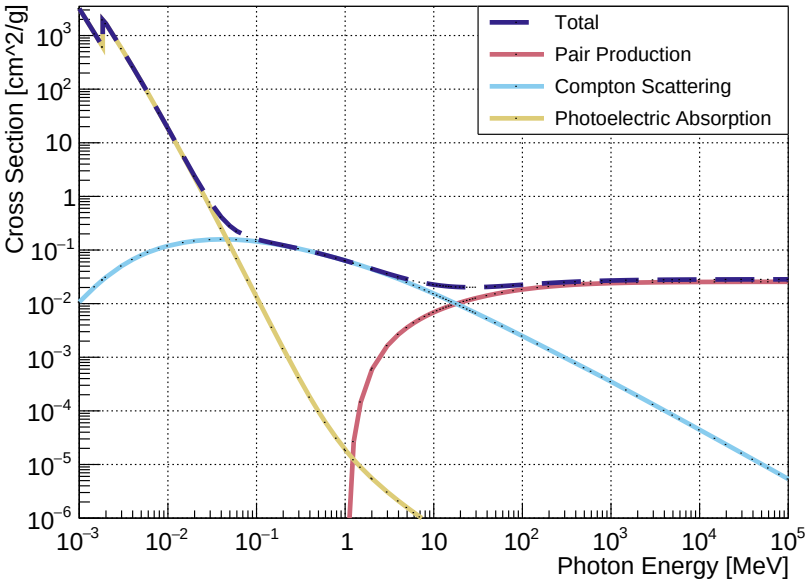

Figure 3.4: *Cross section of gamma rays in fused silica. Depicted are the cross section of the photoelectric absorption, the Compton scattering and the pair production of photons adding up to the dotted total cross sections up to 10 GeV [29].*

The mean path length before an electrons energy is reduced by $1/e$ is called the *Radiation Length* X_0 which is about $\frac{7}{9}$ of the mean free path of γ-rays before undergoing pair production initiating a cascade [30]. This value is material specific and decreases with an increasing atomic number. For this reason it is important that the B-ToF chooses its material carefully and minimizes the material it introduces into the $\overline{\text{P}}$ANDA barrel. The measure of the introduced matter independent of the specific material is the material budget given in radiation lengths. The goal is to

keep the B-ToFs material budget to a few % X_0.

A study done previously shows that the largest contributor to the production of these preshowers is the Barrel DIRC [16]. A detector with a large detection efficiency for charged particles but limited detection ability for photons behind the Barrel DIRC could act as a preshower detector for EMC.

In order for the EMC to tell whether a preshower has been initiated a detector behind the Barrel DIRC is required that interacts with a photon differently than it does with charged particles. Using thin plastic scintillator tiles gives the B-ToF a large detection efficiency for charged particles, but makes it virtually blind to γ-rays. This means that an EMC event without a respective B-ToF hit can be taken as a regular photon hit. A correlating B-ToF hit however signalizes the emergence of an electromagnetic shower produced by a photon interacting in the Barrel DIRC, as shown in Figure 3.5 schematically, or before which has already lost part of its energy. This information then can be used to correct the measurement of the EMC.

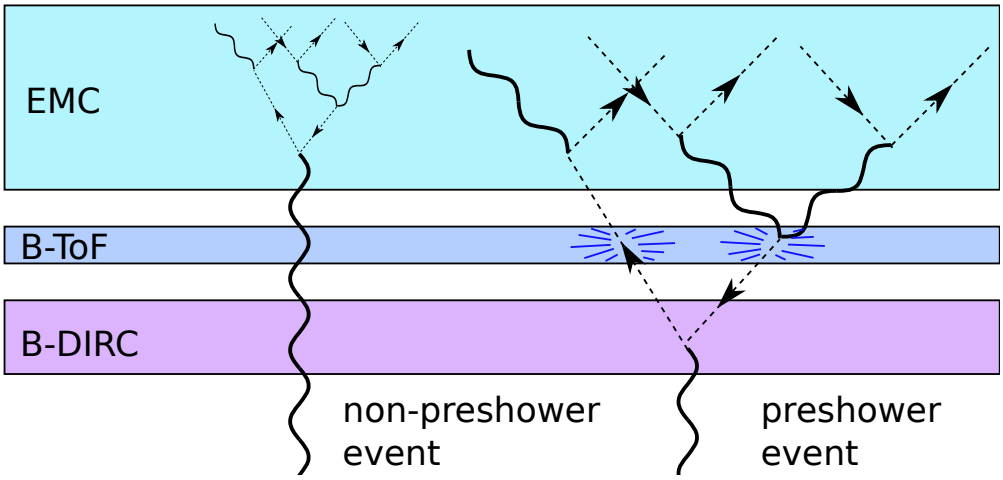

Figure 3.5: *Schematic drawing of two possible photon interactions involving the Barrel DIRC, the B-ToF and the EMC layers, a normal non-preshower event and a preshower event with a hit in the DIRC.*

3.1.6 Radiationhardness

This section has been taken from the Technical Design Report of the Barrel Time-of-Flight Detector [31] as I am the author of that section.

To estimate the expected radiation dose the B-ToF will be exposed to in the $\overline{\text{P}}$ANDA experiment a radiation map first studied by O. Hartmann and refined by K. Makonyi [32], shown in Fig. 3.6 can be utilized. It depicts the absorbed radiation energy in GeV per year for the Barrel DIRC, which is made out of fused silica.

It shows that per bin about 1 to 5 $\cdot 10^7$ GeV per year is absorbed. This value already takes into account that we will have beam-on-target for roughly 50% of the year. In addition the antiproton density in the HESR drops over time and so does

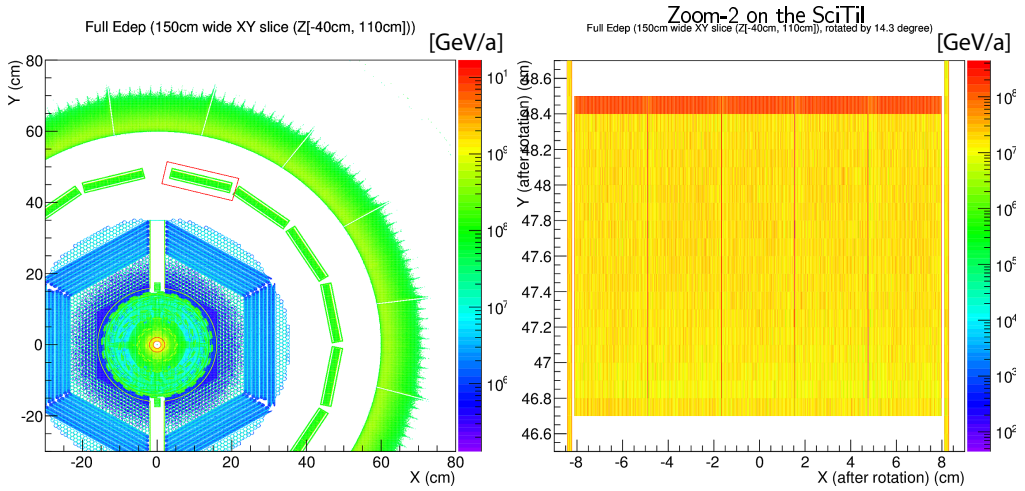

Figure 3.6: *Simulation of the expected radiation for the* $\overline{\text{P}}$ANDA *detector with a close up of a Barrel DIRC tile. Depicted is a cross section of the* $\overline{\text{P}}$ANDA *barrel with the inner tracking detectors, the Barrel DIRC and the EMC. The color of each part encodes the expected absorbed radiation in GeV per year [32].*

the interaction rate, which also has been taken into account. If we now assume that all particles passing the Barrel DIRC are MIPs which deposit 3.737 MeV/cm [33] the amount of passing particles can be estimated.

The dimensions of one bin are $150 \times 1/30 \times 0.1\,\text{cm}^3$. This means the surface area that is exposed to the radiation and absorbs up to $10^7\,\text{GeV/cm}^2$ per year is 5 cm^2 large. Dividing this by the mean deposited energy of Minimum Ionizing Particles (MIPs) we receive the number of passing particles.

$$\begin{aligned} n_{\text{MIP}} &= \frac{10^7\,\text{GeV/cm}^2}{373.7\,\text{keV}}\text{per year} \\ &= 2.67 \cdot 10^{10}\,\text{MIPs /cm}^2 \text{ for 1 year} \\ &\Rightarrow \quad 2.67 \cdot 10^{11}\,\text{MIPs /cm}^2 \text{ for 10 years} \end{aligned} \tag{3.1.1}$$

If we assume these MIPs are protons with an energy of roughly 2 GeV, the 1 MeV neutron equivalent damage to the SiPMs can be calculated by multiplying with the hardness factor 0.62 for 2 GeV protons in silicon, on the basis of the NIEL hypothesis [34].

$$2.67 \cdot 10^{11} \times 0.62 = 1.66 \cdot 10^{11} n_{\text{eq}}/\text{cm}^2 \text{ in 10 years} \tag{3.1.2}$$

This still assumes the high luminosity mode with a mean rate of about 10 MHz is running for the entire duration of the experiment. This will definitely not be the case as this mode will not be ready from the start and studies with the high resolution mode, which has a lower interaction frequency, are also part of the physics program. Assuming the high resolution mode will be running for five of the 10 years we receive a realistic value of

$$\Phi_{eq} \approx \left(\frac{5y}{10y} \times 0.1 + \frac{5y}{10y} \times 1 \right) \Phi_{HL} \tag{3.1.3}$$

$$\approx 9 \cdot 10^{10} n_{\text{eq}}/\text{cm}^2 \text{in 10 years.} \tag{3.1.4}$$

This, however, is only the average number. Due to the kinematics of the experiment the section of our detector in forward direction expects a hit rate roughly 30% higher than the average as one can see in Fig. 3.3. In order to distribute the absorbed dose across all tiles one can reorder the tiles along the detector periodically during maintenance periods to homogenize their exposure.

The energy deposited in the scintillator can also be calculated from the number of MIPs in Eq. 3.1.1. Every MIP deposits 2.02 MeV/cm in polyvinyltoluene [33], the base material of the scintillator which has a density of 1.032 g/cm^3. With this we can calculate the absorbed radiation dose (D) by:

$$\begin{aligned} D &= 2.7 \cdot 10^{11} \frac{\text{MIPs}}{\text{cm}^2} \times 2.02 \frac{\text{MeV}}{\text{cm}} \div 1.032 \frac{\text{g}}{\text{cm}^3} \\ &= 5.4 \cdot 10^{11} \frac{\text{MeV}}{\text{g}} \quad = 5.4 \cdot 10^{20} \frac{\text{eV}}{\text{kg}} \\ &= 83.7 \frac{\text{J}}{\text{kg}} \quad = 83.7\,\text{Gy in 10 years} \\ &\approx 8.4\,\text{krad in 10 years.} \end{aligned} \tag{3.1.5}$$

The detector must resist this dose without deteriorating past the necessary performance goals.

3.2 Design

The Barrel Time-of-Flight Detector is designed as a scintillating tile hodoscope at a radial distance of 50 cm from the target. The active area covers an area from $\theta = 22°$ to $\theta = 140°$ in respect to the beam line.

The general design of the B-ToF detector is constrained by the available space in the $20 \times 185\,\text{mm}^2$ slot between the Barrel DIRC detector and the calorimeter. It also takes on the 16 segment design of the Barrel DIRC. Figure 3.7 depicts a schematic drawing of a B-ToF module and the shared Barrel DIRC and B-ToF holding structure. Each of the 16 independent B-ToF modules is called a *Super-Module*.

Scintillator and Readout

The core elements of the B-ToF detector are the scintillator tiles read out by SiPMs. Plastic scintillator made of EJ-232 by Eljen Technologies have been chosen for their fast signals in order to obtain excellent time resolutions for charged particles. It is made out of a polyvinyltoluene (PVT) base and is designed for fast timing applications with small tile dimensions.

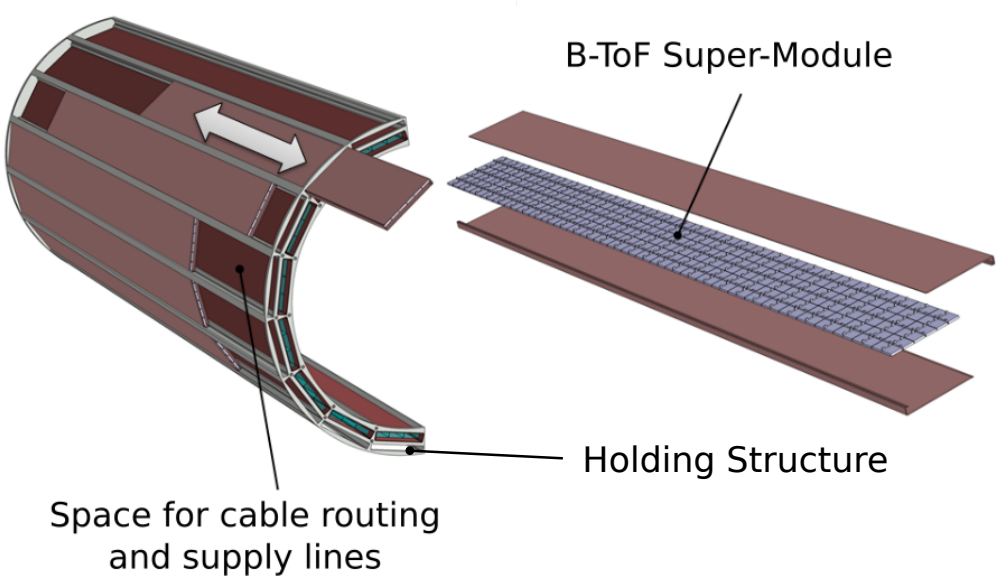

Figure 3.7: *Drawing of the holding structure for the Barrel DIRC and B-ToF detectors [31].*

The compact size of SiPMs makes them the ideal photon detector choice for this application. They are unaffected by magnetic fields, unlike regular PMTs, which allows the application inside of the $\overline{\text{P}}$ANDA solenoid.

Since smaller tiles provide a better time resolution due to shorter internal photon trajectories as well as a better position resolution due to the higher detector granularity the decision was made to form two side by side lines of 60 scintillator tiles along the $1800 \times 180\,\text{mm}^2$ active area of the module. Figure 3.8 shows a half length board with the first 30 channels. The dimensions of the tiles with $87 \times 29.4 \times 5\,\text{mm}^3$ allow just enough separation between each element for wrapping materials and the SiPM readout system. To maximize the coverage of the space in between the scintillator tiles is kept to a minimum.

Sensor-Board

Small printed circuit boards (PCBs) called *Sensor-Boards* are used to hold and connect four SiPMs in series. These boards also house a temperature sensor to monitor the SiPM environment as their performance is very susceptible to temperature changes as well as a small LED for system calibration. An early version of this board without the LED and temperature sensor is shown in Figure 3.9.

To save space the middle Sensor-Board is was double sided in the earlier design with SiPMs soldered onto both sides of the double sided PCB. This means three Sensor-Boards can readout two scintillators as shown in Figure 3.10. This later changed into thinner flexible individual PCB for each scintillator. The SiPMs are glued to the scintillators to hold the scintillators in place and establish a good optical connection between the SiPMs and the tile.

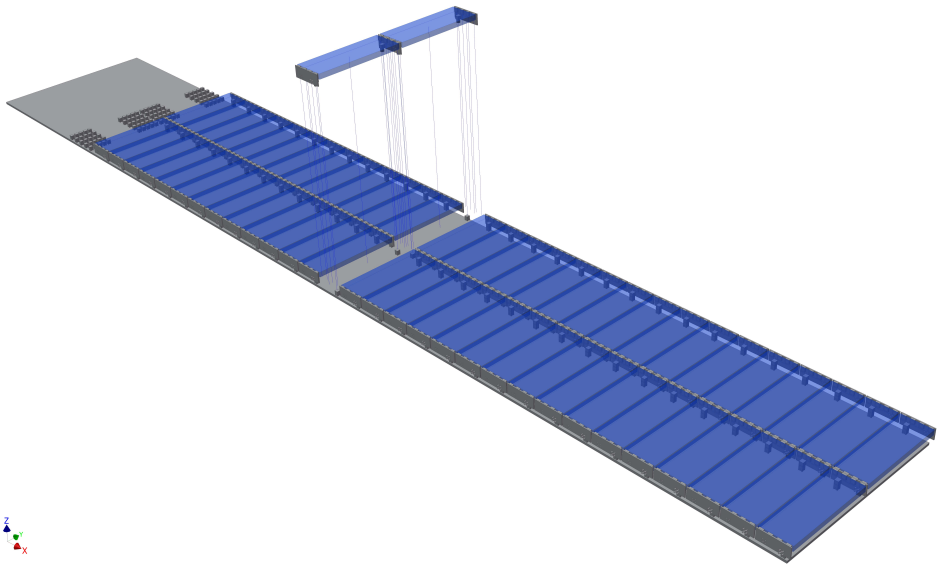

Figure 3.8: *Drawing of a half length Super-Module with two lines of scintillators running up the length of the board. The grey space in the back is left free for the front-end electronics.*

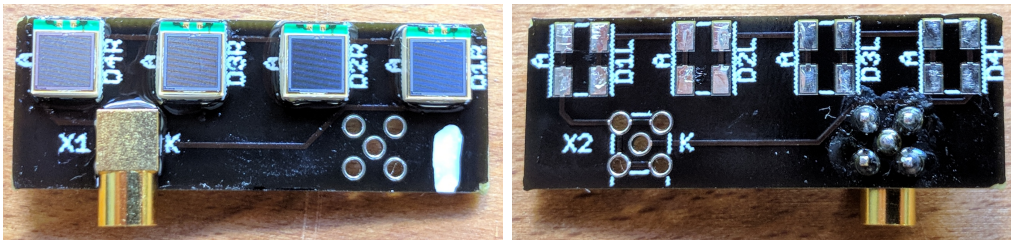

Figure 3.9: *Double sided Sensor-Board with SiPMs attached only to one side. This early version of the board lacks the calibration LED and the temperature sensor.*

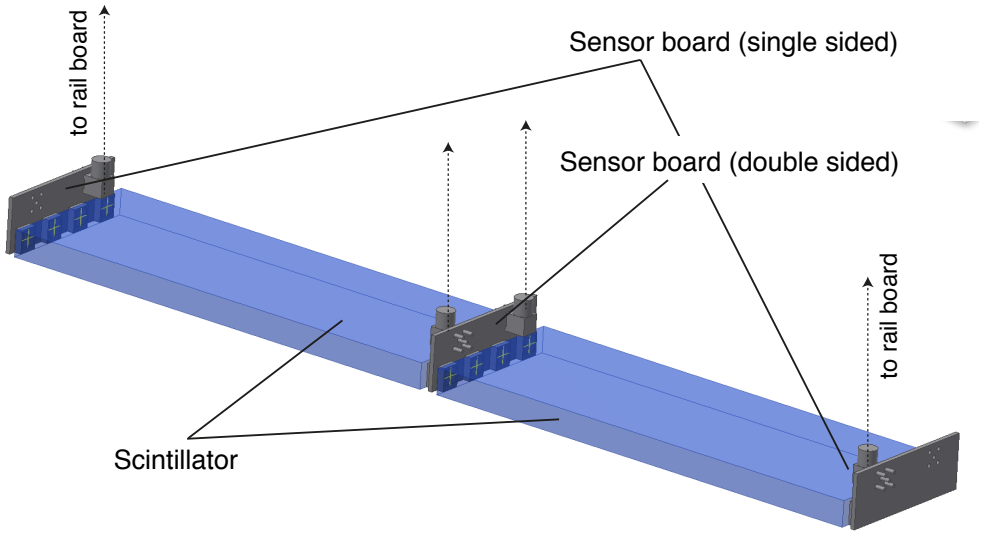

Figure 3.10: *Drawing of two scintillators attached to Sensor-Boards.*

Rail-Board

The Sensor-Boards are connected to a large PCB called the Rail-Board which houses all electrical transmission lines via small MMCX connectors. The Rail-Board connects to the Front-End-Electronics (FEE) positioned on the back side of the board behind the $\bar{p}p$ interaction point. The exact layout of the Rail-Board is discussed in Chapter 5.

To reduce the material budget the Rail-Boards are slotted taking away unnecessary copper and dielectric material in the middle of the PCB where no transmission lines run. A full view of the entire detector with its 16 segments is shown in the drawing in Figure 3.11. Note that the scintillators are turned to the outside to provide coverage of potential photon conversions.

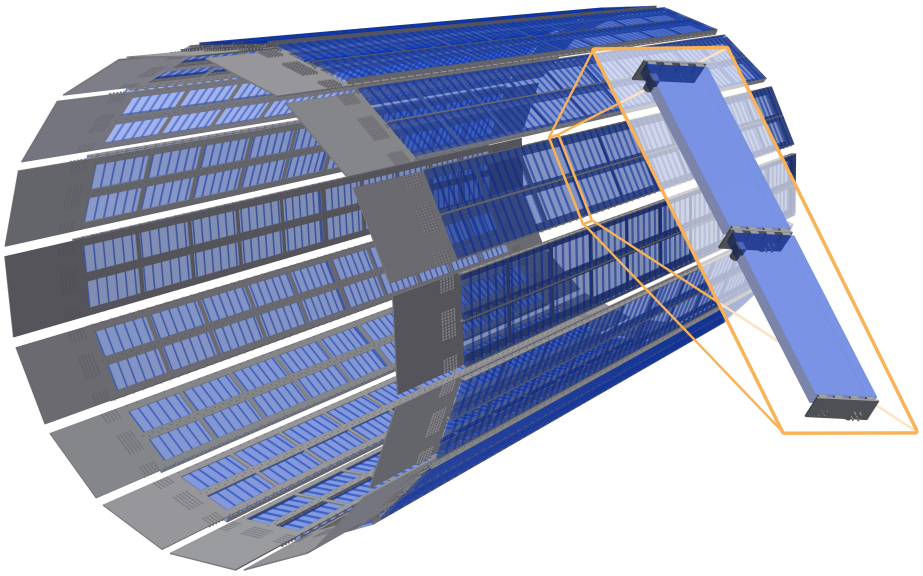

Figure 3.11: *Drawing of the full 16 segment B-ToF detector. The Rail-Boards with cutouts for material reduction are shown in grey with the scintillator tiles in blue. The closeup shows a clear view of the dual modules set on the board.*

The advantage of using a single long PCB over a cable connection is the multi functionality of such a board. Not only does it provide a compact way to connect the SiPMs on the scintillators to the FEE, eliminating bulky cables that introduce a lot of material into the limited space reducing airflow, but it also adds structural stability to the system, being able to carry the components and hold the system together. If not for the Rail-Board another system would have to provide mechanical stability.

3.2.1 Design Overhaul

The rigidity and tight tolerances of the MMCX connectors used on the Sensor-Boards are great for achieving a rigid detector setup with a minimal amount of components. At the same time they make the boards very hard to produce. The

tight tolerances of the connectors require a precise soldering of these connectors and the SiPMs to the board which is not feasible.

The arising minimal tolerances of the system make the whole detector very fragile. Any amount of torque or tension applied to the board, when moving or lifting the detector for example, would directly translate onto the solder and glue joints of the SiPMsĖven if the glue joints do not break, compromised joints could reduce the light collection efficiency of the SiPM readout. Even single damaged SiPM solder joints could cause a complete Sensor-Board failure, due to the SiPM series connection.

In order to avoid this, the connection of the SiPM to the Railboard has been revised. Instead of using a rigid Sensor-Board, the SiPMs, the LED and the temperature sensor are soldered onto a thin flexible PCB which is able to compensate small movements of the scintillator. Such a board is shown in Figure 3.12. It is depicted as a standalone board with SiPMs, the calibration LED with its resistor and the temperature sensor as well as connected to a scintillator.

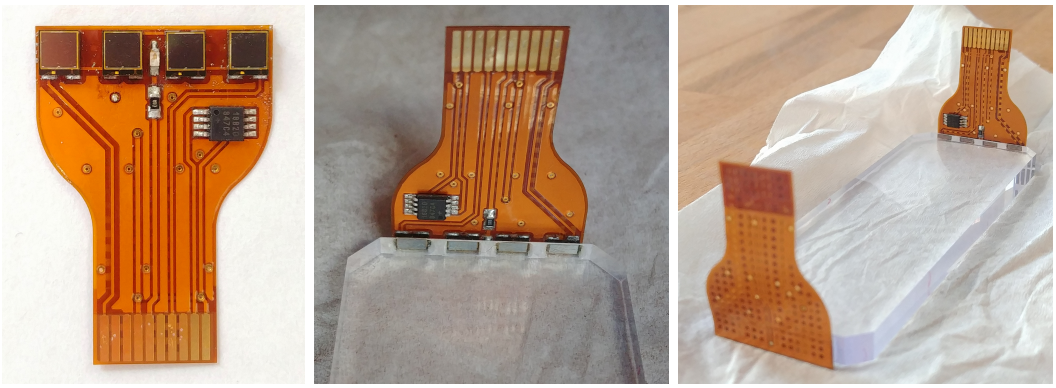

Figure 3.12: *A flexible Sensor-Board on its own (left), attached to a scintillator (middle) and a full active module (right).*

The MMCX connector is replaced with a flat clamping connector by Samtec, called a zero insertion force connector on the Rail-Board. The Sensor-Board is bent by about 90° and inserted parallel to the Rail-Board surface.

The holding structure for the Barrel DIRC and B-ToF only supports the detectors on the edges and does not provide a light tight seal therefore a separate body to support the B-ToF is necessary. This outer layer will be made out of carbon fiber reinforced polymer (CFRP) similar to the housing of the Barrel DIRC. Since the carbon fiber adds an integrated body the Rail-Board is not required to be made out of a single piece anymore but can be made of multiple parts mounted on the carbon frame by plastic screws.

This allows the split of the Rail-Board along the the middle separating the two lines of scintillators since these two sides are electronically independent of one another. Since as explained in Chapter 5 the transmission lines are wider, less material can be cut away. With these smaller boards and smaller cutouts it is easier to cut material on the outer edges rather than inserting slots into the middle of the boards as for the previous design.

For achieve signal optimizations the transmission line width was increased and a new specialized material was used. In order to keep an impedance of $Z_0 = 50\,\Omega$ the Rail-Board almost doubled in total thickness, increasing from (2.25 ± 0.05) mm to (3.45 ± 0.05) mm. This is further discussed in Chapter 5.

The scintillators are held in place by the carbon housing and the Rail-Boardas seen in the detector cross section shown in Figure 3.13. Chamfered scintillator corners allow space for the Rail-Board screws. These spacers also confine the scintillators to the space in between them as can be seen in Figure 3.14.

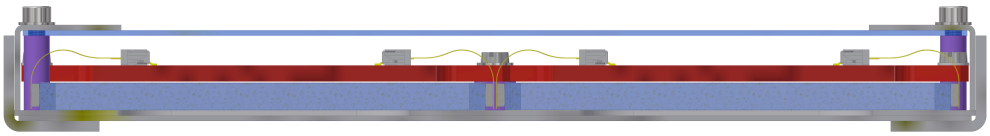

Figure 3.13: *Cross section of the B-ToF showing the carbon frame, the scintillators held in place by purple spacer with SiPMs between the tiles and connected to the Rail-Board via flexible Sensor-Board PCBs.*

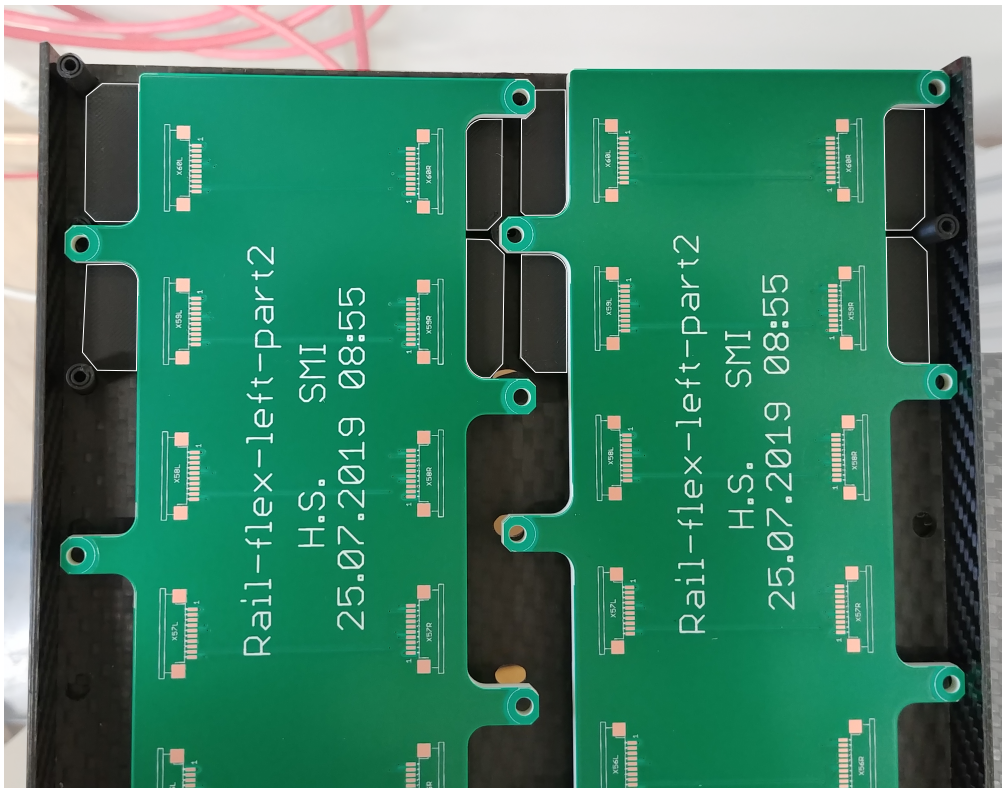

Figure 3.14: *The ends of two Rail-Board parts side by side in a prototype of the carbon frame on top of two scintillator dummies each.*

The gaps between the fixation elements and the scintillator tiles allow slight deformations of the whole detector. The flexible Sensor-Board ensures the optical coupling of the SiPMs to the scintillator is not stressed.

The PCB substrate material (Rogers Material RO4003C) is only produced in sheet lengths up to 48 inch or about 1.2 m. This makes it impossible to produce a board of the full detector length of 1.8 m. Therefore the board must be split in the middle of the long axis and is connected via ribbon cables as seen in Figure 3.15 and is supported by the carbon housing.

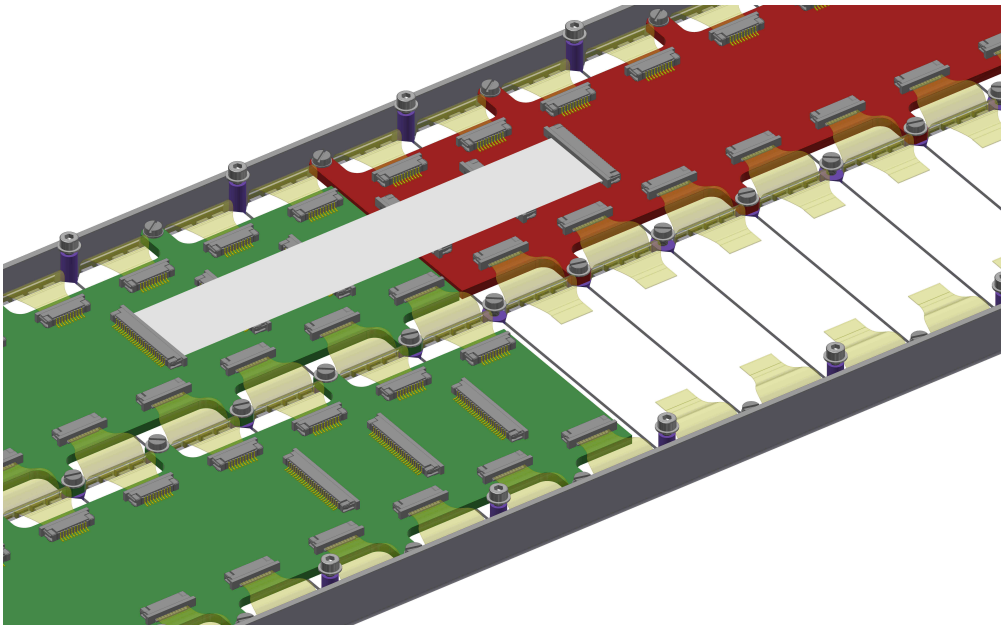

Figure 3.15: *Schematic drawing of the junction of the front (green) and back (red) parts of the Rail-Board. One board is removed to allow a look at the scintillators lying in place underneath the PCB.The spacer are drawn in purple with the flexible Sensor-Board is drawn in translucent yellow connecting SiPMs to the green Rail-Board.*

Other possibilities of connecting the boards were studied but no reliable connector with sufficient contacts in the limited space could be found. Connectors did not have the necessary pitch size to connect 60+ lines without exceeding the space constraints of the detector. For this reason a simple connection with ribbon cables was chosen, at least for this iteration.

3.2.2 Material Budget

In order to affect the calorimeter performance as little as possible the of material in the B-ToF has to be minimized. The impact of the introduced material is measured in radiation lengths X_0.

Although it is possible to calculate an estimation of the radiation length of a certain material, it is advised to use tables of measured radiation lengths [35]. The data for the materials used here is provided by the Particle Data Group [33].

To obtain the radiation length of composite materials one must add the contributions of the individual components as in Equation (3.2.1) weighted by the

components thickness (d_i) or mass [36].

$$\frac{d_0}{X_0} = \sum_i \frac{d_i}{X_i} \tag{3.2.1}$$

Since the detector does not consist of homogeneous layers the individual components must be reduced to their effective thickness spread out over the surface of the detector.

For simplicity I assume the detector consists of an entire 5 mm thick layer of scintillator material (PVT). The carbon fiber (CFRP) housing with its three 1 mm layers, one of which having around 50 % cut out to save material, as well as the side elements are taken into account resulting in an effective thickness of 2.72 mm.

Since every module is equipped with 120 scintillators each read out by 8 SiPMs the 960 SiPMs need to be taken into account. As the basis for this estimation the Hamamatsu S13360-30XXPE was considered [37]. Assuming the SiPMs are made out of pure silicon the SiPMs of one module introduce 23.3 cm^3 of material on 3330 cm^2 of surface area. This produces an effective thickness of 0.07 mm.

The exact material budget for the Rail-Board and all its designs iterations is discussed later in Section 5.6. For this the latest iteration with the best performance will be included. All of these components are listed in Table 3.1 resulting in a total material budget of $d_{\text{eff}}/X_0 = 3.76\,\%$.

Table 3.1: *Material budget estimation of the Barrel Time-of-Flight Detector listed by component, giving their radiation length X_0, effective thickness (d_{eff}) and the resulting material budget contribution (d_{eff}/X_0). The Rail-Board contribution is discussed later in Section 5.6.*

Component	**Material**	**X_0 [mm]**	**d_{eff} [mm]**	**d_{eff}/X_0 [%]**
SiPMs	Silicon	93.70	0.07	0.07
Housing	CFRP	260.00	2.72	1.04
Scintillator	PVT	417.50	5.00	1.20
Rail-Board		-	-	1.45
Sum				**3.76**

3.2.3 Temperature Sensor

In order to monitor the ambient temperature and ensure stable operation conditions the detector will be outfitted with multiple temperature sensors. Since it is not feasible to have a channel for every temperature sensor on the board the bus should use the minimal amount of lines. The chosen sensor, the DS18B20 by *Maxim Integrated* operates on a 1-Wire digital bus. A connection this way only uses one data line and one power line in addition to a ground connection to link all the sensors on one board.

The limit to the number of devices is determined by hard coded 48-bit address of each sensor [38] which far exceeds the number of necessary sensors for one Rail-Board. Since the devices are all connected in parallel as shown in Figure 3.16 having one sensor become unresponsive will not affect the performance of the other devices.

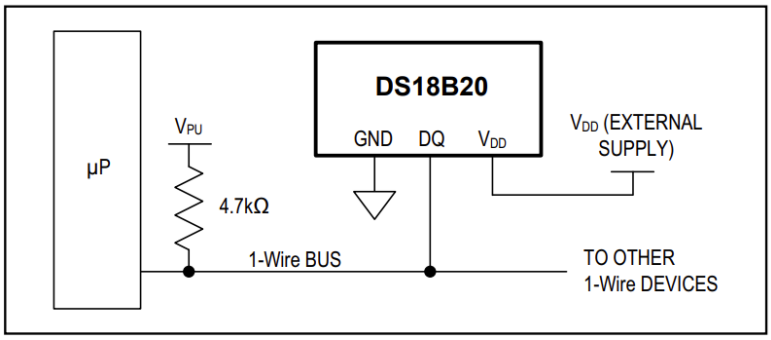

Figure 3.16: *Connection scheme for the DS18B20 temperature sensor connected to a micro processor (µP) [38].*

3.3 Particle Identification and Interaction Time Determination Capabilities of the B-ToF

There are two possible approaches to particle identification with the Barrel Time-of-Flight Detector. The first is very straight forward. By combining information of other detectors on the particles momentum (p) and trajectory (s) delivered by the tracking system with the particles time-of-flight one is able to determine its mass and hence its identity. From the relativistic definition of the momentum $p = \gamma m_0 v$ and the simple translation equation for the trajectory $s = vt$, one receives Equation (3.3.1) given in natural units.

$$m_0 = p \sqrt{\left(\frac{t_{ToF}}{s}\right)^2 - 1} \tag{3.3.1}$$

This method produces separation powers for the three main particles (Protons, Pions, Kaons) of significant values well above 4 σ below the Cherenkov threshold, as Figure 3.17, a simulation taking the relevant uncertainties produced by the detector subsystems into consideration, shows [28]. While the grey shaded are shows the section in which particles begin surpassing the Cherenkov threshold and the Barrel DIRC begins to detect kaons and protons, the front section of the distribution is where the $\overline{\text{P}}$ANDA PID is reliant on the B-ToF. There is no clear transition since the separation power here is plotted against the radial and not the absolute momentum introducing angle dependencies.

Since the $\overline{\text{P}}$ANDA experiment is triggerless and is operated with a coasting beam no regular interaction time or t_0 is available to determine the time-of-flight,

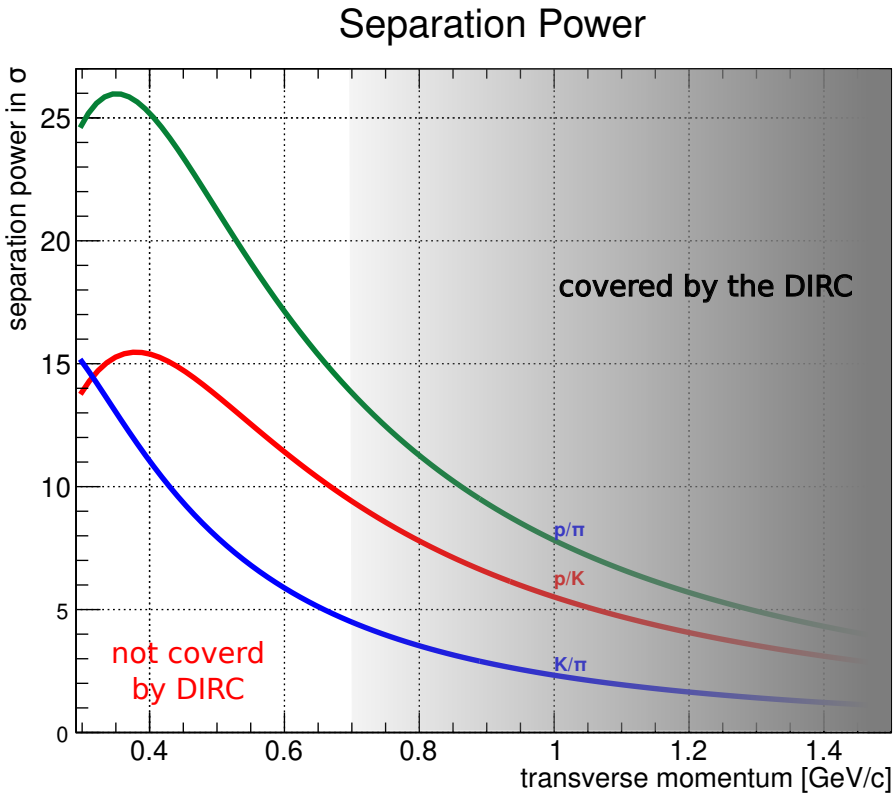

Figure 3.17: *Separation Power of the B-ToF for various particle combinations measured in standard deviations. The grayed out area to the right is the momentum region in which particle begin to produce Cherenkov light and the Barrel DIRC detector begins to work [28].*

$t_{ToF} = t_{\text{B-ToF}} - t_0$. For this reason either another detector system is able to provide a start time or the second method has to be used.

This second method is able to determine t_0 and simultaneously provide PID information on the involved particles. This method is called the relative time-of-flight method.

By assuming that, for short time windows with more than a single detector, all particles responsible for the detector signals originate from the same interaction namely the $\bar{p}p$ annihilation at the center of the detector. Under this assumption, one can iterate through all possible mass assumptions for the particles and determine their respective expected time-of-flight based on momentum and trajectory information provided by other detectors. By doing this, basically reversing the process of the method mentioned above, one receives multiple possible interaction times based on the formula in Equation (3.3.2).

$$t_{0_i} = t_{\text{B-ToF}} - s\sqrt{\left(\frac{m_{0_i}}{p}\right)^2 + 1} \tag{3.3.2}$$

If these particles are part of the same event, the calculated t_0 values should be similar. Figure 3.18 shows a color coded visualisation for this concept. Time stamps for two B-ToF hits or signals are shown as blue lines along a time axis at 7 ns and 7.2 ns. For the first such hit various possible t_0 for different mass assumptions (Proton, Pion, Kaon) are calculated according to Equation (3.3.2) and marked with green lines. The same is done for the second hit with red time stamps. At about $t_0 = 3.1$ ns two t_0 candidates ($m_{0_1} \mathrel{\widehat{=}} p$, $m_{0_2} \mathrel{\widehat{=}} K$), one from each initial time stamp, align. This is the most likely particle identity combination at the most probable interaction time t_0 [28].

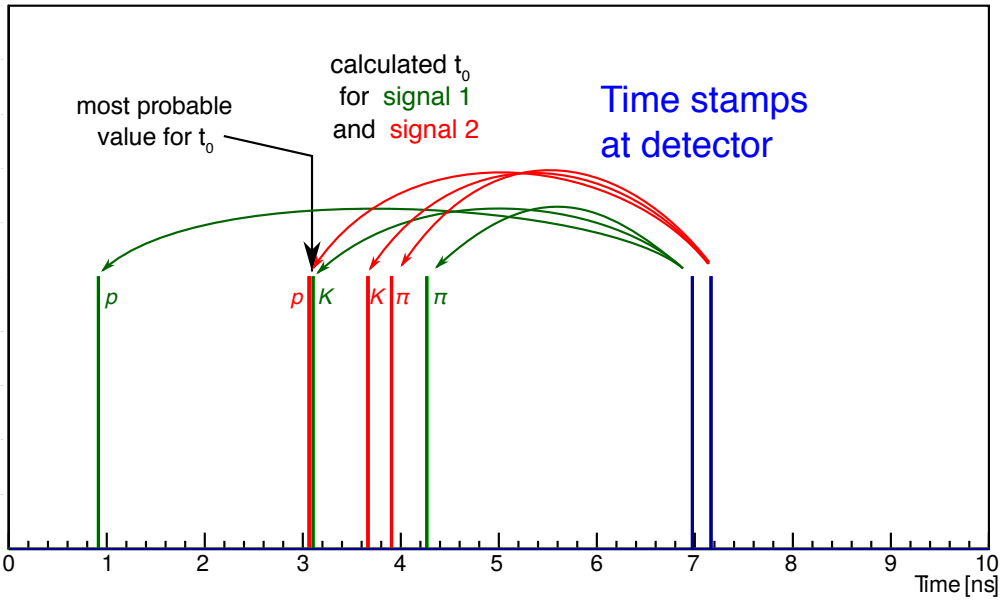

Figure 3.18: *The relative time of flight method works by taking multiple mass assumptions of all involved detector hits here marked with blue lines on the time axis. Different particles show differences in their time-of-flight for the same momentum and trajectory due to differences in their mass and hence velocity. For these assumptions the respective interaction or creation time is calculated and shown color coded; green for the first and red for the second hit. Where interaction times align we assume to have found* t_0 *[28].*

Chapter 4

Silicon Photo Multiplier for the B-TOF

4.1 Detector Technology

4.1.1 Photon Detectors and SiPMs

4.1.1.1 Photomultiplier Tubes and Microchannel Plates

Since the 1930s Photomultiplier Tubes or short PMTs were primarily used for detecting light of low photon count such as in scintillating counter applications. Such PMTs are made up of a photocathode, focusing electron optics, a cascade of dynodes and a charge collecting anode as seen in Figure 4.1. Incoming photons hit the photocathode and release one or more photoelectrons. These are focused and accelerated towards the first dynode sitting at a positive potential difference to the cathode. The dynodes are made of materials with negative electron affinity, designed to absorb the incoming accelerated electron/s and re-emit multiple low energy electrons in a process similar to the photoelectric effect.

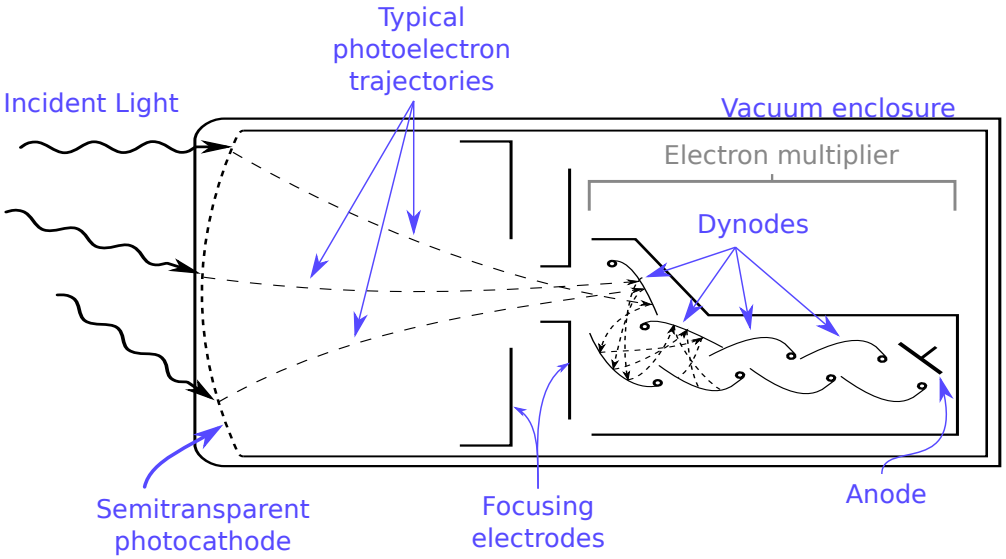

Figure 4.1: *Schematic drawing of a Photomultiplier Tube (PMT).*

The electric potential from the first to the second dynode is increased giving the just emitted electrons a boost towards it where they again get absorbed and

re-emit low energy electrons now moving towards the next dynode. As this process continues the number of electrons increases exponentially until they are finally absorbed by the anode producing a measurable electric pulse. [39]

Although they were the standard photon detection device for scintillators until recently, these detector posses multiple significant downsides.

- The tubes can be very **bulky**, from around $3\,\mathrm{cm}^3$ to $10^5\,\mathrm{cm}^3$ limiting their application in tight designs.
- The precise focusing and accelerating of the electrons internally make **applications in electric / magnetic fields impossible**.
- Due to the ever increasing potential from dynode to dynode, PMTs require **high bias voltage**s in the kV region to operate.
- Non uniform electron trajectories limit the timing performance of PMTs.
- **Low quantum efficiency** of the photocathode since the electrons need to overcome the electric potential and escape the cathode surface.
- **Fragile build** set in a vacuum in a glass housing.

A complete overhaul of the dynode structure but keeping the general principal of operation manages to address some of the issues mentioned above. Microchannel Plates (MCPs) are thin plates made out of lead glass, perforated with small holes throughout the surface. When a potential difference between the front and back side is applied the semiconductor coated holes or channels act as continuous dynodes in the same way as the dynodes of a traditional PMT. By replacing the dynodes with one or more MCPs one receives an MCP photomultiplier tube (MCP-PMT) as can be seen in Figure 4.2.

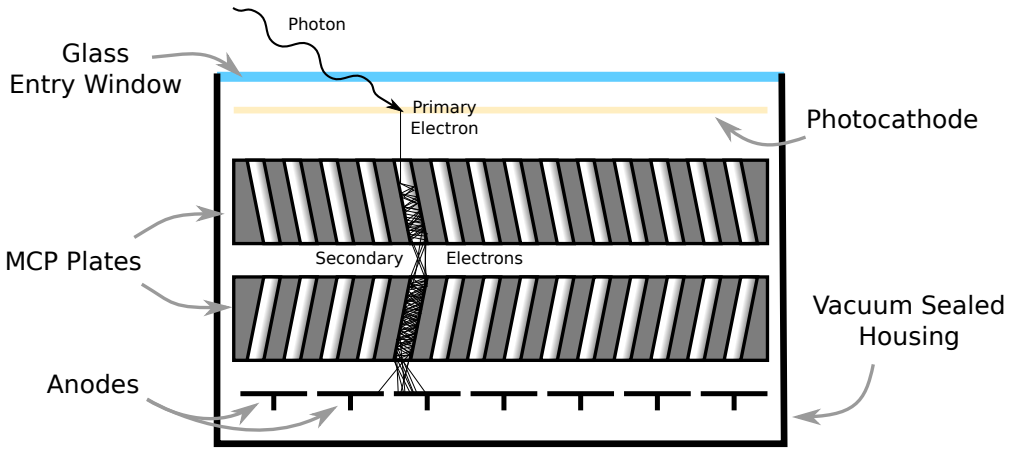

Figure 4.2: *Schematic drawing of an MCP photomultiplier tube employing two individual microchannel plates in a Chevron configuration for a higher gain.*

Incoming photons, electrons or ions hit the photocathode or the inside of a channel and release at least one electron. This electron, due to the applied electric

field, is accelerated towards the back of the plate. Since the channels are set at an angle of 5° to 15° relative to the electric field the produced electrons hit the wall of the channel again producing more electrons. This induces a cascade as seen for PMTs.

Depending on the model the electrons are then picked up by one or multiple anodes. The latter adds a position resolution at the expense of additional readout channels. To increase the gain it is also possible to line up multiple MCPs in a single detector as shown in Figure 4.2.

Due to the smaller dimensions they deliver considerably smaller timing properties compared to conventional PMTs. This also makes them less susceptible to magnetic fields since the electrons travel a shorter distance in the channels. On the other hand MCP-PMTs are very expensive and provide limited reliability.

4.1.1.2 Silicon Photomultiplier

With the rise of semiconductors an alternative to the large PMTs presented itself. By infusing a semiconductor material such as silicon with certain impurities called doping, a diode can be produced allowing the flow of electricity in only one direction. Doping introduces impurities that, depending on the specific dopant, create electrons (n-doped) or holes (p-doped) which are able to freely move along the silicon lattice. By bringing an n- and p-doped region together, a boundary region is formed which is depleted of any free charge carriers, the depletion region. By applying a voltage across this junction, the depletion region is reduced and allows a current to flow or grows in size preventing an exchange of charge carriers, depending on the polarity of the potential difference. A potential of the latter kind is called a reverse bias only producing a small trickle current called the leakage current in an otherwise non conductive state.

Photons that hit this region can be absorbed and create free electron-hole pairs which move towards the anode and cathode respectively creating a current that when amplified can and measured. A device operating under this principle is called a photodiode.

To increase the measurable signal the applied bias voltage can be increased. If the potential difference is large enough free electrons moving to the anode gather enough energy to release more electron-hole pairs along the way inducing an avalanche. For carefully controlled voltages the increasing electron count reaching the anode is proportional to the amount of primary free charge carriers produced for example by incoming photons. The gain of such a detector commonly referred to as an Avalanche Photodiode (APD) is very temperature and bias voltage dependent. The applied voltage can be increased until holes moving in the opposite direction of the electrons start creating their own electron-hole pairs resulting in a runaway effect inside of the semiconductor. The voltage at which this occurs is called the breakdown voltage.

Operation behavior of a photodiode past the breakdown voltage is called Geiger mode. As the name implies the diode functions very much like a gaseous Geiger counter in which a small initial ion pair is able to fully discharge the detector. The resulting avalanche in this mode would be self-sustaining if not quenched in some

way, for example by adding a large resistor which when the avalanche occurs drops the voltage and reduces the electric field in the semiconductor, eventually stopping the ongoing avalanche. Such a device with a single cell is called a single photon avalanche photodiode (SPAD).

Such an SPAD however does not deliver much information since the runaway avalanche can be triggered by a single free electron and is for each discharge similar in amplitude and independent of the initial count of free charge carriers. Everything but the event time of down to a single incident photon is lost. For applications in conjunction with scintillators, where most often the amount of emitted photons is of interest, this is of limited use. However creating an array of such SPADs all connected in parallel offers interesting properties. Such a device is called a Silicon Photomultiplier or SiPM in short.

These detectors manage to integrate hundreds of small SPADs as seen in Figure 4.3 in the order of tens of µm into one device of a few mm squared. With cells of this size the probability of two or more photons hitting the same cell is small enough to assume each incoming photon is detected in an individual cell. If this is the case, the number of incident photons is proportional to the number of firing cells, each connected in parallel and producing a pulse of roughly the same size, adding up to create one pulse. By measuring the resulting pulse amplitude one can determine the number of photon events or photoelectrons (p.e.) and then estimate the amount of emitted scintillator light. An overlay of up to 5 photoelectron peaks is shown in Figure 4.3.

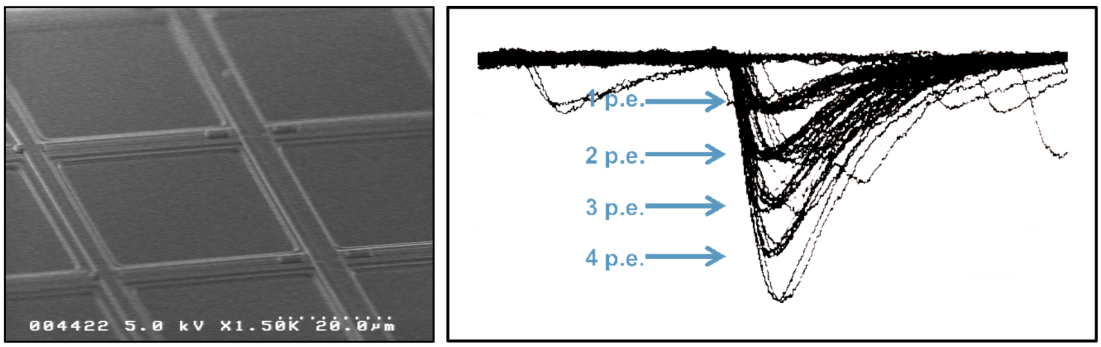

Figure 4.3: *The left image depicts a closeup view of SPADs of a SiPM on its silicon substrate. The right image depicts an overlay of multiple SiPM pulses with up to 4 simultaneously firing SPAD cells or photo electrons (p.e.). [40]*

For reliable operation the applied bias voltage usually is set higher than the breakdown voltage by roughly 5 % to 10 %. This difference of operational voltage to the breakdown voltage is called overvoltage and determines most of the SiPMs characteristics. By increasing the overvoltage the gain increases leading to a shorter leading edge rise time of the resulting pulses. However this also increases the noise level of the detector, so a balance must be struck.

4.1.2 SiPM Characteristics

4.1.2.1 Electrical Properties

All the cells of the SiPM are individual SPADs connected in parallel, each with its own quenching resistor. This being said all cells can be viewed individually. A schematic of the electrical equivalent circuit of a cell is shown in Figure 4.4 with the dotted area being the diode itself. It depicts the diode at which the breakdown voltage (V_{BR}) is applied in series with R_S the resistance of the depletion region of the diode as well as a switch. This switch represents the presence or lack of free electron-hole pairs enabling or prohibiting current flow. When a photon hits, closing the switch, current flows through the diode for $\tau = C_J R_S$ with C_J being the junction capacitance. With the quenching resistor R_Q connected in series this lets the voltage applied to the APD region V_D drop to virtually zero breaking the avalanche initiating the recharge of the capacitance $\tau_{recharge} = C_J R_Q$ typically in the order of a few ns.

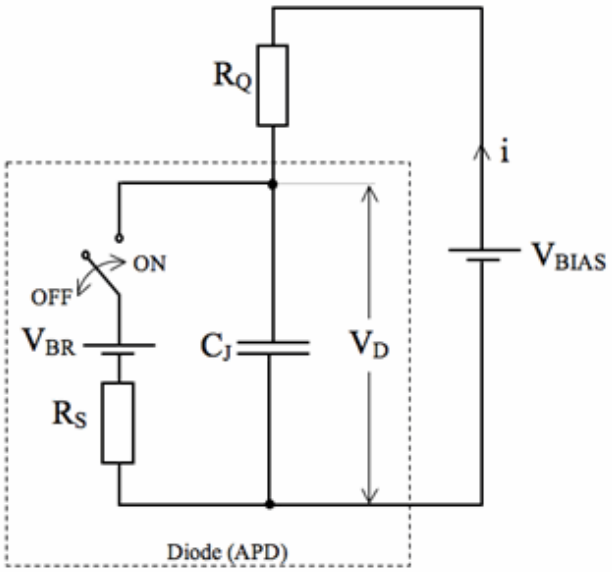

Figure 4.4: *Equivalent electrical schematic of single SiPM cell with the functional APD part marked by the dotted line. V_{BR} is the breakdown voltage, R_S the resistance of the depletion region, C_J its capacitance, V_D the voltage applied to the APD part and R_Q the quenching resistor [41].*

Since all cells are independent, one cell being hit has no effect on the others allowing them to initiate multiple photon events in rapid succession giving the SiPM as a whole a near zero dead time for light pulses of moderate intensity.

4.1.2.2 Photosensor Gain

The gain of the SiPM is measured by the charge released in a single photon event which is the product of the overvoltage and the cell capacitance, $Q_{p.e.} = C_J V_{OV}$. Not immediately obvious but one of the major contributors to a varying gain is

the temperature. This is due to the temperature dependence of the breakdown voltage, which decreases for rising temperatures. Reducing V_{BR} by increasing the temperature while applying a constant operational voltage effectively leads to an increased overvoltage.

Because of the temperature sensitivity of the gain, a close temperature control is necessary for long operation in cases in which the signal pulse height or the amount of photo events is of interest.

4.1.2.3 Photon Detection Efficiency

The ability to detect photons is measured in the photon detection efficiency (PDE). It is the ratio of photons that hit the detector area and the number of detected pulses. It comprises a wavelength dependent factor, the quantum efficiency $\eta(\lambda)$, an overvoltage dependent factor, the probability that an avalanche will be triggered by an electron-hole pair (P_A) and the geometrical fill factor (F_G).

$$PDE = F_G\, \eta(\lambda)\, P_A \tag{4.1.1}$$

The geometrical fill factor is the ratio of sensitive detector surface to the total detector area. Since SiPMs are made up of multiple cells some surface is lost at the boundary dividing the cells and including components such as the quenching resistor or the supply lines. This leads to the cell size dependence of F_G as shown in Figure 4.5, showing SiPM cells of 25 µm, 50 µm and 75 µm with a metal-composite quenching resistor around each cell, leaving proportionally less space for the active area in the smaller cells.

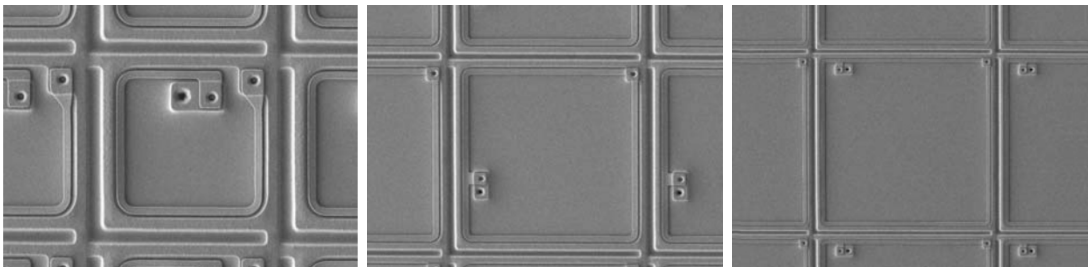

Figure 4.5: *Closeup view of 25 µm, 50 µm and 75 µm SiPM cells with a metal-composite quenching resistor around each cell. [41]*

Since the photon count often dictates the performance of a photomultiplier it is desirable to maximize the PDE. For this the matching of SiPM to the scintillator or vice versa is essential as the quantum efficiency, the ability to convert an incoming photon into a signal, peaks at different wavelengths for different models. When using a fast scintillator often emitting photons in the higher energy blue spectrum the SiPM must be sufficiently sensitive to such wavelengths.

4.1.2.4 Time Resolution

Since SiPMs are made up of many individual SPADs and the SiPM signal is made up of the overlap of all hit cells, the time resolution of the SiPM depends on the

time resolution of a single SPAD or the *Single Photon Time Resolution* (SPTR). The SPTR is determined by the uniformity of the SPADs but is dominated by the electronic noise [42].

The time resolution of the SiPM as a whole is also dependent on the total amount of detected photons ($N_{p.e.}$) and improves with higher statistics. It has been shown that the time resolution follows the behavior shown in Equation (4.1.2) [43].

$$\sigma_{SiPM} \sim \frac{\sigma_{SPTR}}{\sqrt{N_{p.e.}}} \tag{4.1.2}$$

In the following descriptions the time resolution will refer to the standard deviation of a signal time distribution denoted by a σ.

4.1.2.5 SiPM Noise

As all detectors are so are SiPMs affected by noise sources of many kinds. Understanding and limiting these sources is essential to producing an optimal measurement as noise can otherwise limit the resolution and the performance of the detector.

Dark Noise

Due to the high sensitivity of each cell even thermally generated electrons in the conduction-band are able to induce an avalanche. With a sufficient electric field any free electron can be accelerated and create more electron-hole pairs along the way. An avalanche initiated in this way is indistinguishable from a regular detection of a photon. Such events are called Dark Pulses or Dark Noise [41].

As these are random events they will be occurring as long as sufficient bias voltage is applied producing a constant stream of single photon events. The rate of these noise events depends on the silicon temperature as well as the overvoltage. Illustrating this is Figure 4.6 depicting the effect of the temperature on the dark noise for multiple overvoltages measured using a custom version of a Hamamatsu model S10362-11-050C SiPM.

This exponential dark rate dependence on the temperature makes temperature monitoring and cooling essential for a fully controlled experimental environment. Lowering the temperature drastically reduces the dark count rate [41].

Afterpulsing

After an avalanche is created in a cell, there is a finite probability a second pulse is created shortly after. This phenomenon is called afterpulsing. These second avalanches after a regular full avalanche are caused by entrapped electrons in impurities inside of the silicon which are re-emitted after a short delay usually in the order of 1 ns to 10 ns.

Secondary pulses emitted during the recovery phase will not have the same amplitude as primary pulses. If an afterpulse however is released after the cell has recovered it is indistinguishable from a regular pulse except in its timing.

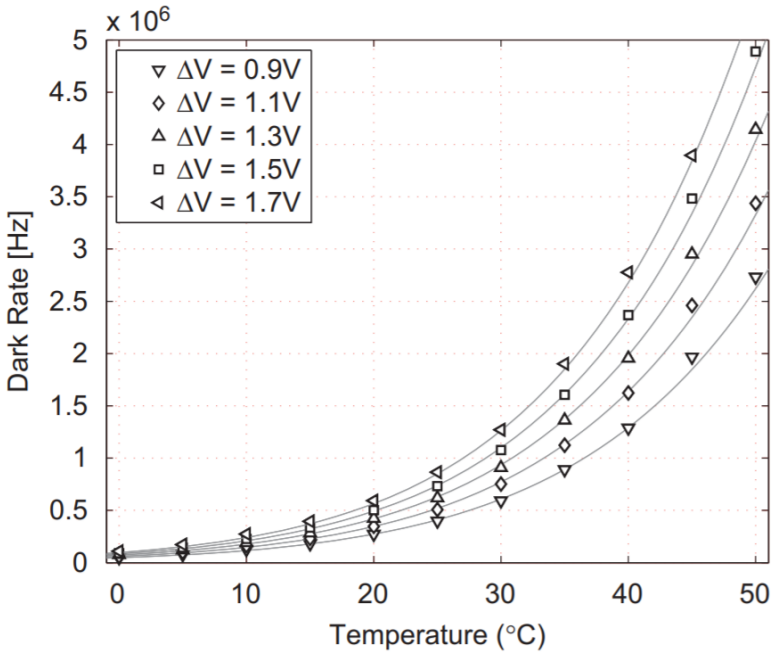

Figure 4.6: *Dark noise as a function of the temperature for various overvoltages (ΔV). [44]*

The probability of this occurring does not depend on the temperature but rather on the applied overvoltage. With a stronger electric field in the depletion region the chance of an electron initiating an avalanche increases raising the efficiency of this process.

Optical Crosstalk

The kinetic energy of the electron during an avalanche does not induce the emission of electrons in every instance. A small probability exists that this energy is converted into photons emitted during a collision. If these photons find their way into a neighboring SiPM pixel a second avalanche might be initiated. This process is called optical crosstalk and occurs virtually simultaneously with the initial event leading to a signal larger than expected.

Having more free electrons increases the chance to produce secondary photons giving the crosstalk probability a gain dependence. To reduce its impact the gain can be reduced by lowering the cell capacitance while keeping the PDE high with a higher overvoltage.

4.1.2.6 Life Time Expectancy

Unlike other detectors such as the MCP-PMTs, which degrade with high integrated anode currents, SiPMs do not suffer from an intrinsic limit of its life time. They however are susceptible to radiation. To make damage done to silicon based detectors comparable across different radiation types the NIEL scaling hypothesis was developed [34].

Sufficiently energetic radiation of any kind may cause lattice displacements inside the crystalline silicon base material of the SiPMs. Defects introduced this way are able to lower the breakdown voltage and cause an increase in dark noise. As the damage accumulates over time the resulting increase in leakage current leads to an increase in temperature further deteriorating the SiPMs performance.

Studies suggest that to mitigate the increase in dark noise that is produced by individual damaged pixel cells one can simply reduce the cell size and increase the number of pixels to reduce the impact radiation damage has on the detectors by spreading the damage to more cells [45].

4.1.3 Series Connection of SiPM

Despite all the advantages one major limitation of SiPMs is their size or their sensitive area. While PMTs are able to cover large areas with a single device, SiPM applications would require multiple detectors each with an individual readout to cover the same surface, increasing the complexity of the necessary front end electronics. Simply adding multiple SiPMs in parallel in the same way the cells are connected would increase the sensitive area per channel at the cost of potentially adding all the downsides too.

For timing applications for example, it is the rise time which heavily influences the performance. A faster rising signal delivers a better time resolution. As described in Section 4.1.2.1 this property depends on the internal resistance and the internal capacitance. Reducing the capacitance of the depletion region would lead to a faster signal.

Without changing the individual cell capacitance it can be reduced by adding multiple SiPMs in series as shown in Figure 4.7 a), leading to a lower effective capacitance over the whole system.

$$C_{total} = \left(\sum_{n=0}^{N} \frac{1}{C_n} \right)^{-1} \tag{4.1.3}$$

Adding SiPMs in parallel as shown in Figure 4.7 b) would have the opposite effect, increasing the capacitance and reducing the signal rise time.

This can be seen in the SiPM response when comparing series and parallel connections of multiple SiPMs to a single SiPM response. Such a comparison can be seen in Figure 4.8. In contrast to the single SiPM with the dotted line in red the finely dotted blue line of the three parallel SiPMs response shows a clear increase in both the rise and fall time. As expected a series connection shows the opposite behavior desirable for timing applications.

In addition to improving the shaping of the SiPM signal connecting, SiPMs in series provide a dynamic adjustment to varying breakdown voltages of the individual SiPMs. A difference in leakage current created by varying breakdown voltages leads to an adjustment of the naturally applied voltage to each SiPM smoothing out any manufacturing differences [46].

A third way to connect multiple SiPMs is shown in Figure 4.7 c), the hybrid connection. By adding resistors and capacitors in between the SiPMs it is possible

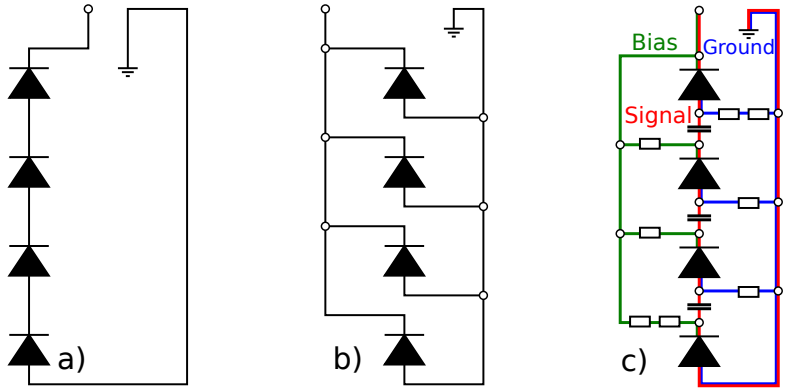

Figure 4.7: *Schematic drawing of different ways to arrange multiple SiPM in a single readout channel. a) serial connection; b) parallel connection; c) Hybrid connection*

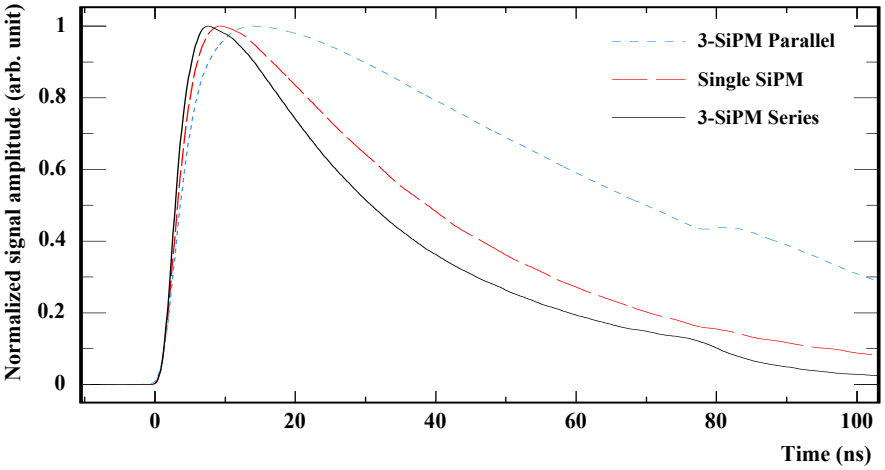

Figure 4.8: *Comparison of normalized pulses of parallel and series connection of SiPMs to a single SiPM. [46]*

to separate the application of the bias voltage which happens in parallel and the signal transmission with all capacitors in series. This provides the timing benefits of a serial connection due to the lower capacitance while keeping the necessary bias voltage low at the level of a single SiPM instead of the sum of all SiPM voltages. This connection however adds complexity to the design which due to the limited space in the B-ToF and to minimize any potential points of failure will need to be avoided.

4.2 Rate Capability Measurements

The B-ToF detector will be subject to varying interaction rates. Although the mean interaction rate of the HESR in high luminosity mode is supposed to be 20 MHz significantly higher rates can be expected for short bursts of multiple consecutive interactions. Resulting hits of the $\bar{p}p$ interactions are distributed over the whole B-ToF meaning single tiles will experience a hit rate lower than the interaction rate. None the less in order not to lose valuable hit information the detector must be able to handle such occasions.

4.2.1 Measurement Setup

The SiPMs studied in this section were produced by Hamamatsu and Ketek. The hybrid connection utilized four of the S13360-3025PE series SiPMs by Hamamatsu. The SiPMs connected in series were of the Ketek PM3350 series.

To study the capability to measure hits in quick succession the amplified signal amplitude as well as the signal integral or area were recorded for short laser pulses of increasing frequency. The laser used for these measurements was the Advanced Laser Diode System PiLas PiL040 emitting blue pulses with a wavelength of (405 ± 15) nm with a pulse width below 45 ps. It is rated for operation up to a repetition rate of 1 MHz above which a drop in pulse intensity can be expected.

The measurement setup can be seen in Figure 4.9. The laser was placed inside a large wooden dark box together with the SiPM setup to ensure no stray light impairs the measurements. To regulate the laser strength an adjustable optical attenuator was placed in the beam as well as a diffuser to spread the beam spot evenly across all SiPMs. Since the laser produces electromagnetic pulses each time it fires it was wrapped in aluminum foil and the SiPMs were shielded by placing them in a large metal box inside a second small metal box. This box holds an array of four SiPMs connected in series or hybrid connection in place as well as the preamplifier for the SiPM signals. To readout the SiPM signals and produce the desired measurements the SiPM arrays preamplifier was connected to a digital oscilloscope.

The diffuser ensures a uniform distribution of photons across all SiPMs. To illuminate individual SiPMs, in order to be able to study different combinations of sensors, some sensor faces are covered by black electrical tape blocking incoming light. In the following the illuminated SiPMs will be named in order from 1 to 4 as seen in the bottom right of Figure 4.9, with 1 being the closest to the cathode

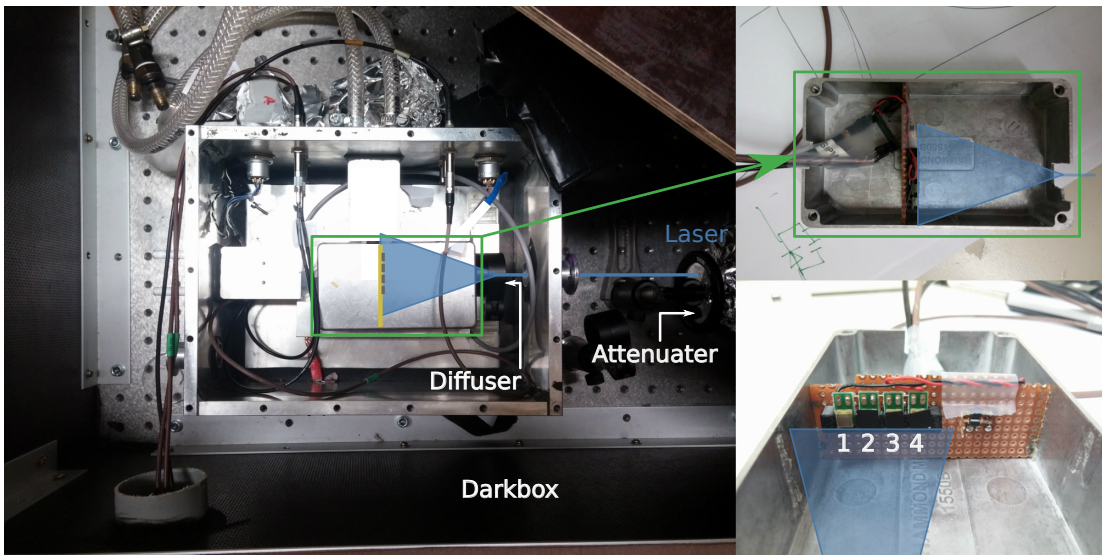

Figure 4.9: *Measurement setup for the rate capability measurements. The image shows three views of the same setup in different angles. Four SiPMs are held in place by a small metal box. This is placed inside a larger metal box shielding it from the laser that is shot through an attenuator and diffuser. All placed inside a wooden dark box and connected to an oscilloscope for the readout.*

and 4 closest to the anode. In this way combinations from illuminating a single SiPM at multiple positions in the series to illuminating all SiPMs were looked at.

4.2.2 Results

When studying a hybrid connection of four Hamamatsu SiPMs measuring the signal amplitude response to an increasing number of illuminated SiPMs we received the distribution shown in Figure 4.10 with the error bars being the standard deviation of the signal amplitude throughout the measurement, recording a minimum of 10^5 pulses per measurement. Illuminating all four SiPMs resulted in the largest SiPM signal pulse response listed as *SiPM 1234* in Figure 4.10. As expected blocking one SiPM leads to a signal reduction of 1/4, since due to the diffuser all SiPMs are illuminated by equal light intensities. After roughly 0.7 MHz the amplitude drops as this is close to the limit of the lasers range of operation. The measurement of the signal area produced the same result.

Looking at the bottom image of Figure 4.10 showing all responses normalized to their respective maximum response, one sees that all SiPM combinations display the same overall pattern equivalent to the response of a single SiPM. The distributions appear stable until roughly 200 kHz to 300 kHz where slight differences in SiPM response appear, but still well within the margin of error.

Measurements of a single SiPM were not included in the top graph depicting absolute signal amplitudes. The single SiPM measurement is only added to the normalized distribution since only their relative distribution shape is of interest.

The measured amplitude distribution for a series connection of SiPMs is shown in Figure 4.11 which shows a distinctly different distribution. As seen in the bottom

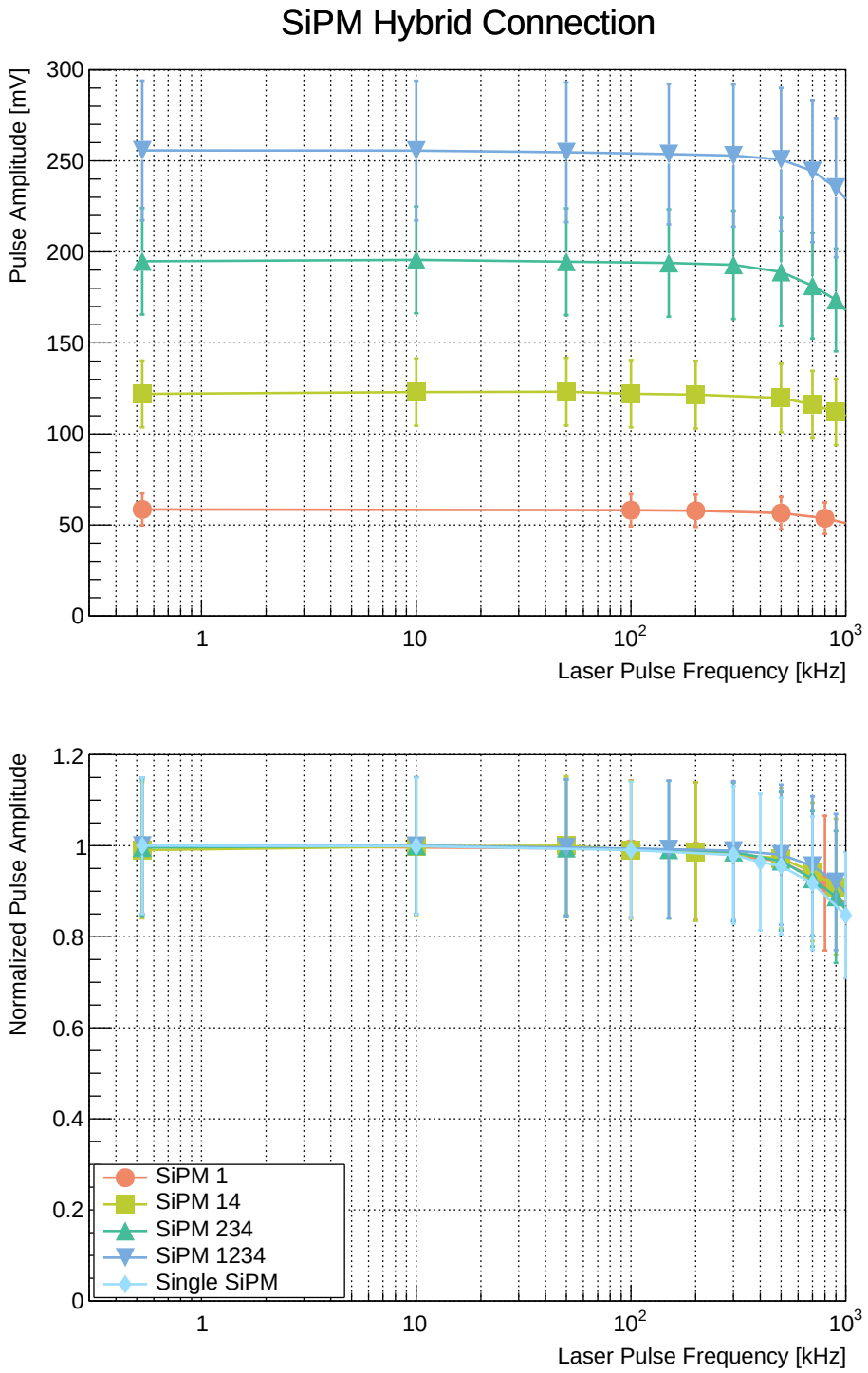

Figure 4.10: *Signal area measured for a hybrid connection of four Hamamatsu S13360-3025PE SiPMs illuminated by a pico second laser of increasing frequency in different SiPM patterns. The bottom image shows a normalized version of the top plot with the legend applying to both distributions.*

plot of Figure 4.11 the full illumination of all SiPMs in a serial connection yields a distribution very similar to a single SiPM. However as soon as at least one SiPM is covered the signal pulse drops in amplitude much earlier with growing laser pulse frequencies. The same is observed for the signal area.

The amplitude difference between the various SiPM combination distributions is also not evenly split as one would expect from a uniform photon distribution, not even at low frequencies. Having at least one sensor covered produces smaller responses than the expected $\frac{1}{4}$, $\frac{1}{2}$ and $\frac{3}{4}$ of the maximum.

The normalized distribution shown on the bottom of Figure 4.11 reveals a clear difference in the rate of amplitude reduction between measurements with different numbers of illuminated SiPMs. A drop-off occurs at slightly higher frequencies for distributions where more SiPMs are illuminated. No configuration however comes close to a full illumination of all sensors.

Studying the distributions position dependence of the illuminated SiPMs shown in Figure 4.12 one sees that the position of illuminated the SiPMs inside of the series connection has no effect on the amplitude response over all frequencies within the margin of error. All distributions show the same frequency dependence as long as the same number of SiPMs are illuminated.

4.2.3 Conclusion

The amplitude drop for SiPMs connected in series at frequencies sooner than for standalone SiPMs as seen above most likely arise from a limited recharge current. This suspicion has been backed by private communications with Hamamatsu and Ketek but series connections of SiPMs are not well studied yet. As described in Figure 4.4 each pixel of a SiPM acts as a capacitor that is depleted every time an avalanche occurs. Recharging this capacitor and reestablishing the operational voltage takes time in the order of micro seconds [47] as confirmed by the measurements above. In occasions, in which avalanches occur in some but not all SiPMs connected in series, the current available to recharge the pixels is limited, since some SiPMs remain in the state of functioning diodes. The only current available in this state is the leakage current of the SiPMs.

The difference in recovery speed for illumination constellations with different numbers of SiPMs most likely stems from a difference in effective voltage applied to the non-illuminated SiPMs. As a SiPM cell is hit by a photon an avalanche is initiated and current starts to flow, hence its resistance drops. As a consequence the applied voltage in a series connection is redistributed among the connected SiPMs, dropping for the illuminated sensors and rising for the ones kept in the dark. If less SiPMs undergo an avalanche process less sensors share the increased voltage. Since the recovery time is determined by the leakage current which is voltage dependent, one can expect a decrease in the recovery time for cases in which fewer sensors stay unilluminatied.

For parallel and hybrid connections the current is not limited in the same way. The bias voltage is always applied directly to the SiPM the same way it is for a single sensor. Due to this it will also behave like a single sensor when observing the frequency dependence or recovery time.

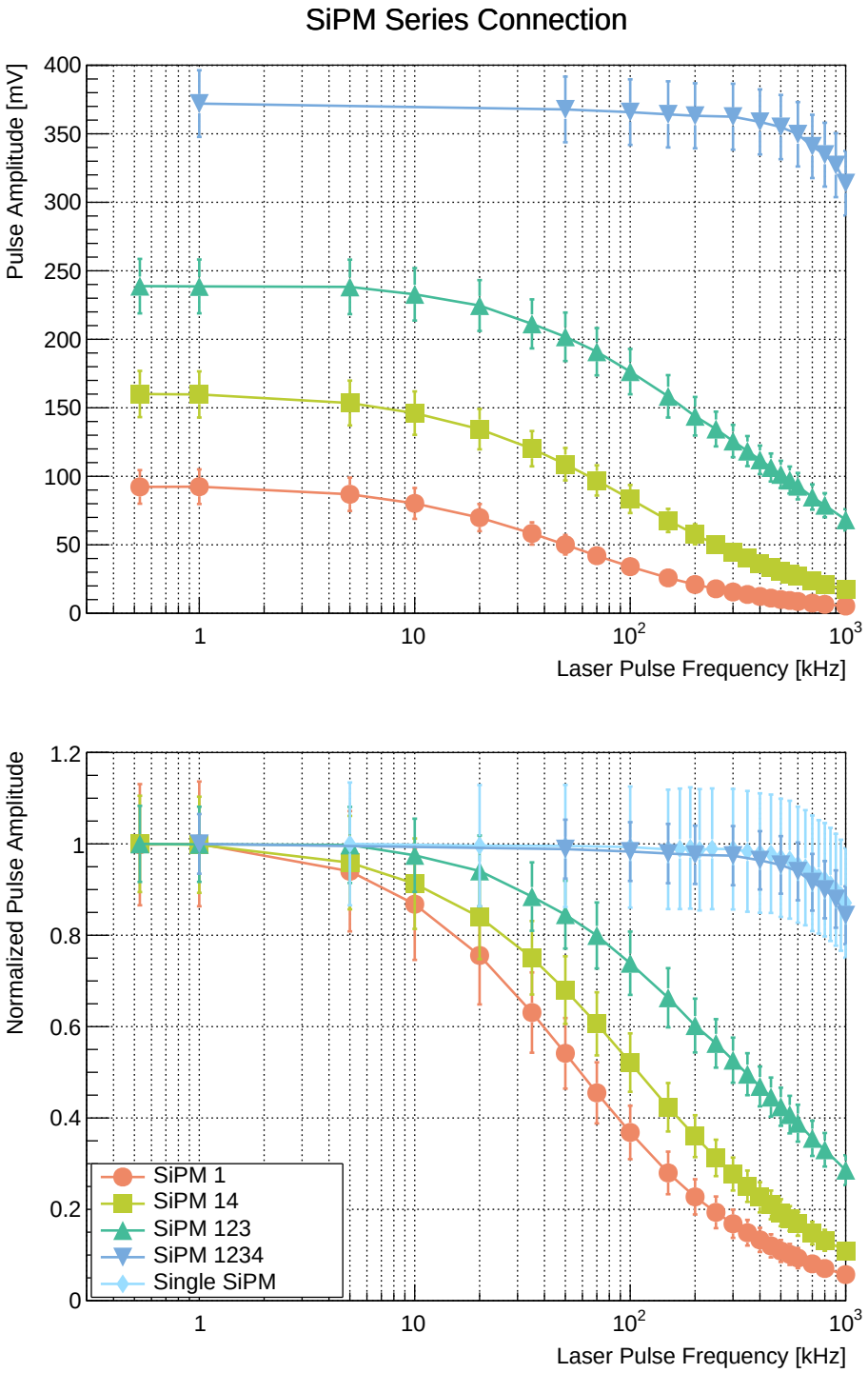

Figure 4.11: *Signal area measured for a series connection of four Ketek PM3350 SiPMs illuminated by a pico second laser of increasing frequency in different SiPM patterns. The bottom image shows a normalized version of the top plot with the legend applying to both distributions.*

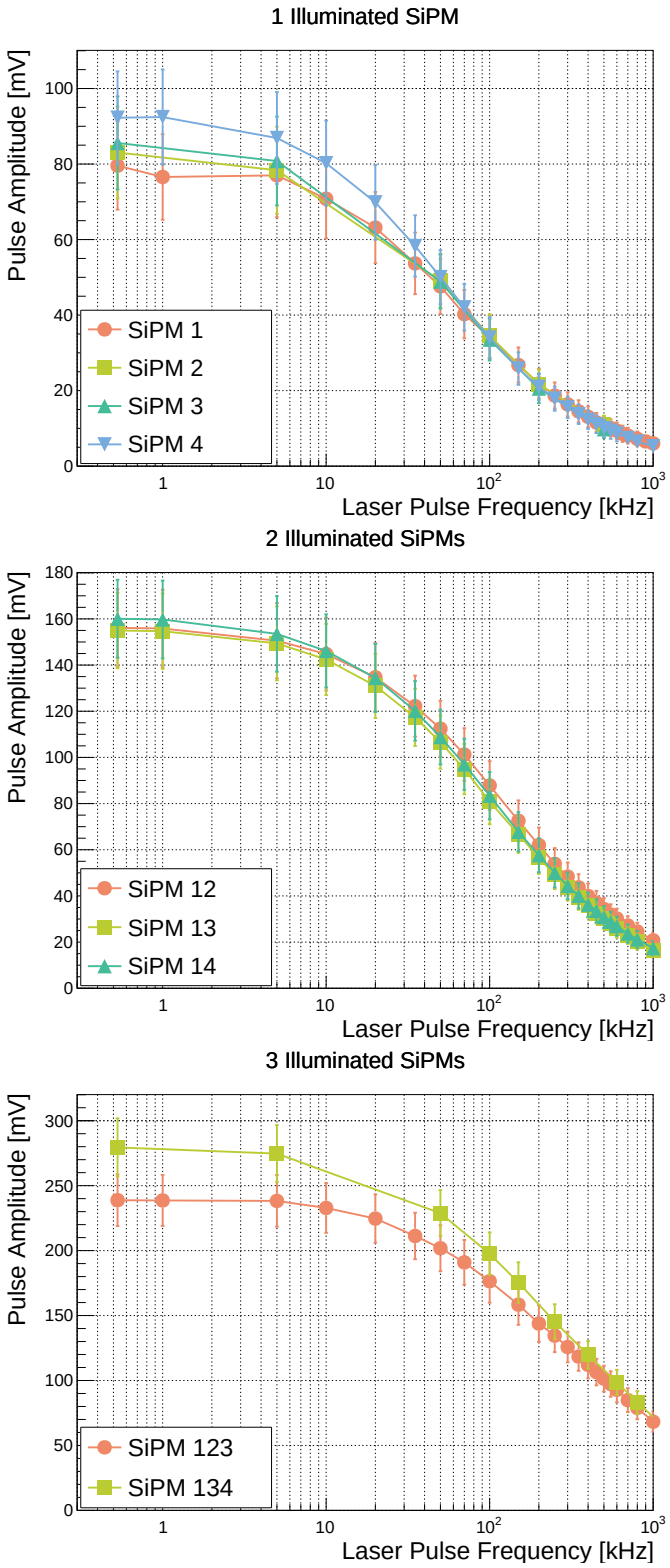

Figure 4.12: *Distributions of the pulse amplitude vs. pulse repetition rate for various combinations of illuminated SiPMs in a series connection. Each graph shows multiple measurements for either one, two or three simultaneously illuminated SiPMs.*

The signal response at low frequencies for the series connection also was slightly lower than the expected quarter fractions. This might indicate that the amplitude drop already occurs at frequencies lower than the measured 530 Hz, the lowest the signal generator for the laser trigger could go.

The observed frequency response is peculiar and needs to be kept in mind but has no immediate influence on the setup and performance of the B-ToF detector. Applied to a small scintillator, where all SiPMs are exposed to photons from the same interactions, the internal reflections provide an even distribution of photons for most hits. Hence every SiPM is exposed to light of similar intensity. This, as seen above, delivers a response comparable to that of a single SiPM. The studied repetition rate range of up to 1 MHz shows tolerable amplitude losses at full illumination most likely extending beyond the operational frequency range of the laser system.

Although the dependency on the amount of photons incident on the sensors has not been studied one can assume that since SiPMs comprise many individual parallel cells no large photon count dependency will be observed. With that one can say that it is only in applications with a light yield of only a few photons where photon detection in every sensor is not guaranteed that the drop-off of signal amplitude for signals with a moderate frequency of a few tens of kHz comes into play. Applications in which multiple SiPMs are deployed to read out separate scintillators with a single channel also need to be aware of these frequency implications. For such instances a hybrid or parallel connection of the SiPMs would be recommended.

In addition one has to consider that these measurements were done for a continuous interaction rate. During the experiment however particles will be scattered all throughout the detector with a mean interaction rate of up to 40 kHz per scintillator tile as can be seen in Figure 3.3. At such frequencies an incomplete illumination of three SiPMs still delivers a signal of about $(87 \pm 7)\,\%$ amplitude. Momentary increases above this level can be expected frequently. For such short bursts this behavior might look differently.

Chapter 5

Transmissionline PCB / Rail-Board

5.1 Motivation

As described earlier the $\overline{\text{P}}$ANDA B-ToF detector was not part of the original concept but was added later as an addition to the Barrel DIRC detector. Due to this circumstance both detectors share the same layout and the B-ToF detector is severely limited to a vertical space of 2 cm. Having 60 channels connected by cables while providing space for mechanical support for the scintillators, integrating temperature monitoring and calibration LED support does not seem feasible while maintaining sufficient air flow for cooling. The solution chosen to address all the above in the simplest possible manner was to use long printed circuit boards (PCBs).

A PCB is able to house many transmission lines on multiple layers unifying SiPM signal transmission as well as control over the LED and the temperature sensors. Due to its rigidity a PCB will also provide mechanical support for the scintillators. With all the transmission lines inside the boards, enough space is freed up to provide airflow down the module, keeping the system from overheating.

This approach also minimizes the total material of the detector. Any material subjected to high energy photons and electrons has the potential to interact with them and deteriorate the EMC performance. So minimizing the introduced material is of high priority.

This approach for signal transmission, is inspired by the MEG II experiment using large PCBs to connect scintillators read out by SiPMs to the front-end electronics (FEE) in their pixelated Timing Counter (pTC) [48].

The large PCB is called the Rail-Board and it derives its name from its design and use case. It provides electrical connections in form of straight long conductor lines along the outside of the scintillators like guide rails directing the sensor signals to the readout electronics.

To find the optimal board layout and transmission line dimensions providing the best performance in terms of signal amplitude attenuation and rise time degradation multiple prototypes have are examined. While optimizing the board performance the focus also needs to be put on reducing the necessary material budget of the board.

In order to understand the behavior of the board design and the influence of each parameter one has to understand the basics of electric circuitry. This will be discussed in the next section.

5.2 Basic Transmission Line Design

The conducting properties of transmission lines depend on whether alternating current (AC) or direct current (DC) is applied. In DC applications where current flows steadily in one direction, capacitors block all current, whereas if AC is applied with quickly alternating directions of current flow, they act like a resistance reducing but permitting a current flow back and forth.

When signal rise times become shorter the separation becomes less clear. Fast signals are able to pass through capacitors like AC signals and are subject to other effects discussed later, reducing the conductance of their transmission lines. The behavior of AC signals depends on their frequency. Single pulses however are subject to the same effects. Their frequency equivalent can be described by the *bandwidth* of the signal.

The bandwidth describes the highest wave frequency component that is significant in a signal. Using the model of a low-pass filter the bandwidth corresponds to the highest frequency above a 3 dB reduction which can be calculated by

$$BW = \frac{0.35}{t_{rt}} \tag{5.2.1}$$

with t_{rt} being the signals 10 % to 90 % rise time. For a signal with a rise time of 1 ns this corresponds to a 350 MHz signal [49].

5.2.1 Printed Circuit Boards

Printed Circuit Boards come in many different sizes, shapes and forms. The most basic board consists of a base material onto which a layer of copper is applied. Into the copper layer a connector structure can be etched either mechanically or chemically. To increase the amount of connection lines per area without adding too much complexity a second copper layer can be added to the bottom side of a board.

The standard base material or *core* for PCBs is a weave of glass fiber yarns reinforced by an epoxy resin, commonly called FR-4. This name however does not specify a certain chemical compound but rather a degree of fire retardant hence the name. Depending on the application, e.g. for high-speed low-loss analogue signal transmission, other base materials can be considered. Core materials and copper foils come in many different sizes and thicknesses determined by their manufacturers.

To further increase the connection line density double copper clad laminate layers can be combined. By using prepreg to bond adjacent sheets, stacks of multiple layers can be assembled one board at a time. While the fully cured core holds two copper foils on either side the prepreg is a weave of glass fiber preimpregnated with a partially cured resin, which cures fully by applying heat and pressure after the board is stacked and assembled.

The practice of bonding double sided laminates leads to multi layer boards with mostly even numbers of layers. Transmission lines inside the board are usually shielded from one another by ground layers. A conductor on the surface with a

single ground layer beneath it is called a micro strip whereas a conductor inside the board with ground layers above and below is called a stripline. Both kinds of transmission lines are shown in Figure 5.1. Since the Barrel Time-of-Flight Detector will use a multi layer board only stripline transmission lines will be used.

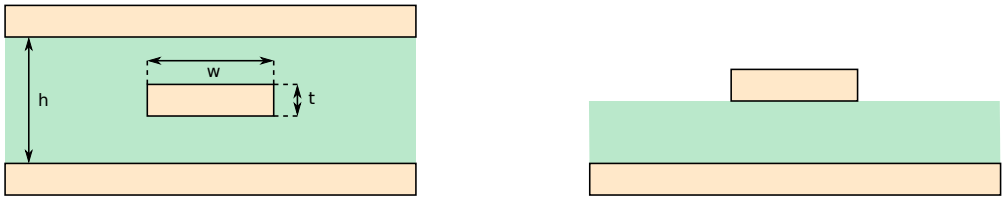

Figure 5.1: *Schematic drawing of shielded transmission line designs. A stripline with the signal transmission line between two ground planes is shown on the left and a micro strip with the transmission line on top of a ground plane on the right.*

To further shield transmission lines additional ground traces on the conductor layer in between signal lines can be added. Such lines are called *guard traces* and need to be connected to the the ground layers in regularl distances. This avoids them becoming sources of crosstalk to other signal lines [50].

5.2.2 Impedance Matching

For signals with fast rise times conductor properties such as the inductance (L) and the capacitance (C) start playing a role in determining signal behavior. A transmission line is described by its characteristic impedance (Z_0). Z_0 is defined as the relation of voltage and current on a transmission line. This makes Z_0 dependent on C and L as described in Equation (5.2.2). Although, like the resistance, the characteristic impedance is given in Ohm (Ω) it does not depend on a transmission lines length (l).

$$Z_0 = \sqrt{\frac{L}{C}} \tag{5.2.2}$$

At boundary regions where one conductor attaches to another with a different characteristic impedance incoming signals are partially reflected. This is a direct result of the need for continuity of the Maxwell Equations. The rate of transmittance at such a boundary is given by the reflection and transmission coefficients

$$\Gamma = \frac{Z_{02} - Z_{01}}{Z_{02} + Z_{01}} \tag{5.2.3}$$

$$T = \frac{2Z_{02}}{Z_{02} + Z_{01}} \tag{5.2.4}$$

$$1 = T - \Gamma,$$

with Z_{01} and Z_{02} being the characteristic impedance of the two connected transmission lines with a signal moving form conductor 1 to 2 [51]. Equations (5.2.3) and (5.2.4) show that the larger the impedance difference is the larger the reflection

coefficient. In cases where both lines have the same impedance the reflection coefficient Γ falls to 0 and the whole signal is transmitted.

To minimize signal losses the characteristic impedance of all components of a circuit including the connectors should match. Reflections otherwise cause reduced signal strength and introduce more noise on the connection. The capacitance and inductance of a signal line is influenced by geometrical and material dependent factors. Since recalculating the inductance and capacitance of multiple different conductor dimensions can be tiresome, an equation has been developed to estimate the impedance of a stripline based on copper thickness (t), the width of the signal lines (w) and the distance to the ground layers (h) as well as the dielectric constant ε_r of the core material [52].

$$Z_0 = \frac{60}{\sqrt{\varepsilon_r}} \ln \frac{1.9h}{(0.8w + t)} \tag{5.2.5}$$

Equation (5.2.5) only gives an approximation. Since it is based in a heuristic approach it is only applicable for a set range of values, when $w/b < 0.35$ and $t/h < 0.25$. Outside of this range more complex formulas have to be employed to get accurate approximations. A more accurate formula can be found in [52]. These formulas however do not consider guard traces which also reduce the impedance.

To match the impedance of the PCB transmission line to the connectors, the conductors dimensions and the board material need to be considered carefully.

The most common characteristic impedance is 50 Ω as it is used for most coaxial cables, which are ordinarily employed in most physics experiments. This will be the target impedance for the following PCB designs.

5.2.3 Transmission Losses

Every transmission line no matter the signal always has losses. A practical transmission line always has a small series resistance. Traces in a PCB show a resistance per length proportional to the trace width (W) and copper thickness (t) and can be calculated with Equation (5.2.6) [51]:

$$R = \frac{\rho_{Cu}}{Wt} \tag{5.2.6}$$

with $\rho_{Cu} = 1.68 \cdot 10^{-8}\,\Omega\text{m}$ being the copper resistivity. This leads to unavoidable signal strength loss or attenuation of the signal.

Skin Effect

With rising signal frequencies the series resistance changes and starts to increase rapidly. This is called the *skin effect*. For most conductors, depending on their geometry, this becomes an issue at around 1 MHz. Fast signals are influenced by the inductance of their transmission line. Conductors with higher inductance show greater resistance to alternating currents or high-speed pulses. Since the inductance along the cross section of a conductor increases towards the middle less

current flows through the center of a transmission line pushing the majority of flowing charge carriers to the conductor surface.

The depth at which 63.2 % of the current flows is called the skin depth and can be calculated by

$$\delta = \sqrt{\frac{\rho}{f\pi\mu_0}} \tag{5.2.7}$$

with ρ being the materials resistivity, μ_0 the permeability in vacuum and f the signal frequency. For a 10 MHz signal in copper this means a skin depth of 21.14 µm.

As soon as the skin depth is smaller than the conductor dimensions the skin effect starts restricting the flow of current increasing the conductor resistance. The frequency at which this happens is the *onset frequency* of the skin effect. Above it the resistance increases as $\sqrt{f}$.

As the frequency continues to rise the skin depth might fall below the conductors surface roughness. This point is generally reached at around 1 GHz and dramatically increases the resistance since the effective surface area increases by a considerable factor [53]. This effect amplified by the fact that in order to increase the adhesion of the laminate sheets to one another the surface is intentionally roughened. By using smoother copper, alternative measures need to be taken to keep the same level of adhesion or *peel strength*.

Dielectric Losses

The core material in between the copper sheets of PCBs is a dielectric material. As such it is able to be polarized by electric fields. Displacing electron clouds of atoms requires some force and produces heat which is energy lost to the system. This effect is described by the dissipation factor, given by many substrate manufacturers, which depends on the materials ability to be polarized. Materials with a larger dielectric constant ε_r are subject to less polarization and hence better suited for high frequency applications.

Inexpensive FR-4 materials were not designed with this effect in mind and are ill suited for signals with a high bandwidth. Different vendors have come up with different materials which feature a reduced dielectric constant and hence a reduction in the dielectric loss experienced. This however comes at a price since these materials are expensive and not available in the same sizes or specifications commonly found for more ordinary materials such as FR-4.

A simulation, done by a student of embedded systems engineering Professor Eric Bogatin at the University of Colorado Boulder [54], of the losses on a stripline with a trace width of 400 µm and a characteristic impedance of 50 Ω on FR-4 depicted in Figure 5.2 shows the expected loss terms, split into resistive losses and dielectric losses adding up to the total loss depending on the signal frequency. These simulations show that the dielectric losses start to dominate from 170 MHz on.

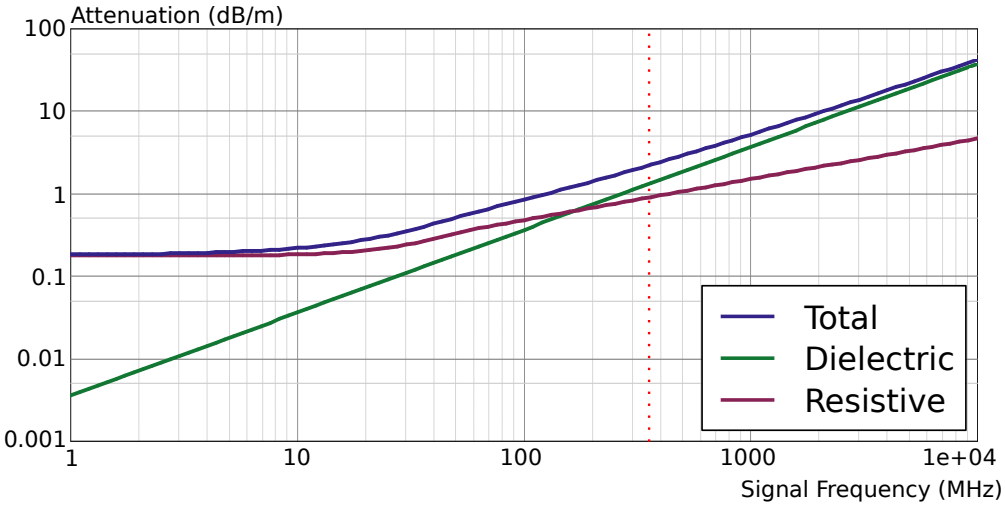

Figure 5.2: *Simulation of the resistive and dielectric losses expected for a 400 µm wide 50 Ω impedance stripline in FR-4 [54].*

5.2.4 Crosstalk

When conductors are placed in close proximity their emerging electric and magnetic fields will overlap. This gives neighboring lines a capacitive and inductive coupling. Depending on the coupling strength a signal propagating along a primary transmission line, the *aggressor*, may cause the deposition of enough energy into a second line, the *victim*, to produce a secondary signal. This effect is called *crosstalk* and is proportional to the rate of voltage change ($\partial V/\partial t$) or respectively the signal rise time.

Two coupling modes need to be distinguished, far-end crosstalk (FEXT) and near-end crosstalk (NEXT). In case signals on two parallel lines are running in opposite directions one speaks of NEXT whereas in the reversed case where signals are traveling in the same direction one speaks of FEXT. The first is usually the more severe concern since coupled signals usually have not undergone much attenuation along the transmission line yet. This however is not the case for our detector since we are only concerned about the signals that reach the front-end electronics, hence the FEXT.

In contrast to NEXT, FEXT also depends on the length the two conductors run in parallel (l) as described in Equation (5.2.8), with the constant of proportionality K_f depending on the lines impedance, capacitance and inductance further described in [50].

$$\text{FEXT} = K_f \, l \, \frac{\partial V}{\partial t} \tag{5.2.8}$$

The crosstalk magnitude is measured in dB, defined in Equation (5.2.9), with the Voltage on the aggressor line being V_a and V_v on the victim line.

$$\text{Crosstalk(dB)} = -20 \log_{10} \left| \frac{V_a}{V_v} \right| \tag{5.2.9}$$

The polarity of the NEXT always matches the aggressor signal. For FEXT however it depends on the relative dominance of the inductive or capacitive coupling. In case the inductive coupling coefficient is larger the FEXT pulse polarity will be opposite of the aggressor signal. In lossless striplines where the inductive and capacitive coupling coefficients are equal no FEXT should be measurable.

5.3 Rail-Board v1

Each of the 16 modules of the B-ToF detector is equipped with two rows of 60 scintillating tiles. Each tile is read out on two sides with the two resulting groups of transmission lines referred to as rails. Four such rails total 240 readout channels. These do not fit next to each other on a flat PCB, neither could surrounding grounding be added. For this reason a multi layered design is necessary. For the B-ToF a total of 16 conductor layers is chosen, made of the standard PCB substrate material FR-4.

Although signal lines inside of a PCB are surrounded by the dielectric material of the board it is offered little to no protection since that material is designed to be minimally conductive. In order to reproduce the coaxial like structure of the coaxial cables usually used, ground layers and grounded conductor lines are added similar to a stripline design but completely isolated from each other. To truly mimic a coaxial cable each signal line (S1 to SN) was surrounded vertically by its own ground layer (SG1 to SGN) and separated by global ground lines horizontally, in contrast to sharing one global ground throughout the board. These horizontal ground traces are called guard traces. A schematic cross section of the first design generation of the Rail-Board is shown in Figure 5.3.

A copper layer thickness of 18 µm was chosen throughout the board with a core strength of 100 µm of FR-4. Each signal line is 180 µm wide with 32 mils or 812.8 µm wide shielding ground traces above and below it forming one cohesive transmission line. Five such transmission lines are stacked on top of each other taking up 15 layers. These stacks are horizontally separated by 320 µm and 300 µm guard traces. Since only boards with even numbers of layer are produced we end up with a 16 layer board. The last free layer is used as a global ground shield on the bottom of the board. This produced a board of (2.25 ± 0.05) mm thickness. A picture of the board and a schematic drawing of the internal transmission lines can be seen in Figure 5.4.

These transmission line dimensions do not produce a board with a characteristic impedance of 50 Ω, the target impedance. Instead Z_0 is closer to 24 Ω. This is due to an error in the spreadsheet provided by the PCB manufacturer used to match the dimensions to the target impedance. All measurements were performed nonetheless keeping in mind that reflections will cause increased signal losses at conductor junctions and potentially interfere with pulse forms. The latter however was not observed.

To manufacture a board of 2460 mm length, spanning the full length of one B-ToF slot is a non trivial and unusual task. This makes their production difficult and expensive since it is hard to find a company able to produce boards of such

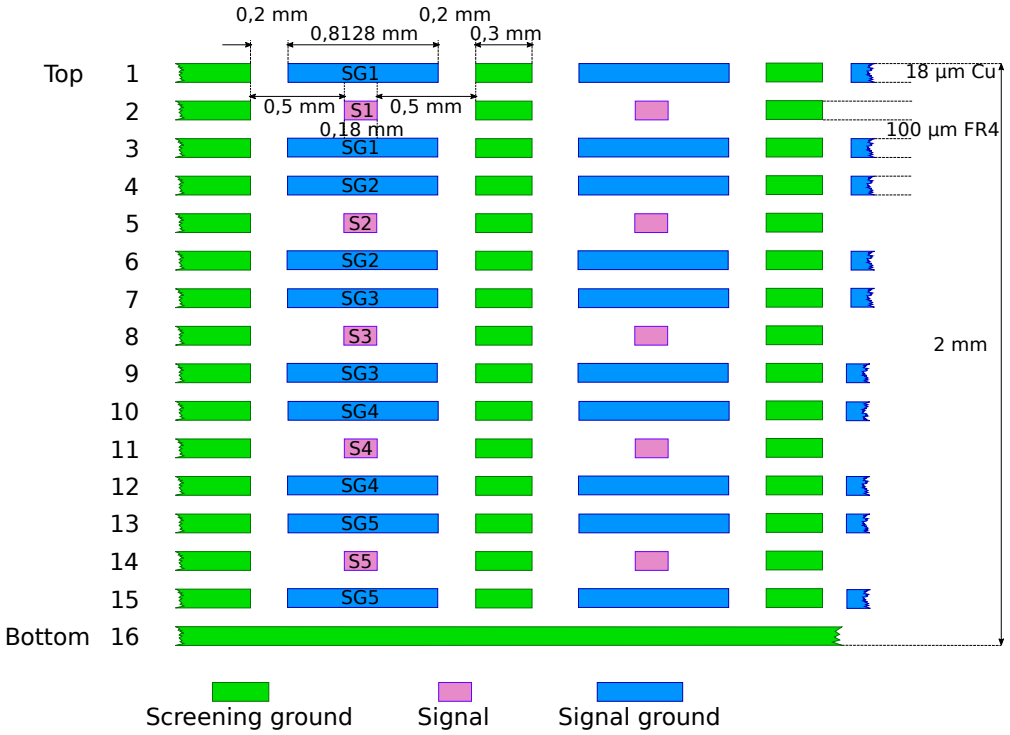

Figure 5.3: *Crossection of the* Rail-Board *in its first generation. S1 to SN denote the signal transmission lines of each channel from 1 to N and are colored in magenta. The corresponding signal ground is colored in blue and labeled as SG1 to SGN. The separate overall ground is colored in green. A copper thickness of 18 µm and a core strength of 100 µm was used.*

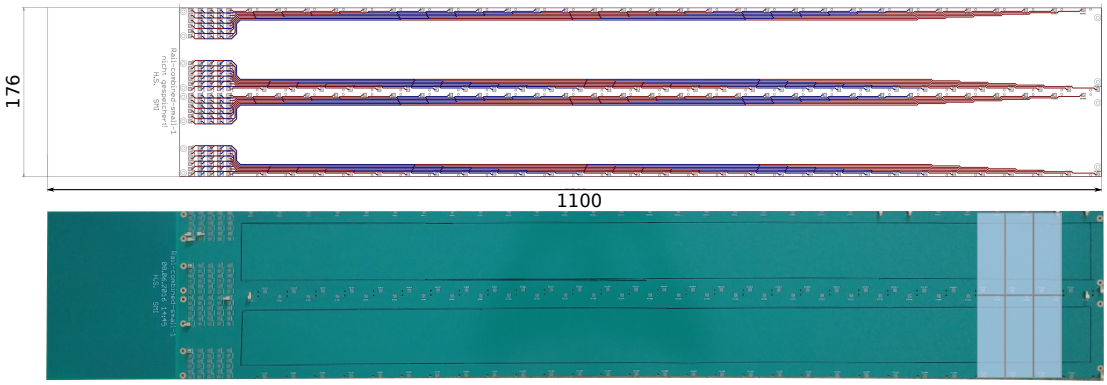

Figure 5.4: *Combined depiction of the internal transmission line layout and a photograph of the first generation board with six scintillators drawn on top.*

lengths. For this reason a board with half of the readout channels was produced by *ELLWEST PCB*.

The board is 180 mm wide and comprises a sensitive part to be equipped with scintillators of 900 mm length as well as 200 mm to fit connectors and the Front End Electronics (FEE) eventually.

5.3.1 Crosstalk Measurements

Setup

To evaluate the performance of the board the crosstalk and attenuation along the board was measured by connecting a pulse generator and inducing a signal on the sensor side. For the crosstalk measurements an aggressor signal, a sine wave of variable frequency, was induced into the longest line (channel 30) of the board which was terminated in a digital oscilloscope capable of recording the necessary data. A schematic drawing of the measurement setup including the oscilloscope and the pulse generator is shown in Figure 5.5.

Figure 5.5: *Schematic of the setup used to measure the crosstalk from neighboring lines. In this case two vertically neighboring lines depicted in blue and orange situated above each other on different layers of the board are probed. A signal is injected on the sensor side (right) and readout out on the FEE side(left).*

In addition both ends of a neighboring line were monitored in the same oscilloscope. Around 10 000 measurements per data point were taken. Since the aggressor signal was connected to the sensor side of the board measuring signals on the victim line on the same side corresponds to NEXT while crosstalk picked up on the FEE side corresponds to FEXT.

Two neighboring victim lines were studied. One was the second longest line (channel 29) with a horizontal gap to the aggressor, situated on the same layer. The second line was of channel 24 stacked on top of the aggressor line three layers above it. The crosstalk pulses were measured in mV and were compared to the aggressor signal on the FEE side after passing through Rail-Board. The crosstalk was calculated according to Equation 5.2.9.

To exclude artificial effects potentially introduced by the continuous periodic nature of a sine wave function the crosstalk was additionally studied with artificial pulses close to the shape of a SiPM signal with a large amplitude of 1 V and a variable rise time set to values from 1 ns to 5 ns and a fall time of 70 ns generated by an arbitrary pulse generator at a frequency of 2 MHz.

Results

The resulting crosstalk measured in dB is shown in Figure 5.6 with measurement errors within the line thickness.

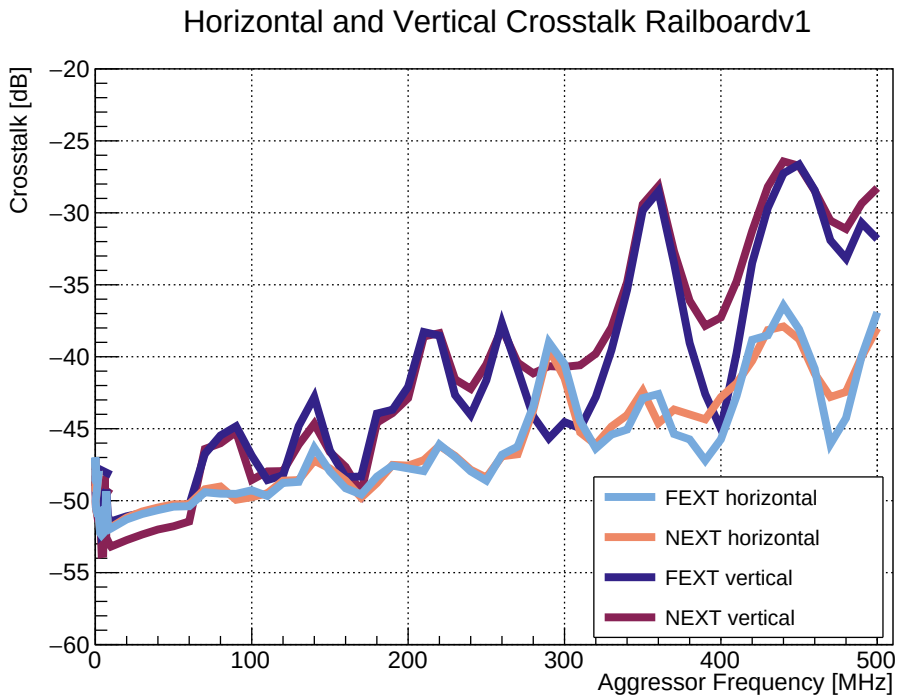

Figure 5.6: *Crosstalk of a horizontally and a vertically neighboring line, measured using a sine wave of various frequencies and an amplitude ranging from 660 mv to 1800 mv increasing from low to high frequencies.*

One sees a clear frequency dependence with an increase in crosstalk for increasing aggressor frequencies. However large resonances seem to appear along the frequency band. Both NEXT and FEXT have a similar response strength for local maxima but at the minima the NEXT response is clearly stronger.

Although the horizontally neighboring line of channel 29 is 20.2 % longer than the line of channel 24 the latter shows a significantly higher level of crosstalk. Both however show no measurable signals at frequencies below 10 MHz where any signal is swallowed by the noise.

For a SiPM signal with a rise time of about 1 ns we can assume a signal bandwidth of 350 MHz according to Equation (5.2.1). For such a signal the measurements say that we can expect −42.5 dB to −29.6 dB for horizontal and vertical crosstalk which corresponds to a crosstalk signal 0.7 % to 3.2 % the amplitude of the aggressor signal. The vertical crosstalk however is only so high because it falls directly into a resonance. Slight variations of the frequency will produce much lower crosstalk levels.

Using a signal closer to the signal expected from a SiPM no crosstalk above the noise level of (1.26 ± 0.14) mV peak to peak could be measured, neither for the vertical nor the horizontal FEXT and NEXT.

Since the crosstalk scales with the connector length, it is to be assumed that for a board double the size a crosstalk signal with two times the amplitude can be expected.

5.3.2 Attenuation and Rise Time Measurements

The B-ToF performance is determined by the systems time resolution. As explained previously in Chapter 6 a shorter rise time leads to a better time resolution as it is less affected by jitter. Having smaller pulses while delivering the same rise time from 10 % to 90 %, produce a leading edge slope less steep. For this reason it is important to keep the signals as large as possible.

Attenuation does not affect the rise time directly but determines the slope of the signal and hence the time resolution. This will also be examined in this section. How exactly these two values will translate to the time resolution however depends on the system readout and the noise level present in the electronics during operation in the full $\overline{\text{P}}$ANDA detector.

Setup and Procedure

To measure the attenuation the same basic setup as for the crosstalk measurements was used taking 2000 measurements for each data point. This time connecting a single transmission line to the oscilloscope. Pulsed signals shown in Figure 5.7 with an amplitude of 1 V and a rise time of 1 ns from 10 % to 90 % from a pulse generator were injected at a rate of 2 MHz into the sensor side of the board.

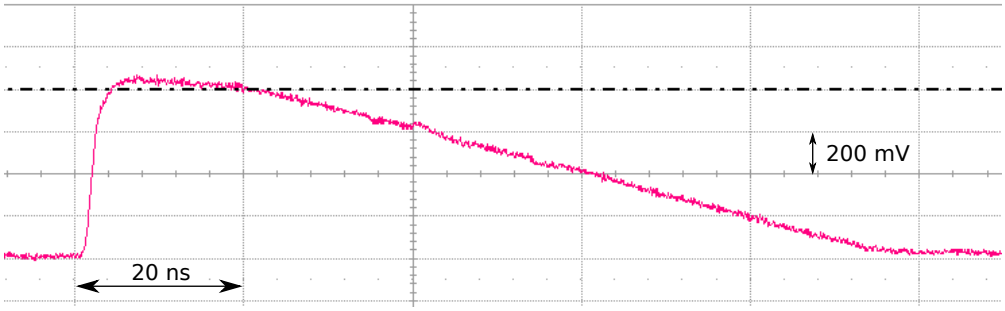

Figure 5.7: *Pulse shape used to measure the signal attenuation.*

The rise time is however measured from 10 % to 70 %. Because faster signal components are attenuated stronger as shown in Section 5.2.3, the signals tend to flatten more at the top of the pulse. This has a large effect on the rise time and makes the measurement very sensitive to amplitude changes. Since during operation the value of interest is the rise time to the discriminator threshold level a lower level of 70 % was chosen. This produces a rise time of (0.84 ± 0.03) ns for our injected signal.

In order to receive a distribution of the attenuation along the board, in order to extrapolate to a full length board, multiple signal channels were examined measuring the reduction of the signal amplitude and the change in the rise time

along the board up to channel 30. A schematic drawing of this setup can be seen in Figure 5.8.

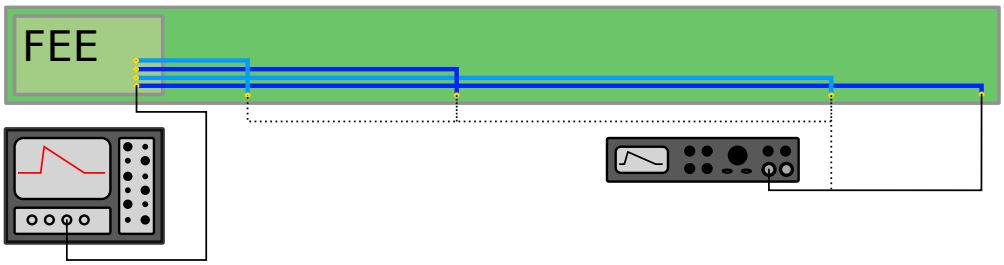

Figure 5.8: *Schematic of the setup used to measure the signal attenuation along the board. A signal is injected into different channels on the sensor side one by one and read out by an oscilloscope on the FEE side.*

Results

Since only a half length board was available the attenuation was fitted and extrapolated to the length of a full board of about 1.93 m, which is the transmission line length of the longest line on the third generation board discussed later. The measured data is plotted in Figure 5.9 and shows signal amplitude measurements for various transmission line channels along the board with standard deviations smaller than the marker size. Additionally, a data point for a standard 2 m long coaxial cable of CERN specification (50CA) [55] for the same input signal is drawn.

The linear nature of this distribution allows a very good estimation of the attenuation of a longer board. For a full length board we would expect to lose up to (27.5 ± 1.8) % of the signal amplitude, depending on the hit position along the board.

A measurement of the signal at the effective connection length of 0 m was recorded by omitting the Rail-Board altogether. This point lies nicely along the extrapolated attenuation line and the small loss of (3 ± 5) mV towards channel 1 is well within the margin of error for either measurement.

The rise time (10 % to 70 %) measurements along the board are shown in Figure 5.10. Channel 1 only shows a marginal worsening of the rise time by (0.05 ± 0.03) ns compared to 0. After that the rise time increases smooth and steadily. It increases from initially around (0.91 ± 0.03) ns to (1.16 ± 0.04) ns, an increase of 27 % from channel 1 to 30. Extrapolated to 60 channels one would expect a rise time of 59 % or (0.33 ± 0.05) ns/m upto (1.45 ± 0.05) ns.

5.3.3 Summary and Discussion

The crosstalk was measured using two different techniques producing two different results. While measuring the crosstalk with a continuous sine wave of different frequencies a whole crosstalk spectrum could be recorded. Using realistic pulsed signal shapes however, no crosstalk above the noise level was measurable.

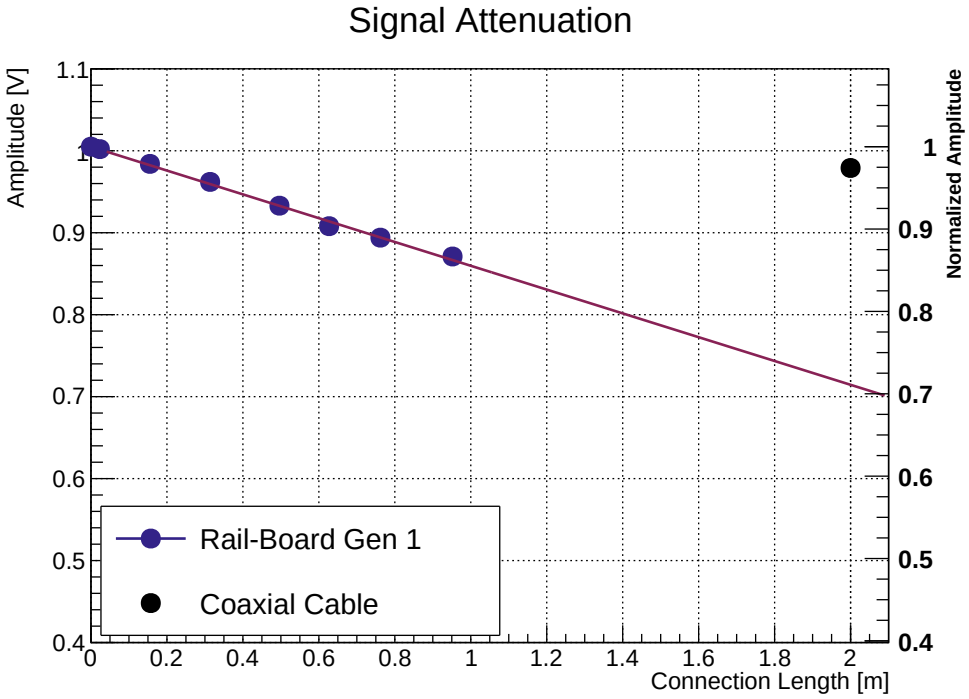

Figure 5.9: *Attenuation of the first generation Rail-Board extrapolated to a full length board using a fit of a linear function.*

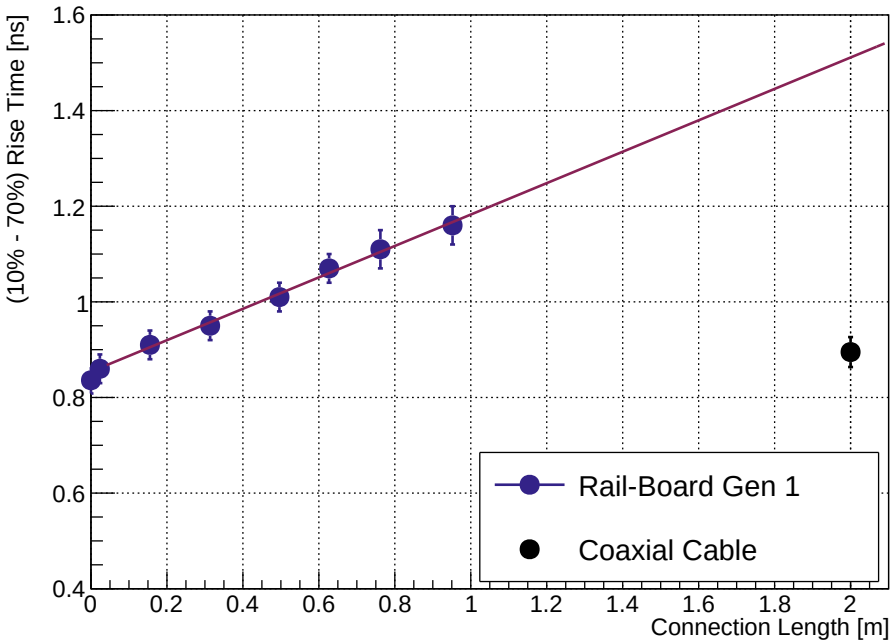

Figure 5.10: *The rise time of a signal from its 10 % to its 70 % level for transmission lines of different length.*

Since a hit rate of below 40 kHz is expected for the scintillator tiles it is safe to assume the transmission lines will not be subjected to a continuous and periodic signal like a sine wave. For this reason we can assume to not see any crosstalk during operation for a board such as this. However, in order to evaluate the potential worst case scenario and receive an upper limit on the crosstalk expectation, we will consider the crosstalk measurements with a sine wave aggressor signal.

The crosstalk depicted in Figure 5.6 shows the measurements for lines on a half length board. Due to the nature of the logarithmic scale of Decibel, doubling the line length and hence expecting a crosstalk signal twice the size makes a difference of $20 \log 2 = 6\,\mathrm{dB}$. This value however does not take considerable attenuation losses into account. Furthermore a design choice explained in the next section will show that the extent of the crosstalk can be easily reduced even more.

Although this is just an estimation it is safe to say that at these levels of up to $-29.6\,\mathrm{dB}$, which corresponds to about 3 % is well within a tolerable range. Since the crosstalk appears not to be a problem the amount of shielding layers seems excessive. It can be safely considered to reduce the amount of copper in the board by reducing the amount of ground layers of the design in order to minimize the amount of high Z count material in the detector in order to keep the material budget, discussed in Section 5.6, low. To achieve this the two copper layers in between each signal layer, which seem to be redundant, should be combined.

The uneven crosstalk response is not unique. Structures like it can be observed in other crosstalk measurements [53]. The crosstalk signal might produce secondary peaks possibly due to internal reflections due to a mismatch of impedance, which create a superposition with the next period of the primary signal increasing or decreasing the amplitude of the sine wave. This effect would also be frequency dependent and produce local minima and maxima depending on the time between the reflections.

The attenuation measurements show a considerable decrease of the signal amplitude along the board. The extrapolated loss of up to $(27.5 \pm 1.8)\,\%$ at 1.93 m transmission line length would have a measurable impact on the time resolution of the system since the timing performance of a system depends on the slope of the rising signal flank. If a signals amplitude is smaller so will be its slope.

The rise time is expected to increase by 59 % from the shortest to the the longest line on this board which flattens the slope. This will result in a worse time resolution for signals on longer lines. The actual extent of its effect on the time resolution however depends on the FEE and the conditions in the experiment and can not be determined at this time since the readout system is not available at the time. Both the amplitude and rise time attenuation of the Rail-Board show a considerably larger effect than a standard coaxial cable.

The effect of the erroneous board impedance on the attenuation also needs to be considered. Reflections caused by the impedance mismatch of the connectors to the PCB transmission line are able to reduce the transmitted pulse height. However no large adverse effects of this impedance mismatch are observed. Moving forward it should be a focus to reduce the attenuation as far as possible.

5.4 Rail-Board v2

To get closer to the target impedance of 50 Ω the signal line width was reduced to 100 µm in all lanes. This is the minimal width the producer was able to handle for copper of that thickness.

Moving from the first to second generation board the focus was set on reducing the material budget. Although the two ground layers per signal line were meant to mimic traditional coaxial cables it is not common to produce transmission lines this way. In order to reduce the material needed for the transmission lines the designs of this board moved from separate ground lines per signal line to a single layer of ground in between vertical signal lines.

Since this board prototype is not meant to be inserted into the B-ToF and does not have to hold scintillators it is possible to study more designs in a single iteration. The PCB, again of only half length, will be equipped with the four standard rails with all channels from 1 to 30. However these rails will all feature different design elements. In addition reduced testing rails with a fraction of the ordinary channels will be positioned in between the main rails. A picture of the board depicting both a drawing of the internal connections on the top and a photograph of the finished board on the bottom can be seen in Figure 5.11.

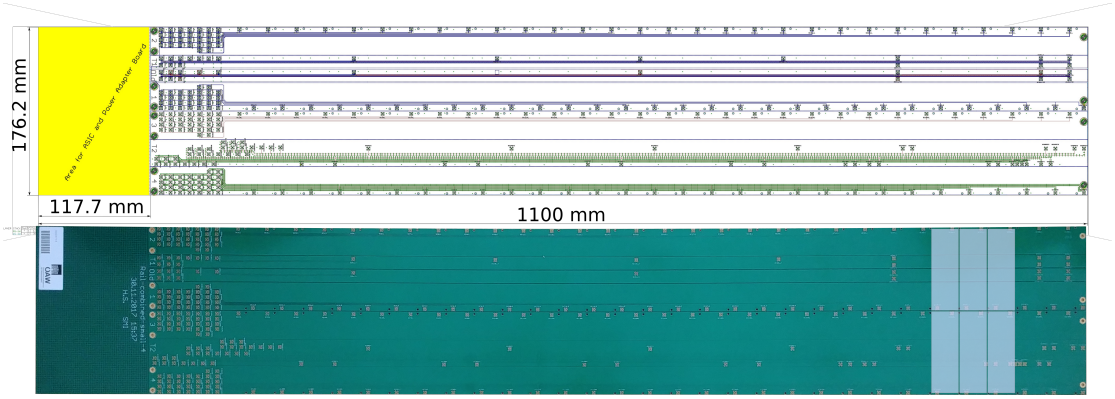

Figure 5.11: *Combined depiction of the internal transmission line layout and a photograph of the second generation Rail-Board with six scintillators drawn on top. The connectors for the additional testing lines can be seen between the four main rails onto which the scintillators are mounted.*

The partial testing rails with a reduced channel count all follow the same layout, an example of which can be seen in design b) of Figure 5.12, featuring line lengths equivalent to channels 5, 15, 24, 29 and 30 in one vertical stack. In addition a second neighboring stack housed line duplicates equivalent to channels 24, 29 and 30 in order to study vertical crosstalk between channel 24 and channel 30 as well as horizontal crosstalk between channel 30 and channel 29.

The second generation board was produced by the same company as the first one and shares its basic dimensions. The copper and dielectric thicknesses are identical with 18 µm and 100 µm respectively resulting in the same (2.25 ± 0.05) mm board thickness.

The new board can be divided into three distinctive design archetypes, which each can have multiple implementations with different parameters. One set of testing lines was dedicated to a re-implementation of the design of the first board. Since all signal lines have their individual ground, this design archetype will be referred to as the *multi-ground-design*.

The second design archetype reduces the amount of ground layers around each signal line. In the original design each signal line was surrounded by individual ground lines specific to this channel resulting in two ground layer between signal lines. Here each vertical stack shares interconnected ground layers with a single copper layer lies between each signal line. Guard traces of a separate global ground are still positioned in between each vertical stack. This design is implemented three times with varying ground line widths of 180 µm, 360 µm and 812 µm. Since it features two separate grounds, one for the signals and a second global ground this design archetype will be referred to the *2-ground-design* (2-GND) with its ground width variations referred to as *narrow*, *middle*, and *wide*.

The third design archetype reduces all separate grounded regions into one and implements a single global ground with continuous copper layers between signal lines interconnected by vias. These are copper clad drill holes connecting multiple layers vertically. The differentiating factor within this archetype was the via density. One full rail was implemented without any vias. Three partial implementations have a decreasing via distance from design to design, from a via every 3 mm to every 2 mm down to every 1 mm. This design archetype will be referred to the *1-ground-design* (1-GND) with *high*, *middle* and *low* via density, since all separate ground layers were combined into a single global ground. All three design archetypes can be seen in Figure 5.12.

The last full rail on the board houses a characteristic layout change of the regular 1-ground design. All transmission line dimensions were kept the same as the other 1-ground variants with a via distance of 1 mm. The other designs feature an ordered transmission line position with channel 1 being above channel 2 and so on. This order however is almost arbitrary and only for the sake of simplicity during the design process. There is no performance reason to order the lines in this way. In the contrary, this positions lines of similar length next to each other maximizing the distance neighboring lines run along side each other.

Since the distance traveled in parallel determines the coupling strength as described in Equation (5.2.8) it is the shorter line that regulates the level of crosstalk. To reduce the crosstalk to a minimum the last rail features a shuffled order of lines placing shorter lines next to longer ones.

The only major limitation is that the lines need to be fed out to the scintillator connectors at some point. This means that, if we assume the connectors to be on the right of the transmission lines, longer lines need to be positioned to the left of shorter lines to avoid rerouting across other layers which introduces transition losses. A reliable methodical approach to this has not been found but one version of a possible design is shown in Figure 5.13 and implemented on the board.

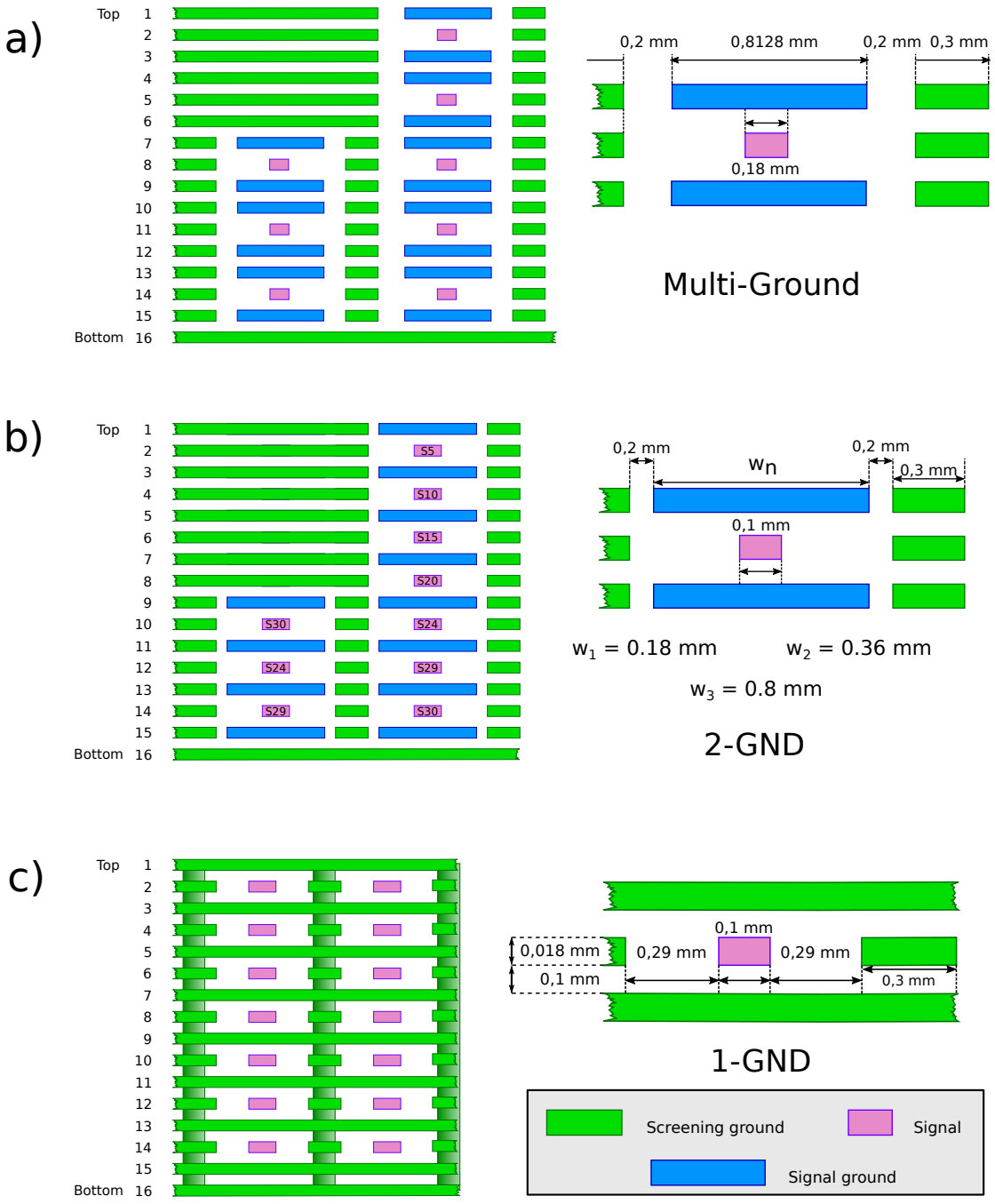

Figure 5.12: *The three basic designs on the second generation Rail-Board each with a copper thickness of 18 µm and a substrate thickness of 100 µm. a) is a re-implementation of the multi-ground-design of the first board. b) shows the 2-ground-design with distinct signal ground and global ground connections. c) shows the 1-ground-design with continuous ground layers and a single ground throughout the board.*

S13	S14	S15	S16	S30
S9	S10	S12	S13	S17
S18	S19	S20	S28	
S5	S6	S7	S8	
S21	S22	S23	S29	
S1	S2	S3	S4	
S24	S25	S26	S27	

Figure 5.13: *Implemented example of a shuffled signal line placement. The signal lines are named S1 to S30 according to their length and position along the board from short to long lines.*

5.4.1 Crosstalk Measurements

Setup and Procedure

As for the first board the crosstalk is measured using realistic pulses with the same setup as shown in Figure 5.5. A pulse generator was connected channel 30 to the longest transmission line on the sensor side of the board and injected 1 V pulses with a variable rise time of 1 ns to 5 ns with a decay time of 70 ns. The vertical crosstalk was measured on channel 29 with horizontal crosstalk on channel 24. All ends of the signal lines were connected to a digital oscilloscope with a termination impedance of 50 Ω measuring the pulse sizes. An example of the measured aggressor and crosstalk pulses is shown in Figure 5.14.

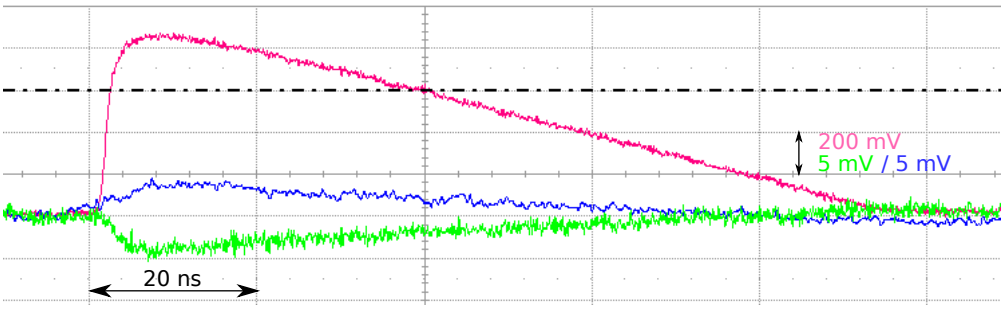

Figure 5.14: *Measured pulse shapes of the aggressor signal (red), the FEXT (green) and the NEXT (blue) on a time scale of 20 ns per horizontal division.*

Measurements with sine waves were not performed as the results are unreliable. However to still record a spectrum of signals of different bandwidths the rise time was modulated.

Results

The measurements are summarized in Figure 5.15 showing crosstalk values at different aggressor signal rise times with standard deviation error bars smaller than the marker. The data is color coded to separate the basic designs. The multi-ground-design is not included since no measurable crosstalk could be seen.

The 2-ground-designs with the comparatively middle and wide ground lines are shades of blue and colors for the 1-ground lines range from olive to purple. In order to produce a compact plot the measurements for the 2-GND rail with narrow ground lines was excluded since it shows the by far worst crosstalk with values around −32 dB equivalent to 2.51 %.

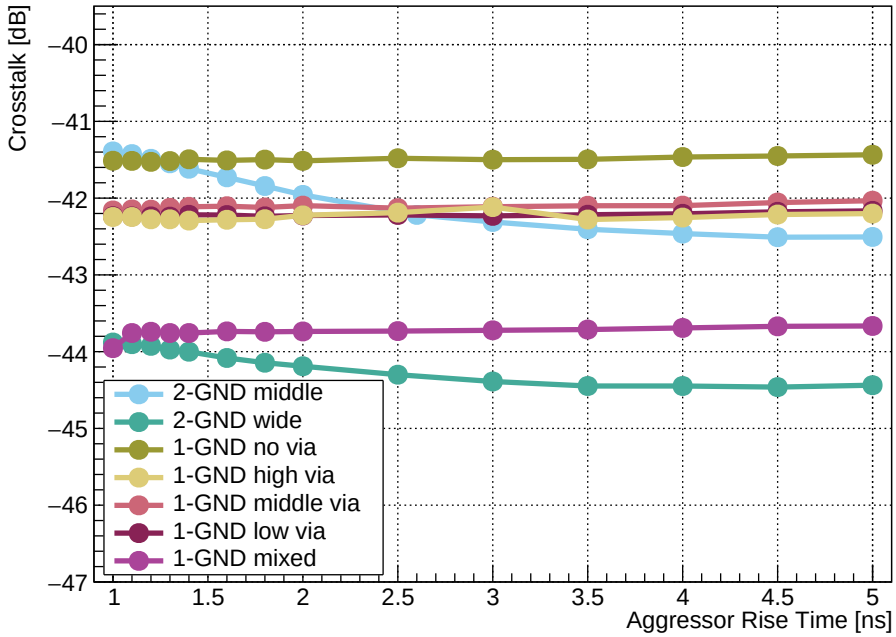

Figure 5.15: *FEXT measurements in decibel for various signal rise times in the different transmission line designs.*

The two depicted 2-GND rails show a slight rise time dependence as one would expect from Equation (5.2.8), with a stronger FEXT response at lower rise times reducing gradually by 1.1 dB for 2-GND middle and 0.58 dB for the 2-GND wide rails. All other measurements for the 1-GND rails show little to no rise time dependence. In addition all crosstalk distributions are smooth without rapid changes of the measured values.

The best performing layouts are the wide 2-GND-design as well as the 1-GND layout with mixed transmission line positions. The latter shows a mean crosstalk of (-43.74 ± 0.07) dB whereas the 2-GND-design produces a mean crosstalk of (-44.18 ± 0.23) dB which is equivalent to around 0.6 %.

As described earlier however these values are crosstalk signals measured peak to peak. Apart from small reflections or other signal artifacts the majority of the FEXT signal is below the 0 V baseline since the polarity of the crosstalk signal is reversed.

5.4.2 Attenuation and Rise Time Measurements

Setup and Procedure

The measurements of the attenuation were performed the same way as for the previous board. Signal pulses with an amplitude of 1 V and a rise time of 1 ns were injected into the sensor side of the board and read out by an oscilloscope on the FEE side as seen in Figure 5.8.

Transmission lines of all designs and different lengths were probed. The test rails with a reduced channel count provide a limited number of points of measurement. The same channels were used for measurements on the full rails although more channels are available.

Results

Measurements of all designs fitted by a linear function to extrapolate to a full length board of 1.93 m are shown in Figure 5.16. Each design is color coded just like for the crosstalk measurements.

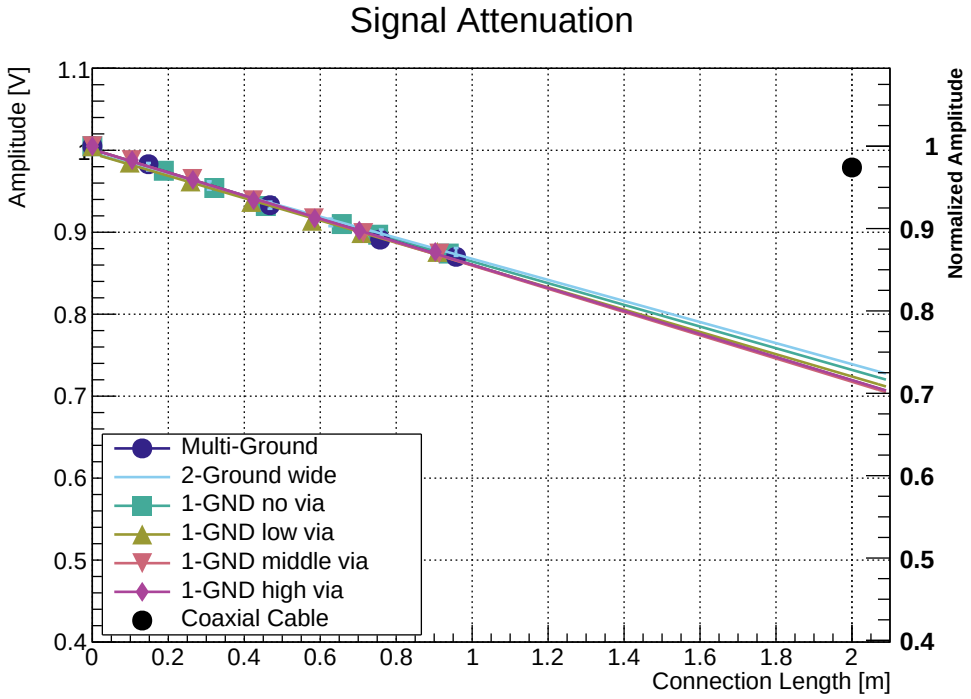

Figure 5.16: *Attenuation of the second generation Rail-Board for multiple design iterations extrapolated to a full length board using a fit of a linear function.*

Measurements for the 2-ground-designs with middle and narrow ground lines were not included in the figure mentioned above. This is due to reflections seen on the shorter transmission lines of those designs distorting the measurement by reducing the signal amplitude. The 1-GND design with mixed channel positions is also omitted since it basically is identical to the 1-GND high via layout with vias every 1 mm.

As seen in Figure 5.16 no major differences between the designs can be established. All perform nearly identical to each other. Same as for the first generation Rail-Board no significant coupling loss can be seen comparing measurements with and without the Rail-Board at an effective transmission length of 0 mm. The measurements show that over the full length of the board, which is assumed to be 1.93 m in order to be comparable to the third generation Rail-Board, the signal amplitude can be expected to reduce by around (26.3 ± 0.8) %, similar to the first Rail-Board.

The measured attenuation effect on the signal rise time (10 % to 70 %) is shown in Figure 5.17 for all aforementioned layouts. The data overlays each other to illustrate the similarity between all measurements. The behavior of all 1-GND lines are basically identical within the margin of error.

All 1-GND lines show an identical performance better than the other two design archetypes increasing from (0.88 ± 0.05) ns to (1.44 ± 0.13) ns at 1.93 m. This is an increase of 64 %. The multi-ground-design shows the worst performance with a higher initial rise time giving the series of points an offset in addition to a steeper slope increasing the rise time gain per mm slightly resulting in a rise time of (1.53 ± 0.14) ns after 1.93 m. The wide 2-GND lines in contrast to the multi-ground lines start off with a similar rise time which however increases faster than the 1-GND-designs resulting in an extrapolated rise time of (1.53 ± 0.13) ns at 1.93 m.

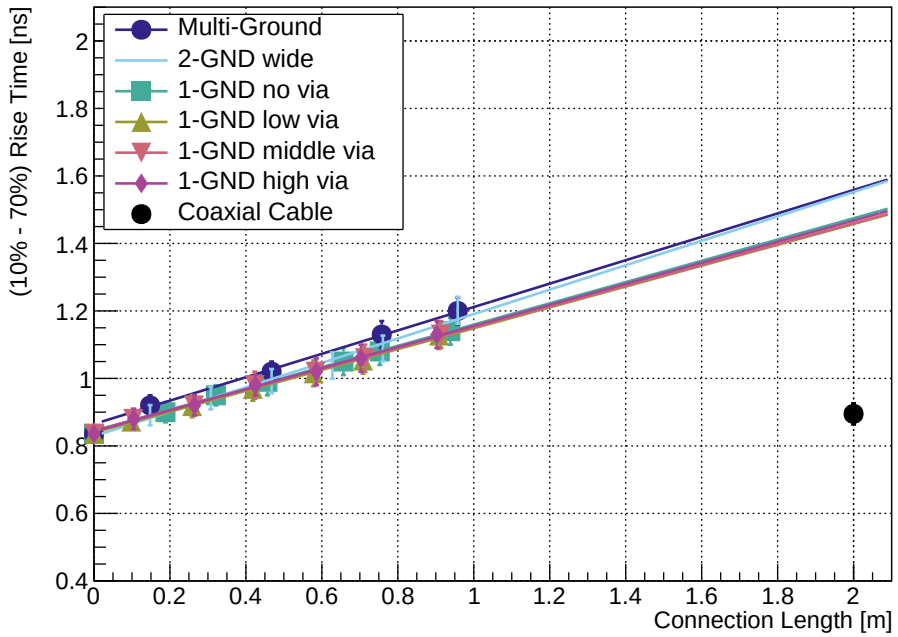

Figure 5.17: *The rise time (10 % to 70 %) for various layouts of the second generation Rail-Board. All data overlays each other fitted to extrapolate the behavior beyond the limits of the short board to the expected full board length performance.*

5.4.3 Discussion

Comparing the crosstalk measurements done here with realistic signal pulses to the measurements done for the first generation Rail-Board one sees a much smoother distribution without distinct local maxima or minima, even though slight rise time, respectively bandwidth or frequency dependencies are visible. This shows that crosstalk measurements with continuous sine waves are not suitable for applications with independent and individual pulses such as for the SiPMs of the B-ToF.

The fact that the crosstalk pulses show a reversed signal polarity plays very much in favor of the detector performance. The data acquisition system for the detector will later operate similar to the system of the time resolution measurements done at the University of Erlangen described in Section 6.4 where signal will have to pass a threshold to be recorded. Since the FEXT measured for this board produces signals of opposite polarity most of the measured signal extends to voltages below the ground or negative voltages while the detection threshold is set to positive voltages. This means that although signals are induced into the lines, with detection thresholds above a minimum level, no crosstalk will be picked up by the FEE.

Nonetheless, the best performing design without line shuffling appears to be the 1-GND-design with wide ground lines. As discussed later however it is the design with the largest material budget since the transmission lines are spaced so far apart. The marginal improvement seen here does not justify the necessary increase in material. The second best configuration appears to be the 1-GND-design with vias placed along the transmission lines. The via density however seems to have little effect past the 3 mm between the connection tested here.

The measurements also show that by applying this simple design tweak and thoughtfully positioning lines the crosstalk can be reduced considerably.

The attenuation measurement shows no difference in performance between all tested designs. The reason for the reflections seen on the omitted layouts is not well understood. The reflections appeared in lines of the full rails of the 2-GND-designs with narrow and middle ground line widths but not on the partial rails. This suggests a possible impedance changes when introducing the lines into a group of many neighboring lines. Since simple estimation methods were used to calculate the necessary signal line parameters for striplines of 50 Ω the horizontal distance from line to line was not factored in. To study and remedy this an analysis with a spectrum analyzer to determine the actual Z_0 would be necessary in addition to electric field solving software to simulate the conductor behavior and determine the required parameters.

The rise time measurements also only reveal a low layout dependence of the signal slope. Although the difference is small the 1-GND-designs consistently show an identical rise time increase lower than what can be seen for the multi- and 2-GND-layouts. For this reason and to save material the next generation Rail-Board was chosen to follow 1-GND-layout, the standard stripline layout.

5.5 Rail-Board v3

Moving from the second to the third Rail-Board generation the board structure has undergone a complete redesign as described in Chapter 3.2.1. This change in structural design and shape however has no impact on the electrical elements of the board except for the connector choice, moving from small male MMCX connectors to flat band cable connectors by samtec, so-called *zero insertion force connectors*. One board now houses two rails instead of four and it was necessary to produce two smaller boards which are connected by ribbon cables. These smaller boards are the same size as the half length boards studied so far. Such a board is shown in Figure 5.18 with a look at the internal connections and an image of the board itself.

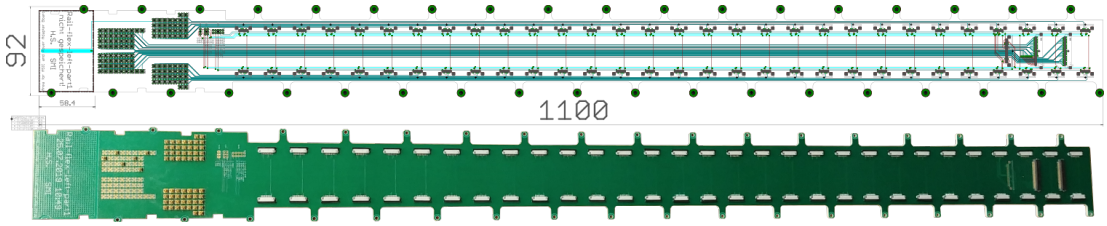

Figure 5.18: *Combined depiction of the internal transmission line layout and a photograph of the front part of the third generation Rail-Board.*

The main focus of this board was to reduce the signal attenuation as far as possible. To achieve this the two main sources of losses, as described in Section 5.2.3, the skin effect and the dielectric losses had to be addressed.

To reduce losses due to the skin effect the surface area of the conductor lines has to be increased. For thin and wide geometries increasing the thickness has only a fraction of the impact on the surface size as an increase in width. For this reason the copper thickness stays unchanged and the signal line width is increased. In order to receive a characteristic impedance of 50 Ω the substrate thickness has to be increased too. The exact ratio however depends on the chosen substrate material and its available laminate thicknesses.

As one can see in Figure 5.2, dielectric losses still dominate for the described transmission line geometry in FR-4. In addition analogue applications like our transmission board make every possible loss saving count. For this reason FR-4 was replaced by a Rogers 4000 series material, the RO 4003C. It is a hydrocarbon/ceramic material designed for low losses at higher frequencies with a dielectric constant of $\varepsilon_r = 3.55$ [56] instead of $\varepsilon_r \approx 4.4$ for FR-4. This increases the cost of the board by 33 % compared to a board made out of FR-4 [57].

Figure 5.2 shows that in FR-4 dielectric losses start to dominate at 170 MHz for a board with 400 µm wide and 18 µm thick striplines. At the expected signal bandwidth of around 350 MHz we see a resistive contribution of (0.88 ± 0.03) dB/m versus a dielectric contribution of (1.29 ± 0.03) dB/m. This makes the contribution of dielectric losses 47 % higher than resistive losses in FR-4 at the given conductor dimension. By moving to RO 4003C this difference can be reduced to a 29 % higher dielectric contribution of (1.19 ± 0.03) dB/m [54].

Since the thinnest available copper layer for this material is 17 µm and vertical space is limited a laminate thickness of 0.406 mm was chosen which resulted in a necessary conductor width of 400 µm to achieve an impedance of roughly 50 Ω. A cross section of a sample of the board can be seen in Figure 5.19. The ground lines are not interconnected by vias.

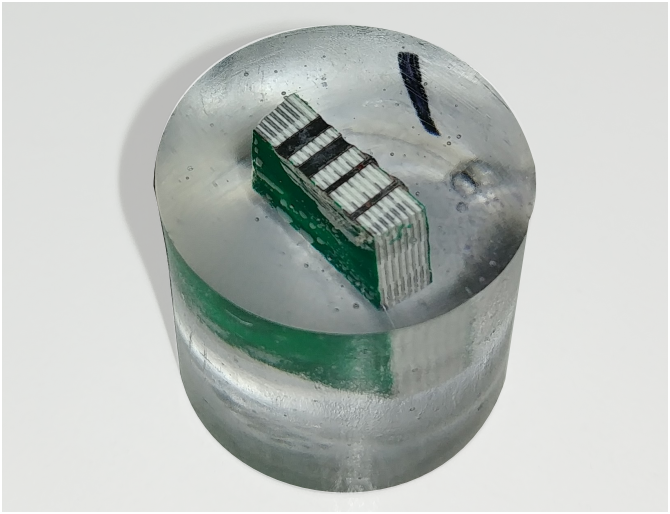

Figure 5.19: *Cross section of a 16 layer sample of the generation 3 Rail-Board.*

Internally the transmission lines were arranged the same way the second generation board was. All transmission lines were placed with increasing line lengths from top to bottom.

5.5.1 Crosstalk Measurements

Setup and Procedure

As for the previous crosstalk measurements the same setup shown in Figure 5.5 was used. This time however since the board does not feature MMCX connectors anymore the sensor boards shown in Figure 3.12 had to be modified. To induce the signal pulses from the pulse generator one end of a coaxial lemo cable was cut open and soldered onto the Sensor-Board to substitute the SiPM signal. This introduces additional effects of the sensor board itself not present for the previous measurements.

Results

Two examples of a measurement of the FEXT recorded with a digital oscilloscope are shown in Figure 5.20. It shows the aggressor (red) and FEXT victim line pulses (green). Each division on the horizontal axis corresponds to a time of 50 ns. For the aggressor signal each division corresponds to a voltage of 500 mV and of 2 mV for the FEXT signal. The top measurement was done for an aggressor signal rise time of 1 ns whereas the bottom image depicts a pulse with 5 ns rise time.

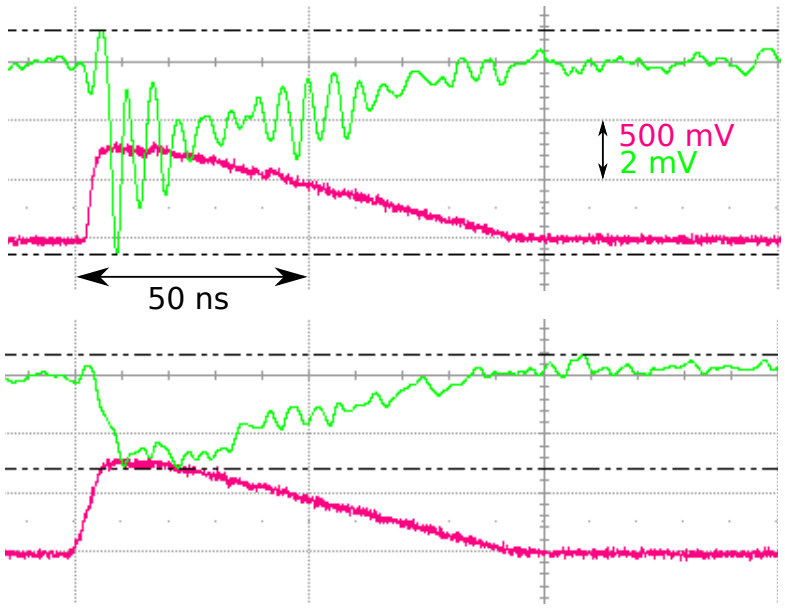

Figure 5.20: *Aggressor (red) and FEXT victim line pulses (green) measured with an oscilloscope show the level of crosstalk. The top measurement was done for an aggressor signal rise time of 1 ns whereas the bottom image depicts a pulse with 5 ns rise time.*

The crosstalk distribution depending on the rise time of the aggressor signal is shown in Figure 5.21. In addition to the crosstalk of this third generation Rail-Board drawn in indigo, the measurements for the second generation board were included with reduced opacity. This helps put the performance of the new board into perspective.

Compared to the older measurements the new board shows a much stronger rise time dependency dropping from (-40.3 ± 0.3) dB to (42.5 ± 0.4) dB, a difference of 2.1 dB. While the drop is initially rather strong it flattens out after a signal rise time of 3 ns.

5.5.2 Attenuation and Rise Time Measurements

Setup

The setup is as shown in Figure 5.8 and is identical to previous measurements. As mentioned previously however the signal is induced via the new Sensor-Board which might introduce additional effects not seen previously. Since this is the first full length Rail-Board prototype measurements up to the last channel with a transmission line length of 1.93 m were performed.

Results

A small artifact, most likely a reflection produced at the junction from Sensor-Board to Rail-Board sits right on top of signal pulse measured on the FEE side, which moves back with increasing transmission line lengths, compromises the attenuation measurements. For this reason the taken attenuation data points

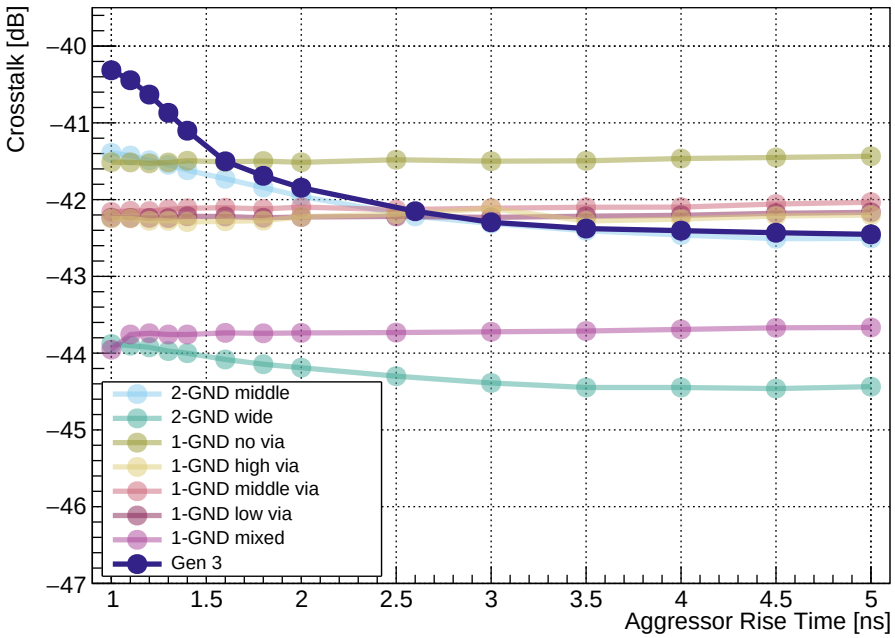

Figure 5.21: *FEXT measurements of the third generation Rail-Board including the rails on second generation Rail-Board as comparison.*

shown in Figure 5.22 show large systematic errors especially at the junction of the first to the second board, while keeping a small standard deviation or statistical error. Nonetheless a fit with a linear function reproduces the signal amplitude attenuation rather well and no obvious step between the measurements of the front and back board colored in indigo and teal can be seen. For the longest line of 1.93 m a signal loss of (11.7 ± 0.5) % was measured.

The same artifacts lead to large systematic errors for the rise time measurements which are shown in Figure 5.23 split into data points for the first and second part of the Rail-Board. The measurement of the first channel on the second board at 1.19 m stands out especially and is grayed out in the figure. It is ignored in the further analysis. Additionally we see a rise time increase of 0.36 ns or when transmitting the signal pulse through the Sensor-Board and Rail-Board in channel 1 compared to measurements forgoing these boards, with an effective connection length of 0 m.

A fit of data points along the two boards shows a signal rise time increase of (0.35 ± 0.02) ns/m equally large to the increase seen in equivalent lines on the second generation Rail-Board of (0.31 ± 0.05) ns/m, the data points of which are also plotted in Figure 5.23 with reduced opacity as comparison. Over the full length of the board the rise time increases from 835 ps to 1720 ps, an increase of 885 ps or 106 %.

Looking at the data from the front and back boards individually we see two distinct almost parallel lines for the rise time increase for both subdatasets. The resulting connection length dependencies are also drawn with dotted lines in

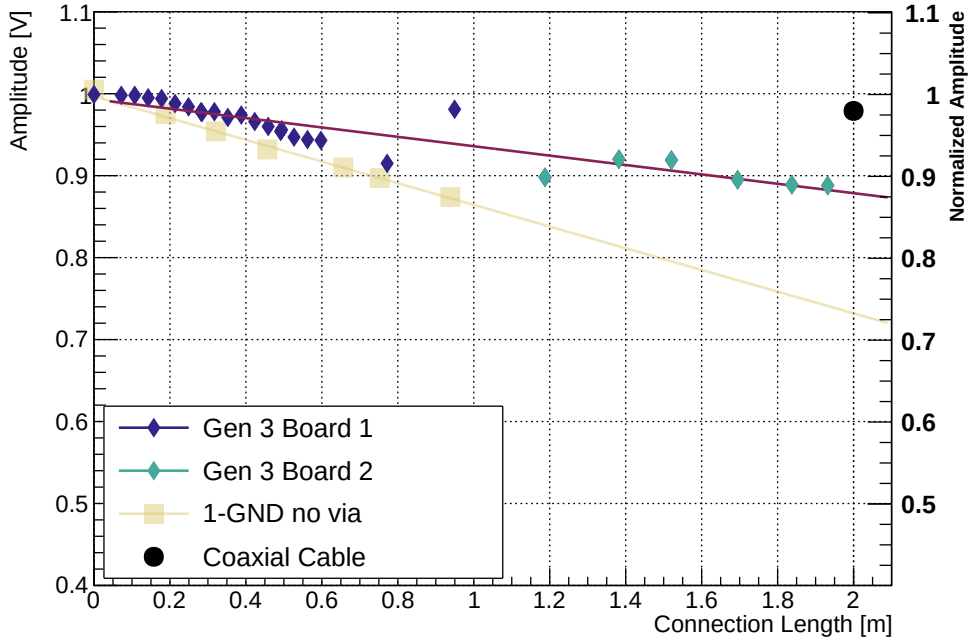

Figure 5.22: *Signal amplitude attenuation measurements along both parts of the third generation Rail-Board color separated for the front (Board 1) and back board (Board 2).*

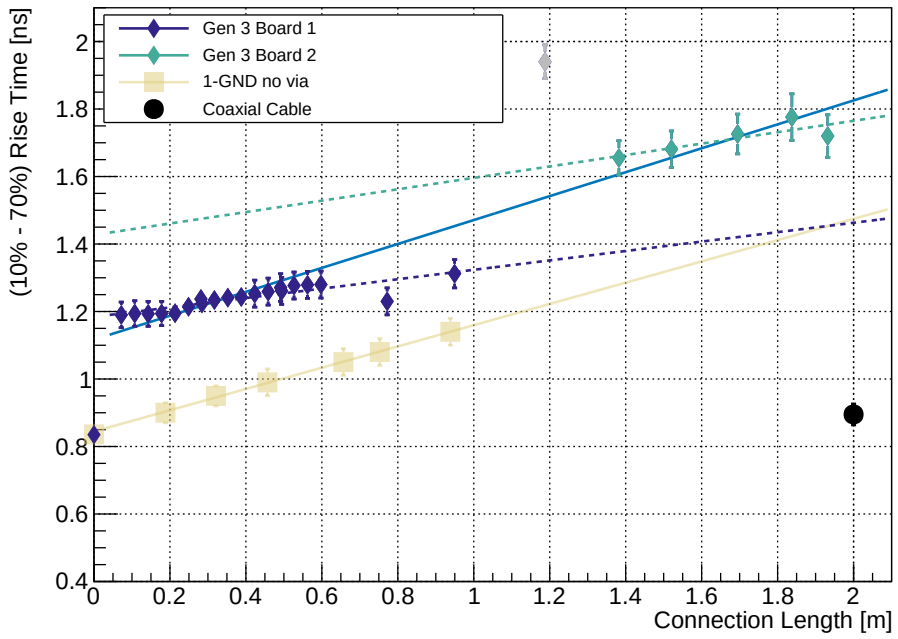

Figure 5.23: *Comparison between the rise time increase measured for the third generation Rail-Board split into data for the front (Board 1) and back board (Board 2) separated by color, and the measurements for the second generation Rail-Board design with the same basic layout.*

Figure 5.23 with slopes of (0.14 ± 0.04) ns/m and (0.17 ± 0.13) ns/m and an offset of (0.24 ± 0.23) ns.

5.5.3 Discussion

The measured crosstalk shows a high degree of rise time dependence compared to previous FEXT measurements. While the crosstalk initially shows a larger coupling between the lines it decreases for growing rise times. A crosstalk level larger than the one measured for the 1-GND lines of the second generation board is to be expected since lines are wider which increases its mutual capacitance [50]. This however does not explain the large frequency dependence.

Looking at the signal shape for the FEXT signal in Figure 5.20 one sees large periodical local peaks. The origin of these is unclear but for growing rise times they slowly become smaller and almost disappear for a rise time of 5 ns. This ringing is what produces the large crosstalk amplitudes we see at short rise times. Since the origin is unknown these measurements can not tell if they will be present for real SiPM signals. Apart from that, no significant performance difference to previous boards can be seen. In any case, the inverted signal polarity again results in an inconsequential crosstalk level relevant to the readout electronics.

Although the signal amplitude attenuation could be reduced, it and especially the signal rise time increase are still far from the performance measured for a standard coaxial cable. From the data points around the junction between the front and back boards at around 0.9 m it is impossible to tell the true extent of any signal amplitude loss due to the connectors. Judging by the smooth alignment of the first and last data points to the fitted straight the losses can at least be considered small.

Junction effects are even unclearer for the rise time measurements. While a clear increase in the rise time is observed when connecting the signal generator to the Rail-Board, the observation of such an effect in between the two Rail-Board parts is not directly possible since the measurements are affected by reflections. These reflections could either be caused by the junction of coaxial cable to Sensor-Board or Sensor-Board to the Rail-Board.

On the one hand the rise time increase rate measured over the whole board is very similar to the measurement of the same layout on the second generation Rail-Board. This is plausible since they only differ in material and transmission line dimensions. The rise time of a signal is proportional to the lines time constant $\tau = RC \sim t_{rise}$ [49]. While the resistance falls proportional to the line width, the capacitance slightly exceeds a proportional increase raising the rise time for wider striplines [50]. The capacitance however is also proportional to the dielectric constant which has been reduced by moving to the low loss Rogers material by a factor of 0.81. Whether these effects cancel each other out would need to be studied with more rigorous simulations of the boards. On the other hand if we assume to see a worsening effect of the connector one would receive two independent lines for the front and back board with a similar slope and a offset in between them as we do when considering the data of the two Rail-Board parts individually.

The rise time of the third generation Rail-Board shows a general increase over

the first and second generation Rail-Boards. This offset can be attributed to the connection between the coaxial cable carrying the signal and the Rail-Board. As mentioned earlier this connection involves the Sensor-Board and a ribbon cable connector in contrast to simple MMCX connectors without the Sensor-Board for the previous boards. Although a clear determination which of these two components contributes the most to the rise time can not possibly be drawn from this data set, it is clear that the connection offers room for improvement. This can be achieved by improving the connector for example by moving back to MMCX connectors while keeping the flexible Sensor-Board and by improving the electrical properties of the Sensor-Board itself by considering a shielded multilayer approach similar to the implementation of the Rail-Board.

The effects of the signal amplitude attenuation as well as the rise time increase are only relevant in the context of the time resolution the system is able to achieve. While a smaller signal pulse and a larger rise time will reduce the performance the true impact will have to be determined in conjunction with the final front-end electronics by studying the achieved time resolution. The improvement from the first to the third generation however by reducing the attenuation from a loss of $(26.3 \pm 0.8)\,\%$ to $(11.7 \pm 0.5)\,\%$ will impact the overall performance positively.

5.6 Material Budget

This section is an extension of the discussion of the detectors material budget in Section 3.2.2 which focused on the scintillators, SiPMs and the housing structure. In this section the different Rail-Board designs discussed above will be examined.

5.6.1 Radiation Length Estimation of Rogers Material

Since the Rogers Material is not such a widely used PCB substrate material no information on its radiation length is available. The only information supplied by the Rogers Corporation was that it is a hydro carbon based material filled with a ceramic (most likely Al_2O_3) and reinforced by glass fibers [58] and provided the image shown in Figure 5.24 with no further explanation. From the image and density information of the relevant materials one can roughly estimate the composition and its radiation length.

To calculate the radiation length, information on the material composition is necessary as seen in Equation (3.2.1). The exact hydro carbon is unknown and with it its density and radiation length. By estimating these values as well as the fraction of fiber glass in the board the material composition can be calculated.

Since the density (ρ) of the Rogers Material is known the other densities can be estimated. The density of an object is the sum of the density of its components weighted the fraction of the volume it occupies as described in Equation (5.6.1).

$$\begin{aligned} \rho_{RO} &= a\ \rho_{\text{ceramic}} + b\ \rho_{\text{hc}} + c\ \rho_{\text{glass}} \\ 1 &= a + b + c \end{aligned} \tag{5.6.1}$$

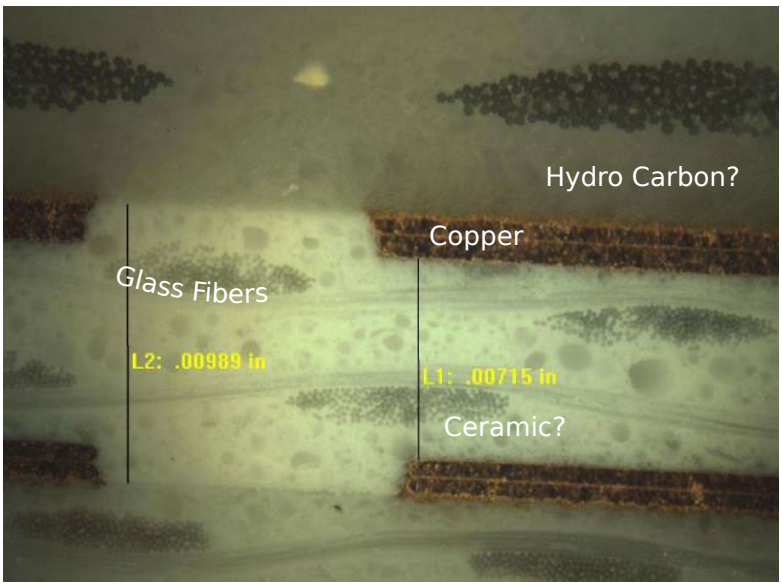

Figure 5.24: *Image of the cross section of a sheet of Rogers Material RO4003C, showing copper conductors surrounded by layers of a hydrocarbon substrate, filled with a ceramic (Al_2O_3) and reinforced with glass fibers. [58]*

The list of relevant parameters is shown in Table 5.1, with estimated values highlighted in blue. Solid hydrocarbons tend to have a density of of around $\rho_{\text{hc}} = (1.10 \pm 0.15)\,\text{g/cm}^3$. The fibers visible in Figure 5.24 take up roughly 20 % of the visible layer. Assuming a fiber packing density 2/3 that of tightly packed spheres means a volume occupancy of around 10 %. The density dependent radiation length of hydrocarbons is rather stable no matter the exact composition with $(42 \pm 2)\,\text{g/cm}^2$. With the additional condition that the volume fractions have to add up to 1 Equation (5.6.1) can be solved for $b = 0.705 \pm 0.026$ and $c = 0.195 \pm 0.026$ giving us the material composition. Given the radiation length of Al_2O_3 and glass a radiation length of $X_0 = (180 \pm 15)\,\text{mm}$ can be calculated for the Rogers Material.

Table 5.1: *Values for the calculation of the radiation length of the PCB substrate material RO 4003C which is drawn in red. Values in blue are estimates and values in black are provided by [33].*

Material	Composition	$\rho[\text{g/cm}^3]$	X_0 [g/cm^2]
RO4003c	1.000	1.79	**32.2 ± 1.5**
AL2O3	0.195 ± 0.026	3.97	27.94
Hydro Carbon	0.705 ± 0.026	**1.10 ± 0.15**	**42.00 ± 2.00**
Glass	**0.100 ± 0.050**	2.4	25.66

5.6.2 Rail-Board Comparison

All boards are equipped with 4 rails each with 60 lines. These however do not span the entirety of the board but due to their decreasing length form a triangle with effectively the same area as 30 full length lines. Ground layers and PCB substrate material are also only assumed to be around where signal lines are present.

To reduce the impact of the substrate material as it comprises most of the material budget contribution since the copper layers are so thin, unnecessary material will be cut out. The third generation board was produced with material trimmed around the edges only leaving small bridges and screw holes. The other boards are supposed to have excess material cut out of the middle. The amount of redundant material is determined by the width of the signal line structure. The wider the signal and ground lines are the less material can be reduced.

The effective material thickness (d_{eff}) and the radiation length contributions of the copper and substrate material for all designs from the first generation Rail-Board(Gen 1), the two designs of the second generation board (2-GND, 1-GND) to the third generation board (Gen 3) are listed in Table 5.2. It also lists the possible amount of redundant material that can be cut out based on the copper distribution. An additional 20 % margin is added to account for material necessary to achieve sufficient structural stability.

As mentioned before, Table 5.2 shows that the copper, although it has a higher absolute radiation length, contributes less to the material budget than the substrate material, be it FR-4 or Rogers Material. The 2-GND design with narrow shielding ground lines produces the lowest material budget with 0.31 % followed by the 1-GND design with 0.41 %. This is due to the small width of the signal and ground lines allowing closer spacing of the lines reducing necessary surface area on the board. The 2-GND design also does not have a continuous ground layer reducing its copper contribution compared to the 1-GND design.

The first three designs all contribute less than half as much as the third generation board which has a material budget of 1.45 X_0. This is due to the large increase in size of the signal transmission lines over the other designs. Moving up to a width of 400 µm however only has a marginal effect on the effective copper thickness. The main increase in material budget comes from the increased board material due to both an increase in laminate thickness to keep the characteristic impedance of 50 Ω as well as an increase in necessary material due to the wider transmission lines. Producing the third generation board with FR-4 the substrate would increase the material budget even more because the larger dielectric constant of FR-4 necessitates an increase in substrate thickness of 25 %. Such a board would have a material budget of 1.97 X_0.

The decision on which design to use has to be weighed by the achievable time resolution which are still to be determined against the impact on the EMC performance hit due to the additional material. From a purely performance oriented perspective the third Rail-Board design would be the primary choice, since all designs show negligible crosstalk and the third generation board suffers from less attenuation.

Table 5.2: *Radiation length of the Rail-Board designs split into contributions from the copper and the substrate material, either being FR-4 or Rogers Material RO4003C. Also listed are the effective material thickness on the board and the surface fraction that can be cut out as it does not house any electrical connections.*

	Material	X_0 [mm]	d_{eff} [mm]	d_{eff}/X_0 [%]	Cutout [%]
Gen 1	Copper	14.4	0.03	0.21	
	FR-4	155.0	0.71	0.46	52.9
	Sum			**0.67**	
2-GND wide	Copper	14.4	0.03	0.21	
	FR-4	155.0	0.50	0.32	66.4
	Sum			**0.54**	
2-GND narrow	Copper (GND)	14.40	0.02	0.11	
	FR-4	155.00	0.29	0.19	80.4
	Sum			**0.31**	
1-GND	Copper	14.4	0.03	0.20	
	FR-4	155.0	0.33	0.22	77.8
	Sum			**0.41**	
Gen 3	Copper	14.4	0.04	0.29	
	Rogers	197.2	2.08	1.15	30.8
	Sum			**1.45**	
Gen 3 FR-4	Copper	14.4	0.04	0.29	
	FR-4	155.0	2.59	1.67	30.8
	Sum			**1.97**	

5.7 Summary and Conclusion

In this chapter three successive Rail-Board generations are introduced. The performance of the boards was evaluated in three categories, the crosstalk level, the signal amplitude attenuation and the signal rise time increase. For all of these measurements signal pulses close to SiPM pulse shapes with a rise time of 1 ns and a fall time of 70 ns from a pulse generator are sent through the respective boards and evaluated using a digital oscilloscope.

Crosstalk measurements using sine waves were performed for the first generation board for various frequencies but produced highly frequency dependent results much larger than what was measured using distinct pulses. All such measurements produced negligible crosstalk levels of below $-40\,\mathrm{dB}$ or 1 %, measured from peak to peak, if measurable at all. Additionally it was shown that the FEXT signal is of reversed polarity. This reduces the impact of crosstalk even further since pulses have to cross a predetermined threshold to be registered.

Moving from the first to the second generation board the goal was to reduce the material budget since the crosstalk was shown to be inconsequential. This goal was achieved by reducing the number of shielding ground lines. Depending on the signal line dimensions this lead to a reduction of between 19 % to 54 %. The board performance otherwise stayed the same between generations and the different transmission line designs implemented on the board, showing signal amplitude attenuation levels leading to a loss over the full length of the Rail-Board of up to $(26.3 \pm 0.8)\,\%$, much larger than what one would expect from a standard coaxial cable.

For the third generation Rail-Board the focus was set on reducing the signal attenuation by using materials better suited for high bandwidth signals. By changing the PCB substrate material from FR-4 to Rogers Material RO 4003C the signal amplitude attenuation was successfully reduced and the signal amplitude increased, only losing $(11.7 \pm 0.5)\,\%$ of the amplitude after passing through the entire board. Making this the first choice in this regard.

After going through a redesign of the detector and changing the the way the SiPMs on the scintillators connect to the Rail-Board the rise time measurements show a stark increase after connecting to the board. This large increase of almost 43 % was not observable for measurements of previous boards. This however is not necessarily due to the new connector of the third generation Rail-Board but also due to the way the measurement was performed. The easiest way to connect to this new board was through the reworked Sensor-Board which was not included in the previous measurement. The rise time measurements of the third generation Rail-Board also potentially show a worsening effect due to the connection between the front and back part of the Rail-Board. Eliminating this connection between boards by moving back to the more widespread substrate material of FR-4 would benefit the rise time. This however would lead to an increase in material budget due to the associated increase in PCB substrate thickness. In any case this rise time increase is detrimental to the performance of the detector and should be reduced by paying closer attention to matching the impedance of all components. As it stands the newest Rail-Board shows the worst signal rise time increase. By

optimizing the connections however the rise time increase can be improved.

Measurements of all boards show a rise time increase that by far exceeds what is measured using standard coaxial cables. PCB transmission lines however will always be at a disadvantage towards coaxial cables since to reduce their losses to the skin effect their width has to be increased increasing their capacitance, whereas the cables are made using stranded and woven copper wires greatly increasing their surface area without increasing the capacitance.

When prioritizing the material budget of the board the new design with wide transmission lines would not be the first choice. Improving the signal characteristics which necessitates increasing the trace dimensions runs contrary to the desire of a small material budget. The exception being the substrate material since Rogers Material allows thinner boards than FR-4 would. The balance between signal pulse optimizations and the material budget needs to be reassessed when the exact influence of the signal shape on the time resolution of the detector has been determined.

Chapter 6

Time Resolution Scan and Scintillator Comparison

6.1 Introduction

Since the inceptions of the Barrel Time-of-Flight Detector its development was closely tied to the Barrel DIRC detector and its groups. The group by A. Lehmann at the Friedrich-Alexander Universität Erlangen-Nürnberg, working on various performance aspects of MCP-PMTs for the $\overline{\text{P}}$ANDA Barrel DIRC was also involved in the design of the B-ToF early on.

Previous measurements done there studied the scintillator material, trying to determine which product delivered the best performance, as well as the optimal wrapping material of the individual scintillator tiles.

In November of 2017 we traveled to Erlangen in order to make use of the automated system for time resolution measurements setup in a facility with a reduced electromagnetical noise background. Their laboratory is placed in a decommissioned particle accelerator facility and is equipped with a precise stepper motor capable moving a radioactive source allowing to take automated time resolution measurements over the entire surface of our scintillators.

Our goal for these measurements was to study the influence of the scintillator thickness on the time resolution using a fixed array of $3 \times 3\,\text{mm}^2$ SiPMs examining whether matching the thickness of the tiles to the readout produces a superior performance. In addition to this concerns were brought up that the planned polishing considered for the final production of the scintillators might deteriorate the surface quality of the scintillators potentially leading to a larger amount of internal diffuse reflections and hence a worse time resolution. Evaluating the quality of the polish also became a goal.

6.2 Motivation

During the review process of the B-ToF TDR it was suggested that by optimizing the fit of the scintillator to the readout SiPMs we would be able to achieve a better timing performance since less light would be lost. Since the most common form factor offered by SiPM manufacturers is $3 \times 3\,\text{mm}^2$ we chose to study the effect of reducing the proposed tile thickness of 5 mm down to 3 mm to match the SiPMs

dimensions. In addition 4 mm and 6 mm scintillators were studied, in order to gain a complete picture.

The rational behind this idea was that an increase of the detection efficiency of the setup by increasing the ratio of sensitive to dead area on the small sides of the scintillator where no reflector will be mounted would improve the time resolution by shortening traveled distances of reflected photons and losing less photons close to the readout. Four $3 \times 3\,\mathrm{mm}^2$ SiPMs create an active are of $36\,\mathrm{mm}^2$ where incoming photons can be turned into electrical signals. A 5 mm thick scintillator tile with the width of 29.4 mm has a surface of $147\,\mathrm{mm}^2$ of which 24.5 % is readout. A 3 mm thick scintillator tile however has 40.8 % of its surface connected to SiPMs.

While increasing the detection efficiency is desirable in almost any case, in this instance it might come at a cost of increasing the total amount of internal reflections by reducing the scintillator thickness instead of increasing the sensor size. Which effect has a larger influence on the time resolution of the detector is the main goal of this chapter.

6.3 Previous Measurements

Previous measurements performed at this location by L. Gruber and M. Chirita studied the influence of the scintillator and wrapping material. Their measurements concluded that the scintillator material EJ-232 slightly outperformed EJ-228 by as little as 7 ps.

The tested wrapping materials included aluminized Mylar foil, Tyvek hardstructure 1057D, Enhanced specular reflector (ESR), Teflon tape and aluminum foil. The best photon collection was obtained with Teflon tape. The time resolution of this run however was the worst out of all materials with a time resolution of (59.4 ± 0.3) ps, even worse than no wrapping with (55.0 ± 0.3) ps. The best time resolution was achieved with aluminized Mylar foil reaching a time resolution of 52.7 ps.

It was concluded that due to the diffuse scattering properties of Teflon, while it provided the highest photon count, the increased amount of internal reflections has a detrimental effect on the rising edge of the signal and with that the time resolution of the setup.

6.4 Experimental Setup

As mentioned before the measurements were done in the hall of a decommissioned particle accelerator at the Friedrich-Alexander Universität in Erlangen-Nürnberg with the help of the local $\overline{\text{P}}$ANDA group by A. Lehmann. In this hall all detectors were setup in a copper plated dark box isolating it from potential electromagnetic noise sources and most importantly light.

The material of the $87 \times 29.4 \times 5\,\mathrm{mm}^3$ scintillator was studied here previously as explained in Section 6.3, in which it was determined that both organic scintillators EJ-232 and EJ-228 produced time resolutions considerably better than the set

requirements. For the following measurements we however focused on the slightly better performing EJ-232 and one of its variants.

EJ-232 produced by *Eljen Technology* is an organic scintillator made out of Polyvinyltoluene (PVT), equivalent to the Saint-Gobain / Bicron BC-418. Although EJ-232 is already made for precise timing applications with a fast signal rise time of 350 ps, Eljen Technology offers a variant for ultra-fast timing applications with a quenching agent added to the scintillator, reducing the rise time to 110 ps and lower. This is achieved by adding benzophenone to the scintillator material. It does not change the emission spectrum but reduces the scintillation efficiency [59]. The addition of the agent also reduces the attenuation length from (17 ± 1) cm for the standard material to (6.0 ± 1.5) cm [60].

To increase the light yield the tiles were wrapped in aluminized Mylar for most measurements. This was determined to be the best wrapping material, maximizing the photon collection while reducing diffuse scattering. The shortest sides were left uncovered since the four SiPMs are mounted there and already take up more than 24 % of the surface.

The used box is seen in Figure 6.1 and also housed the preamplifier as well as an adjustable red pedestal for the positioning of the scintillator modules and the stepper motor moving a radioactive ^{90}Sr source in two directions along the scintillator surface, synchronized with the measurement plan. Movement along the long 87 mm side corresponds to the x axis where as movement along the 29.4 mm side corresponds to the y-axis. The scintillator is held by 3D printed receptacles and pressed onto the SiPMs with bolts and nuts as shown in Figure 6.2. A thin layer of optical grease is applied to the SiPMs to reduce reflection losses.

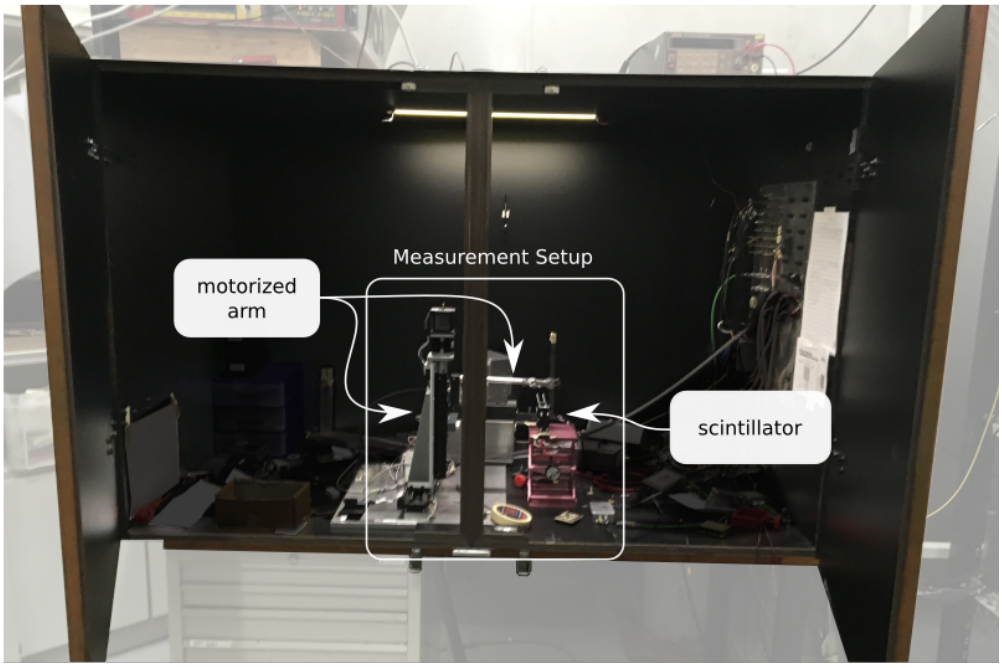

Figure 6.1: *The copper clad dark box used for the time resolution measurements at the Friedrich-Alexander Universität in Erlangen with the scintillator on the rose colored pedestal and the motorized source to the left of it.*

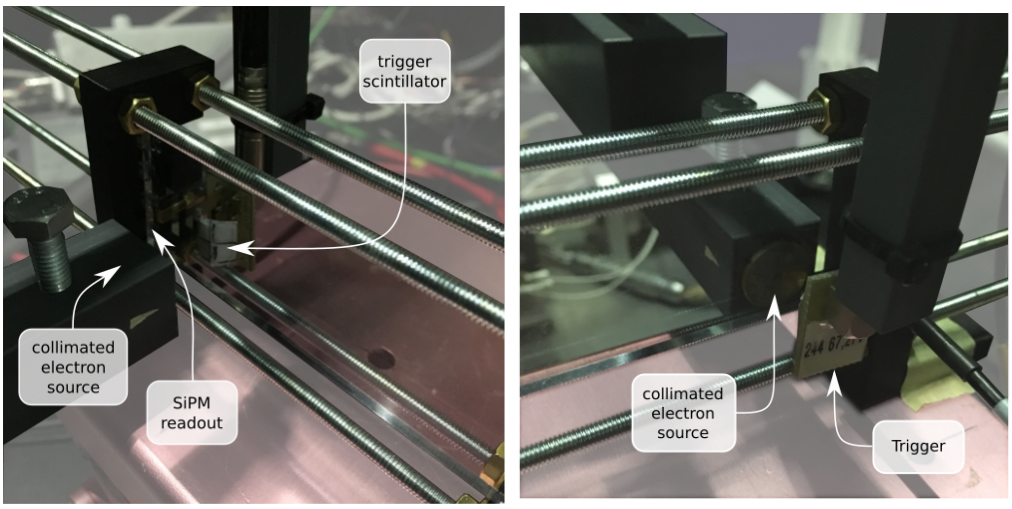

Figure 6.2: *Two images showing either side of the scintillator held by 3D printed receptacles and pressed onto the SiPMs by nuts and bolts as well as the trigger and the collimated ^{90}Sr source opposing each other.*

Figure 6.2 also shows the $5 \times 5 \times 5\,\mathrm{mm}^3$ trigger in the first picture, an organic scintillator on a SiPM protected by a piece of paper behind the scintillator tile. The second picture reveals the radioactive source collimated by a brass cylinder featuring a small hole for the passage of the particles opposite of the trigger.

^{90}Sr is a β^- source that produces electrons of up to 0.55 MeV in a primary decay to ^{90}Y which then again rapidly decays under yet another β^- emission of electrons up to 2.28 MeV, to ^{90}Zr. Since β decays are a three body process the energy freed in the decay is randomly distributed among the nucleus, neutrino and electron with no discrete energy levels for the electrons but rather a spectrum of energies up to the maximum mentioned above.

All SiPMs used for the measurements were produced by Hamamatsu and are of the `S13360-3050PE` series with a 50 µm pitch and a break down voltage of around 52.5 V. The four SiPMs are soldered to the sensor boards and are connected in series. The same set of SiPMs was used for all measurements and was moved from scintillator to scintillator. The sensors were then connected to the preamplifier. Outside the box the amplified signals, along side the signals from the trigger, then went through several electronical data acquisition systems in order to record their timing information as well as their signal strength.

The signals were split in order to be able to record two signal properties with separate electronics. Firstly the timing of the signals relative to the trigger was determined in a VME *time-to-digital converter* (TDC) by CAEN (`CAEN V775`) and secondly their amplitude or rather their charge was measured within a set time frame provided by a gate signal in a 32 channel VME *charge-to-digital converter* (QDC) by CAEN (`CAEN V792`). The exact time the TDC records is determined by a leading edge discriminator. If the trigger detector signal passes the discriminator threshold it produces a box signal which is fed into the TDC and starts the time measurement. Once the SiPM input signal crosses the threshold, the discriminator signal acts as the stops signal to the TDC for the respective

channel. The discriminated trigger signal is also used as the gate signal for the QDC controlling the width of the time window for the charge collection. The exact height of the optimal discriminator threshold has also been determined and is part of the following analysis.

The trigger signal was not only used as a reference time but also as the name implies as a start signal to the whole readout chain. If events are registered in the detectors but no signal is produced by the trigger no data is recorded. This not only cleans the data by removing random events caused by only one of the detectors but also allows us to use the trigger scintillator as an additional collimator. Although the ^{90}Sr source is enclosed in a metal housing with a single hole at the front the position of the trigger scintillator reduces the solid angle of accepted particles yielding a more precise position measurement. In addition to that it introduces a threshold on the electron energy necessary to trigger an event as particles with insufficient energy will not reach it. The comprehensive schematic of the wiring can be seen in Figure 6.3. It includes delays for all signals in order to place the detector signals within the discriminator response, the gate.

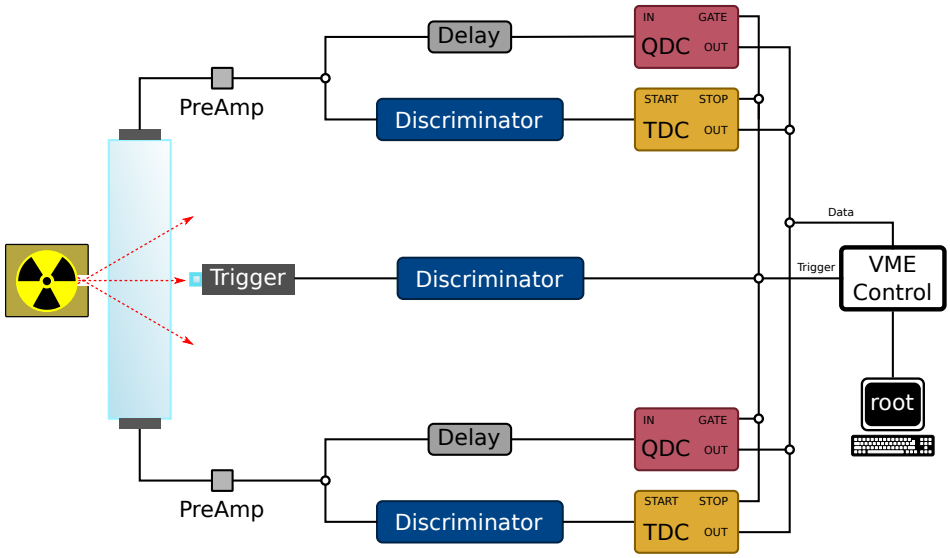

Figure 6.3: *Schematic of the readout and control electronics of the measurements setup. The trigger PMT after passing a discriminator provides the gate signal for all other readout devices and a start signal to the VME control. Once it receives a signal the control module collects data from the QDC and TDC and forwards it to a PC running a root script.*

All readout modules were connected to the VME control module, managing the data taking, starting and stopping the recording of each event as well as communicating with and transmitting data to the root script running on a PC.

6.5 Analysis Preparation

6.5.1 Discriminator Threshold Scan

The detection of a signal pulse is always subject to discrimination since all electric systems are affected by external noise sources and a general level of background. Determining which signals to include and exclude is imperative to generating reliable data and a well defined signal time.

Scintillator signals are never instantaneous. As particles traverse the material photons are constantly being created by de-excitation of excited electron shells that absorbed energy of the passing particle. This means a signals rise time depends primarily on the de-excitation process and its speed, different for every material, but also on the random distribution of collisions when looking at a very small time scale for fast scintillators such as the ones used in the B-ToF. Photons are also not emitted in the same direction every time but in random directions. This introduces variations in the flight path and its length for the photons that hit the detector and produces photons that are not detected by the photosensor at all.

All these effects lead to variations in the time it takes to detect the photons emitted by a hit in the scintillator. For a growing number of photons this effect however grows smaller by a factor of $1/\sqrt{N}$, with N being the number of detected photons. So choosing a threshold of detection at higher photons counts, meaning at a larger signal amplitude leads to a more stable measurement and hence to a better time resolution. Setting the threshold too high however means losing many events and introduces other variables exasperating the effect of individual changes or jitter in the pulse shape as the slope of the rising pulse flattens. More importantly it increases the impact of late photons that undergo multiple scattering. The random path lengths of these photons produce large differences in arrival times.

To find the ideal threshold the time resolution of signals with an amplitude of roughly 1.4 V was measured in three positions. The measurement points were all along the center of the scintillator on its long axis, 1 cm from either end and in the center, and done at various threshold levels. The mean time resolution and its sample standard deviation were then noted and are plotted in Figure 6.4.

From the figure it is not directly clear that the time resolution worsens for higher thresholds. If we look at the errors however, one sees a deteriorating performance manifesting as a decreasing time resolution uniformity through larger standard deviations. This stems from a worsening of the time resolution at the center of the scintillator. Since we observed the best time resolution and a comparably low standard deviation at a threshold of 20 mV, it was chosen as the discriminator threshold for all following measurements.

6.5.2 Bias Voltage Scan

A SiPMs performance is heavily influenced by the applied voltage. To be more precise, it is the overvoltage, the voltage difference of the applied bias to the breakdown voltage of the SiPM that determines the gain, the dark count rate and the noise. A higher gain means an increased signal rise time of the detector, which

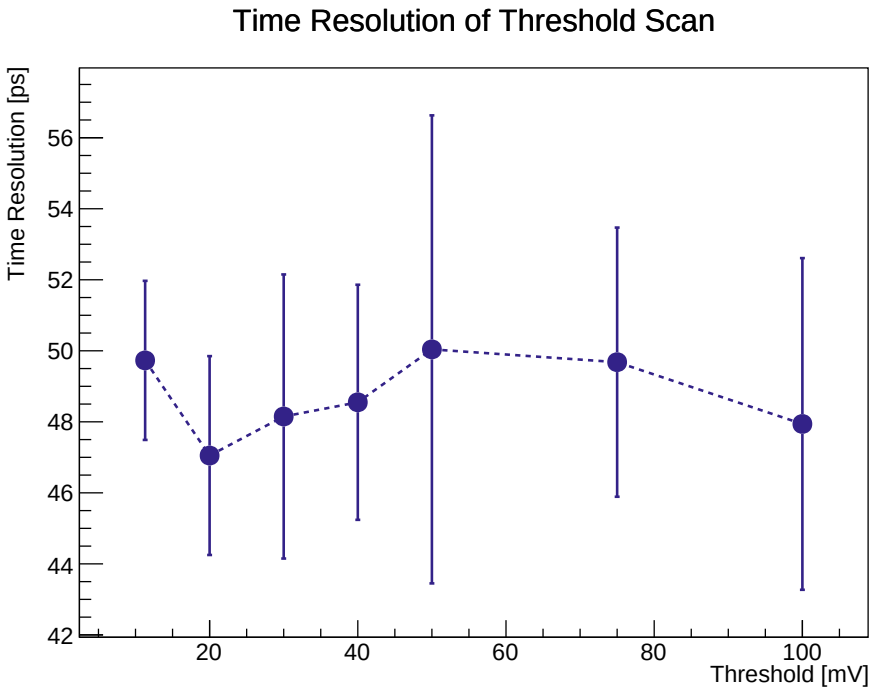

Figure 6.4: *Scan of the discriminator threshold on the x-axis given in mV and the resulting mean time resolution in ps on the y-axis. The error bars are the standard deviation. These results are based on measurements of three points along the scintillators long, central axis.*

is beneficial to every timing measurement. Increased noise however is something to be avoided and is detrimental to our time resolution measurements. For these reasons a sweet spot, balancing the positive effects of higher gain and noise, can be expected when scanning the detector response at increasing bias voltage.

All SiPMs are slightly different. This is expressed in the individual break down voltage for example. All SiPMs used have a breakdown voltage of around 52.5 V, pre measured by Hamamatsu. To achieve the characteristic SiPM behavior an overvoltage has to be applied, pushing the operational voltage slightly above the breakdown voltage. Since the SiPMs are soldered onto the sensor boards in a serial connection we have to apply the sum of all individual operational voltages of around 230 V. The sums of the break down voltages for the SiPMs on the sensor boards show a slight difference of 1 V. For this reason we increased the bias of the second sensor board by that amount. The difference was kept constant and not adjusted proportionally since it makes up less than 0.5 % of the applied voltage.

In order to determine the optimal operational voltage of the detector systems, a scan of the bias voltage while measuring the time resolution was conducted. Same as for the threshold scan in section 6.5.1 the time resolution of three positions, in the middle of the scintillator and 1 cm from either side, was averaged. The bias voltage was increased incrementally in 3 V steps starting at 221 V going up to 242 V.

The usual time resolution behavior for these scans, which we also expected

to see here, is an initial drop as the overvoltage reaches the optimum followed by a turnaround towards rising resolutions. SiPMs run at operational voltages only marginally above the break down voltage produce small signals. As the overvoltage is increased the signal amplitudes grow producing a leading edge with an increasingly steep slope. The moment such a signal crosses a threshold is therefore less susceptible to noise and produces better timing results.

This is balanced out by the fact that higher operational voltages introduce a higher degree of noise. At higher voltages it becomes increasingly easier for a pixel of the SiPM to misfire as the threshold for such induced by random surges of thermal energy is lowered. The resulting rise in dark noise effectively introduces a jitter into the signal pulses that negatively affects the time resolution measurement.

The three point mean time resolution depending on the applied voltage is drawn in Figure 6.5 with the sample standard deviation as the error bars. It clearly shows a drop of the time resolution with a growing bias voltage, reaching a minimum at 236 V and 237 V and rising there after as expected. Due to the correlation of increasing bias voltage and dark noise we leaned towards lower voltages and used 234 V for following measurements.

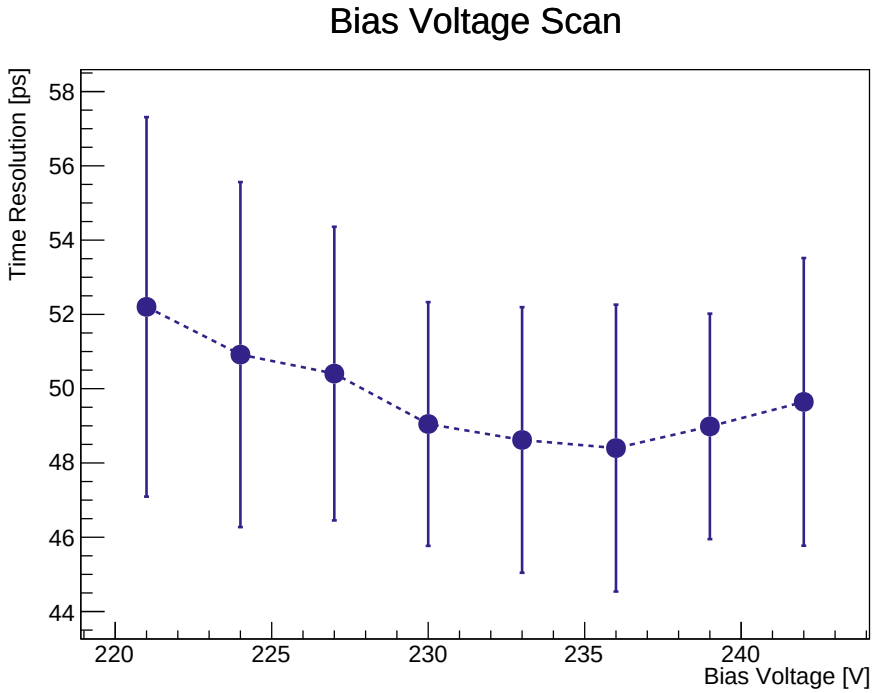

Figure 6.5: *Bias voltage scan for the serial connection of four SiPMs in order to determine the optimal operational voltage for time resolution measurements. The time resolution of three points was averaged and the sample standard deviation plotted as the error bars.*

6.5.3 Photon Count Calibration

For a better understanding of the setup and the measurements it is important to have a gauge on how many photons are detected per hit. The electronics however only measure the collected charge. To how many photons the collected charge equates to, depends mainly on the gain of the SiPM determined by the applied bias voltage.

To calibrate the QDC results single photon spectra were recorded at the previously determined optimal bias voltage of 236 V and 237 V. To do this pulsed low intensity laser light was diffused and directed at the four SiPMs without a scintillator. The signals were then amplified by the preamplifier and recorded in a digital oscilloscope.

One such recorded spectrum can be seen in Figure 6.6. It shows a persistent image of multiple SiPM signals with negative pulses from the preamplifier overlaid on top of each other in the top left. The color of the line indicates the signal density in that spot with low signal densities going from green to blue for higher concentrations of signals.

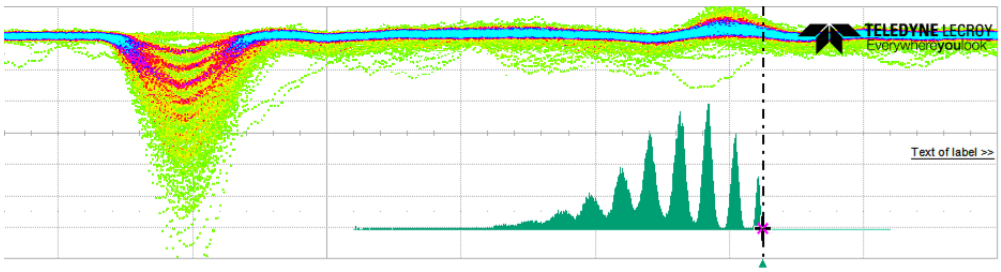

Figure 6.6: *Single photon spectrum recorded in persistence mode of an oszillograph by LeCroy. Each line represents one measured signal in the last about 3 s. Color changes from Green to Red to Blue indicate the density of recorded pulse shapes. Every horizontal division corresponds to 2 ns. Every division vertically corresponds to 50 mV. A histogram of the signal amplitudes is shown in the bottom right with the origin at the dotted line.*

The baseline has a high degree of overlap as it should be. Looking at the pulses one sees distinct pulse heights. Measuring the amplitude of each pulse and plotting the peak position in the histogram seen on the bottom right of Figure 6.6 we are able to see multiple well defined overlapping lines. These are the signals of individual photoelectrons, photoelectron pairs, triplets and so on manifesting as distinct peaks in the histogram. An amplitude of 0 mV in the histogram is marked by the dotted line. From there the rising number of photoelectrons are plotted to the left since signals with a falling flank and a peak below the baseline are assigned negative amplitudes.

Measuring the distance of the peaks in mV and determining the mean distance gives us a better idea of the amplitude of a single photoelectron than looking at one peak alone. It allows us to minimize the effect of the underlying noise. For this measurement we received an amplitude of 8.15 mV per photoelectron with a standard deviation of 0.56 mV.

Another unknown is the calibration of the QDC and what signal amplitude corresponds to what charge or QDC value. For this the ^{90}Sr source is moved

into the center of the scintillator. At this fixed position we compare the signal amplitude measured from the base line to the peak minimum in the oscilloscope with the value seen in the QDC after subtracting the smallest peak representing the zero measurement called the pedestal from the QDC value.

The factor of Volts per QDC channel divided by the amplitude of a single photoelectron in Volts allows us then to convert the measured charge into an estimate of the amount of photons registered in each SiPM array on each side of the scintillator.

6.6 Data Processing

The QDC and TDC data of all three detectors is collected and saved in single `.root` files for each source position. Every position was held until a predetermined amount of trigger hits was registered or the set time had elapsed.

The setup delivers two independent measurements of each signal pulse, the event time and the pulse charge which is proportional to the amount of detected photons. These properties of the events are, as described above recorded with separate electronics and hence also processed individually.

6.6.1 The Charge Measurement

In order to determine the amount of measured photons the collected charge was measured. This charge corresponds to the amount of released photoelectrons which depend on the amount of photons that hit the SiPMs as explained in Chapter 4. The time window of this measurement is set by a gate signal determining for how long the charge will be collected before it is evaluated.

The charge is measured against a reference signal. Using a reference below the signal base line allows the electronics to capture the full signal, but also elevates the measured data by a fixed amount giving the measured data the appearance of sitting on a pedestal giving this phenomenon its name. The so-called pedestal can be seen in the charge distribution histogram as a narrow peak in front of the main data, sitting at the same level for every measurement. An example clearly showing the pedestal slightly above channel 100 in the QDC measurement can be seen in Figure 6.7. To receive the true charge value the pedestal has to be determined and subtracted for every measurement.

Excluding the pedestal the average detected charge is determined. This is done for both the left and right SiPM array individually. Using the calibration we gained in Section 6.5.3 we are able to convert QDC channels into detected photoelectrons. To evaluate the photon collection across the entire scintillator the arithmetic mean of the detected photoelectrons on both side 1 and side 2 can be calculated.

For comparability between measurements the determination of a single value for the average detected amount of photoelectrons across the entire scintillator is essential. This value is determined by adding the calculated mean amount of detected photoelectrons for every position to a histogram and fitting it with a Gaussian distribution. This reduces the influence of boundary effects along the

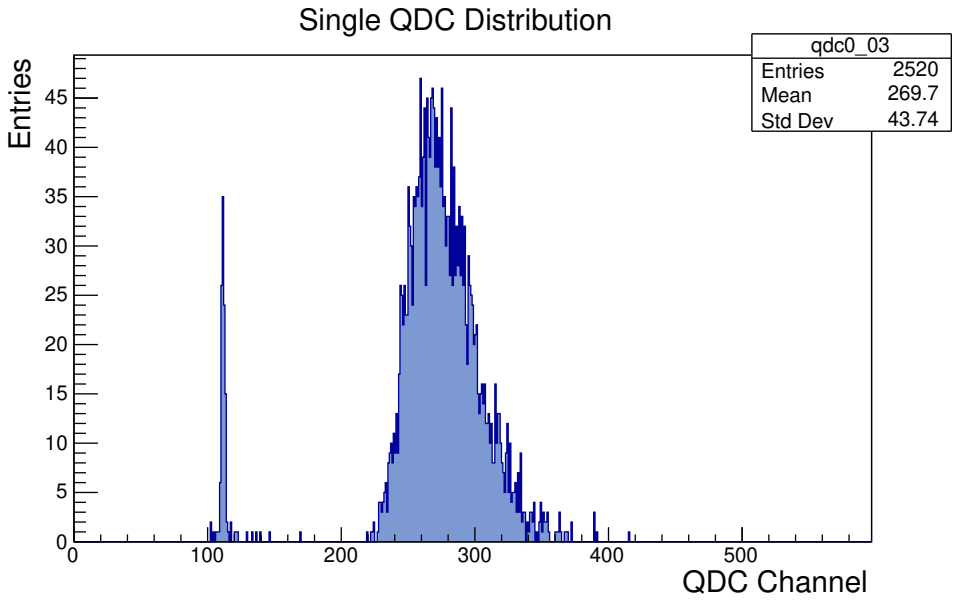

Figure 6.7: *Charge measurement histogram for a total of 2520 measurements including SiPM signals recorded with the QDC for a 5 mm thick scintillator at a single position. It clearly shows the pedestal around channel 110 and the detector signals above channel 200.*

outer edges of the scintillator where the amount of detected photons is low and unreliable.

6.6.2 The Timing Signal

A timing signal on its own holds little information. Only referenced against another related signal do we gain a grasp on the performance the detector system delivers. The trigger detector is only used to produce a signal for the DAQ and is not part of the following analysis since the timing properties of its signal are not optimized.

The only other signals at our disposal are the SiPM array signals left and right of the scintillator. So in order to determine the time resolution a distribution of the time difference, measured by subtracting the detected signal time of the SiPMs on the left and right side of the scintillator, is created. This distribution is expected to have a Gaussian form since the exact arrival time of the necessary amount of photons to cross the threshold depends on the random emission direction of the photons in the scintillator and the path they take before arriving at the SiPMs.

This distribution is then fitted with a Gaussian function. The parameter of interest in this context is the width of the distribution given by the standard deviation σ. This however gives us the time resolution of a convoluted system of both sides of our module and not of our module itself.

The measured time difference resolution (σ) depends on the individual resolutions of the left (σ_L) and right (σ_R) SiPM arrays. This relation can be easily derived

from Equation (6.6.1) via the propagation of uncertainty.

$$t_{diff} = t_L - t_R \tag{6.6.1}$$

$$\begin{aligned}\sigma_{diff} &= \sqrt{\left(\frac{\partial t_{diff}}{\partial t_L}\,\sigma_L\right)^2 + \left(\frac{\partial t_{diff}}{\partial t_R}\,\sigma_R\right)^2} \\ &= \sqrt{\sigma_L^2 + \sigma_R^2}\end{aligned} \tag{6.6.2}$$

Since the SiPMs used in the left and right array are identical we can assume that the time resolution of the left and right SiPM array are the same ($\sigma_L = \sigma_R = \sigma_{L/R}$). This allows us to simplify Equation (6.6.2) to

$$\sigma_{diff} = \sqrt{2}\,\sigma_{L/R}$$

and transform it into

$$\sigma_{L/R} = \frac{1}{\sqrt{2}}\,\sigma_{diff}\,. \tag{6.6.3}$$

In order to determine the timing resolution of the detector system, the way it is supposed to function in the experiment, we now however need to understand how the timing of an event in the module is determined. This is done by averaging the left and right SiPM signals of the module to receive a single event time (t_E).

$$t_E = \frac{1}{2}\,(t_L + t_R)$$

The time resolution of this setup can then be calculated as the propagation of uncertainty from the individual resolutions of the two SiPM arrays.

$$\begin{aligned}\sigma_E &= \sqrt{\left(\frac{\partial t_E}{\partial t_L}\,\sigma_L\right)^2 + \left(\frac{\partial t_E}{\partial t_R}\,\sigma_R\right)^2} \\ &= \sqrt{\left(\frac{1}{2}\,\sigma_L\right)^2 + \left(\frac{1}{2}\,\sigma_R\right)^2}\end{aligned} \tag{6.6.4}$$

Again assuming that the resolutions of the two sides are identical Equation (6.6.4) can be simplified to

$$\sigma_E = \frac{1}{\sqrt{2}}\,\sigma_{L/R}\,. \tag{6.6.5}$$

If we now substitute $\sigma_{L/R}$ in Equation (6.6.5) with the expression in Equation (6.6.3) we receive the statement

$$\sigma_E = \frac{1}{2}\,\sigma_{diff}\,. \tag{6.6.6}$$

This means that by halving the resolution of the time difference between the left and right side of the scintillator we receive the event time resolution we can expect from the module under normal operation. In this way all time resolutions

presented here if not otherwise specified relate to the normal operational time resolution.

Once this resolution has been calculated it is added to a plot with the x and y position of the source and trigger for this measurement as coordinates, showing the distribution of the achieved time resolution along the scintillator surface as shown in Figure 6.8 with the actual dimensions and position of the scintillator indicated by a dotted red line. The time resolution is color coded ranging from 40 ps in dark blue to 65 ps and all values above in yellow.

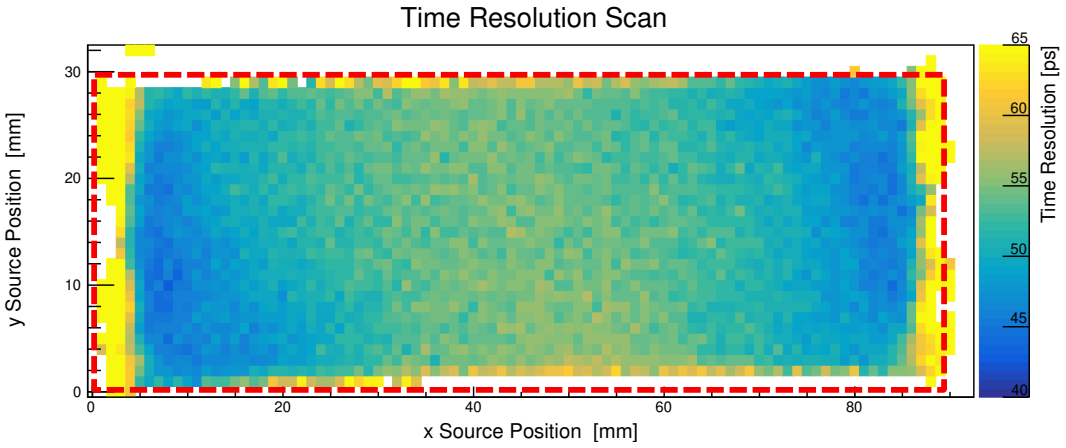

Figure 6.8: *Time resolution scan of a Mylar wrapped 5 mm thick scintillator along its surface. The scintillator dimensions are indicated by the dotted red line.*

Positions where less than 200 events were registered were left blank since such a low trigger count meant the electrons were for example being obstructed by the holding structure and not hitting the trigger correctly. This in any case only should be the case on the edges and around the scintillator and not in the area of interest. Additionally when the source and trigger are outside of the scintillator range the trigger count remains high but in the SiPM arrays attached to the scintillator the number of events with a charge above the pedestal remain low, since no electrons are passing through the scintillator any more and the electrons are hitting the trigger directly. To filter out such events any measurement with mean photoelectron count of less than 5 was cut.

In order to produce a single time resolution value that is easily comparable across measurements all determined time resolutions are added to a summary histogram. To exclude edge effects this distribution is then fitted by a Gaussian distribution giving us the mean time resolution of the entire scintillator.

6.7 Measurement Results

The value of interest in these measurements is the time resolution. In order to better understand this value we will also be looking at the amount of detected photons and the uniformity of the time resolution distribution across the scintillator surface. For completeness, using the acquired data we are also able to determine

the effective scintillator attenuation length and the position resolution of the B-ToF module for events along the x axis.

All measurements were done for multiple scintillators of varying thickness ranging from 3 mm to 6 mm increasing in 1 mm steps. In addition two variant of the 5 mm scintillator were studied. These however are discussed in sections 6.8 and 6.9.

6.7.1 Scintillator Efficiency

6.7.1.1 Expected Photon Yield

Particles traveling through a medium continually loose energy along the way depending on their energy at any given moment. This means they have a limited range depending on their initial kinetic energy. The continuous slowing down approximation (CSDA) range plotted in Figure 6.9 using data from the National Institute of Standards and Technology [61] shows how far electrons of various energies are expected to travel before coming to a stop. Not all emitted electrons however will have the necessary energy to travel through the B-ToF scintillator tile and produce a signal in the trigger scintillator. The necessary mean energy to traverse the scintillator tile of a given thickness ranges from 0.75 MeV for a 3 mm thick scintillator to 1.31 MeV for a 6 mm thick scintillator as seen on the right side of Figure 6.9. Excluding a large portion of the emitted electrons.

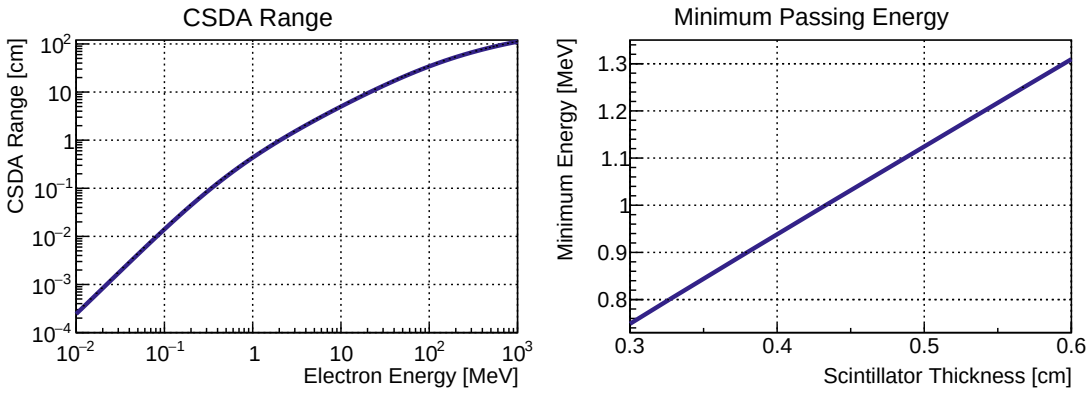

Figure 6.9: *The continuous slowing down approximation (CSDA) range for electrons in PVT on the left and the resulting minimum energy necessary to traverse a scintillator of given thickness on the right [61].*

Given the information in Section 6.4 and the scintillation efficiency η_{sc} of 8400 photons per 1 MeV, provided by Eljen Technology [59] we can get an estimate of the produced photons. The stopping power of PVT reaches its minimum at around 2 MeV, making the most energetic electrons emitted from the ^{90}Sr source minimum ionizing, depositing 0.56 MeV to 1.11 MeV for 3 mm to 6 mm thick scintillators [61]. Electrons with less kinetic energy are expected to deposit more energy per cm. The maximum amount of energy is deposited by electrons that loose all energy inside of the scintillator and basically fall out the other side. These electrons deposit the maximum energy of 0.75 MeV to 1.31 MeV.

Assuming all photons hitting the side of the scintillator on which the SiPMs are mounted that do not fall into a SiPM are lost, then the amount of detected photons is proportional to the ratio of active to dead area mentioned earlier in Section 6.2. In addition to that SiPMs also have a limited photon detection efficiency (PDE). The model used here only registers roughly 40 % of photons that hit the semiconductor [37]. Taking this information into account we can expect to see a wide range of produced photons per hit for ^{90}Sr electrons that take the shortest path through the scintillator.

The amount of photons that hit the sensors can be estimated by considering how much energy is deposited and how large the photosensors are. The deposited energy depends on the mean energy loss per path length ($\frac{\mathrm{d}E}{\mathrm{d}x}$) and can be calculated by (6.7.1).

$$E = x \cdot \frac{\mathrm{d}E}{\mathrm{d}x} \tag{6.7.1}$$

The amount of emitted photons depending on the scintillator efficiency η_{sc} then follows as

$$N_{\mathrm{ph}} = \eta_{\mathrm{sc}} \cdot E$$

Considering the loss of photons due to the insufficient coverage at the scintillator ends another geometric efficiency factor (η_{geo}) is added, giving us the effective amount of photons that should be hitting the SiPMs,

$$\begin{aligned} \eta_{\mathrm{geo}} &= \frac{A}{x \cdot b} \\ N_{\mathrm{eff}} &= \eta_{\mathrm{geo}} \cdot N_{\mathrm{ph}} \\ &= \frac{A}{x \cdot b} \cdot \eta_{\mathrm{sc}} \cdot x \cdot \frac{\mathrm{d}E}{\mathrm{d}x} \\ &= \frac{A}{b} \cdot \eta_{\mathrm{sc}} \cdot \frac{\mathrm{d}E}{\mathrm{d}x} \end{aligned} \tag{6.7.2}$$

with A being the surface area of the SiPMs attached to the scintillator surface and b being the width of the scintillator tile. As Equation (6.7.2) shows, the only influence the scintillator thickness has on the deposited energy is by filtering low energetic electrons. The resulting estimated photon distribution can be seen in Figure 6.10.

What the calculation above and the Figure 6.10 do not take into account however are losses inside of the scintillator either in form of absorption in the scintillator material or reflective losses at the PVT air boundary. In addition to that the expected photon count rate distribution does not reflect the fact that passing electrons need sufficient energy to produce enough photons for a detectable signal in the trigger scintillator, overestimating the amount of expected photons on the high end.

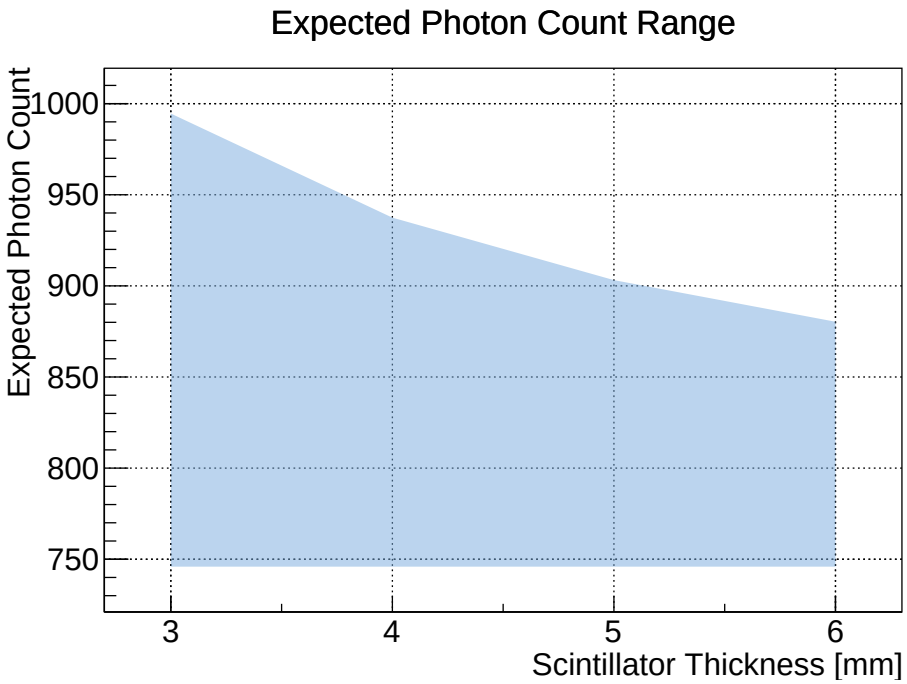

Figure 6.10: *The expected range of photons per passing ^{90}Sr electron.*

6.7.1.2 Measurements

Since the time resolution depends on the amount of collected photons the first thing to evaluate is the distribution of detected photoelectrons along the scintillator. Figure 6.11 shows the average photoelectron distribution along the x-axis as seen by one SiPM array on a 5 mm thick scintillator. The error bars refer to the standard deviation of all measurements along the y-axis. Along the y-axis the photoelectron count is very uniform except for about 7 mm to 18 mm in front of the SiPMs. There a large count increase falling off sharply towards the long edges to the level of the other positions all along the scintillator can be seen.

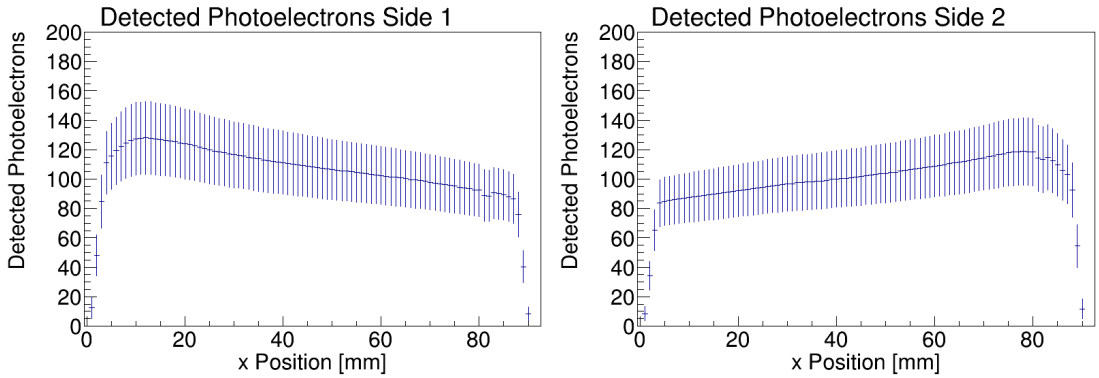

Figure 6.11: *Projection of detected photons along a 5 mm thick scintillator in the first (left) and second (right) SiPM array. Each point is the mean of all measured values along the y-axis for the respective x position, with the standard deviation as error bar.*

Surprisingly the amount of detected photons drops significantly for events 7 mm from or closer to the SiPMs right behind the peak of measured photoelectrons. This phenomenon has not been studied more closely, but one hypothesis is that events too close to the SiPM array produce photons that are hard to be picked up by SiPMs further away from the interaction due to the large incident angle that comes from being that close to the edge reducing the volume of the solid angle leading into each SiPM. More importantly however a large part of the solid angle of emitted photons will be lost in between the SiPMs as there is no reflective material present there and the incident angle of incoming photons is too small. This is supported by the fact that for events directly in front of a SiPM the photoelectron count rises significantly.

Looking at the profile of the entire distribution moving away from the relevant SiPMs a clear reduction of detected photons can be seen along the x-axis. These distributions also let us determine the effective attenuation length, the distance light has to travel to be reduced by a factor of $1/e$, of light inside the scintillator by fitting an exponential function

$$L(x) = L_0\, e^{-\frac{x}{\lambda}},$$

with λ being the attenuation length and L_0 the initial light intensity.

Since the scintillator dimensions are relatively small compared to the attenuation length of the scintillator the geometry will play a larger role. Scattering effects and reflections along the scintillator boundary prevent a determination of the true attenuation length. What we can measure is the effective attenuation length for the specific scintillator and its dimensions.

Photons emitted in the scintillator are not only absorbed in the material but are also lost at the scintillator boundaries. If their incident angle is larger than Brewster's Angle they are reflected back inside the scintillator (total reflection). In case of an incident angle smaller than Brewster's Angle we see a partial reflection where light is lost to the outside. To reduce these losses the scintillator is wrapped in reflective aluminized Mylar foil. Since the foil is not completely flat some light will be scattered backwards. For this reason we can expect a dependence of the attenuation length on the thickness of the scintillator tile since a thinner tile leads to more internal reflections before reaching the readout.

An example of the combined average photoelectron distribution calculated by taking the arithmetic mean of the photoelectron count of both sides is shown in Figure 6.12. In both directions along the x-axis we see a sharp drop off of the measured photoelectrons right in front of the SiPMs as we have seen in Figure 6.11. This effect is however rather negligible for the overall mean photon count. The depicted distribution for example shows a mean of 106.3 photoelectrons with a standard deviation of all involved data points across the scintillator of 5.5 photoelectrons.

The photoelectron count and attenuation length measurements performed as descried earlier are summarized for all scintillators in Figure 6.13. The mean amount of detected photoelectrons, plotted in the left image, shows a clear increase in the amount of photons that reach the SiPMs and are detected for 3 mm to 5 mm thick scintillators.

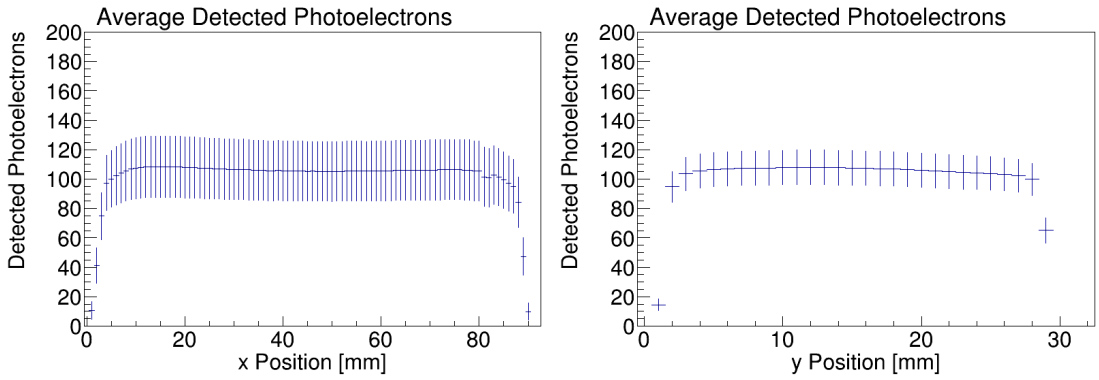

Figure 6.12: *Projection of the average detected amount of photoelectrons along the x or y axis of the scintillator, averaging multiple values into one point, plotted along the respective other axis. The error bars represent the standard deviation.*

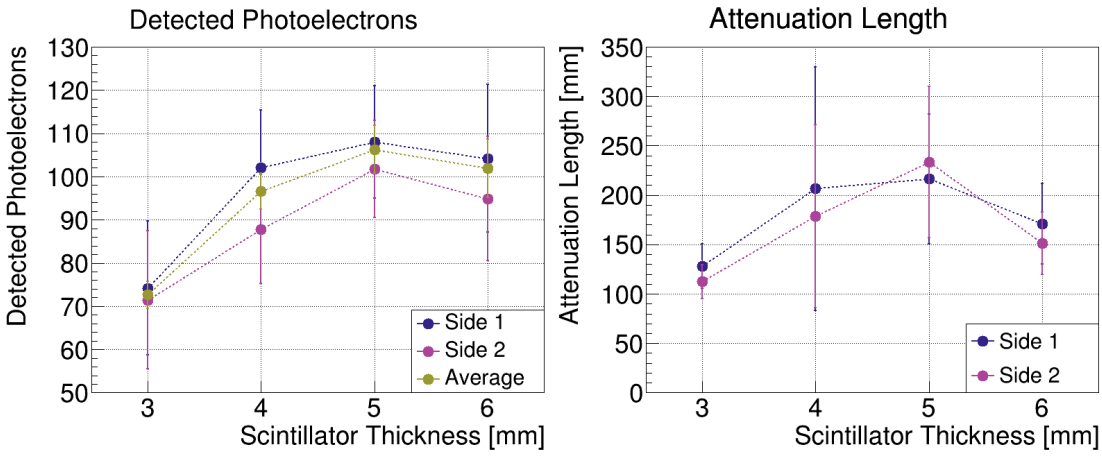

Figure 6.13: *The left figure depicts the measured photoelectrons for the studied scintillator thicknesses. The right figure shows the effective attenuation length of those scintillators.*

This effect however is reversed going from 5 mm to 6 mm. What we can observe here is the overlay of multiple effects. Firstly one can expect that the more material has to be traversed the more energy is deposited and that consequently more photons are created and hence detected. This as shown above is not the case, at least for higher energy electrons. For lower energy electrons the trend of the expected amount of photons is even reversed, increasing as the geometric efficiency of the readout improves although less photons are produced.

Not considered here is the energy distribution of the emitted electrons but a general trend can be determined none the less. On the energetical high end the amount of detected photons is the same for all tile thicknesses. Only moving towards thinner scintillators, less energetic electrons manage to produce a signal in the trigger scintillator which produce more detectable photons, increasing the average amount of detected photons.

Secondly though the amount of internal reflections is proportional to the thickness of the tile meaning a 3 mm thick scintillator will produce twice the amount of reflections a 6 mm scintillator does. As the trajectory length from interaction point to the readout also is thickness independent the reflection losses remain as the only main explanation of the drop in detected photons towards thinner scintillators. At 6 mm the significant loss in geometric efficiency of the readout appears to outweigh the benefits of reduced reflections, causing a decrease in photoelectron count.

Noticeable when comparing the expected with the measured photoelectrons is the disparity between the order of magnitude between them. Trusting in the calibration one sees roughly 10 % of the expected photons. Looking at the photon distribution along the x axis shown in Figure 6.11 one only sees a fraction of the photoelectrons. Even close to the SiPMs where attenuation and reflection losses should be almost negligibly small, the photon count is less that 20 % of what is expected. Either the calibration, which clearly is not perfect since side 1 consistently reports more detected photons compared to side 2, was not done correctly or another undiscovered effect is at play here.

The measured effective attenuation length depicted on the right side of Figure 6.13 with the fit errors as the error bars, seems to follow roughly the same pattern, rising from 3 mm to 5 mm and then dropping for 6 mm. All determined attenuation length fits show values within 2σ of each other around the standard attenuation length of (17 ± 1) cm. The large error bars prevents the determination of a clear trend. Noteworthy however is the similar but independently determined behavior of the values for the left and right side.

This rise and drop is again due to two competing phenomena. On the one hand photons traveling inside of a thinner tile on average undergo more internal reflections before they reach the readout potentially loosing photons each time they reflect on the surface boundary. Increasing the thickness reduces the amount of experienced reflections before reaching the SiPMs leading to a decreased photon loss along the way. On the other hand it however decreases the chance of an incoming photon to be registered in a SiPM since the growing length disparity of the SiPM edge length to the length of the side of the scintillator decreases the efficiency. If a photon reaching the end of the scintillator is not lost to the outside

it is internally reflected all the way back to the other side where it might be picked up by the other SiPMs. This effectively increases the total trajectory length of the average photon presenting increased opportunity of absorption which appears to take over after a thickness of 5 mm. The trajectory length from an interaction point to the readout side of the scintillator otherwise for the same emission angle stays the same.

6.7.2 Time Resolution

The time resolution profile follows a similar pattern as the photoelectron distribution. As expected from Section 4.1.2.4 the best time resolution of the scintillator can be found where the most photoelectrons are detected. This is about 0.7 mm in front of the SiPMs on both sides. The distribution also reveals a slight drop in the middle of the tile. Figure 6.14 shows the correlation of detected photoelectrons to the time resolution with the amount of photoelectrons on the horizontal axis and the time resolution in the vertical. A clear time resolution reduction for an increased detection efficiency can be seen.

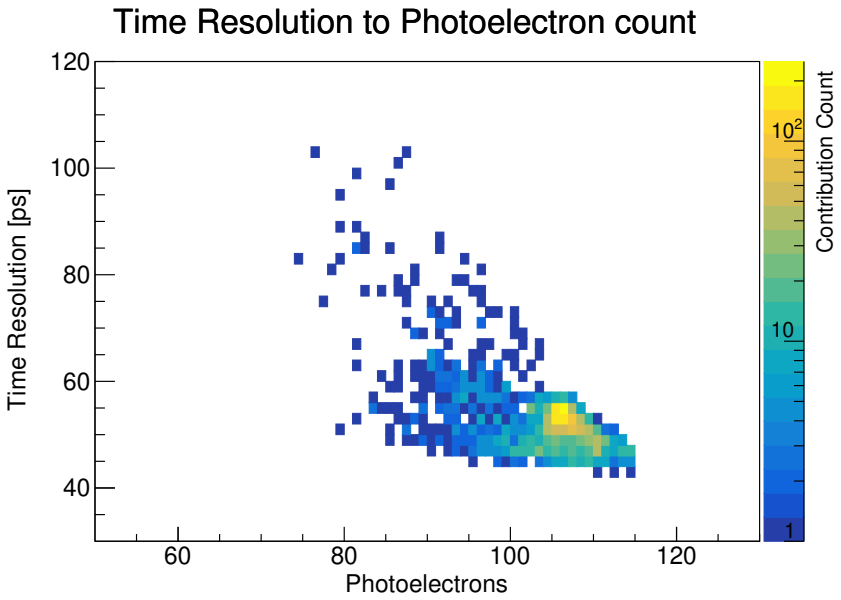

Figure 6.14: *Distribution showing the correlation of the time resolution to the amount of detected photoelectrons.*

Following the same narrative the time resolution on the edges of the scintillator and immediately in front of the SiPMs as seen in Figure 6.8, shows the worst time resolution going above 65 ps. These regions are where the photoelectron count was the lowest.

The mean time resolutions the studied scintillators achieved in the study are shown in Figure 6.15. The error bars in this plot are the standard deviation of the overall time resolution distribution as described in Section 6.6.2. The figure shows a clear improvement of the time resolution for 5 mm and 6 mm thick

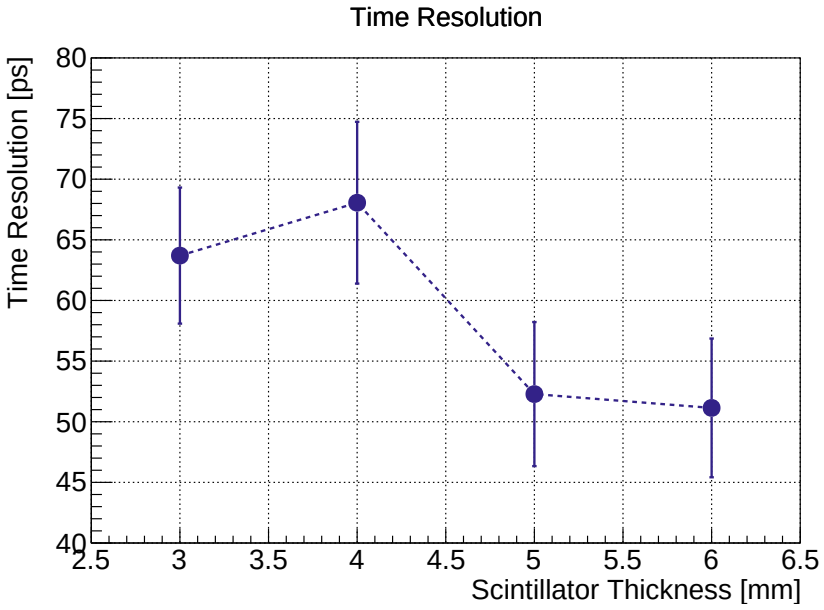

Figure 6.15: *Time resolution comparison of the studied scintillator thicknesses. The error bars are the standard deviation of the overall time resolution distribution.*

scintillators with (52.3 ± 5.9) ps and (51.1 ± 5.7) ps over 3 mm and 4 mm thick tiles with (63.7 ± 5.6) ps and (68.1 ± 6.7) ps. Apart from the 4 mm scintillator the time resolution improves with increased thickness. The 6 mm scintillator however only showing a marginal improvement over the 5 mm thick scintillator tile.

The time resolution distribution of the studied scintillators is shown for 3 mm, 4 mm, 5 mm and 6 mm thick tiles in this order from top to bottom in Figure 6.16. Judging by the color the results in Figure 6.15, the large performance gap between the 3 mm and 4 mm to the 5 mm and 6 mm thick scintillators can be confirmed. All distributions also show a similar degree of homogeneity with worse performance in the middle of the tile improving towards the SiPMs.

Apart from the 4 mm thick scintillator a trend of improvement for scintillators with growing thickness can be seen. The reverse behavior for the 4 mm scintillator seems out of the ordinary and does not fit to the expected correlation of detected photoelectrons and the time resolution.

6.7.3 Position Resolution

As explained in Section 6.6.2 the time resolution is determined by evaluating the variance in the time difference for a single event to be picked up on both sides of the scintillator. The exact time difference is irrelevant for the time resolution. However when compared over the entire scintillator surface one sees a distinct position dependence of this time difference moving along the x axis since while the distance to one scintillator side is decreased it grows for the other. This can bee seen in Figure 6.17 showing an example distribution for a 5 mm thick scintillator tile. For events in the middle of the scintillator a perfectly calibrated system would have no time difference and symmetrically increasing absolute values towards the

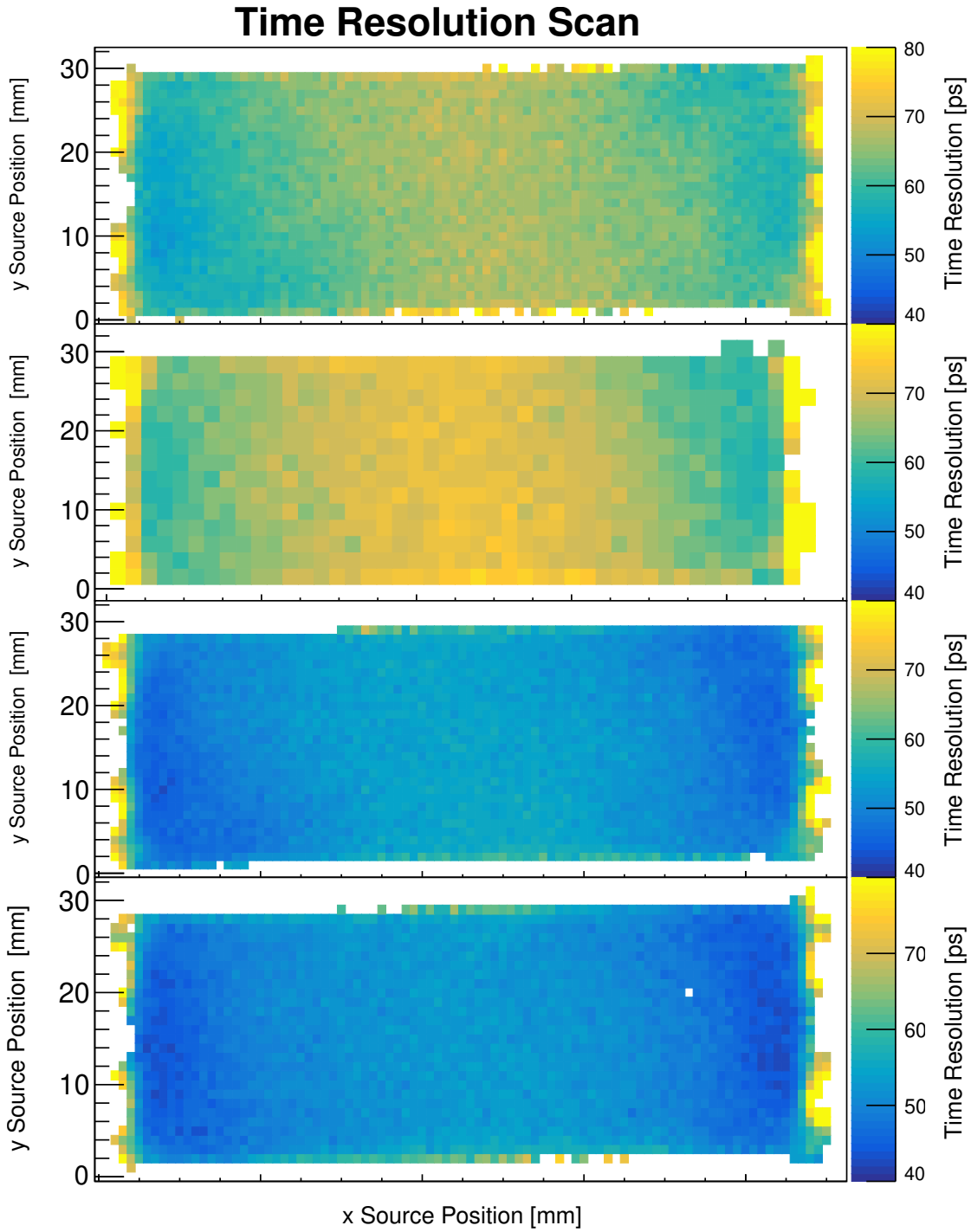

Figure 6.16: *Comparison of the time resolution distribution of 3 mm to 6 mm thick scintillator tiles in that order from top to bottom. Each image uses the same time resolution color scale from 40 ps to 80 ps.*

outer edges. Since cable lengths are not accounted for here a constant delay term pushes the time difference below 0. This does not have an effect on the slope since this delay is constant between all measurements.

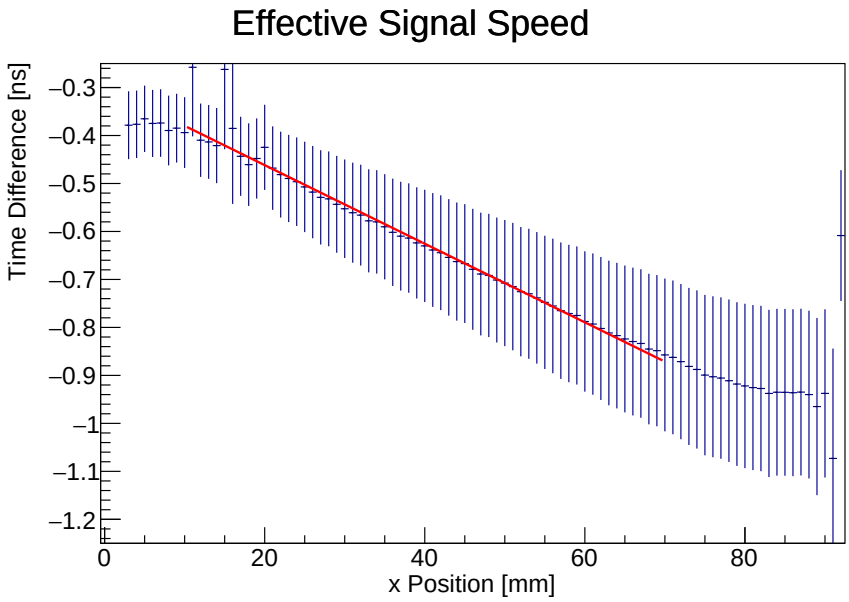

Figure 6.17: *The mean time difference depends on the event position along the x axis.*

The slope of this distribution equates to the effective signal speed inside of the scintillator tile, the time necessary for a signal to travel a fixed distance and be detected by the SiPMs. For the example above we measured an inverted signal speed, by applying a fit with a linear function, of 8.2 ps/mm or 0.12 mm/ps, considerably slower than the speed of light inside of the PVT scintillator material at 0.19 mm/ps. This slower effective speed can be attributed to a combination of two things. Firstly, an event is not registered until a certain amount of photons have reached the SiPMs determined by the discriminator threshold. Secondly, to surpass the threshold many photons from different trajectories have to trigger a signal in one of the SiPMs.

Only a small fraction of the photons reach the SiPMs on a straight line. Most photons will have been reflected at least once and taken a considerably longer path compared to the direct trajectory. In addition to that the events timing is determined by the n^{th} photon that pushes the SiPM signal above the threshold and not the first. Chance dictates that this photon will not have taken the shortest route to the SiPMs but have been reflected, increasing the necessary time of flight and hence reducing the effective signal speed. A speed reduction as observed above would be due to 19 and more internal reflections.

Using the information above, given a sufficient time resolution, we can calculate the position of an event along the x axis from the time difference (t_{diff}) of the SiPM signals we see from the left and right scintillator sides (t_1, t_2), as long as our system

is calibrated. The position can be expressed as

$$\begin{aligned} x(t_1, t_2) &= m\,(t_1 - t_2 + t_0) \\ x(t_{\text{diff}}) &= m \quad t_{\text{diff}} \quad + x_{t_0} \end{aligned} \tag{6.7.3}$$

with m being the slope or the effective signal speed and t_0 being a calibration term or the offset, ideally equal to zero.

To determine the resolution of these calculations the time resolution needs to be considered. Looking at the propagation of errors we receive

$$\Delta x = \sqrt{(t_{\text{diff}}\,\Delta m)^2 + (m\,\sigma_{\text{diff}})^2}$$

and by substituting σ_{diff} as shown by (6.6.6) we receive

$$\Delta x = \sqrt{(t_{\text{diff}}\,\Delta m)^2 + (m\,2\sigma_E)^2} \tag{6.7.4}$$

for the position resolution.

For the mentioned 5 mm scintillator this equates to a position resolution of 12.8 mm, resulting in considerable accuracy of the estimation along the entire scintillator surface. For events close to the SiPMs however the resolution worsens as the time difference distribution loses its linearity towards the edges.

Comparing the effective signal speed of all scintillator tiles as seen in Figure 6.18, we see a strong correlation to the time resolution distribution seen in Figure 6.15. The 4 mm thick scintillator again shows an effective signal speed well worse than the other tiles with an error twice as large as the next worse signal speed.

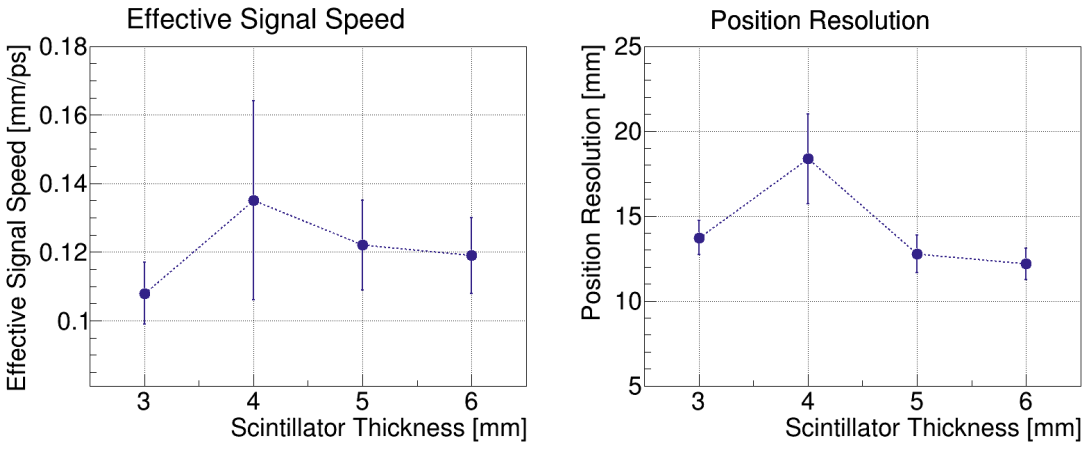

Figure 6.18: *The left image shows the effective signal speed as a function of the scintillator tile thickness. The right image depicts the position resolution resulting from the effective signal speed and the time resolution.*

This consequently results in a similar distribution for the position resolution which depends on the effective speed and time resolution as described in equation (6.7.4). Yet again the position resolution of the 4 mm scintillator raises concerns.

6.8 Polished Scintillator

Plastic scintillator material is very sensitive. Manipulating the surface by cutting a slab from a larger block or improper handling of the surface can lead to damaged scintillators. Although they look fine initially over time these pieces then develop cracks and produce an opaque surface, reducing the photon yield of any detector.

To avoid this the detector slabs were cast as large tiles in the wanted thickness and then carefully cut out to our specification. This process on the other hand however introduces large tolerances on the produced thickness of the scintillator. Eljen Technology produces 5 mm sheets with self claimed tolerances of $(+0.56/-0.46)$mm in a sheet size of $60 \times 101\,\mathrm{mm}^2$ [62]. This corresponds to an almost 20 % difference from minimum to maximum. These large variances might produce ill performing detector tiles.

To study the influence of careful machining and the large tolerances, one scintillator was cast as a 6 mm tile and then carefully polished down to 5 mm by G-Tech, Corp. the representative company of Eljen Technology in Japan. This scintillator now can be compared to the 5 mm cast scintillator discussed in previous sections.

The following tables show the measured data for both the polished (EJ-232) as well as the unpolished (EJ-232 P) scintillator. Table 6.1 lists the mean number of detected photoelectrons and the attenuation length each for both sides, all relevant information concerning the detected photoelectrons. Table 6.2 shows the measured time resolution as well as the effective signal speed and the resulting position resolution.

Table 6.1: *Comparison of photon yield measurements of the polished and casted 5 mm thick EJ-232 scintillators.*

	Photoelectrons						Attenuation Length [mm]			
	1		2		Average		1		2	
EJ-232	108	± 13	102	± 11	106.3	± 5.5	216	± 66	234	± 77
EJ-232 P	104	± 17	99	± 17	101.4	± 6.1	153	± 32	139	± 26

Table 6.2: *Comparison of timing measurements of the polished and casted 5 mm thick EJ-232 scintillators.*

	Time Resolution [ps]		Effective Signal Speed [mm/ps]		Position Resolution [mm]	
EJ-232	52.3	± 5.9	0.122	± 0.013	12.8	± 1.1
EJ-232 P	51.8	± 5.1	0.110	± 0.010	11.4	± 1.1

Contrary to the concerns that the scintillator will suffer from a potential degradation of its surface, no significant or relevant difference in performance could be established at this time. Long term degradation of the polished surface however can not be entirely excluded. All measurements are well within the margin of error

of each other. The only value that shows a prominent difference is the effective attenuation length for both the left and right side. Since the scintillators however are well within both determined values and the time resolution is within 0.5 ps of each other it appears not to have an effect on the performance of the B-ToF.

6.9 Quenched Scintillator

As mentioned previously Eljen Technology produces a variant of their EJ-232 scintillator designed for applications that necessitate the best time resolution possible with an added quenching agent, the EJ-232Q. By adding Benzophenone in this case 0.5 % the detection efficiency is reduced. This has no effect on the emission spectrum but lowers the rise time by 240 ps to 110 ps, the decay time by 0.9 ns to 0.7 ns and the pulse width by 940 ps to 360 ps [59]. This should improve the time resolution for certain measurements, especially when using it for small detectors. Since less photons are produced scintillators of larger geometries with increased losses will suffer more from this. Whether deployment in our detector makes sense will be studied in this section.

To compare the measurements of the standard 5 mm thick EJ-232 scintillator to its quenched variant the EJ-232Q, all determined values are listed in the tables 6.3 and 6.4. The tables list the data concerning the detected photoelectrons in Table 6.3 showing the amount of detected photoelectrons per event and the effective attenuation length along the x-axis and data concerning timing such as the time resolution, the effective signal speed and the resulting position resolution in Table 6.4.

Table 6.3: *Comparison of photon yield measurements of the 5 mm thick EJ-232 scintillator and its quenched variant.*

	Photoelectrons						Attenuation Length [mm]			
	1		2		Average		1		2	
EJ-232	108	± 13	102	± 11	106.3	± 5.5	216	± 66	234	± 77
EJ-232Q	74	± 16	71	± 16	72.8	± 3.1	128	± 22	112	± 17

Table 6.4: *Comparison of timing measurements of the 5 mm thick EJ-232 scintillator and its quenched variant.*

	Time Resolution [ps]		Effective Signal Speed [mm/ps]		Position Resolution [mm]	
EJ-232	52.3	± 5.9	0.122	± 0.013	12.8	± 1.1
EJ-232Q	63.7	± 5.6	0.108	± 0.009	13.7	± 1.2

Looking at Table 6.3 one clearly sees the effects of the reduced detection efficiency. Less photoelectrons are registered on both sides of the scintillator. The attenuation

length which is not specified by Eljen Technologies seems to be affected too since the geometry is the same but the effective attenuation length shows a significant reduction by a mean 46 %.

This reduction in photoelectron count clearly outweighs any improvement the reduced decay time and pulse width might yield as the measured mean time resolution as shown in Table 6.4 is reduced to 63.7 ps, 22 % worse than the regular EJ-232 scintillator.

6.10 Discussion and Conclusion

The measurements of the photoelectron count as well as the time resolution and the resulting position resolution all support the initial 5 mm scintillator design as described in the TDR. Although the results show a marginal superiority of the 6 mm thick scintillator in time and position resolution the pressure to keep the material budget low and the space constraints of the design favor the thinner equally well performing tile.

Looking at the correlation of the amount of detected photons to the time resolution the link between the two can not be established as a dominating determinator for a tiles performance given geometric differences. Moving from 5 mm to 6 mm a drop in detected photoelectrons was measured while the time resolution improves. The increase in thickness and consequent decrease in the amount of reflections and scattering effects appears to benefit the time resolution more than the slight decrease in photoelectron count.

The attenuation length determined for all studied tiles is a property that certainly needs to be taken into account when designing a detector but study shows it is not essential to determining the performance of the setup since although we see a drop in the attenuation length from 5 mm to 6 mm the opposite is the case for the time resolution.

Throughout all measurements involving timing, the 4 mm thick scintillator showed the worst performance. This was not only the case for the measurement set presented here but also in a preliminary measurement of the same tile. The 4 mm thick scintillator presented the worst time resolution of all measured tiles as well as the fastest effective signal speed. The reason for this behavior is not clear. It is not due to a bad connection between the scintillator and the SiPMs since the photon count and distribution shows no sign of a connection issue. Apart from that the same equipment, namely the same SiPM arrays as well as the same preamplifier and readout system, were used. The most likely explanation at this point is that since the tiles were all cast in different thicknesses and are not part of the same batch, the tile might have been compromised. In order to determine whether the reason for this bad timing behavior is due to a bad scintillator or a geometrical issue, separate tests repeating these measurements for multiple tiles are necessary.

The achieved x-axis position resolution of (12.8 ± 1.1) mm means that the B-ToF is able to determine the position of an event with a higher resolution along its long axis than along the shorter y-axis, as there is no possibility to estimate the events

y position making any point along the 29.4 mm long side a possible interaction point.

The studies also showed that no significant difference in performance could be found between polished and cast scintillator tiles of 5 mm thickness at this time. Both show results within the margin of error of the other. In order to exclude long term surface degradation effects often seen for manipulated scintillators, followup measurements would be necessary. Regardless, since the measurements do not show an influence of the potentially inconsistent tile thickness it could be shown that polishing is not necessary. The measurement however showed that, since the only significant difference was the attenuation length, the accuracy of those result are questionable and should not be taken for granted.

The investigation of the quenched scintillator material concluded that the geometry of the tiles designed for the B-ToF is too large to benefit from the reduced scintillator efficiency and improved decay time and pulse width. This can be attributed to the photon yield which is significantly reduced and the measured reduction of the attenuation length for the quenched scintillator.

Overall this analysis concludes that a 5 mm scintillator produces the best result given the limitations on geometry and material budget the $\overline{\text{P}}$ANDA experiment demands. To improve the overall weight of these results a study not limited to measurements of a single tile per thickness would be necessary, especially to confirm the results acquired for the 4 mm thick scintillator.

Chapter 7

Beam Test at CERN T9

7.1 Introduction

Together with prototypes for the Barrel DIRC and Disc DIRC, data for the B-ToF was taken in July and August of 2018 at the T9 beam line of the East Area at CERN. This data serves as the base for the following analysis.

The T9 beamline provides secondary particles from a 24 GeV proton beam shot on a target, with a momentum in the range of 1 GeV/c to 15 GeV/c [63]. The main objective of the experiment was dedicated to the DIRC prototypes and not the B-ToF, which defined the used beam momentum and irradiation schedule.

The goal for the B-ToF was to test the detector performance close to $\overline{\text{P}}$ANDA experimental conditions using a wide array of particles of different energies, examining the timing performance of different SiPM manufacturers, the influence of the number of series connected SiPMs as well as the impact of the particles incident angle on the time resolution.

All tests were performed with positively charged particles from the electron enriched target. The particle mix of the beam depends on the used target, the magnet settings as well as the beam momentum. It contains mainly protons, pions and kaons in addition to a growing fraction of positrons towards lower beam momenta. At medium momenta pions make up the majority of particles. Beyond 6.3 GeV/c the proton content starts to dominate. The momentum dependent composition, up to 10 GeV/c can be seen in Figure 7.1. The muons are not shown.

7.2 Experimental Setup

All detector systems were placed along the beam in the main hall of the T9 beamline. The ToF system, which is subject of this thesis, consists of two stations, (28.64 ± 0.05) m apart, with separate aluminum box housings for every detector as shown in Figure 7.2. Two boxes, with one B-ToF and one MCP-PMT each, make up the first ToF station (*TOF1*). The second station (*TOF2*) was set up identically with a third B-ToF module. As can be seen in Figure 7.3 depicting the TOF stations, all the housings of the ToF stations were simply held down by clamps, for an easy change of the incident angle (α) of the beam through the scintillator of the B-ToF modules. and the particles paths through the material.

All other involved detector systems, shown in Figure 7.4 and 7.5 were setup in between the ToF stations. The first MCP-PMT and B-ToF module, which were

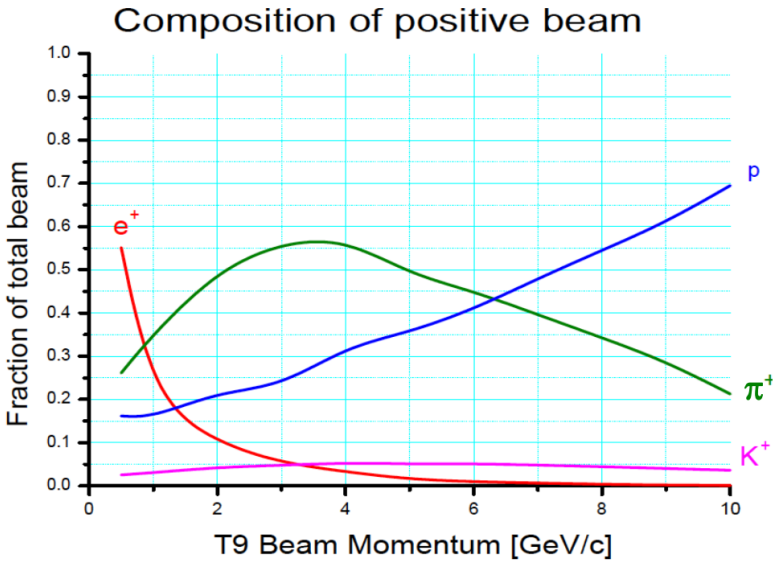

Figure 7.1: *Composition of the positive charged beam of the T9 beam line using the electron enriched target. The used hadron target produces a profile where electron component of the beam is strongly reduced [64].*

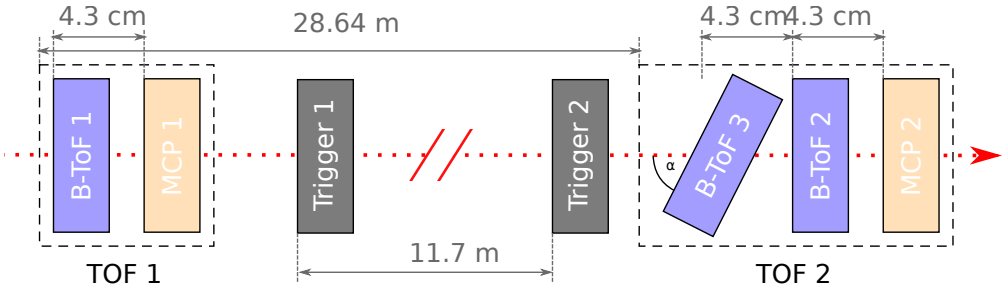

Figure 7.2: *Positioning of the time-of-flight detectors, consisting of B-ToF modules and MCP-PMTs in the* TOF *stations along the beamline. The trigger counters are placed between the TOF stations.*

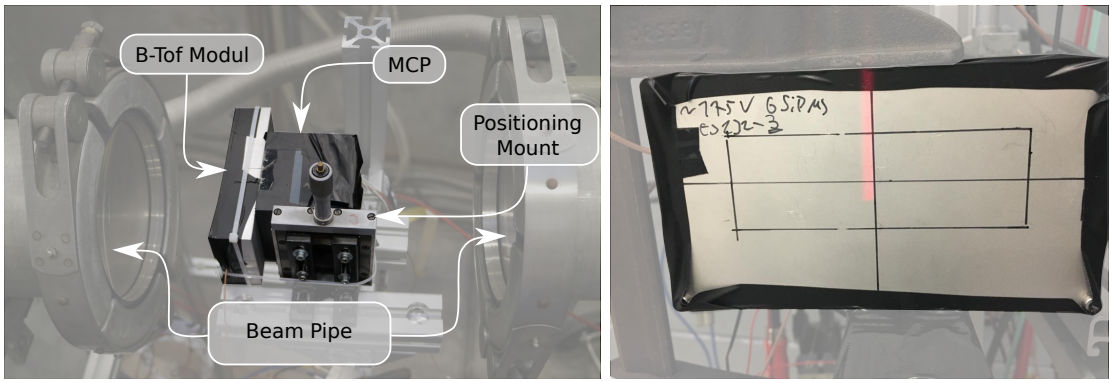

Figure 7.3: *The* left *image depicts the ToF Station 1* `(TOF 1)`*, positioned in a gap in the beam pipes 20 m in front of the rest of the setup. The* right *image shows one of the B-ToF modules of ToF station 2* `(TOF 2)`*.*

set up in a separate room, in a gap in the beam line pipes, are the first detectors of the experiment.

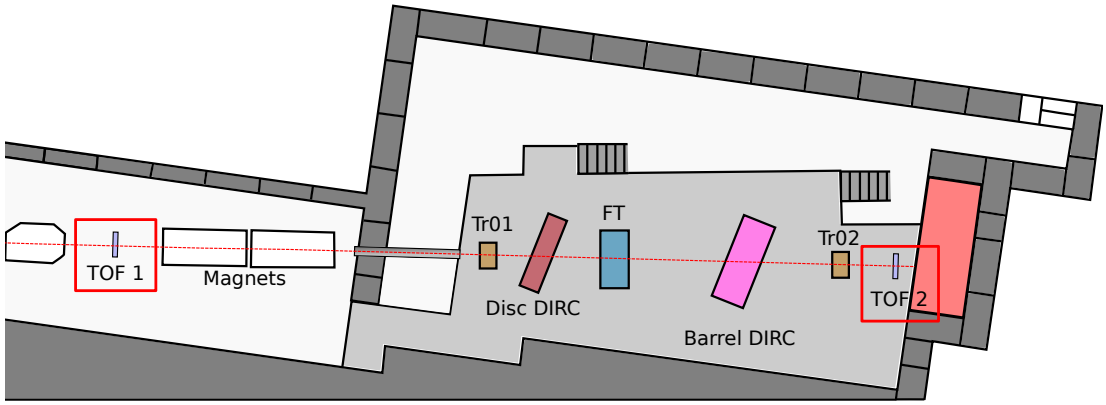

Figure 7.4: *Schematic view of the T9 beamline and hall, and the tested* $\overline{\text{P}}$ANDA *subsystems. It shows the* TOF 1&2 *stations, comprising B-ToF scintillator modules and MCP-PMTs, the* Disc *and* Barrel DIRC *prototypes, the* fiber tracker (FT) *and the* trigger counters *(*Tr01 *and* Tr02*) for the DAQ.*

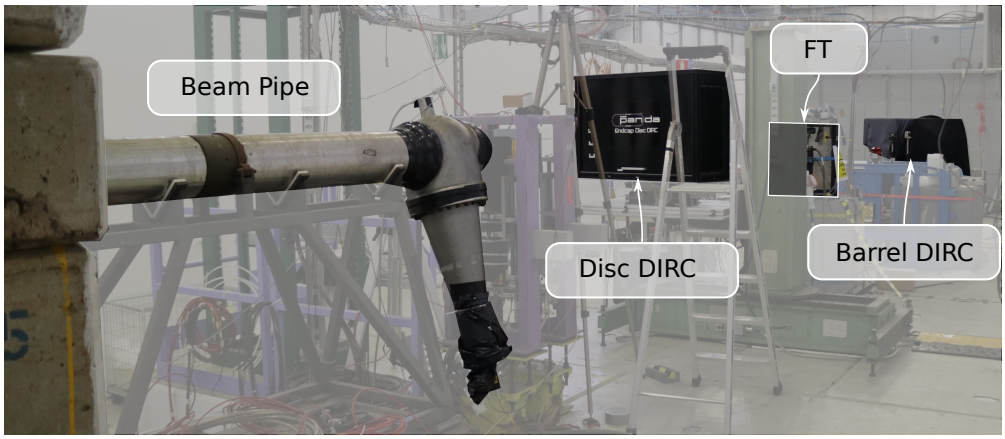

Figure 7.5: *The main setup of the DIRC groups as seen in the previous schematic, set in between our detectors.*

A *trigger (TR01)* was placed farther down the beam line consisting of a scintillator with a PMT. The second trigger counter *trigger (TR02)* was positioned in front of the TOF 2 station. Following the trigger the *Disc DIRC prototype*, a detector mostly made up of a plane of synthetic fused silica, a high quality glass plate 20 mm thick, read out by MCP-PMTs [14], was located. It was followed by the *fiber tracker (FT)*, a small device with scintillating fibers aligned vertically and horizontally, to check the beam profile and alignment of all systems. The *Barrel DIRC prototype* was the next detector along the beam line. Similar to the Disc DIRC it is made out of 17 mm thick fused silica rods that are again read out by MCP-PMTs [13]. A common readout was used for all the detectors, consisting of synchronized PaDiWa and TRBv3 boards, which together make a multi purpose time-to-digital data acquisition (DAQ) system developed at GSI [65]. The setups schematic is

shown in Figure 7.6. The detector signals are amplified and processed by the 16 channel PaDiWa 1 discriminator board. If coincident with both trigger signals the produced timing signals are then processed in the TDCs of the FPGA-based TRBv3 boards, where rough pulse height information is measured by determining the time-over-threshold (ToT).

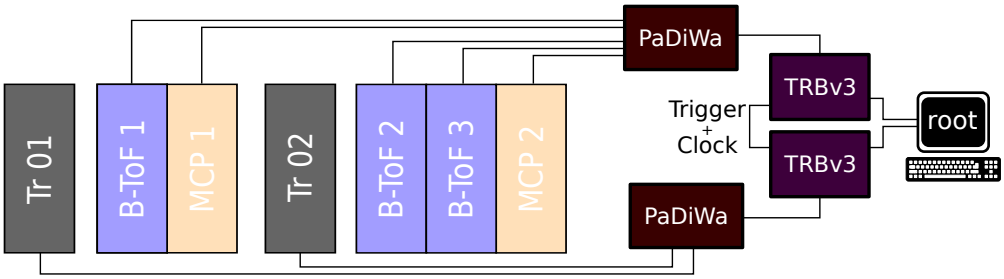

Figure 7.6: *Detector readout scheme using the PaDiWa and TRB boards.*

The SiPMs used for the detector modules were the Hamamatsu `S13360-3050PE` with a cell size of 50 µm in the B-ToF 1 module, the Ketek `PM3350` with a cell size of 50 µm in the B-ToF 2 module and the AdvanSiD `ASD-NUV3S-P` with a cell size of 40 µm in the B-ToF 3 module. All SiPMs had a sensitive are of $3 \times 3\,\mathrm{mm}^2$. The MCP-PMTs were `PLANACON XP85112` by Photonis. These were sensors with an edge length of 53 mm [66]. They were attached to acrylic glass as a radiator material and positioned with the sensitive side towards the beam.

7.3 Procedure

Data is taken over multiple days. Measurements with beam momenta from 1.5 GeV/c to 10 GeV/c increasing from 2 in integer steps were taken with regular momentum changes between runs. Data for beam momenta below 3 GeV/c or at 10 GeV/c are not included in the analysis. These runs show either a lack of statistics or too little separation between protons and pions to reliably determine the ToF difference.

The momentum resolution of the beam can be influenced via a dedicated collimator. A wider slit of the collimator lets more particles pass, increasing the particle current, allowing an experiment to collect more data in a shorter amount of time. Decreasing the slit's width narrows the acceptance of the beam, leading to a higher momentum accuracy at the cost of statistics. Throughout the data taking period the collimator was set to either ±5 mm or 10 mm. However, only data for the former setting are discussed in the analysis.

Particle timing measurements were performed throughout the beamtime for all measurement runs. The only setup changes of the B-ToF were swapping the SiPM array and the B-ToF angle for some measurements described in sections 7.5.1 and 7.5.2.

The radiation program of the DIRC groups includes studying their detector response under multiple incident angles. For this reason most measurements with consecutive runs at a constant beam momentum were performed for angle scans

for the DIRC prototypes. For this they were turned regularly throughout the data taking. Although this has a small influence on scattering effects in between the TOF stations, due to a lack of coherent measurement runs this change was not considered in the analysis.

7.4 Data Analysis

Since multiple runs with identical B-ToF but different DIRC settings were performed, longer consecutive runs and runs performed towards the end of the beam time were prioritized and selected for analysis.

The position of the passing particles can not be entirely controlled, so measuring the time resolution of the left and right sensor arrays of a single device will not deliver accurate results. Position resolution measurements descried in Section 6.7.3 show a large position dependence of the timing signals. For this reason timing differences between detector modules will be analyzed.

7.4.1 Data Preparation

If a detector produces a signal above the discriminator threshold it is considered a hit. All detector hits are equipped with a time stamp relative to the trigger. Depending on the distance of the trigger detector to the other detector and the length of the cables used to connect them to the DAQ, a certain time window for the signals can be expected. Due to an element added to the DAQ for the DIRC readout signal reflections are observed, manifesting as periodic peaks in the event timing distribution which have to excluded by applying proper cuts. The distribution of the timing signals measured on the leading edge can be seen in Figure 7.7 with a width of 13 ns to 14 ns corresponding to the beam bunch size. Figure 7.8 shows the reflections in a zoomed out view.

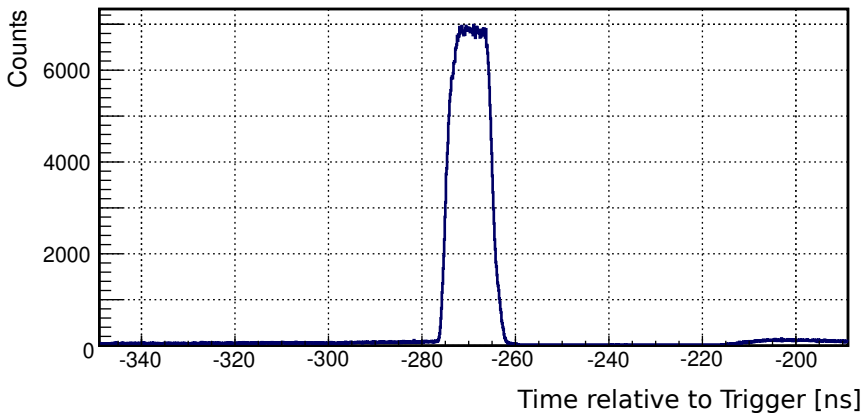

Figure 7.7: *Timing signal distribution histogram of a run at 6 GeV/c.*

After the individual time cuts 10 ns before and after the mean of the first peak in the distribution in Figure 7.8 are applied the time resolution of each

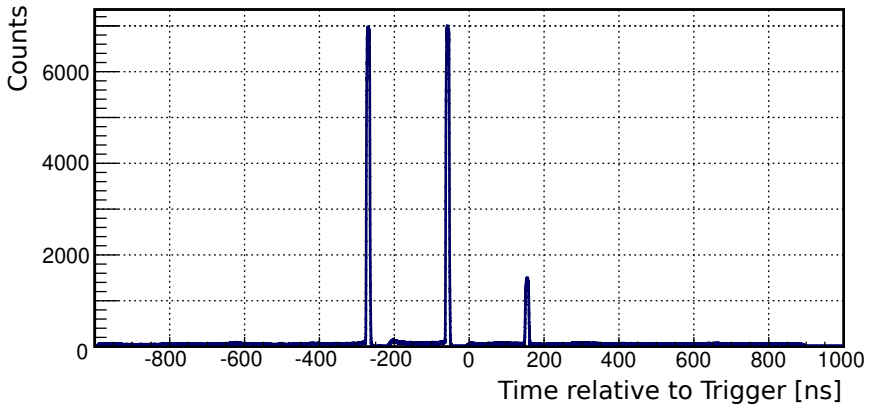

Figure 7.8: *This image depicts broader view of the previous distribution and reveals the reflections of the primary signal.*

measurement can be determined. The resolution can only be determined in relation to another timing signal provided by one of the other ToF stations. This gives us ten combinations of the three B-ToF modules and two MCP-PMT modules for which we can measure combined or convoluted time resolutions.

Events are saved in several runs as packets containing all associated detector hits and time stamps. If within such a packet two or more detectors show a hit, the respective time difference is calculated. This is the time-of-flight from one detector to the other. Depending on the beam momentum and distance between the involved detectors the ToF distribution will show multiple peaks for various particles contained in the beam. Particles with similar mass, will be harder to distinguish than particles with a larger mass difference as their velocity will differ more at the same momentum. The distribution of the ToF measurement between the first and second B-ToF modules, at a beam momentum of 6 GeV/c is shown in Figure 7.9.

The absolute uncalibrated time-of-flight value as used in Figure 7.9 is of little significance since cable lengths are not accounted for which give this measurement a constant unknown offset. To receive the true time-of-flight the detectors would need to be calibrated by measuring a signal simultaneously, in order to know the influence of e.g. the cable lengths. This however has no influence on the determination of the time resolution and still leaves us with the possibility to evaluate the time-of-flight differences of the two peaks.

The two ToF stations were setup (28.64 ± 0.05) m apart. With 6 GeV/c protons traveling at 0.9882 c, pions at 0.9997 c and kaons at 0.9966 c, we expect a time-of-flight difference between the two ToF stations for protons and pions of $\Delta t_{\mathrm{p}\pi} = 1.1$ ns, corresponding to the peak gap seen in Figure 7.9 and for pions and kaons of $\Delta t_{\mathrm{K}\pi} = 0.3$ ns. For this reason and considering the particle distribution shown in Figure 7.1 we can be sure to see pions and protons. The small time difference of pions and kaons however can not be resolved. For this reason and due to the small kaon contribution to the beam content, pions and kaons will not be handled separately.

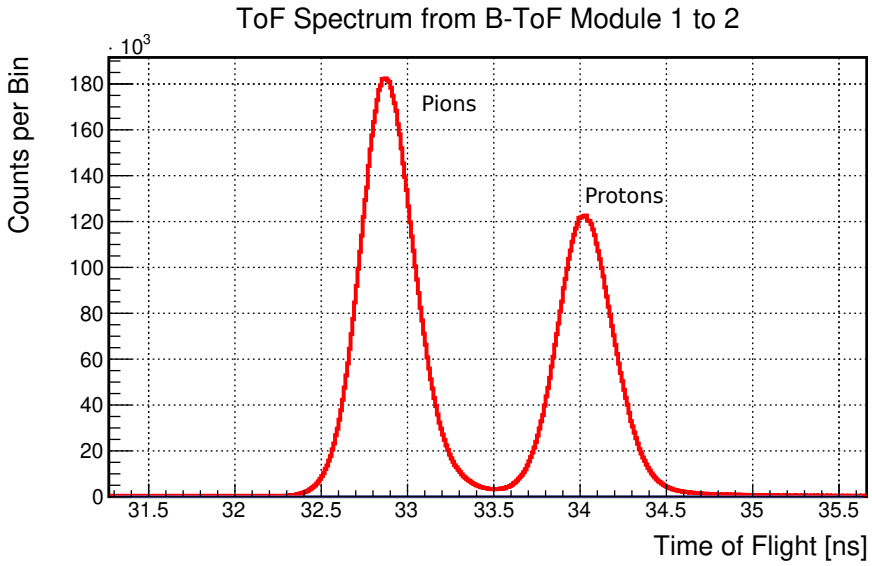

Figure 7.9: *This is a time-of-flight distribution, from the first to the second B-ToF module, of all events measured at a beam momentum of 6 GeV/c. A clear separation between two particles (pions and protons) can be seen.*

7.4.2 Efficiency

The readout is started after a hit in the trigger is registered. Not all trigger hits correspond to an event in all other detectors. The most efficient detectors with the most hits compared to the trigger and an average efficiency of 91.3 % and 92.4 % are the detectors of Station 1, the B-ToF Module 1 and MCP-PMT 1, as they are the first detectors in the beamline. Detectors of the second ToF station show a significantly reduced hit rate, especially for lower momenta with efficiencies of as small as 22.2 % at 3 GeV/c up to 59.8 % at 10 GeV/c. The corresponding data is shown in Table 7.1.

Table 7.1: *Recorded hits for all ToF detectors for the analyzed beam momenta. The trigger count is given in million hits. Hits in the other detectors are given relative to the trigger count.*

Momentum	[GeV/c]	3	4	5	6	7	8	10
Trigger	[$\times 10^6$]	10.64	19.29	2.13	33.69	14.08	17.61	17.05
B-ToF 1	[%]	89.9	91.2	93.1	92.6	87.6	92.3	92.2
MCP-PMT 1	[%]	88.2	91.3	93.8	94.0	89.7	94.8	94.9
B-ToF 2	[%]	22.9	32.5	34.5	40.4	47.3	48.4	52.8
B-ToF 3	[%]	22.2	31.4	33.3	39.8	46.9	46.7	53.1
MCP-PMT 2	[%]	29.0	39.3	41.9	48.4	59.0	57.6	59.8

The B-ToF modules are made up of two separate internal detection channels, the SiPMs on either side of the scintillator. All data is based on hits in which the SiPMs on both sides of the scintillator detect a hit. This is the case for at least

97.4 % of the hits on either side of the scintillator.

7.4.3 Time Walk Correction

As described earlier the amplitude of a SiPM signal is determined by the amount of detected photons. Depending on the electronics, the amplitude of the signal influences its exact timing. Large signals have a steeper leading edge slope for the same signal rise time. By crossing a detection threshold earlier than signals with an amplitude closer to the threshold itself, larger signals are detected earlier than smaller signals, as illustrated in Figure 7.10. This effect is called *time walk*.

The employed electronics does not measure the signal amplitude directly, it merely provides the ToT, an estimation of the amplitude. As the name implies, it measures the time an electrical signals pulse remains above a set voltage threshold, effectively measuring the width of a pulse at a given height. Given the same pulse shape, a signal with a larger amplitude also has a wider time spread, as shown in Figure 7.10. These two properties however do not scale linearly.

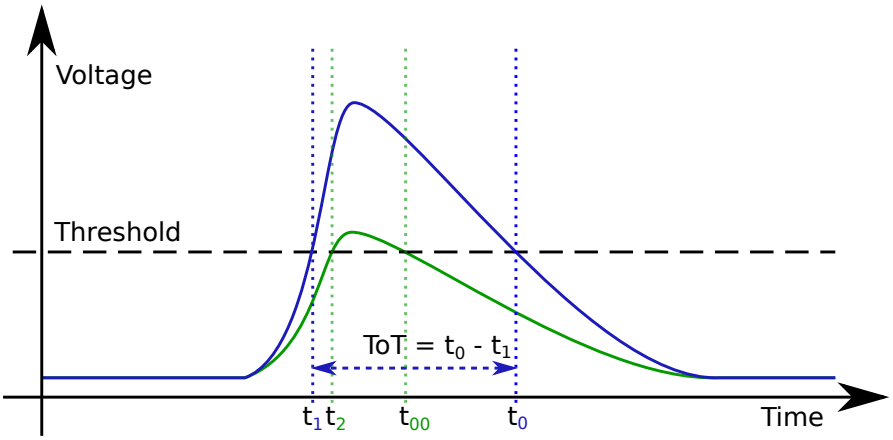

Figure 7.10: *Two signal pulses with different amplitude from the same detector are depicted. Given this amplitude difference they cross the set threshold at different times although their point of origin is the same, t_1 and t_2 respectively. This difference of t_1 and t_2 is called* time walk. *The difference in amplitude also leads to a difference in the amount of time the signal is above the threshold, the so called* time-over-threshold.

Since multiple consecutive data runs were combined to increase the available statistics, slight variations between runs can be accounted for by subtracting the mean time-of-flight of each run from every ToF measurement. The mean is determined by fitting a double or single peak function to the distribution and using the center of the two peaks as the relevant data point. For the analyzed set of data, this however only had a marginal effect of below 1 ps, when comparing resulting time resolutions. Nonetheless this correction was applied before adding them to a 3 dimensional distribution of ToF measurements vs the ToT of the involved detectors. The exact function used for the fits is discussed later in section 7.4.4.

In order to correct for time walk, the ToF measurements of all detected events are sorted and binned according to the signal amplitude in both detectors involved

in the corresponding ToF measurement. This gives us a 3 dimensional distribution of all hits, with a measure of the amplitudes on the x- and y-axis and the time of flight on the z-axis. Every ToF-amplitude combination, quantized to 100 x 100 bins, corresponds to one bin in this distribution. For measurements, with a larger distance between the detectors, such as from the TOF 1 station to TOF 2 station, we again expect a distribution with two distinct formations for protons and pions respectively, which manifest as two plains orthogonal to the z-axis. Compiling all ToF measurements for a single ToT combination into one distribution gives us a similar form to the one seen in Figure 7.7, this time however free of the effects of time walk, since these hits all share the same ToT values.

These distributions were then fitted again to find the relevant mean or center time of flight, the center of the two particle peaks. Subtracting this fitted center of each bin from the uncorrected center time of flight of all hits gives us a distribution of the difference of all signal amplitude combinations to the mean uncorrected ToF.

This ToT combination specific difference can then be used as a correction term, which is subtracted from every single ToF measurement, decreasing the spread of the original distribution. In this way a time walk correction is applied to all the measurements.

Figure 7.11 depicts two projections of such a resulting correction term distribution for the *B-ToF 1 - MCP-PMT 1* time-of-flight measurement. Each depicted distribution shows one slice of the correction term distribution of either the B-ToF 1 or the MCP-PMT 1 timing value, averaging the correction terms of the other detector from −1 ns to 1 ns.

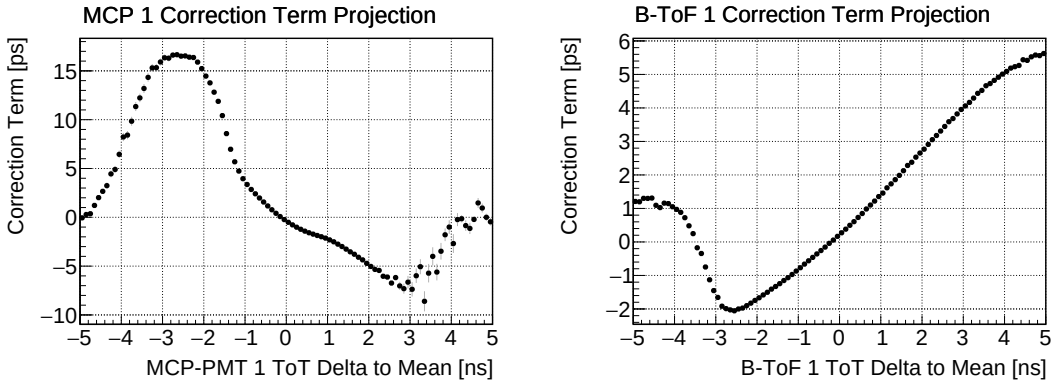

Figure 7.11: *Projection of the correction terms for the B-ToF 1 - MCP-PMT 1 distribution over all events averaging values of the respective other detector from −0.1 ns to 0.1 ns.*

7.4.4 Combined Time Resolution

After processing the data as described in the previous sections, we receive the time walk corrected and optimized ToF distributions of the various detector combinations. By fitting the produced distributions to the expected function one can determine the width of the distributions and receives the time resolution of each detector pair.

Although, based on the limitations of the detectors, such as the time variance of the photons produced in the scintillator, as they propagate to both SiPM arrays in the B-ToF modules, a Gaussian distribution is expect. However one will not find this to be true even for a perfectly calibrated beam. The beam particles traverse multiple layers of material of varying thickness, especially in between the two ToF stations where the DIRC detectors make up the bulk of the material.

During the passage of the particles through the matter they undergo *scattering* and lose energy. In addition to this, for materials of sufficient thickness, they undergo *small angle multiple scattering* increasing the distance the particles travel along their trajectory [36]. These two effects produce an asymmetric skew of the distribution towards slower particles and hence towards a higher ToF. The by scattering deposited energy, in materials of moderate thickness, follows a so called *Landau distribution* [67, 68].

Since for the scope of this thesis only the time resolution is of interest, which is determined by the width of the peaks, and the influence of the Landau distribution is small, a simple fitting function with the minimal amount of parameters should produce a suitable estimation of our detector performance. The skewed influence of beam processes will be estimated and accounted for in a future step. For this reason the following analysis is based on fits with simple Gaussian distributions, providing a simple measure of the peak height or amplitude, mean and width. Although they do not fit perfectly, they are still able to provide close enough results, as can be seen in Figure 7.12.

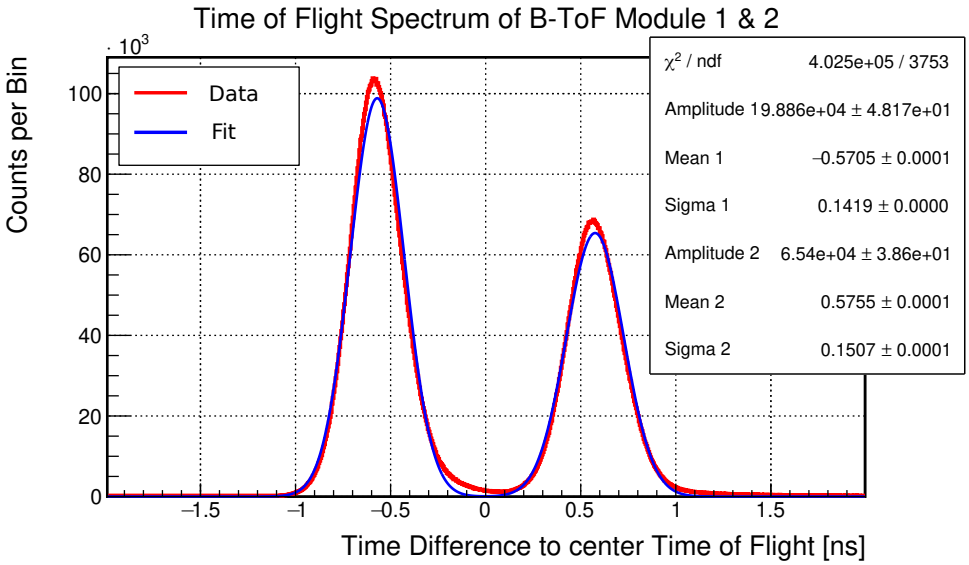

Figure 7.12: *Fit of corrected ToF distribution with a double Gaussian.*

Not all detector combinations were fit with a double Gaussian. For detectors very close together, i.e. within one ToF station, a single Gaussian was used as ToF differences for protons and pions of less than 7 ps can not be resolved in distributions with a standard deviation of about 150 ps.

The fits of the ToF difference distributions with Gaussian distributions deliver three parameters, *the amplitude, the mean and the standard deviation.* The standard

deviation (σ), which parameterizes the width of the Gaussian distribution on the time axis, is used as a measure of the time resolution of the detector combinations. Since we have two peaks for two particles we get two sets of measurements, one for the pions and one for the protons. The time resolution of the various detector combinations for pions and protons respectively is plotted in Figure 7.13. Since for combinations within one ToF station the distance between the detectors is not sufficient to resolve the ToF difference between protons and pions we assume the same time resolution for both. For this reason and for comparison sake they are drawn twice, once in the proton time resolution distribution and once in the pion distribution.

The ToF resolution for protons of various detector combinations show either one of two distinct momentum dependencies. ToF measurements within one ToF station show little to no momentum dependency and vary between 94 ps to 140 ps. Measurements between ToF stations, with a larger distance between the detectors, however clearly show a worsening of the time resolution towards lower beam momenta and slower particles. Time resolutions at a higher momentum are comparable to, yet slightly worse than combinations within one station.

The bottom Figure of 7.13 shows the ToF resolutions for the various pion measurements. The opacity of the same station time-of-flight resolutions however has been reduced to convey that these are duplicates from above. Looking at the pion distribution we see similar time resolutions, however without the characteristic increase of the time resolution at lower beam momenta.

From the time resolution measurements it is evident that the MCP-PMT 2 does not perform as well as the other detectors. ToF spectra involving MCP-PMT 2 also show a more pronounced tail, indicating that something was not working correctly. At this point there is no way to correct for this or to determine the reason for the malperformance of the detector. For this reason and analysis results outlined in the next section, all measurements involving MCP-PMT 2 will not be considered in the analysis moving forward.

7.4.5 Determining the Module Time Resolution

Since it is impossible to extract the time resolution of each module from a single ToF measurement, the ToF distribution of all combinations of timing detectors are compiled into a single system. This produces multiple combinations containing information of the individual detectors, hence creating an overdetermined system. To extract the time resolutions from this system, due to the nature of overdetermined systems to provide conflicting analytical information, a fit is required.

The resulting distributions, as seen in Figure 7.12 for example, are a convolution of the detector time resolutions based on Gaussian distributions, each with their own width, and a contribution from the beam, here assumed also to be a Gaussian distribution. As such, with the underlying assumption that the time resolution of all modules is independent, the total time resolution can be expressed as the square root of the quadratic sum of the individual systems Gaussian time resolutions or as Equation (7.4.1).

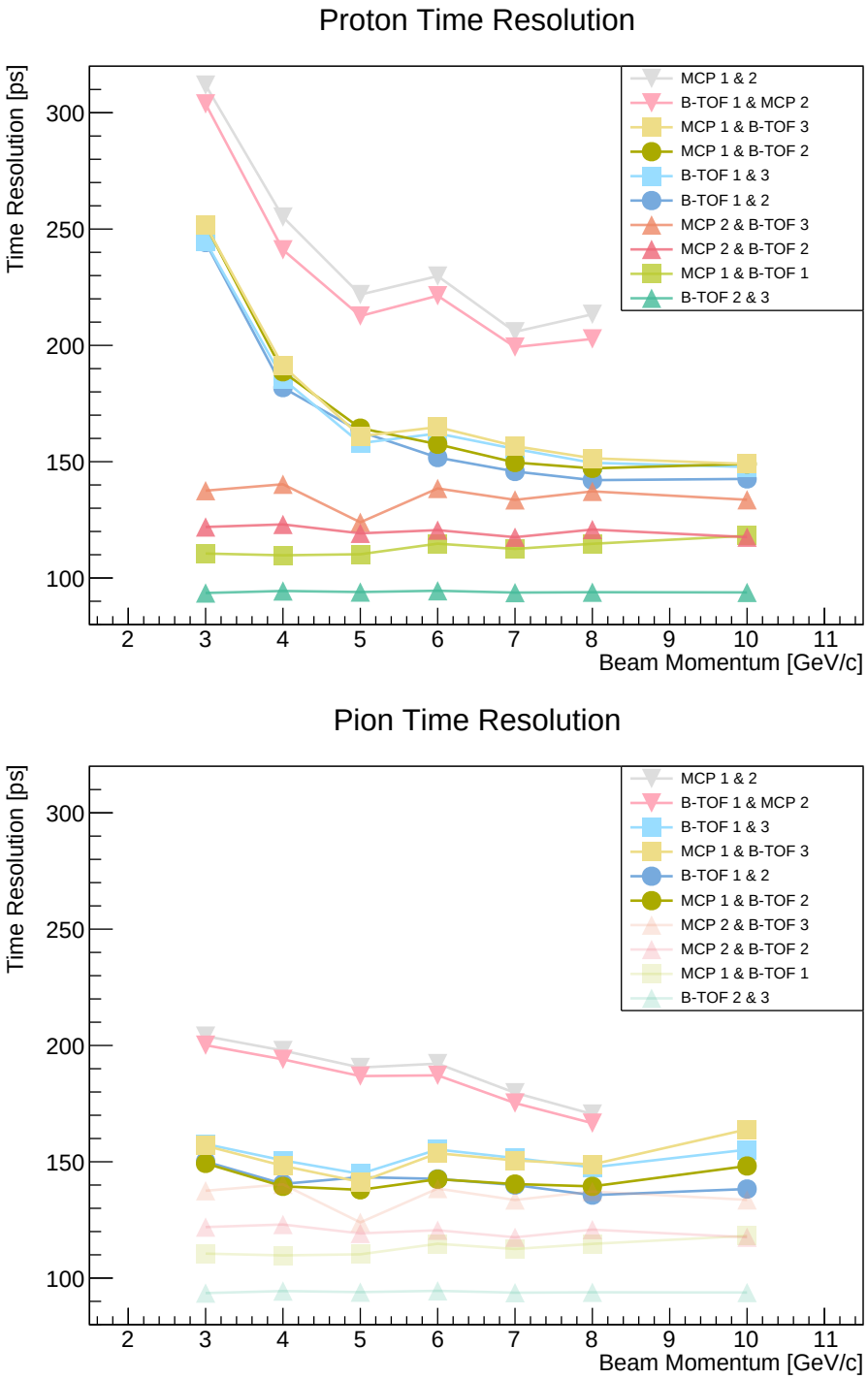

Figure 7.13: *Time Resolution measured for protons and pions, determined by fitting Gaussian functions to the corrected time-of-flight distributions of all detector combinations. Error bars for the fit error are technically included here, but they are smaller than the marker for the data points. The combinations of detectors that sit in the same ToF station are drawn with a reduced opacity in the pion distribution, since they are the same as for protons.*

Table 7.2: *Improvement of the time resolution shown as the weighted mean of the relevant detector combinations over all beam momenta up to 8 GeV/c, scaled by the amount of detected hits for the respective runs.*

Detector Combination	**Time Resolution Improvement [%]**	
	Pion	Proton
B-ToF 1 & 2	11.4 ± 1.3	8.8 ± 3.1
B-ToF 1 & 3	9.2 ± 1.6	8.1 ± 2.6
B-ToF 2 & 3	—	14.4 ± 1.9
MCP-PMT 1 & B-ToF 1	—	17.9 ± 1.0
MCP-PMT 1 & B-ToF 2	11.5 ± 2.4	9.1 ± 3.2
MCP-PMT 1 & B-ToF 3	7.8 ± 1.8	7.0 ± 1.7

$$\Delta t_{system} = \sqrt{\sum_{n=1}^{\infty} (\Delta t_n)^2}$$

or

$$(\Delta t_{system})^2 = \sum_{n=1}^{\infty} (\Delta t_n)^2 \,. \tag{7.4.1}$$

This gives us a system of equations involving each detector. As mentioned above, for detector combinations involving detectors that are further apart we get three contributing terms, the two detectors time resolutions and a beam term,

$$\Delta t_{ToF}^2 = \Delta t_1^2 + \Delta t_2^2 + \Delta t_{beam}^2.$$

Detectors within one ToF station however are too close together for large trajectory differences to appear or small differences in beam velocity to have a measurable effect. This leaves us with equations composed of two terms instead of three,

$$\Delta t_{ToF}^2 = \Delta t_1^2 + \Delta t_2^2.$$

Leaving out measurements involving MCP-PMT 2, we receive a system of 6 quadratic equations; four with and two without the beam term.

To find the single detector time resolution values that reproduce the measured ToF resolutions the best, the squared ToF resolutions and the corresponding equations are each assigned a bin in a graph and the resulting function is fitted, producing the most probable values. This is done separately for all beam momenta

from 3 GeV/c to 8 GeV/c as well as for pions and protons, due to their different momentum dependence. The resulting time resolutions, separated by beam particle type, are shown in Table 7.3 and 7.4. Apart from the small momentum dependence of the energy deposition, the time resolution should not be influenced by the beam momentum and we expect constant values for the time resolution.

Table 7.3: *Proton peak results of the single detector time resolution fit, listed for all measured beam momenta* p*. The statistical fitting errors are omitted since they are all below 0.1 ps.*

p [GeV/c]	B-ToF 1 [ps]	B-ToF 2 [ps]	B-ToF 3 [ps]	MCP 1 [ps]	Beam [ps]
8	77.83	59.47	72.66	84.26	103.88
7	77.07	55.86	75.26	81.98	111.22
6	76.85	55.24	76.70	85.22	119.48
5	75.56	71.37	61.12	80.24	124.98
4	69.72	62.26	71.00	84.77	156.27
3	65.66	65.77	66.53	88.90	225.98
Mean	73.8 ± 5.2	61.7 ± 7.5	70.5 ± 6.8	84.2 ± 4.5	———

Table 7.4: *Pion peak results of the single detector time resolution fit, listed for all measured beam momenta* p*. The statistical fitting errors are omitted since they are all below 0.1 ps.*

p [GeV/c]	B-ToF 1 [ps]	B-ToF 2 [ps]	B-ToF 3 [ps]	MCP 1 [ps]	Beam [ps]
8	78.84	53.66	77.05	83.32	97.26
7	79.82	52.99	77.31	79.30	102.57
6	81.91	51.96	78.96	80.37	105.09
5	81.91	63.82	68.97	73.75	98.20
4	79.16	55.56	76.35	76.03	102.37
3	78.90	56.71	74.41	77.38	114.40
Mean	80.1 ± 1.5	55.8 ± 4.3	75.5 ± 3.5	78.4 ± 3.4	———

During this step of the analysis it became clear, that MCP-PMT 2 was compromised in some way. Omitting it and measurements involving it, the fitted curve got much closer to the measured values and the χ^2/ndf[1] decreased significantly from an average of over 600 to roughly 3.

Looking at the beam contribution first we see, as expected from the time resolution distributions in Figure 7.13, a decreasing term for higher beam momenta for the protons and only a very slight momentum dependence for the pion term. The beam term values for the proton peaks range from 104 ps at 8 GeV/c to 226 ps at 3 GeV/c, where as for pions they sit between 97 ps at 8 GeV/c and 114 ps at 3 GeV/c.

[1] number of degrees of freedom

7.5 Increasing the Photon Count

The time resolution, as mentioned in chapter 6, is subject to statistical processes. Timing signals of scintillators depend on the time the photons need to travel from their point of origin to the readout and be detected. In order to reduce the amount of noise picked up by the SiPMs a detection threshold was set which further increases the amount of photons necessary to trigger a readout. The consistency of how fast the required photons reach the detector follows $1/\sqrt{N}$. The more photons are detected or produced the smaller the variance of the detection time.

7.5.1 Time Resolution Comparison of 4 vs. 6 SiPMs

A simple way to increase the amount of detected photons is to increase the sensitive area, the area to which our readout detectors are attached. In the standard configuration 4 SiPMs of $3 \times 3\,\mathrm{mm}^2$ readout a detector side of $5 \times 29\,\mathrm{mm}^2$. This leaves a lot of dead space. Increasing the amount of SiPMs on both sides from 4 to 6 increases the sensitive area by 50 %.

As mentioned initially, B-ToF Module 3 was used to test different SiPM configurations. For the majority of measurements it was equipped with 4 SiPMs just like the other two B-ToF modules. For a few measurements at 4 GeV/c, 6 GeV/c and 8 GeV/c beam momentum, the SiPM sensor board was swapped with a board that was mounted with 6 SiPMs of the same model. The resulting ToF resolutions for the various detector combinations are listed in Table 7.5 and Table 7.6.

Table 7.5: *Proton time resolution measurements comparing 4 and 6 SiPMs in B-ToF Module 3. The Errors are omitted but are all well below 0.4 ps. The names of detector combinations are shortened as follows, B-ToF Module 1 to B-ToF Module 2 (B12), B-ToF Module 1 and MCP-PMT 1 (B1M1), MCP-PMT 1 to B-ToF Module 2 (M1B2), B-ToF Module 1 to B-ToF Module 3 (B13), B-ToF Module 2 to B-ToF Module 3 (B23) and MCP-PMT 1 to B-ToF Module 3 (M1B3).*

Momentum [GeV/c]	B-ToF Module 3	B12 [ps]	B1M1 [ps]	M1B2 [ps]	B13 [ps]	B23 [ps]	M1B3 [ps]
8	4 SiPMs	142.1	114.7	147.1	149.5	93.9	151.5
	6 SiPMs	138.5	112.8	144.9	143.2	88.5	144.9
6	4 SiPMs	151.8	114.8	157.5	162.1	94.5	164.9
	6 SiPMs	151.2	112.5	155.4	152.1	89.2	154.2
4	4 SiPMs	181.8	109.8	188.6	185.5	94.4	191.2
	6 SiPMs	180.5	110.2	189.2	180.6	92.8	187.5

Due to the conditions of the beamtime the measurements could not be performed consecutively nor to the desired extent. For this reason direct comparability and statistics are limited. Table 7.5 and Table 7.6 both show an overall improvement of the time resolution across all detector combinations.

Table 7.6: *Pion time resolution measurements comparing 4 and 6 SiPMs in B-ToF Module 3. The Errors are omitted but are all well below 0.4 ps. The names of detector combinations are shortened as follows, B-ToF Module 1 to B-ToF Module 2 (B12), B-ToF Module 1 and MCP-PMT 1 (B1M1), MCP-PMT 1 to B-ToF Module 2 (M1B2), B-ToF Module 1 to B-ToF Module 3 (B13), B-ToF Module 2 to B-ToF Module 3 (B23) and MCP-PMT 1 to B-ToF Module 3 (M1B3).*

Momentum [GeV/c]	B-ToF Module 3	B12 [ps]	B1M1 [ps]	M1B2 [ps]	B13 [ps]	B23 [ps]	M1B3 [ps]
8	4 SiPMs	135.7	114.7	139.4	147.6	93.9	148.9
	6 SiPMs	133.5	112.8	135.8	142.3	88.5	143.2
6	4 SiPMs	142.6	114.8	142.5	155.3	94.5	153.7
	6 SiPMs	141.5	112.5	139.9	146.6	89.2	144.6
4	4 SiPMs	138.4	110.2	138.5	144.5	92.8	142.4
	6 SiPMs	140.5	109.8	139.4	150.6	94.4	148.3

7.5.2 B-ToF at an Angle

A second way to increase the amount of detected photons is to increase the amount of emitted photons. In scintillators the photons are produced as a consequence of excitations in the electron shell due to the energy deposition of passing particles along their trajectory. Increasing the length of said trajectory will also lead to more photons. This can be done as studied in Chapter 6 by increasing the thickness of the scintillator or in this case by simply rotating it to have the particles enter at an angle.

This is not something that we will be able to influence in the final detector as particles will travel outwards from a central collision point, but it is something that will occur naturally for the majority of the particles. For this reason it is of interest to evaluate the impact particle's incident angles have on the time resolution.

To study this multiple data sets were taken at a beam momentum of 7 GeV/c. The first measurements were done with B-ToF Module 3 at an angle of 45°. In addition to that another run was performed with B-ToF Module 2 at the same angle. The resulting ToF resolution is listen in Tables 7.7 and 7.8.

Table 7.7: *Proton ToF resolution comparing tilted and untilted B-ToF modules at 7 GeV/c. The errors are omitted since they are all below 0.1 ps.*

Proton	B12 [ps]	B1M1 [ps]	M1B2 [ps]	B13 [ps]	B23 [ps]	M1B3 [ps]
Untilted	145.8	112.5	149.7	155.5	93.7	156.7
B-ToF 3 tilted	145.2	113.6	154.4	152.8	93.0	156.4
B-ToF 2&3 tilted	155.7	114.4	157.0	152.7	79.2	157.4

Table 7.8: *Pion ToF resolution comparing tilted and untilted B-ToF modules at 7 GeV/c. The errors are omitted since they are all below 0.1 ps.*

Pion	B12 [ps]	B1M1 [ps]	M1B2 [ps]	B13 [ps]	B23 [ps]	M1B3 [ps]
Untilted	140.0	112.5	140.4	151.6	93.7	150.6
B-ToF 3 tilted	140.4	113.6	146.2	149.5	93.0	149.2
B-ToF 2&3 tilted	152.0	114.4	149.9	151.7	79.2	150.5

7.6 Discussion

Efficiency

As seen in Section 7.4.2 the detector efficiency compared to the trigger counter depends on the beam momentum as well as the detector position along the beamline. The high momentum dependency of the detectors in the second station stems from their distance to the trigger and the negative correlation of the mean exit angle of particles going through small angle multiple scattering, to the momentum and velocity [36]. Would the detectors be closer or have less matter between them, we would not see such a large efficiency drop and momentum dependence. More particles would fall into the acceptance range of the detectors at the second ToF station, since the accepted solid angle would be larger or displacement by scattering smaller.

The efficiency of the B-ToF module and the MCP-PMT in the first station are very close. For the second station however we see a larger difference, with the MCP-PMT showing a higher detection rate. This is not simply due to any potential size difference since the MCP-PMT and the B-ToF scintillator are very similar in size, 2580 mm^2 and 2809 mm^2 respectively. The influence of the difference in geometry however might affect the results since the MCP-PMT is square and has more active detector surface closer around the beam trajectory compared to the elongated rectangle shape of the B-ToF. Confirming this however would require a closer study of the beam profile.

The high internal efficiency of the B-ToF modules of up to 97.4 % shows that the modules work well. Almost no event is missed by the B-ToF modules and by having the left and right SiPM array signal in coincidence noise can be suppressed.

Time Walk Correction

The time walk correction term distributions, examined in Section 7.4.3 depicted in Figure 7.11, both show a clear continuous dependence of the correction term on the time-over-threshold. We do not expect a linear behavior since the signal amplitude and the time walk are not linearly correlated. The B-ToF distribution shows a very smooth behavior, whereas MCP-PMT 1 shows a steeper and irregular rise indicating a stronger time walk effect. This can be due to the threshold level being at a different height relative to the mean signal amplitude, which at this point can not be checked. A lower threshold, closer to the base line means, more

time walk, where as a threshold set closer to the signal peaks produces a smaller timing difference between signals. The values at the edges of these distributions become very irregular. These regions however only include a very small fraction of the overall events and hence have only a marginal impact on the overall timing performance.

A directional difference of the correction term trend is also clearly visible. This is to be expected. While the general time walk effect is the same for all detectors, its influence on the ToF however depends on the detectors position relative to the other detector. We know a signal with a small amplitude has a retarded timing signal. If this delay applies to the first detector the ToF ($t_{ToF} = t_2 - t_1$) will be shortened compared to a larger signal. For the second detector a small signal means an increase in the measured ToF. For this reason the B-ToF detector in Figure 7.11 shows an increase of the correction term for signals with a larger amplitude and a decrease for larger MCP-PMT 1 signals.

Understanding the Setup

In order to gain a better understanding of the measured data one can look at the distribution of the fit parameter. The ratio of the *amplitudes* multiplied by the standard deviation or width of the distributions, gives us the relative abundance of pions and protons shown in Figure 7.14. This information on the composition of the beam can be compared to Figure 7.1. A good reproduction of the general trend of an increasing proton content towards a higher beam momentum can be seen. When comparing these figures one however has to keep in mind that this analysis can not distinguish between pions and kaons, which in Figure 7.14 are both included jointly in the round data points. This inclusion of kaons pushes the point at which the proton content starts to dominate beyond 7 GeV/c which in Figure 7.1 lies slightly above 6 GeV/c. Otherwise the distributions are very comparable.

To make sure the setup is well understood the ToF difference calculated from the peak position of the fitted Gaussian distributions can be compared to expected ToF differences for the respective beam momentum. Figure 7.15 shows an overlay of the measured and estimated ToF difference between the proton and pion peak in the ToF distributions of B-ToF Module 1 to B-ToF Module 3 as seen in Figure 7.12. Comparing the measured against the estimated times in the figure one sees that the measured ToF difference is consistently slightly larger than one would expect for a distance of (28.64 ± 0.05) m which was determined with a laser distance meter. It comes closer to an estimated 29.4 m. This discrepancy of roughly 74 cm can only be partially attributed to the fact that due to the wall in between the ToF stations a precise measurement was not easy to achieve and the margin of error underestimated for this particular measurement.

This figure gives us certainty that the measured distance between the detectors is plausible. It confirms that the detectors were labeled correctly and sit where we expect them to. More importantly however it also tells us that the particle momentum of the beam roughly matches the momentum suggested by the settings in the control room. A small discrepancy here however might explain the distance

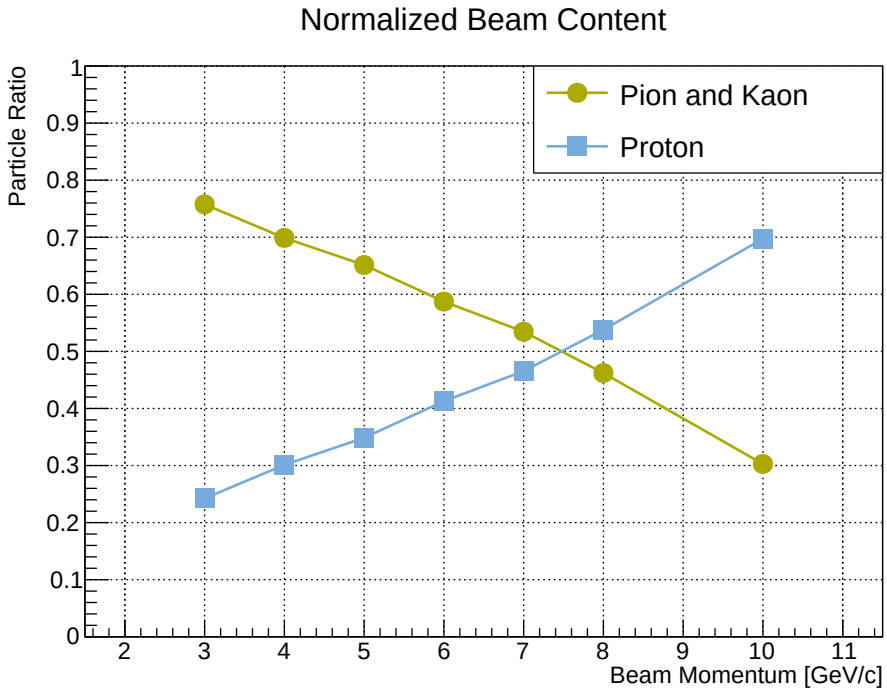

Figure 7.14: *Beam content determined by the amplitude and width of the Gaussian functions fitted to the time-of-flight distribution of B-ToF Module 1 and 2, with error bars smaller than the data markers.*

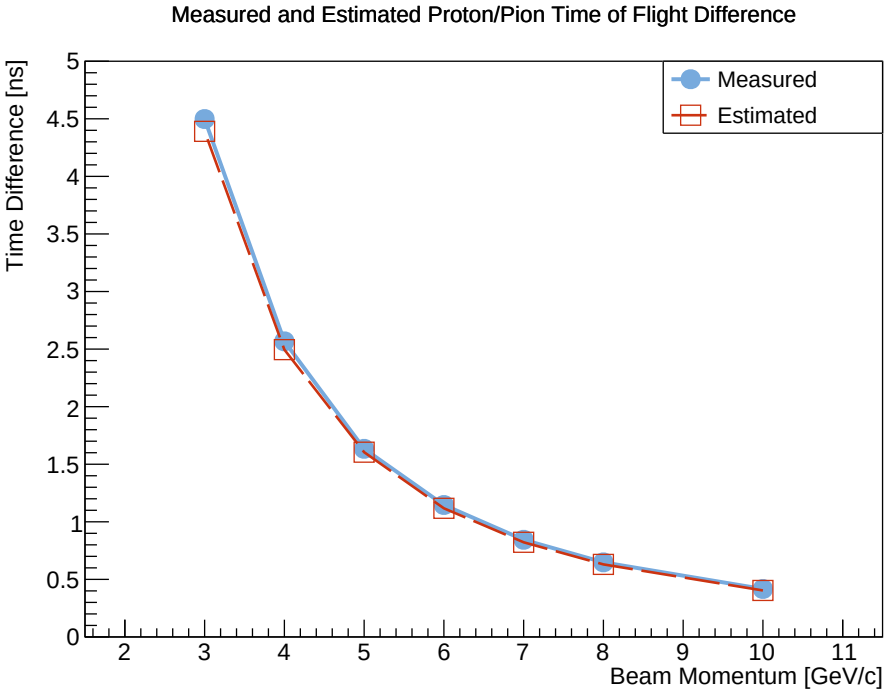

Figure 7.15: *Overlay of the measured and estimated ToF difference for protons and pions based on the measured distance of the B-ToF Module 1 and 3 of* (28.64 ± 0.05) *m. The error bars are too small to be seen.*

discrepancy.

Time Resolution

The parameter of interest is the standard deviation or time resolution. It depends, among other things, on the amount of collected photons. Since the particles at the used momenta are both minimally ionizing, we can expect them to emit roughly the same amount of photons when traveling through the scintillator along the same trajectory. This means that we can expect a similar time resolution from both particle peaks. Another consequence of the minimum ionizing momentum regime is, that we expect no significant momentum dependency of the time resolution. This would result in a flat distribution of the time resolution if plotted against the beam momentum.

As observed earlier, the time resolution shows two distinct behaviors, especially in the proton time resolution distribution. There lower momentum particles produce a larger time resolution than particles with higher momentum in detector combinations setup at a large distance from each other in Station 1 and Station 2. Withing one station however the time resolution is slightly better and seems to only depend on the detectors involved in the measurement. This momentum independent distribution is, as discussed earlier, in accordance with our expectations.

These two types of behavior suggest that the observed time resolution worsening is exasperated by the increase in distance and leaves the beam and its properties as the most likely cause. Effects such as the influence of the momentum spread of the beam and beam straggling or *small angle multiple scattering*, grow in strength as the detector distance grows, dense material is introduced and energies are reduced.

As discussed earlier, high energy particles traveling through matter undergo *small angle multiple scattering*. Every time an incident particle is deflected by electrons or nuclei in the matter they lose energy. In addition to that, depending on the mean scatter angle, their path length compared to a non disturbed particle, is increased, which then results in small ToF differences. The scatter angle, described by Rutherford depends on four parameters, the momentum, velocity and charge number of the incident particle and the scattering object [36]. The velocity and the momentum both have a negative correlation to the scattering angle. A smaller particle momentum leads to a higher mean scattering angle and hence a larger effect on the ToF distribution.

The pion data however does not show the large time resolution increase towards particles with lower momentum seen for protons. The literature does not explain this difference in behavior of protons and pions as it does not indicate any dependency of scattering effects on the type of projectile [69, 70]. The small difference in velocity between particles, 0.9882 c for protons and 0.9997 c for pions, is also not decisive as its effect does not explain the complete lack of momentum dependency for pions.

By fitting the ToF resolutions the individual detector time resolutions, listed in Table 7.3 and 7.4, could be isolated. Additionally a term for the uncertainty contributed by the beam could be determined. As mentioned earlier the beam contribution is a result of two effects, the beam spread, the particle momentum

distribution in the beam, and scattering causing a momentum loss and an increase in traveled distance by multiple small angle scattering processes. The first effect is subject to the settings of the beamline.

At the set collimator width of ±5 mm we expect a precision of the beam momentum of roughly below 1 %. For the used momentum range this means an error of less than 88.9 ps down to 13 ps for protons and 1.9 ps down to 0.3 ps for pions depending on the momentum. Compared to the measured beam contribution we see that other effects must dominate the term the beam adds to the time resolution.

The majority of the beams contribution to the spread of the time resolution can be attributed to scattering effects. These are subject to the particle momentum and velocity as well as the thickness of the scattering medium, in this case mostly the DIRC detectors. Both DIRC detectors are made out of synthetic fused silica and are rotated multiple times throughout the beamtime, changing their effective thickness. Angles range from 20° to 150°, increasing the effective thickness up to 2.9 times compared to particles hitting the plate head on at 90°. These changes are not accounted for in the analysis and can lead to varying contributions of beam to the time spread of the detectors. This is a possible explanation for the varying beam term in the pion data in Table 7.4. The beam term for the protons shows a reduction with rising beam momentum as seen in Figure 7.16 consistent with the $1/p$ behavior of the mean deflection angle for Rutherford scattering which for small angles is proportional to the increased travel distance and its effect on the time of flight. To reduce this, measurements without additional detectors in the beam line would be necessary.

Looking at the detector resolutions we expect roughly the same time resolution since all of them are equipped with 4 SiPMs. They are all from different producers (B-ToF 1: Hamamatsu, B-ToF 2: Ketek, B-ToF 3: AdvanSiD) so minor differences can be expected. Comparing the pion to the proton results, one sees that they are of the same order of magnitude but well outside their respective margin of error of each other. In the proton data, we see a clear distinction between the B-ToF modules and the MCP-PMT. The MCP-PMT has a resolution distinctively worse than of any B-ToF module. Although there is a 12.2 ps difference between the B-ToF resolutions they are all within each others margin of error with a mean B-ToF time resolution of 69 ps across all three modules.

The pion data shows a much larger time resolution discrepancy between the modules with values ranging from a mean 55.8 ps to 80.1 ps for B-ToF 1 and B-ToF 2 respectively with B-ToF 3 at 75.5 ps.

Comparing the uncorrected to the time walk corrected time resolution one finds that the correction improves the time resolution between 7.0 % to 17.9 % depending on the detector combination. The weighted mean time resolution improvement of every detector combination averaged over all beam momenta from 3 GeV/c to 8 GeV/c, are shown in Table 7.2. The improvement is especially pronounced for detectors in the same ToF station. These are again only listed in the proton column since for those distributions pions and protons are indistinguishable.

Figure 7.12 shows clearly that the approximation of the distribution with a Gaussian distribution does not produce an ideal replication. In order to improve

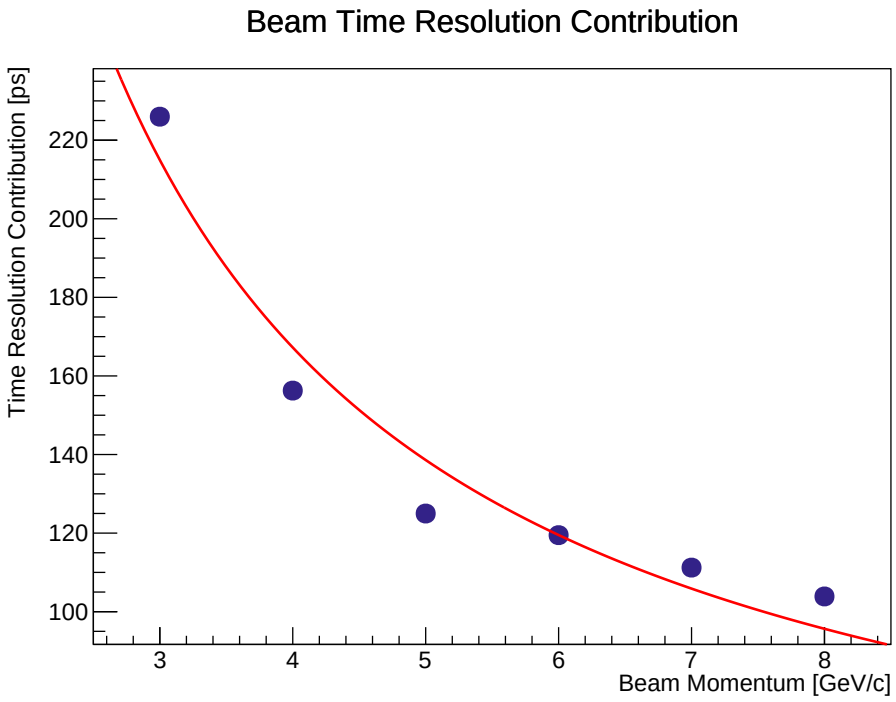

Figure 7.16: *The time resolution contribution of the beam term for protons over the studied momentum range, taken from Table 7.3 and fitted with a function* $\sim 1/p$ *expected from the angle dependent scattering.*

this the small influence of the scattering processes between the ToF stations would need to be taken into account. As mentioned earlier the energy and momentum loss in the DIRC detectors can be described with a Landau distribution. This energy loss distribution is overlaid with the intrinsic normal distribution of every time-of-flight measurement. This means that in order to fit the measured distributions precisely one would have to use a convoluted Gaussian and Landau distribution. Such a function is not readily provided by *ROOT*[2], the analysis framework used to evaluate the measurements. However `langau.C`, a macro that is part of most ROOT distributions, originally written in Fortran by R. Frühwirth and later adapted for C++/ROOT, implements a fitting algorithm for a single such convoluted peak. This algorithm is based on a numerical approximation of the landau distribution which is convoluted with a Gaussian distribution. It fits the distributions according to four parameters, the *Width* and *Most Probale value* (MP) referring to the maximum of the Landau distribution as a probability density function, which are both values describing attributes of the convoluted Landau distribution, as well as the *Area* defined as the integral from $-\infty$ to ∞, and *GSigma*, the standard deviation of the convoluted Gaussian.

After implementing a double peak structure, well fitting plots can be achieved (Figure 7.17). This algorithm however, applied to this data set, often does not converge or produces results clearly not compatible with the underlying data. This holds true especially for the secondary values such as the true peak position and

[2]https://root.cern.ch

the FWHM which are estimated from the primary fit parameters. As an example, for a ToF difference distribution at a beam momentum of 8 GeV/c a FWHM value of 1.8 ps is estimated. Since the results were not reliable this analysis approach was abandoned.

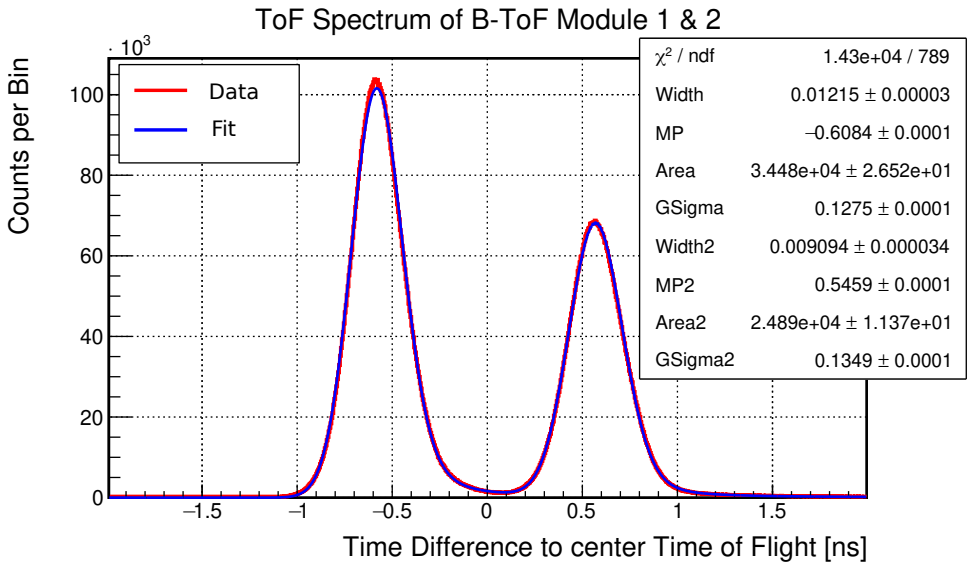

Figure 7.17: *Fit of time walk corrected ToF distribution with a Landau-Gauß Convolution for a beam momentum of 6 GeV/c.*

Time Resolution Comparison of 4 vs. 6 SiPMs

The increase in sensitive of 50 % going from 4 to 6 SiPMs increases the amount of detected photons to 150 % and should result in a reduction of the time resolution by $1/\sqrt{1.5} \approx 0.82$ according to the $1/\sqrt{N}$ relation of the amount of detected photons (N) to the time resolution. This means a time resolution improvement of slightly more than 18 %.

Since an overall improvement of the time resolution can be observed from one data set to the next, the relative improvement of detectors involving B-ToF Module 3 to the improvement of detectors without said module can be looked at. What caused this improvement can not be determined at this point but is most likely due to changes in the beam.

Figure 7.18 depicts the relative improvement of the time-of-flight resolution at 8 GeV/c from one data set with a 6 SiPM module to a data set without a 6 SiPM module. Three detector combinations involving the 6 SiPM module consisting of B-ToF Module 1 to B-ToF Module 3 (B13), B-ToF Module 2 to B-ToF Module 3 (B23) and MCP-PMT 1 to B-ToF Module 3 (M1B3), as well as three detector combinations without the 6 SiPM module namely B-ToF Module 1 to B-ToF Module 2 (B12), MCP-PMT 1 to B-ToF Module 2 (M1B2) and B-ToF Module 1 and MCP-PMT 1 (B1M1) are listed in the figure.

Looking at the first three data points of detector combinations not involving B-ToF 3, one can see that the time resolution has generally improved by 1.9 %.

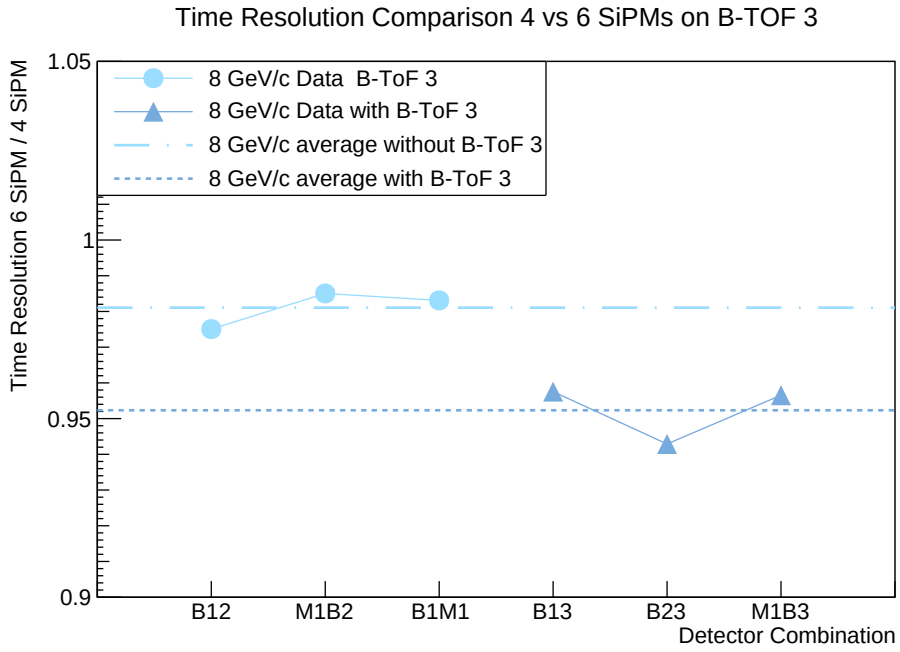

Figure 7.18: *Relative time resolution improvement of 6 over 4 SiPMs for protons.*

For detectors involving the new 6 SiPM module it has improved by 4.8 %. That means the performance improved by 2.9 % by adding 2 SiPMs per side for one Module. Similar results can be seen for measurements at 6 GeV/c and 4 GeV/c, which show improvements of 5.0 % and 2.1 % due to the additional SiPMs. As this is the effect of one part of a convolution of two Gaussian distributions of roughly the same dimension, we can expect an effect $\sqrt{2}$ times larger on the isolated B-ToF module 3 time resolution. Including the measurements at other beam momenta an improvement of 4.1 %, 7.1 % and 3.0 % can be expected at 4 GeV/c, 6 GeV/c and 8 GeV/c.

Another way to evaluate a possible performance improvement is again by fitting the single detector time resolutions to the measured combined resolution, as done previously. The resulting time resolutions of these fits, comparing 4 to 6 SiPMs in B-ToF Module 3 are shown in Table 7.9 and 7.10, listing all determined resolutions and also technically unaffected fit components. Although we do not expect any changes for the B-ToF 1 and 2 modules as well as for the MCP-PMT and the beam, a change of one parameter might lead to variations of other parameters during the fitting procedure. The general time resolution improvement observed earlier has to be taken into account too.

As expected the time resolution for B-ToF1 and to a similar degree MCP-PMT 1 are largely unaffected, both in the pion and proton measurements with an average improvement of 0.9 ps for both detectors. The beam resolution sees a slightly larger drop of 3.6 ps on average. The results for the B-ToF 2 however shows a worsening of the time resolution of 3.9 ps, which is not consistent with the mere swapping of B-ToF 3 elements. As predicted though, B-ToF 3 presents the largest change, an improvement for measurements at all evaluated momenta with an average

improvement of 8.3 ps or 13.2 %.

Table 7.9: *Pion peak results of the single detector time resolution fit comparing 4 vs. 6 SiPMs in B-ToF Module 3 at 4 GeV/c, 6 GeV/c and 8 GeV/c. The fitting errors are omitted since they are all below 0.1 ps.*

Momentum [GeV/c]	SiPMs [Number of]	B-ToF 1 [ps]	B-ToF 2 [ps]	B-ToF 3 [ps]	MCP 1 [ps]	Beam [ps]
8	4	78.84	53.66	77.05	83.32	97.26
	6	78.32	53.00	70.89	81.13	94.76
6	4	81.91	51.96	78.96	80.37	105.09
	6	81.18	57.24	68.37	77.96	100.97
4	4	79.16	55.56	76.35	76.03	102.37
	6	78.79	60.01	70.78	77.04	97.43

Table 7.10: *Proton peak results of the single detector time resolution fit comparing 4 vs. 6 SiPMs in B-ToF Module 3 at 4 GeV/c, 6 GeV/c and 8 GeV/c. The fitting errors are omitted since they are all below 0.1 ps.*

Momentum [GeV/c]	SiPMs [Number of]	B-ToF 1 [ps]	B-ToF 2 [ps]	B-ToF 3 [ps]	MCP 1 [ps]	Beam [ps]
8	4	77.83	59.47	72.66	84.26	103.88
	6	76.11	61.48	63.68	83.21	100.79
6	4	76.85	55.24	76.70	85.22	119.48
	6	76.50	63.27	62.84	82.55	114.77
4	4	69.72	62.26	71.00	84.77	156.27
	6	68.06	66.69	64.52	86.66	153.81

The time resolution improvements for the B-ToF Module 1 as well as MCP-PMT 1 and the beam most likely stem from general improvements in the underlying distributions of the detector combinations. The worsening of the time resolution for B-ToF 2 seems like a balancing reaction of the fitting algorithm to the reduction of the time resolution of B-ToF 3, revealing correlations between the time resolution values. Since not all time resolutions comparing 4 to 6 SiPMs moved in the same direction, eg. the B-ToF 2 resolution got worse, it is not possible to evaluate the magnitude of the improvement 6 SiPMs offer over 4 but in all instances the time resolution of B-ToF 3 improved suggesting a considerable benefit of increasing the amount of SiPMs per scintillator.

B-ToF at an Angle

A tilt of 45° leads to an increase of the particle trajectory through scintillator material by a factor of $\sqrt{2}$ or 1.4, causing an expected increase by the same factor of photons and a decrease in time resolution of a factor of 29 %.

Due to the limitations of the beamtime these measurements are also not directly comparable. In this case that leads to the measured data delivering conflicting results for both methods explored in section 7.5.1. Tables 7.12 and 7.11 show improvements for the B-ToF Module 3 but at the same time time resolution deterioration of the B-ToF Module 2. The correlation matrix of the time resolution fit reveals sizable correlations for detector resolutions in one station. In these data sets no trend for the B-ToF Module 2 and 3 could be determined, leading to the conclusion that the expected effect of the incident angle of passing particles could not be observed, neither positively nor negatively.

Table 7.11: *Fit results for tilted and untilted time resolution measurements for protons.*

Proton	B-ToF 1 [ps]	B-ToF 2 [ps]	B-ToF 3 [ps]	MCP 1 [ps]	Beam [ps]
Untilted	77.1	55.9	75.3	82.0	111.2
B-ToF 3 tilted	73.9	59.9	71.2	86.2	111.4
B-ToF 2&3 tilted	77.9	57.7	54.2	83.7	120.7

Table 7.12: *Fit results for tilted and untilted time resolution measurements for pions.*

Pion	B-ToF 1 [ps]	B-ToF 2 [ps]	B-ToF 3 [ps]	MCP 1 [ps]	Beam [ps]
Untilted	79.8	53.0	77.3	79.3	102.6
B-ToF 3 tilted	77.7	58.6	72.2	82.8	103.2
B-ToF 2&3 tilted	82.4	55.8	56.2	79.3	114.6

The potential issue here is that the measurements were not performed consecutively and not under completely identical conditions since DIRC angles were changed and the beam trajectory adjusted in between measurements.

Summary

Moving from measurements with electrons at energies in the MeV range discussed in the previous chapter to protons and pions with energies of a few GeV permits a look at the detector performance in a less controlled environment and under conditions closer to the expectations in the $\overline{\text{P}}$ANDA experiment.

A mixed secondary beam of mainly protons and pions was aimed at a system of three B-ToF modules and two MCP-PMTs. The measurements and the analysis focused on the timing performance, trying to determine the time resolution achievable with the detector system.

Potential for improvement in the analysis lies within the fitting function used to determine the parameter of the ToF distributions. Having a function that reproduces the exact shape of these distributions reliably, would increase the

strength of the results and potentially capture the influence of the beam better. Not only could one try this by optimizing the previously discussed Landau and Gaussian convolution but also by using a Vavilov distribution instead of the Landau distribution, more suitable for particles passing through material of intermediate thickness [30]. This distribution reduces to a Landau distribution for applications where the ratio of the mean energy loss to the maximum energy transfer goes towards 0 and to a Gaussian distribution for its limit towards infinity.

The initial design goal was set at 100 ps and is surpassed by all modules each with different SiPMs. The wide range of time resolution results ranging from 55.8 ps to 80.1 ps was measured for SiPMs made by Hamamatsu, Ketek and AdvanSiD. However a clear performance decrease can be seen moving from electrons of a ^{90}Sr source described in Chapter 6 to the pions and protons used at the T9 beamline at CERN.

The large differences in sensor performance between the beam momenta and manufacturers are noteworthy. Large performance differences from run to run also hint at strong correlations of the time resolution values in the fit and a nonideal experimental setup. The B-ToF Module 2 equipped with Ketek SiPMs consistently showed the best time resolution. Due to the large variations between the time resolution measurements additional studies should be performed to confirm this. Controlled studies such as in the previous chapter would be necessary for a decisive conclusion.

Comparing the measurement for the proton and the pion peak, the proton results are closer to our expectations. The large time resolution spread and the unexpected behavior of the beam contribution shows that the pion response of our measurement is not well understood and would need further careful investigation. This can potentially be attributed to the mixed beam content. While protons have a considerable mass gap to other particles and hence a large ToF separation pions are much closer to other particles like kaons and electrons in their ToF. This mixing is not properly accounted for.

Nonetheless improvements in the time resolution for 6 vs. 4 SiPMs on B-ToF Module 3 were observable. Due to the limits of the parasitic arrangement of the beamtime for the B-ToF measurements the effective improvement is hard to quantify. Measurements to determine the influence of the incident angle were not successful. The measured resolutions were inconclusive concerning the tilted modules.

Chapter 8

Summary and Outlook

The $\overline{\text{P}}$ANDA Barrel Time-of-Flight Detector is designed to provide particle identity information and interaction time information for the $\overline{\text{P}}$ANDA experiment, which is being built at the future Facility for Antiproton and Ion Research (FAIR) at Darmstadt, Germany. To achieve the design goals a time resolution of below 100 ps is necessary. This body of work is set in the context of the development of this detector, depicting changes to some design choices, time resolution performance tests and progress of the signal transmission system.

A brief summary of the envisaged physics program for $\overline{\text{P}}$ANDA including charmonium spectroscopy, the study of hybrids and investigations into hadrons in a nuclear medium, with an overview of the various components for the experiment is given in Chapter 2. The role of the B-ToF in the experiment is expanded upon in Section 3.3 showing how the detector is able to determine the interaction time from a single time stamp per particle via relative ToF measurements. The development of the detector is also put into perspective in Section 3.1 examining the requirements and constraints of the detector, the concept of which was added to a preexisting layout of the experiment and is designed to complement the PID of the DIRC detectors in the momentum range below 1 GeV/c.

SiPMs were chosen to read out scintillators tiles. These are capable of measuring the photon yield inside of a strong magnetic field and fit into the limited space between the Barrel DIRC and the EMC. By connecting them in series the signal profile is improved while increasing the sensitive area without increasing the number of readout channels. The limits of such a connection are explored in Chapter 4. While illuminating all sensors in a series connection of SiPMs equally produces a behavior comparable to a single sensor. Partial illumination however decreases the repetition rate the sensors are able to operate at by limiting the SiPM recharge current. While this might become an issue for large scintillators where the SiPMs are spread out this should not affect applications with small scintillators such as for the B-ToF.

The Rail-Board, the backbone of the detector connecting the SiPMs to the front-end electronics, has undergone multiple design and layout iterations. Chapter 5 gives a closer look at the design decisions and the performance of every board prototype. The boards were all evaluated using pulses close to the expected SiPM signals, with a short rise and long fall time, studying the crosstalk, and attenuation levels of different designs. Although a steady improvement of the signal characteristics could be observed from one prototype to the next, the rise time

experiences a strong increase for the third generation board. The new Sensor-Board and its connection to the Rail-Board as well as the connection between the front and back Rail-Board parts appear to increase the rise time significantly which is the largest downside of that layout. To reduce the rise time degradation a new shielded flat cable is designed paying closer attention to matching the transmission line impedance.

While the newest generation board performs the best, with negligible levels of crosstalk and signal amplitude attenuation closer to but still significantly worse a coaxial cable of the same length, it is the most expensive version in terms of monetary costs and material budget but staying with cheaper FR-4 would increase the material budget further still. The measurements show that the board concept is suitable as the transmission line solution for the detector but in order to truly analyze the performance of the Rail-Board designs the boards needs to be evaluated using pulses produced by SiPMs on a scintillator. Based on such measurements and a clearer understanding of the influence of the rise time changes on the time resolution, the price to performance can be evaluated and the best suited board be chosen.

The achievable time resolution of the detector not only depends on the utilized sensors and materials but also on the dimensions of the scintillator. While the material and outline of the scintillator tiles has been studied before the tile thickness was not yet optimized. In order to do this, time resolution scans along the scintillator surface for tile thicknesses from 3 mm to 6 mm were performed, using a collimated ^{90}Sr source and is discussed in Chapter 6. While for equally energetic electrons the same number of detected photons are expected for the same readout system no matter the scintillator thickness, the number of internal reflections increases when reducing the tile thickness. This negatively impacts the detectors time resolution which was determined to be best for 5 mm and 6 mm thick scintillator tiles. Additionally the measurements determined that, while adding a quenching agent to the scintillator material might be beneficial for some ultra-fast timing applications, this is not the case for the B-ToF tiles. The influence of the treatment of the scintillator surface was also to be determined by comparing simply cast and cut tiles to polished scintillators. To make a final determination of the polished scintillator the performance needs to be reevaluated after letting the tile sit since the surface deterioration needs time. Since no significant difference in performance could however be observed using polished scintillators adds no value just risk and will not be considered for the Barrel Time-of-Flight Detector.

Time resolution measurements using a mixed beam of mainly protons, kaons and pions were performed at a beamtime at the T9 beamline at CERN and are presented in Chapter 7. In addition to determining the time resolution of the B-ToF system under conditions closer to the expectations of the $\overline{\text{P}}$ANDA detector, a setup with two additional SiPMs was subject of investigation. While the achieved time resolution using the mixed beam was worse than for the measurements done with a ^{90}Sr source it was still well below the design goal of 100 ps. SiPMs by Hamamatsu, Ketek and AdvanSiD were also studied. Due to large time resolution differences between runs even for the same detector no clear best performing

device can be determined. Additional tests under a more controlled environment would be necessary to motivate the sensor choice. It could also be shown that by increasing the number of sensors from four to six SiPMs the time resolution could be improved. Studies under a more controlled environment are necessary to decide whether the performance improvements of additional SiPMs is worth the cost and which SiPM sensor is best suited for the B-ToF detector.

In summary this work shows that the individual parts from the scintillators to the SiPM readout and the signal transmission, discussed here will produce a capable timing detector suitable for the $\overline{\text{P}}$ANDA experiment. This however needs to be confirmed by measurements of the fully integrated setup.

One major component of the detector is still missing. A data acquisition system based on an ASIC developed for fast timing time-of-flight positron emission tomography (PET) needs to be developed. The TOFPET2 ASIC by PETsys Electronics provides all necessary data acquisition features for the successful operation of the detector. The system consists of two main stages. Analogue boards would be placed in close proximity to the detectors, each housing two TOFPET2 ASICs able to read out 64 channels each, recording the event time as well as either the time-over-threshold or the collected charge. To receive the best possible time resolution the timing threshold will have to be optimized. For this two separate thresholds for event detection and timing can be set individually for every channel. The analogue boards, two of which would be placed per Super-Module, are connected to FPGA based digital boards handling the readout, synchronization and control of the system. Because the signals transmitted from the analogue to the digital boards are digital signals they can be farther away, placed outside of the detectors limited space and magnetic field of the experiment. Since the board by PETsys does not provide a system to control the peripheral components such as the temperature sensors and the calibration LEDs additional controls are required and will have to be developed for the successful application of the detector system.

List of Figures

List of Tables

Abbreviations

APD Avalanche Photodiode

ASIC Application-Specific Integrated Circuit

B-ToF Barrel Time of Flight Detector

CERN European Organization for Nuclear Research

CFRP Carbon Fiber Reinforced Polymer

CT Central Tracker

DAQ data acquisition

DIRC Detection of internally reflected Cherenkov light

EMC Electromagnetic Calorimeter

FAIR Facility for Antiproton and Ion Research

FEE Front-End Electronics

FEXT Far-End Crosstalk

FPGA Field Programmable Gate Array

FR-4 Fire Retardant 4

FS Forward Spectrometer

FT Fiber Tracker

FWHM Full Width Half Maximum

GEM Gas Electron Multiplier

GSI GSI Helmholtzzentrum für Schwerionenforschung

HADES High Acceptance Di-Electron Spectrometer

HESR High Energy Storage Ring

MCP-PMT Microchannel Plate Photomultiplier Tube

MMCX Micro-Miniature Coaxial

MVD Micro Vertex Detector

NEXT Near-End Crosstalk

NIEL Non Ionizing Energy Loss

PaDiWa $\overline{\text{P}}$ANDA DIRC WASA

$\overline{\text{P}}$anda AntiProton Annihilations at Darmstadt

PCB Printed Circuit Board

PDE Photon Detection Efficiency

PET Positron Emission Tomography

PID Particle Identification

PMT Photo Multiplier Tube

PVT Polyvinyltoluene

QCD Quantum Chromodynamics

QDC Charge to Digital Converter

QED Quantum Electrodynamics

SiPM Silicon Photo Mulitiplier

SPAD Single Photon Avalanche Photodiode

SPTR Single Photon Time Resolution

STT Straw Tube Tracker

TDC Time to Digital Converter

TDR Technical Design Report

ToF Time of Flight

ToT Time-over-Threshold

TRB Trigger and Readout Board

TS Target Spectrometer

UNILAC Universal Linear Accelerator

VME Versa Module Eurocard-bus

Bibliography

[1] T. Stöhlker, V. Bagnoud, K. Blaum, A. Blazevic, A. Bräuning-Demian, M. Durante, F. Herfurth, M. Lestinsky, Y. Litvinov, S. Neff, *et al.*, "Appa at fair: From fundamental to applied research," *Nuclear Instruments and Methods in Physics Research Section B: Beam Interactions with Materials and Atoms*, vol. 365, pp. 680–685, 2015.

[2] B. Friman, C. Höhne, J. Knoll, S. Leupold, J. Randrup, R. Rapp, and P. Senger, *The CBM physics book: Compressed baryonic matter in laboratory experiments*, vol. 814. Springer, 2011.

[3] C. Scheidenberger, "Collaboration report nustar progress in 2013," *GSI Scientific Report 2013*, p. 95, 2014.

[4] W. Erni, I. Keshelashvili, B. Krusche, M. Steinacher, Y. Heng, Z. Liu, H. Liu, X. Shen, O. Wang, H. Xu, *et al.*, "Physics performance report for panda: Strong interaction studies with antiprotons," *arXiv preprint arXiv:0903.3905*, 2009.

[5] R. Baer, U. Krause, V. Schaa, and P. Schütt, "The new fair accelerator complex at gsi: project, controls challenges and first steps," *TOAB01, ICALEPCS*, 2007.

[6] A. Lehrach, O. Boine-Frankenheim, F. Hinterberger, R. Maier, and D. Prasuhn, "Beam performance and luminosity limitations in the high-energy storage ring (hesr)," *Nuclear Instruments and Methods in Physics Research Section A: Accelerators, Spectrometers, Detectors and Associated Equipment*, vol. 561, no. 2, pp. 289–296, 2006.

[7] U. Kurilla, *PANDA full setup labeled.* PANDA Collaboration, Nov 2018.

[8] The PANDA Collaboration, "Technical design report for the panda internal targets: The cluster-jet target and developments for the pellet target," March 2012.

[9] The PANDA Collaboration, "Technical design report for the: Panda micro vertex detector," November 2011.

[10] The PANDA Collaboration, "Technical design report for the: Panda straw tube tracker," December 2012.

[11] F. Sauli, "The gas electron multiplier (gem): Operating principles and applications," *Nuclear Instruments and Methods in Physics Research Section A:*

Accelerators, Spectrometers, Detectors and Associated Equipment, vol. 805, pp. 2–24, 2016.

[12] The PANDA Collaboration, "Technical design report for the solenoid and dipole spectrometer magnets," February 2009.

[13] The PANDA Collaboration, "Technical design report for the: Panda barrel dirc detector," August 2017.

[14] The PANDA Collaboration, "Technical design report for the: Panda endcap disc dirc," December 2019.

[15] The PANDA Collaboration, "Technical design report for the: Panda forward time of flight detector (ftof wall)," January 2018.

[16] The PANDA Collaboration, "Technical design report for the: Panda electromagnetic calorimeter (emc)," August 2008.

[17] M. Albrecht, "The forward endcap of the electromagnetic calorimeter for the panda detector at fair," in *J. Phys.: Conf. Ser.*, vol. 587, p. 012050, 2015.

[18] The PANDA Collaboration, "Technical design report for the panda luminosity detector," September 2018.

[19] I. Konorov, H. Angerer, A. Mann, and S. Paul, "Soda: Time distribution system for the panda experiment," in *2009 IEEE Nuclear Science Symposium Conference Record (NSS/MIC)*, pp. 1863–1865, IEEE, 2009.

[20] B. Aubert, A. Bazan, A. Boucham, D. Boutigny, I. De Bonis, J. Favier, J.-M. Gaillard, A. Jeremie, Y. Karyotakis, T. Le Flour, and et al., "The babar detector," *Nuclear Instruments and Methods in Physics Research Section A: Accelerators, Spectrometers, Detectors and Associated Equipment*, vol. 479, p. 1–116, Feb 2002.

[21] B. Collaboration *et al.*, "The belle detector," *Nuclear Instruments and Methods in Physics Research, Section A: Accelerators, Spectrometers, Detectors and Associated Equipment*, vol. 479, no. 1, pp. 117–232, 2002.

[22] Y. S. Kalashnikova, A. Kudryavtsev, and A. Nefediev, "Quark and meson degrees of freedom in the x (3872) charmonium," *Physics of Atomic Nuclei*, vol. 73, no. 9, pp. 1592–1611, 2010.

[23] D. Bettoni, "Physics with the panda detector at gsi," in *Journal of Physics: Conference Series*, vol. 9, p. 309, IOP Publishing, 2005.

[24] V. Mochalov, P. A. collaboration, *et al.*, "Physics with antiprotons at p^- anda," *Nuclear Physics B-Proceedings Supplements*, vol. 245, pp. 124–131, 2013.

[25] K. Saito, K. Tsushima, and A. W. Thomas, "Nucleon and hadron structure changes in the nuclear medium and the impact on observables," *Progress in Particle and Nuclear Physics*, vol. 58, no. 1, pp. 1–167, 2007.

[26] P. Bühler, P. collaboration, *et al.*, "Studying hadrons in matter with panda," in *EXA 2011*, pp. 105–110, Springer, 2012.

[27] K. Goetzen, H. Orth, G. Schepers, L. Schmitt, C. Schwarz, and A. Wilms, "Proposal for a scintillator tile hodoscope for panda," *PANDA Note, March*, 2011.

[28] D. Steinschaden, *Optimization Studies and Performance Simulations for the Time-of-Flight System of PANDA*. PhD thesis, Technische Universität Wien, 2018.

[29] "Nist xcom: Photon cross sections database." https://www.nist.gov/pml/xcom-photon-cross-sections-database. Accessed: 2020-09-02.

[30] W. R. Leo, *Techniques for nuclear and particle physics experiments: a how-to approach*. Springer Science & Business Media, 2012.

[31] The PANDA Collaboration, "Technical design report for the: Panda barrel time-of-flight detector," July 2018.

[32] K. Makonyi, "Radiation map." private communications.

[33] "Atomic and nuclear properties of materials." https://pdg.lbl.gov/2009/AtomicNuclearProperties/. Accessed: 2020-08-28.

[34] G. Lindström, "Radiation damage in silicon detectors," *Nuclear Instruments and Methods in Physics Research Section A: Accelerators, Spectrometers, Detectors and Associated Equipment*, vol. 512, no. 1-2, pp. 30–43, 2003.

[35] M. Gupta, "Calculation of radiation length in materials," tech. rep., 2010. Technical Note CERN.

[36] C. Patrignani, D. Weinberg, C. Woody, R. Chivukula, O. Buchmueller, Y. V. Kuyanov, E. Blucher, S. Willocq, A. Höcker, C. Lippmann, *et al.*, "Review of particle physics," *Chin. Phys.*, vol. 40, p. 100001, 2016.

[37] "Mppc s13360-3050pe datasheet." https://www.hamamatsu.com/resources/pdf/ssd/s13360_series_kapd1052e.pdf, 8 2016. Accessed: 2020-07-15.

[38] "Programmable resolution 1-wire digital thermometer." https://datasheets.maximintegrated.com/en/ds/DS18B20.pdf, 7 2019. Accessed: 2020-08-23.

[39] G. F. Knoll, *Radiation detection and measurement*. John Wiley & Sons, 2010.

[40] "Introduction to the silicon photomultiplier." https://www.sensl.com/downloads/ds/TN-IntrotoSPMTech.pdf, 8 2018. Accessed: 2020-08-05.

[41] "Physics and operation of the mppc silicon photomultiplier." https://hub.hamamatsu.com/jp/en/technical-note/sipm-physics-operation/index.html, 2 2014. Accessed: 2020-07-15.

[42] F. Acerbi, A. Ferri, A. Gola, M. Cazzanelli, L. Pavesi, N. Zorzi, and C. Piemonte, "Characterization of single-photon time resolution: from single spad to silicon photomultiplier," *IEEE Transactions on Nuclear Science*, vol. 61, no. 5, pp. 2678–2686, 2014.

[43] S. Gundacker, E. Auffray, N. Di Vara, B. Frisch, H. Hillemanns, P. Jarron, B. Lang, T. Meyer, S. Mosquera-Vazquez, E. Vauthey, *et al.*, "Sipm time resolution: From single photon to saturation," *Nuclear Instruments and Methods in Physics Research Section A: Accelerators, Spectrometers, Detectors and Associated Equipment*, vol. 718, pp. 569–572, 2013.

[44] A. Vacheret, G. J. Barker, M. Dziewiecki, P. Guzowski, M. D. Haigh, B. Hartfiel, A. Izmaylov, W. Johnston, M. Khabibullin, A. Khotjantsev, *et al.*, "Characterization and simulation of the response of multi-pixel photon counters to low light levels," *Nuclear Instruments and Methods in Physics Research Section A: Accelerators, Spectrometers, Detectors and Associated Equipment*, vol. 656, no. 1, pp. 69–83, 2011.

[45] A. Heering, Y. Musienko, R. Ruchti, M. Wayne, A. Karneyeu, and V. Postoev, "Effects of very high radiation on sipms," *Nuclear Instruments and Methods in Physics Research Section A: Accelerators, Spectrometers, Detectors and Associated Equipment*, vol. 824, pp. 111–114, 2016.

[46] P. W. Cattaneo, M. De Gerone, F. Gatti, M. Nishimura, W. Ootani, M. Rossella, and Y. Uchiyama, "Development of high precision timing counter based on plastic scintillator with sipm readout," *IEEE Transactions on Nuclear Science*, vol. 61, no. 5, pp. 2657–2666, 2014.

[47] S. Cova, M. Ghioni, A. Lacaita, C. Samori, and F. Zappa, "Avalanche photodiodes and quenching circuits for single-photon detection," *Applied optics*, vol. 35, no. 12, pp. 1956–1976, 1996.

[48] A. Baldini, F. Cei, C. Cerri, S. Dussoni, L. Galli, M. Grassi, D. Nicolo, F. Raffaelli, F. Sergiampietri, G. Signorelli, *et al.*, "Meg upgrade proposal," *arXiv preprint arXiv:1301.7225*, 2013.

[49] S. Hall and H. Heck, *Advanced Signal Integrity for High-Speed Digital Designs*. Wiley - IEEE, Wiley, 2011.

[50] S. C. Thierauf, *High-speed circuit board signal integrity*. Artech House, 2017.

[51] S. Hall, G. Hall, and J. McCall, *High-Speed Digital System Design: A Handbook of Interconnect Theory and Design Practices*. A Wiley-Interscience publication, Wiley, 2000.

[52] H. Johnson and M. Graham, *High-speed Digital Design: A Handbook of Black Magic*. Prentice Hall Modern Semiconductor Design, Prentice Hall, 1993.

[53] H. Zhang, S. Krooswyk, and J. Ou, *High Speed Digital Design: Design of High Speed Interconnects and Signaling*. Elsevier Science, 2015.

[54] A. Ramdurgkar, "Loss vs frequency." private communications. University of Colorado.

[55] "Coaxial according to cern specification 461 rev. 6." https://www.prysmiangroup.com/sites/default/files/business_markets/markets/downloads/datasheets/hf32e_1.0.pdf, 08 2009. Accessed: 2020-09-26.

[56] Rogers Corporation, *RO4000-RO4003C-RO4350B-RO4835 Laminates Data Sheet*, 2018.

[57] R. de Oliveira. private communications. Micro-Pattern Technologies CERN.

[58] V. Judin, "Rogers 4003c radiation length." private communications. Rogers Corporation.

[59] "Fast timing plastic scintillator ej-232, ej-232q." https://eljentechnology.com/images/products/data_sheets/EJ-232_EJ-232Q.pdf, 5 2016. Accessed: 2020-07-15.

[60] A. Ebran, J. Taieb, G. Belier, A. Chatillon, B. Laurent, J.-F. Martin, and E. Pellereau, "Picosecond resolution on relativistic heavy ions' time-of-flight measurement," *Nuclear Instruments and Methods in Physics Research Section A: Accelerators, Spectrometers, Detectors and Associated Equipment*, vol. 728, pp. 40–46, 2013.

[61] "Estar, pstar, and astar: Stopping-power and range tables for electrons, protons, and helium ions." https://physics.nist.gov/PhysRefData/Star/Text/ESTAR.html. Accessed: 2020-09-02.

[62] "Plastic scintillator sheet sizes and thickness tolerances." https://eljentechnology.com/images/technical_library/Sheet_SizesThickness_Tol.pdf, n/a. Accessed: 2020-07-15.

[63] L. Durieu, M. Martini, and A.-S. Muller, "Optics studies for the t9 beam line in the cern ps east area secondary beam facility," in *PACS2001. Proceedings of the 2001 Particle Accelerator Conference (Cat. No. 01CH37268)*, vol. 2, pp. 1547–1549, IEEE, 2001.

[64] J. Bernhard, "Beamline for schools 2018," Sep 2018.

[65] A. Neiser, J. Adamczewski-Musch, M. Hoek, W. Koenig, G. Korcyl, S. Linev, L. Maier, J. Michel, M. Palka, M. Penschuck, *et al.*, "Trb3: a 264 channel high precision tdc platform and its applications," *Journal of Instrumentation*, vol. 8, no. 12, p. C12043, 2013.

[66] "Planacon, technical information." https://www.photonis.com/products/planacon, 10 2020. Accessed: 2020-09-26.

[67] L. D. Landau, L. Landau, L. Landau, L. LanDau, and L. Landau, "On the energy loss of fast particles by ionization," 1944.

[68] P. Vavilov, "Ionization losses of high-energy heavy particles," *Sov. Phys. JETP*, vol. 5, pp. 749–751, 1957.

[69] H. A. Bethe, "Molière's theory of multiple scattering," *Phys. Rev.*, vol. 89, pp. 1256–1266, Mar 1953.

[70] G. Shen *et al.*, "Measurement of Multiple Scattering at 50-GeV/c to 200-GeV/c," *Phys. Rev. D*, vol. 20, p. 1584, 1979.

Acknowledgments

First and foremost I want to thank my supervising professor Kai Brinkmann for providing guidance and the economic opportunity to continue my studies as well as for connecting me to the SMI and allowing me to pursue physics in Vienna. In this regard I also want to thank Hans Marton for providing the contact to Vienna and the guidance throughout my studies.

I also want to express my gratitude towards all the staff members and colleagues, former and current at the Stefan-Meyer-Institute that make it a great working environment. My thanks go out to Ken Suzuki for showing me what is expected of a graduate student and pushing me to participate in international conferences. I want to thank Hannes Zmeskal for helping me in the lab whenever I would be stuck or needed guidance and for pushing the project along, as well as Svetlana Chesnevskaya for the help with the measurements of the Rail-Boards. I also want to thank Julia and the other staff members for all the technical support you provided and my colleagues for the fun evenings of competitive N64.

A special thanks goes out to PD Dr. A. Lehmann and Merlin Böhm without whom I would not have been able to complete the time resolution studies, who helped me throughout with good advice and enabled the recording of the necessary data. I also thank you for the hospitality you showed us during our visit to Erlangen.

I received unexpected help from Ameya Ramadurgakar and Prof. Eric Bogatin for the UCCS Applied Electromagnetics Research Laboratory in Colorado, helping me better understand the losses of the Rail-Board for which I am very grateful.

I am also grateful for everyone who helped write this dissertation from my colleagues in the EMC working group in Gießen as well as to my good friend Simon Resch who provided valuable advice and feedback during the writing process.

Most importantly however I want to thank by precious wife Ida, who supported me tirelessly throughout my studies, giving me the strength to always move forward. Helping me push through the last stretch of my studies, I want to dedicate this work to my unborn child. You have given me the drive to do my best at all times and have given me a deadline I can not postpone. Again, thank you to you all.

Selbständigkeitserklärung

Hiermit versichere ich, die vorgelegte Thesis selbstständig und ohne unerlaubte fremde Hilfe und nur mit den Hilfen angefertigt zu haben, die ich in der Thesis angegeben habe. Alle Textstellen, die wörtlich oder sinngemäß aus veröffentlichten Schriften entnommen sind, und alle Angaben die auf mündlichen Auskünften beruhen, sind als solche kenntlich gemacht. Bei den von mir durchgeführten und in der Thesis erwähnten Untersuchungen habe ich die Grundsätze guter wissenschaftlicher Praxis, wie sie in der, Satzung der Justus- Liebig-Universität zur Sicherung guter wissenschaftlicher Praxis‘ niedergelegt sind, eingehalten. Gemäß § 25 Abs. 6 der Allgemeinen Bestimmungen für modularisierte Studiengänge dulde ich eine Überprüfung der Thesis mittels Anti-Plagiatssoftware.

Datum	Sebastian Zimmermann